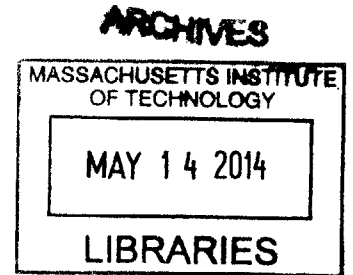


Synthesis of III-V Nitride Nanowires with Controlled Structure, Morphology, and Composition

by
Samuel Curtis Crawford
B.S. Chemical Engineering
Washington University in St. Louis, 2008



Submitted to the Department of Materials Science and Engineering
In Partial Fulfillment of the Requirements for the Degree of

Doctor of Philosophy
at the
Massachusetts Institute of Technology

February 2014

© 2014 Massachusetts Institute of Technology. All rights reserved.

Signature of Author: _____
Department of Materials Science and Engineering
September 4, 2013

Certified by: _____
Silvija Gradečak
Associate Professor of Materials Science and Engineering
Thesis Supervisor

Accepted by: _____
Gerbrand Ceder
R. P. Simmons Professor of Materials Science and Engineering
Chair, Departmental Committee on Graduate Students

Synthesis of III-V Nitride Nanowires with Controlled Structure, Morphology, and Composition

by
Samuel Curtis Crawford

Submitted to the Department of Materials Science and Engineering on September 4, 2013
In Partial Fulfillment of the Requirements for the Degree of
Doctor of Philosophy in Materials Science & Engineering

The III-V nitride materials system offers tunable electronic and optical properties that can be tailored for specific electronic and optoelectronic applications by varying the (In,Ga,Al)N alloy composition. While nitride thin films tend to suffer from high dislocation densities due to the lattice mismatch with growth substrates, nanowires can be grown dislocation-free on highly mismatched substrates including silicon. Furthermore, axial and radial junction configurations offer unique nanoscale device architectures that enable more optimal device design. In order to realize the potential benefits of III-V nitride nanowires, precise control of nanowire synthesis is required. This thesis describes the development of experimental techniques and theoretical models that guide the synthesis of III-V nitride and other compound semiconductor nanowires with control over material structure, morphology, and composition.

First, GaN nanowires were synthesized with control over nanowire orientation, morphology, and defect density. Substrate orientation was used to control whether nanowires grew preferentially in the polar [0001] direction or the nonpolar [1-100] direction. Film deposition on the nanowire sidewalls was effectively minimized by reducing the Ga precursor flux and inter-nanowire spacing. Using nonpolar-oriented GaN nanowires with uniform diameter, the diameter-dependent growth rate was modeled to demonstrate that growth is limited by nucleation at the perimeter of the seed/nanowire interface. Finally, Ni- and Au-seeded GaN nanowires were directly compared, and the higher growth rate and reduced defect density in Ni-seeded nanowires were consistent with a reduced seed/nanowire interfacial energy.

Next, nonpolar-oriented InN/InGaN axial heterostructure nanowires were grown by introducing Ga precursors during InN nanowire growth. The formation of GaN shells placed an upper limit on the allowable Ga precursor flux. Shell deposition was minimized by operating at higher temperature and pressure. However, a reduction in the local supply of Ga to the seed particle also limited InGaN formation. Therefore, brief high-flux pulses were used at lower pressure to form InN/InGaN axial heterostructures with minimal shell formation. Electron tomography and energy dispersive X-ray spectroscopy were used to analyze the Ga-driven changes in nanowire morphology and composition, respectively. The reduction in nanowire diameter upon the introduction of Ga was found to be driven by changes in seed particle composition.

A flow-controlled approach was developed to modulate the diameter along individual nanowires, which can enable unique properties including enhanced light trapping in nanowire arrays and increased phonon scattering in thermoelectrics. In InN nanowires, a reduction in V flow produced segments with larger diameters and slower growth rates. A reduction in III flow

in GaN nanowires also produced segments with slower growth rates, but thinner diameters. These trends are a consequence of the separate pathways traveled by the III and V sources to the site of reaction, enabling control over the incorporation rate of III source into the seed particle and the extraction rate of III source out of the seed particle, respectively.

Based on these promising results, models were developed to explore the potential for template-free nanowire diameter modulation via particle-mediated growth. The results from diameter-modulated InN and GaN nanowires were evaluated considering contributions of seed particle volume, wetting angle, and three-dimensional morphology to the observed diameter changes. To achieve large diameter ratios using liquid seed particles, significant changes in both seed particle volume and wetting angle are necessary. Furthermore, the model was used to evaluate the surface energy and morphology of the liquid/solid interface. The interface was found to not be flat, contrary to common assumptions, which has significant implications for nanowire growth models.

Finally, we extended the flow-controlled diameter modulation approach to GaAs nanowires, demonstrating that the technique is generally applicable to particle-mediated compound semiconductor nanowires. Both the III and V sources were varied during growth, producing similar trends in diameter and growth rate as with III-V nitride nanowires. Notably, three different types of [111]B-oriented nanowires were observed and had discrete differences in diameter modulation, growth rate, and cross-sectional shape, which were attributed to differences in seed particle phase. By controlling growth conditions during nanowire nucleation, each of the three types of nanowires were preferentially produced, indicating that the seed particle phase can be controllably varied in compound-forming seed alloys.

Together, these results provide a foundation for fabricating III-V nitride and other nanowires with control over material structure, morphology, and composition. Experimental techniques and theoretical models were developed that enable control over growth direction, tapering, growth rate, defect density, composition, and diameter. These tools are helpful in achieving nanowires with rationally tailored properties for functional nanowire-based devices.

Thesis Supervisor: Silvija Gradečak

Title: Associate Professor of Materials Science & Engineering

Acknowledgements

I have been incredibly fortunate to not only have the opportunity to engage in this thesis work, but also to have such a wonderful network of mentors, colleagues, friends, and family who have provided me with all types of support that have made this work possible and enriched my experience during the past few years.

My advisor, Prof. Silvija Gradečak, has been an incredible mentor who has challenged me to grow as a scientist and has been remarkably patient and supportive. In addition to her scientific expertise, she has helped me greatly in prioritizing my efforts and effectively communicating my work. I also greatly appreciate the contributions from my other committee members: Prof. Geoffrey Beach, who has not hesitated to help me when I have needed it, whether by taking over a spot on my committee, working on 3.014 labs, or helping me prepare for my oral examination; and Prof. Carl Thompson, who has also been incredibly helpful over the years and has offered great insight and thought-provoking questions.

It has been a pleasure to work (and play) with the great minds and personalities of the Gradečak Group. Everyone has been amazingly helpful, collaborative, and friendly. Special thanks go out to: Dr. Sung Keun Lim for teaching me the ropes of MOCVD, nanowire growth, and electron microscopy; Dr. Megan Brewster for minimizing my interactions with the e-beam evaporator and for helping to connect me with my match, Sarah Valentine; Dr. Matt Smith for always been willing to take time to help others get their work done and for orchestrating countless palace gatherings and weekend trips to help us take a break from work; Jordan Chesin and Xiang Zhou for help maintaining the nitride reactor and for plenty of quality scientific and non-scientific discussion; Eric Jones and Sema Ermez for helping me down the stretch with critical work on GaAs nanowires; and John Hanson for organizing regular group lunches. I have had the privilege to spend my days with some great office mates: Sung Keun, Dr. Shenqiang Ren, Dr. Sehoon Chang, Dr. Xiaosheng Fang, Dr. Filippo Fabri, and Amirreza Kiani. My experience here has been made better by all the other members with whom I have been fortunate enough to share time: Jayce Cheng, Paul Rekemeyer, Hyoungwon Park, Tina Safaei, Christopher Francis, Dr. Chun-Hao Tseng, Dr. Mingsheng Wang, Dr. Ming-Yen Lu, Prof. Amal Abdulla Al Ghaferi, Dr. Xiaosheng Fang, Dr. Kamal Baloch, Dr. Matteo Seita, and Dr. Hyesung Park.

I am deeply grateful for the collaborative efforts of my colleagues, which were absolutely essential to this work. I worked closely with both Sung Keun and Megan in my initial efforts on GaN nanowire growth and later worked closely with Jordan and Xiang on various nitride nanowires. Sung Keun fabricated some of the nanowires discussed in this thesis, including the GaN nanowires for the nucleation-mediated growth model in Chapter 4, some of the InN/InGaN axial heterostructures in Chapter 5, and the InN nanowires in Chapter 6. Also, Xiang grew the Au-seeded and Ni-seeded GaN nanowires discussed in Chapter 4. In each case, they also contributed greatly to nanowire characterization and theoretical development. Georg Haberschlager (CEA-Leti) performed the electron tomography analysis both in Chapter 5 on InN/InGaN nanowires and in Chapter 8 on GaAs nanowires. Steven Boles (KIT) performed the

bending tests on the GaN nanowires in Chapter 6. Sema and Eric helped me to grow the GaAs nanowires in Chapter 8 and provided critical expertise. I am also grateful for collaborations with Shenqiang and Mike on nanowire photovoltaics and with Ming-Yen and Xiang on GaN/ZnGa₂O₄ nanostructures, which produced publications not described in this thesis.

A variety of staff at MIT were essential in making this work possible. Special thanks to: Yong Zhang, Shiahn Chen, and Patrick Boisvert in the Center for Materials Science and Engineering for training me on electron microscopy equipment and for working daily to keep the equipment up and running; Kurt Broderick for making trips to the Exploratory Materials Laboratory much more enjoyable; and Angelita Mireles and Elissa Haverty in the department's academic office for helping me with numerous logistical questions over the years.

I would not have had this opportunity if it were not for some great mentors in life. I thank my parents, Gary and Emily Crawford, for providing me with so many opportunities in life and for teaching me how to make the most of them. They, along with my sister Jill, have always been there for me with love, support, and sage advice. I have had many wonderful teachers, but particularly want to thank Bill Davis for teaching me how to think critically and Michelle Radio Buche for giving me the inspiration and self-confidence to set ambitious goals for myself. Additionally, I greatly appreciate Prof. Pratim Biswas, Prof. Daniel Giammar, and Dr. Vince Battaglia for giving me the opportunity to perform undergraduate research, as well as Elijah Thimsen, James Noel, and Honghe Zhang for providing with guidance during those experiences.

I could not imagine getting through the past 5 years without all of my friends. Friends from Wash U – Adam D'Agostine, John Godfrey, Seth Goodman, and Sharad Wadwhani – helped to make the transition from St. Louis to Boston much easier. Meanwhile, Matt Connors, Jo Engel, and Katy Hartman made the transition from chemical engineering to materials science much easier. I have countless memories from adventures with everyone in Awesom-O and particularly appreciate everyone at the palace – Sal Barriga, Brian Beliveau, Tom Fellows, Rahul Malik, and Matt Smith – for regularly hosting our crew, as well as Joan Mao and Matt for making P-Day weekend one of the highlights of my year every year. My roommates at 80 Webster, Matt Connors and Chris Ng, made daily life awesome, and I appreciate them puttNg up with my level 10 flipouts during KU games. Life in grad school would not have been the same without the guys in MechE: Kevin Cedrone, Dave Fenning, Bill Polacheck, and Joe Sullivan. The highlight of my time here was meeting Sarah Valentine, who has made every experience since then more enjoyable. Being rich where I am deficient, she has been the perfect teammate to help me navigate my way through grad school and life.

This work was supported in part by a National Science Foundation (NSF) Graduate Research Fellowship, the MRSEC program of the NSF under award DMR-0819762, NSF CAREER award DMR-0745555, ENI SpA under the ENI-MIT Solar Frontiers Program, and the MIT-Masdar Program. Shared facilities in the Center for Materials Science and Engineering supported in part by the MRSEC program of the NSF under award DMR-0213282.

Table of Contents

List of Figures.....	11
List of Tables	15
Chapter 1: Introduction	17
1.1. Nanowire-based devices	17
1.2. III-V nitride nanowires	20
1.3. Nanowire fabrication	21
1.4. Thesis outline	22
Chapter 2: Fundamentals of Nanowire Growth	25
2.1. Nanowire fabrication techniques	25
2.1.1. <i>Top-down nanowire fabrication</i>	25
2.1.2. <i>Anisotropic nanowire growth</i>	26
2.1.3. <i>Particle-mediated nanowire growth</i>	27
2.2. Fundamentals of particle-mediated nanowire growth.....	29
2.2.1. <i>Fundamental processes</i>	29
2.2.2. <i>Nucleation and the liquid/solid interface</i>	32
2.2.3. <i>Seed material</i>	35
2.3. Nanowire architectures	35
2.3.1. <i>Crystallographic growth direction</i>	36
2.3.2. <i>Tapering</i>	38
2.3.3. <i>Nanowire junctions and heterostructures</i>	39
2.3.4. <i>Diameter modulation</i>	41
Chapter 3: Experimental Methods.....	43
3.1. Synthesis of III-V nitride nanowires.....	43
3.1.1. <i>Experimental setup</i>	43
3.1.2. <i>Substrate preparation</i>	45
3.1.3. <i>GaN nanowire growth</i>	45
3.1.4. <i>InN nanowire growth</i>	46
3.1.5. <i>Growth of InN/InGaN axial heterostructures</i>	47
3.2. Synthesis of GaAs nanowires	47
3.2.1. <i>Experimental setup & growth conditions</i>	47
3.2.2. <i>Substrate preparation</i>	48
3.3. Electron microscopy characterization.....	49
3.3.1. <i>Scanning electron microscopy</i>	51

3.3.2.	<i>Transmission electron microscopy</i>	52
3.3.3.	<i>Scanning transmission electron microscopy</i>	53
3.3.4.	<i>Energy-dispersive x-ray spectroscopy</i>	54
3.3.5.	<i>Electron tomography</i>	55
3.4.	Data analysis and modeling techniques	56
3.4.1.	<i>EDS measurements of seed particles and nanowires</i>	56
3.4.2.	<i>Evolution of diameter along the nanowire axis</i>	58
Chapter 4: Structural & morphological control of GaN nanowires		61
4.1.	Control of GaN nanowire growth direction and tapering	61
4.1.1.	<i>Control of crystallographic growth direction</i>	62
4.1.2.	<i>Tapering minimization</i>	64
4.2.	Nucleation-mediated growth model	66
4.2.1.	<i>Diameter-dependent growth rate</i>	67
4.2.2.	<i>Effect of hydrogen</i>	71
4.3.	Defect minimization through seed material selection	73
4.3.1.	<i>Morphology</i>	73
4.3.2.	<i>Structure</i>	76
4.4.	Summary	79
Chapter 5: InN/InGaN axial heterostructure nanowires		81
5.1.	Ga incorporation into InN nanowires	81
5.1.1.	<i>InN nanowire basis</i>	82
5.1.2.	<i>TMG flux</i>	83
5.1.3.	<i>Pressure</i>	85
5.1.4.	<i>Temperature</i>	86
5.1.5.	<i>Seed particle composition</i>	88
5.2.	InN/InGaN axial heterostructures	89
5.2.1.	<i>Structure & composition</i>	90
5.2.2.	<i>Cross-section evolution</i>	91
5.3.	Summary	95
Chapter 6: Growth of diameter-modulated GaN & InN nanowires		97
6.1.	Modulation of InN diameter with the V source	98
6.1.1.	<i>Diameter and growth rate changes in InN nanowires</i>	98
6.1.2.	<i>Seed particle composition</i>	100
6.1.3.	<i>Mechanism of V-flow-induced diameter modulation</i>	102
6.2.	Diameter modulation of GaN nanowires with the III source	104
6.2.1.	<i>Ga-induced changes in diameter and growth rate</i>	104
6.2.2.	<i>Mechanism of III-flow-induced diameter modulation</i>	106

6.3.	Diameter modulation for controlled fracture	107
6.3.1.	<i>Producing thin-diameter notches</i>	108
6.3.2.	<i>Preferential fracture</i>	110
6.4.	Summary	112
Chapter 7:	Modeling diameter-modulated nitride nanowires.....	115
7.1.	Theoretical model	115
7.1.1.	<i>Calculation of wetting angle</i>	115
7.1.2.	<i>Surface Evolver for non-cylindrical nanowires</i>	116
7.1.3.	<i>Model accuracy</i>	118
7.1.4.	<i>Liquid/solid interface morphology</i>	120
7.2.	Factors affecting diameter modulation	121
7.2.1.	<i>InN nanowires and the role of cross-sectional geometry</i>	121
7.2.2.	<i>GaN nanowires and the role of seed particle composition</i>	125
7.3.	Morphology of the liquid/solid interface	127
7.3.1.	<i>Potential morphologies</i>	128
7.3.2.	<i>Force balances</i>	128
7.3.3.	<i>Surface energies</i>	130
7.3.4.	<i>Nanowire diameter evolution</i>	131
7.4.	Opportunities, limitations, and the role of materials selection	134
7.5.	Summary	136
Chapter 8:	Diameter modulation of GaAs nanowires	139
8.1.	Diameter modulation with both the III & V sources	139
8.1.1.	<i>Diameter modulation with the III & V sources</i>	140
8.1.2.	<i>The role of the III & V sources in nanowire growth</i>	142
8.2.	Variations between different nanowires	144
8.2.1.	<i>Nanowire types</i>	144
8.2.2.	<i>Cross-sectional shape for different nanowire types</i>	146
8.2.3.	<i>Origin of differences in cross-sectional shape</i>	150
8.3.	Control of nanowire type	153
8.3.1.	<i>Diameter dependence</i>	154
8.3.2.	<i>Substrate dependence</i>	156
8.3.3.	<i>Dependence upon growth conditions</i>	159
8.4.	Summary	162
Chapter 9:	Conclusions	165
9.1.	Summary & implications of thesis work	165
9.2.	Suggested future work	167
9.2.1.	<i>Alternative seed metals for III-V nitride axial heterostructures</i>	168

9.2.2. <i>Quantitative fracture analysis of notched nanowires</i>	168
9.2.3. <i>Role of seed particle in phase in ternary alloy growth</i>	169
List of Abbreviations	171
References	173

List of Figures

Figure 1-1. Radial and axial nanowire heterostructures	18
Figure 1-2. Planar vs radial p/n junction solar cells.....	19
Figure 2-1. Methods of nanowire fabrication	26
Figure 2-2. Vapor-liquid-solid (VLS) mechanism of nanowire growth.....	28
Figure 2-3. Fundamental processes in III-V nitride nanowire growth.....	30
Figure 2-4. Liquid/solid interface morphology during nanowire growth.....	33
Figure 2-5. Growth mechanisms for faceted liquid/solid interfaces.....	34
Figure 2-6. Surface energies affecting growth direction	36
Figure 2-7. Nitride crystallography.....	38
Figure 2-8. Tapered nanowire	39
Figure 3-1. Chemical vapor deposition system for nitride nanowire growth	44
Figure 3-2. Setup for CVD and MOCVD GaN nanowire growth	46
Figure 3-3. Setup for InN and InN/InGaN nanowire growth.....	47
Figure 3-4. Chemical vapor deposition system for GaAs nanowire growth.....	48
Figure 3-5. Signal production by high-energy electrons in electron microscopy	50
Figure 3-6. Scanning electron microscopy	51
Figure 3-7. Transmission electron microscopy.....	53
Figure 3-8. Scanning transmission electron microscopy	54
Figure 3-9. Energy dispersive X-ray spectroscopy	54
Figure 3-10. Electron tomography	55
Figure 3-11. Models for cross-sectional EDS linescans	57
Figure 3-12. Model for nanowire diameter evolution.....	58

Figure 4-1. Controlling the growth direction of GaN nanowires.....	63
Figure 4-2. Tapering control in GaN nanowires.....	65
Figure 4-3. GaN nanowires grown using different carrier gas composition.....	67
Figure 4-4. Diameter-dependent growth rate of GaN nanowires	68
Figure 4-5. Nucleation-mediated nanowire growth.....	69
Figure 4-6. Liquid/solid interface morphology.....	71
Figure 4-7. Hydrogen-driven reduction in supersaturation.....	72
Figure 4-8. Morphology of Au-seeded and Ni-seeded nanowires.....	74
Figure 4-9. Structure of Au-seeded and Ni-seeded nanowires	76
Figure 4-10. Distribution of stacking faults in Au-seeded nanowires	77
Figure 4-11. Surface energy of stacking fault formation.....	78
Figure 5-1. Structure of InN nanowires	82
Figure 5-2. Effect of TMG flux on axial InGa _N growth and radial GaN growth.....	84
Figure 5-3. Effect of system pressure	85
Figure 5-4. Effect of temperature on growth rate	87
Figure 5-5. Effect of temperature on InGa _N formation.....	88
Figure 5-6. Morphology of caterpillar-shaped InN-InGa _N heterostructures.....	90
Figure 5-7. Composition of InN-InGa _N heterostructures and seed particles	91
Figure 5-8. Tomography of caterpillar-shaped InN-InGa _N heterostructures	92
Figure 5-9. Diameter and composition changes in InN-InGa _N heterostructure.....	94
Figure 6-1. InN nanowires oriented in the <i>m</i> - and <i>c</i> -directions	99
Figure 6-2. Diameter-modulated InN nanowires via V source reduction.....	100
Figure 6-3. Au-In seed particle composition	101

Figure 6-4. Mechanism of InN nanowire diameter evolution.....	103
Figure 6-5. Diameter-modulated GaN nanowires using via III source reduction.....	105
Figure 6-6. Anisotropic diameter evolution in GaN nanowires.....	106
Figure 6-7. Mechanism of GaN nanowire diameter evolution	107
Figure 6-8. Applications of controlled fracture in nanowires.....	108
Figure 6-9. Notched GaN nanowires	109
Figure 6-10. Notched GaN nanowire with variable carrier gas composition	110
Figure 6-11. Bending tests of notched GaN nanowires	111
Figure 7-1. Wetting angle of the seed particle	116
Figure 7-2. Surface Evolver model.....	117
Figure 7-3. Actual versus nominal wetting angle	118
Figure 7-4. Comparison of Surface Evolver model with <i>in situ</i> TEM studies	119
Figure 7-5. Effect of nanowire corner curvature on measured wetting angle	120
Figure 7-6. Effect of extra tilted facet at liquid/solid interface edge on seed morphology	121
Figure 7-7. Diameter modulation maps of InN nanowires with different cross-sections.....	123
Figure 7-8. GaN nanowires with large diameter ratios.....	126
Figure 7-9. Surface energies and force balances at the triple-phase boundary for different liquid/solid interface morphologies	128
Figure 7-10. Evolution of III-V nitride nanowire diameter via varied precursor flux.....	133
Figure 7-11. Contributions of changes in surface to changes in nanowire diameter.....	135
Figure 8-1. Diameter-modulated GaAs nanowires	141
Figure 8-2. Diameter-modulated GaAs nanowires with V and III variation in a single growth	142
Figure 8-3. Defects resulting from low V/III ratios.....	143
Figure 8-4. Variable diameter modulation between different GaAs nanowires	145

Figure 8-5. Cross-section-dependent diameter modulation	147
Figure 8-6. Cross-section evolution.....	148
Figure 8-7. Facet orientation.....	149
Figure 8-8. Type B straight nanowires with no change in AsH ₃ flow	150
Figure 8-9. Parameters affecting GaAs nanowire growth	152
Figure 8-10. Diameter dependence of nanowire type	155
Figure 8-11. Substrate dependence of nanowire type	158
Figure 8-12. Dependence of nanowire type on nucleation temperature	160
Figure 8-13. Dependence of nanowire type on V/III ratio during nucleation	161

List of Tables

Table 7-1. Parameters for thin (d_1) and thick (d_2) segments of diameter-modulated InN nanowires with different cross sections.....	122
Table 7-2. Required changes in volume and wetting angle for observed changes in diameter of hexagonal InN nanowires	124
Table 7-3. Parameters for diameter-modulated GaN nanowires	127
Table 7-4. Surface energies during diameter-modulated InN and GaN nanowire growth.	131

Chapter 1: Introduction

Semiconductors are the foundation of today's electronic and optoelectronic devices, from computers to solar cells. Further advances in semiconductor devices are necessary for electronics to keep pace with Moore's law, for more efficient and cost-effective lighting technology, for generation of renewable solar energy, and for effective integration of intermittent energy sources into the electric grid. Conventional semiconductor devices are generally based upon films of semiconducting material – usually silicon – but demands for improved device performance will require the use of novel materials and non-planar device architectures. Nanowires, with their unique quasi-one-dimensional geometry, offer a promising platform for fabricating devices with geometries and materials that are optimally tailored for specific applications.¹⁻³

The III-V nitride materials system is a promising alternative to conventional semiconductors such as silicon, as optical properties can be tailored by varying the composition of GaInAlN alloys.¹ While nitride films are rife with threading dislocations, which are defects caused by lattice mismatch with the underlying substrate, nanowires can be grown dislocation-free on highly mismatched substrates.² Nanowires can therefore enhance the properties of III-V nitride materials and enable their integration with other semiconductor materials, including silicon. To realize the advantages nanowire-based devices, it is necessary to exercise precise control of nanowire structure, morphology, and composition, which remains a challenge.³⁻⁸ The focus of this thesis is to investigate fundamental mechanisms of nanowire growth in order to develop theoretical models and experimental techniques that lay the foundation for controlled growth of III-V nitride nanowires.

1.1. Nanowire-based devices

The unique quasi-one-dimensional geometry of nanowires – which have nanometer-scale diameters and micron-scale lengths – offers a variety of advantages in comparison to the planar geometry of thin films, including efficient strain relaxation and alternative device geometries via axial and radial variations in material composition and properties. The high surface-to-volume ratio of nanowires allows efficient strain relaxation such that nanowires can be grown dislocation-free on lattice-mismatched substrates.² While silicon is today's standard for

semiconductor-based devices, other materials offer superior properties for various applications. For example, the wide bandgap of GaN-based materials offers higher voltages, higher frequencies, and high-temperature operation for power electronics. Unfortunately, the lack of lattice-matched substrates available for epitaxial GaN growth results in high threading dislocation densities in GaN thin films (10^6 – 10^{12} cm⁻²),⁹ which have been associated with high leakage current in electronic devices,¹⁰ yellow defect luminescence,¹¹ and non-radiative recombination.¹² However, GaN nanowires can be grown dislocation-free on highly mismatched substrates, including Si.²

Nanowires provide a versatile platform for building nanoscale devices. In particular, electronic homojunctions and heterojunctions can be generated either radially or axially (Figure 1-1). For many electronic and optoelectronic devices, these nanowire architectures can offer enhanced performance compared to planar device geometries. In electronics, vertically aligned nanowires with a radially coated gate offer the ability to create a high density of transistors.¹³ Furthermore, this gate-all-around configuration allows for junctionless transistors that control switching without the need for *p/n* junctions,¹⁴ which is particularly valuable because control of dopant levels becomes significantly more challenging as the transistor size is reduced.

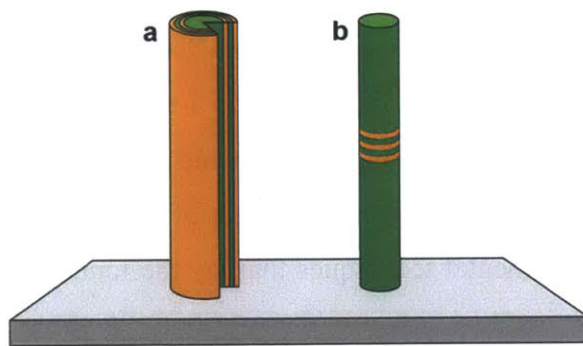


Figure 1-1. Radial and axial nanowire heterostructures. (a) Schematic illustration of a radial nanowire heterostructure with a wedge-shaped section removed to show the radial variation in composition. (b) Axial heterostructure in which discs of different composition are placed along the nanowire. Green and orange regions represent different material composition.

Effective thermoelectric energy conversion requires that the material effectively scatter phonons to reduce heat conduction, but conduct electrons to allow current to flow. These effects are generally coupled, limiting the performance of thermoelectric devices.¹⁵ Nanowires, however, have diameters significantly smaller than the wavelength of phonons but greater than

the wavelength of electrons. Consequently, nanowires with axial p/n junctions can achieve significantly higher thermoelectric figures of merit in comparison to their planar counterparts.^{16,17}

For photovoltaics, radial p/n junction nanowires allow light absorption and carrier transport processes to be geometrically decoupled. Most commercial photovoltaic (PV) devices today consist of a planar film of material (e.g. Si) with an electron-conducting n -type region and a hole-conducting p -type region layered on top of one another. Light absorption increases with thickness, but this also increases the probability that photoexcited carriers will lose their energy through recombination processes before being collected at the electrodes. By utilizing radial heterojunction nanowires (Figure 1-2), transport occurs across the width of the nanowires, reducing the distance that carriers must travel without recombining. This allows the length of the nanowires to be increased, therefore enhancing absorption, without deleterious effects on carrier transport. Furthermore, nanowire arrays reduce reflection off of the top surface due the presence of pores and then effectively trap the light that enters those pores. Consequently, their absorptance can be much greater than films of the same thickness and can approach near-unity values.^{18,19}

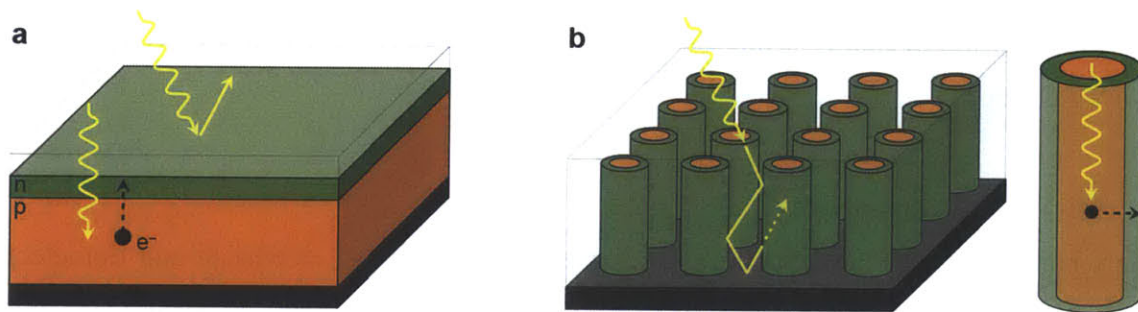


Figure 1-2. Planar vs radial p/n junction solar cells. (a) Planar p/n junction illustrating how light absorption and charge carrier transport processes each depend on the film thickness. Reflection off of the top surface is also shown. (b) Radial p/n junction nanowire array illustrating light trapping within the array (left) and the decoupling of absorption and transport processes, which occur vertically and laterally, respectively, within an individual nanowire (right). Green and orange regions represent n - and p -type layers, respectively. Yellow lines and black dots represent photons and electrons, respectively. Transparent and black layers represent electrodes.

Organic photovoltaics (OPVs) offer the ability to fabricate lightweight PV modules on flexible substrates using roll-to-roll processing. These devices could reduce both module and

installation costs, each of which comprise about half of total installed PV system costs.²⁰ However, the performance of OPVs is hindered by limited absorption due to sub-optimal bandgaps, poor carrier separation because of the short exciton diffusion length in organic materials, and poor carrier transport due to the low electron conductivity in acceptor materials and a lack of direct transport pathways in bulk heterojunctions.^{21,22} A promising alternative is a hybrid photovoltaic device that integrates inorganic nanowires with organic materials. Nanowires offer complementary absorption, high electron conductivity, and improved carrier separation and transport via ordered arrays with direct transport pathways to the electrode.^{23,24}

Nanowires also offer many performance enhancements for semiconductor light emitting diodes (LEDs) and lasers, which utilize multiple-quantum-wells (MQWs) to tune the wavelength of emitted light and spatially confine electrons and holes to promote radiative recombination. By moving from films to nanowires, this confinement is enhanced.²⁵ Radial heterostructures can also provide more total surface area for recombination than planar films.²⁶ Because nanowires function as free-standing Fabry-Perot cavities, low lasing thresholds can be achieved.²⁷ In addition to enhancing light emission, nanowires also enhance light extraction. Total internal reflection limits the performance of LEDs, but the presence of multiple facets on nanowires reduces this effect.²⁸ Periodic nanowire arrays can act as photonic crystals that enhance directional emission of light,²⁹ while individual nanowires can also promote directional emission via waveguiding.³⁰⁻³²

1.2. III-V nitride nanowires

GaN-based materials are excellent candidates for a variety of electronic and optoelectronic devices, including some of those described above. In addition to their direct bandgaps and high carrier mobilities, alloys of III-V nitrides offer bandgap tunability from infrared (InN = 0.7 eV) to ultraviolet (GaN = 3.4 eV, AlN = 6.0 eV) photon energies. For electronics, the wide bandgap of AlGaN offers higher voltages, frequencies, and operating temperatures in comparison to conventional Si-based materials. For photovoltaics, InGaN alloys offer strong and tunable light absorption, as well as high radiation resistance.¹ Due to visible light emission and efficient carrier recombination, InGaN materials are already being used in commercially available LEDs.

Single-crystalline GaN is difficult to grow from a melt due to decomposition into Ga and N₂ prior to reaching its high melting point (2500°C).³³ Instead, it is generally grown on a foreign

substrate that can offer a lattice-matched template for epitaxial growth. Although GaN can be grown on a variety of substrates including sapphire, SiC, and silicon,^{34,35} GaN films are plagued by high densities of threading dislocations due to the mismatch between the GaN lattice and the host lattice of the substrate.⁹ As stated previously, nanowires offer the ability to grow dislocation-free III-V nitrides on highly mismatched substrates, including Si.²

In addition, nanowires offer the ability to grow III-V nitrides in nonpolar directions. The III-V nitrides generally adopt a wurtzite crystal structure in which the arrangement of atoms the unit cell produces spontaneous polarization in the $\langle 0001 \rangle$ *c*-direction. Because available substrates for GaN growth offer the best lattice match in the *c*-direction, most GaN-based films are grown in this polar orientation to minimize threading dislocations. However, polar orientations are non-ideal for light recombination. Nitride LEDs use a MQW structure which promotes carrier recombination by localizing electrons and holes within the InGaN quantum wells. For polar heterojunctions, strain between GaN and the InGaN quantum wells causes piezoelectric effects that induces band bending and a consequent spatial separation of electrons and holes. This effect, called the quantum-confined Stark effect (QCSE),³⁶ can be avoided by orienting the heterojunctions along a nonpolar direction.³⁷ Although it is challenging to grow nonpolar GaN films with low dislocation densities, it is possible to grow high-quality nonpolar-directional GaN in the form of nanowires.³⁸

1.3. Nanowire fabrication

While nanowires offer much promise for a variety of electronic and optoelectronic devices, the performance of nanowire devices is largely limited by the ability to controllably fabricate nanowires with the properties necessary for these devices. Nanowires are often “grown” by bottom-up techniques including particle-mediated growth, in which a metallic nanoparticle serves as a “seed” for growth by collecting nanowire precursors and confining semiconductor formation to the interface between the particle and the underlying material, resulting in a quasi-one-dimensional nanowire. The properties of these nanowires depend on their structure, morphology, and composition, which are in turn highly dependent upon growth parameters including temperature, pressure, and flow rates. In order to tailor the properties of nanowires, it is necessary to understand fundamental mechanisms of nanowire growth and the impact that growth parameters will have on those processes.

Structural factors include the crystallographic growth direction and defect density. The growth direction is important for both geometry and crystallography. Depending on the application, it may be desirable to grow nanowires either in-plane³⁹ or out-of-plane¹⁸ with the substrate. Furthermore, the crystallographic orientation of the nanowire can significantly affect its properties. As described above, III-V nitride with nonpolar-oriented heterojunctions can achieve significantly higher efficiencies.³⁷ Certain crystal structures have been fabricated only as nanowires, including unique polytypes⁴⁰ and both polytypic and twin-plane superlattices.⁴¹

Morphological factors include tapering, length, and diameter. Inadvertent radial film growth on nanowires sidewalls during axial nanowire growth yields a tapered morphology and can significantly affect the doping profile⁴² and composition⁴³ of the nanowire. The nanowire length affects photovoltaic conversion efficiency,⁴⁴ and the precise position of axial quantum wells in LEDs affects their efficiency.³⁰ The diameter affects the gate voltage required for switching in gate-all-around transistors,⁴⁵ and thin diameters in lightly doped or undoped nanowires can cause depletion of carriers and inhibit carrier conduction.⁴⁶ When the radius of the nanowire approaches the Bohr exciton radius of the material, radial quantum confinement occurs, which alters the electronic bandgap of the nanowire.⁴⁷ Modulation of the diameter along the nanowire axis can be used to enhance light trapping in photovoltaics,¹⁸ improve thermoelectric conversion efficiency,⁴⁸ or modify the bandgap of radially quantum-confined nanowires.

Spatial variations in composition are essential for many nanowire-based devices. Control of dopant levels is necessary for achieving *p/n* junctions with the desired current-voltage characteristics and depletion widths. Heterostructures with significant changes in composition are the basis for many devices, including high electron mobility transistors,⁴⁹ LEDs,⁵⁰ lasers,²⁷ and multijunction photovoltaics.¹

The focus of this thesis is to expand fundamental understanding of nanowire growth mechanisms and utilize that information to develop experimental techniques and theoretical models that provide a foundation for controllably fabricating III-V nitride and other nanowire-based devices.

1.4. Thesis outline

This thesis is organized as follows. First, important theoretical background and experimental details are described to provide a framework for the studies in this thesis. Chapter 2 provides

essential information about nanowire synthesis and structure, as well as motivations for the specific techniques and investigations that are chosen. Chapter 3 describes the experimental and theoretical techniques utilized for nanowire growth, characterization, and modeling.

Chapter 4 describes the growth of GaN nanowires with controlled structure and morphology. Control over the crystallographic growth direction, tapering, growth rate, and defect density are all achieved. A nucleation-mediated growth model is developed that explains the diameter-dependent nanowire growth rate and demonstrates that nucleation occurs preferentially along the perimeter of the liquid/solid interface. Defect density is reduced by appropriate material selection of the particles that seed nanowire growth, and this effect can be understood based on factors affecting nucleation.

Chapter 5 describes the synthesis of nonpolar-oriented InN/InGaN axial heterostructure nanowires. These are achieved by using intermittent, high-flux pulses of TMG to produce InGaN discs within InN nanowires. The observed change in nanowire shape in response to introduction of Ga was investigated by utilizing various electron microscopy techniques to probe and then explain the nanoscopic evolution occurring during growth.

The rest of the work focuses on nanowire diameter modulation. First, in Chapter 6, a technique is developed to vary the diameter along the axis of individual InN and GaN nanowires by adjusting the fluxes of the III & V precursors during nanowire growth. The III source can be used to control the incorporation rate of the III element into the seed particle, while the V source can be used to control the extraction rate of the III element out of the seed particle. A model is developed in Chapter 7 to elucidate the relative contributions of changes in both seed particle volume and wetting angle to the experimentally observed changes in nanowire diameter. Furthermore, this model provides a foundation for the synthesis and characterization of nanowires in other materials systems and allows the liquid/solid surface energy to be calculated, providing insight into the structure of the liquid/solid interface. Finally, in Chapter 8, diameter-modulated GaAs nanowires are synthesized, demonstrating that this flow-controlled approach can be applied to other compound semiconductors. Furthermore, distinct differences in diameter modulation and growth rate between nanowires were observed and attributed to differences in seed particle phase. By manipulating nucleation conditions, diameter modulation behavior was effectively controlled.

Chapter 2: Fundamentals of Nanowire Growth

While semiconductor nanowires offer advanced design of electronic and optoelectronic devices compared to their thin-film counterparts, realization of enhanced device performance requires the ability to fabricate nanowires with desired structure, morphology, and composition. These characteristics are affected by growth parameters such as temperature, pressure, and precursor fluxes. By relying upon fundamental understanding of the nanoscale processes occurring during growth, as well as the thermodynamic and kinetic factors that affect them, it is possible to tune these parameters in order to achieve desired nanowire properties.

This chapter describes the techniques used to fabricate nanowires, with a special emphasis upon the particle-mediated approach that is the chosen technique for the following experimental investigations. The fundamental processes in nanowire growth are described in detail, as well as the thermodynamic and kinetic factors affecting them. Specific considerations necessary for the growth of III-V nitride nanowires are also described. Finally, different nanowire architectures and strategies for fabricating them are discussed.

2.1. Nanowire fabrication techniques

Nanowires can be fabricated by a variety of approaches, which fall under two main categories: top-down and bottom-up. Bottom-up approaches can be further segmented into particle-free and particle-mediated approaches. The advantages and disadvantages of these approaches are described below, as well as the reasons for choosing particle-mediated growth as the technique used in this thesis work.

2.1.1. *Top-down nanowire fabrication*

Top-down approaches anisotropically etch material from films to leave free-standing nanowires (Figure 2-1a). Lithographic techniques – including optical lithography, electron lithography, and nanosphere lithography –^{51,52} are used to define which areas that will be etched. Etching techniques include wet etching, electrochemical etching, reactive ion etching, and metal-assisted etching.^{53,54} These approaches are useful for generating uniform arrays of nanowires with well-defined pitches and diameters, but they do have significant limitations. The production of thin nanowires is challenging and depends upon the ability to achieve extremely

high aspect ratios via etching. Furthermore, integration of different materials is difficult with this process. For axial heterojunctions, the etchant must preferentially etch all the materials in the same manner. Most importantly for III-V nitrides, the defects that were present in the film remain present in the nanowires. Because the original films do not have the benefit of efficient strain relaxation, defects in lattice-mismatched materials would remain an issue.

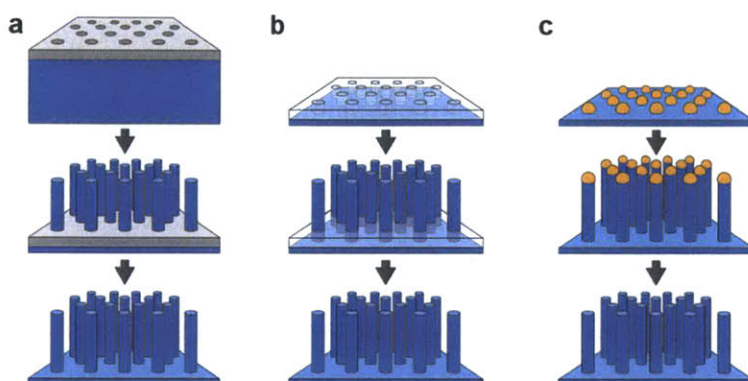


Figure 2-1. Methods of nanowire fabrication. (a) Top-down metal-assisted etching begins by lithographically templating a metal film to define where etching occurs (top). After the film is selectively etched (middle), the metallic film is then etched (bottom). (b) Bottom-up selective area epitaxy begins by templating an oxide film that leaves holes where nanowire growth can occur (top). Nanowires are grown under conditions in which certain facets grow much faster than others (middle). After growth, the oxide layer is removed (bottom). (c) Bottom-up particle-mediated nanowire growth begins by depositing metallic nanoparticle “seeds” on the growth substrate (top). Nanowires are produced by confining growth to the bottom interface of seed (middle). The seeds can then be selectively etched after growth (bottom). Gray, blue, transparent, and orange represent metal, nanowire material, oxide, and metal, respectively.

2.1.2. Anisotropic nanowire growth

One method of growing bottom-up nanowires leverages anisotropic growth, in which certain crystal facets grow faster than others.⁵⁵ Selective area epitaxy is commonly used to grow ordered nanowire arrays and prevent nanowires from aggregating into dense nanowire films (Figure 2-1b).^{56,57} While useful for certain systems and applications, anisotropic growth of nanowires has a few drawbacks. First, the achievable aspect ratios between nanowire length and diameter are limited by the ratio between vertical and lateral growth rates. Also, this approach utilizes relatively slow growth rates,⁵⁶ which can be costly due to low throughput and the high temperatures required for growth. A significant issue for nitrides is that anisotropic nanowire

growth occurs preferentially in the polar c -direction,⁵⁸ whereas nonpolar-directional nanowires would be preferable for axial heterojunctions in order to minimize the quantum-confined Stark effect.³⁷

2.1.3. Particle-mediated nanowire growth

Particle-mediated growth utilizes a nanoparticle – referred to here as the “seed”, which is usually metallic – that provides an interface for preferential nucleation and confines subsequent ledge growth to that interface.^{59,60} This technique offers a high degree of control, as the diameter and position of the nanowire can be controlled by the size and position of the seed particle (Figure 2-1c). Because the diameter and length of the nanowire can be tuned independently, arbitrary aspect ratios can be achieved. Electron beam lithography is not required to grow these nanowires: thin metallic films can be deposited via evaporation,³⁸ or colloidal nanoparticles can be deposited via solution.⁶¹ Furthermore, the seed particles alter the thermodynamics and kinetics of the growth process in such a way that it is possible to exercise control over the crystallographic growth direction of the nanowire.⁶² Notably, III-V nitride nanowires with both polar and nonpolar orientations have been achieved via particle-mediated growth.^{63,64}

Particle-mediated growth commonly proceeds according to the vapor-liquid-solid (VLS) mechanism, which was first described by Wagner and Ellis in 1964.⁵⁹ This process is illustrated in Figure 2-2 using an example of Si nanowires grown using gold seed particles. First, nanoparticles are deposited on an appropriate growth substrate (likely a Si wafer in this case). Methods of Au nanoparticle deposition include direct deposition of colloids from solution, electron beam lithography, and electron beam evaporation. The latter involves the deposition of a nanometer-scale film that, when heated, leads to dewetting into nanoparticles. These substrates are placed into the growth chamber, heated to a temperature above the Au-Si eutectic (363°C), and grown by the following steps, illustrated in Figure 2-2:

1. Si precursors (e.g. SiH_4) are introduced into the system and decompose into Si adatoms, which incorporate into the solid Au seed particle and form a Au-Si alloy.
2. When the alloy reaches a high enough Si concentration, it eventually reaches the liquidus and becomes a liquid.
3. At even higher concentrations, excess Si in the liquid alloy provides a driving force for solid Si growth.

- Due to Si supersaturation, nucleation of solid Si occurs, followed by ledge growth along the liquid/solid interface, leading to a layer of Si between the seed particle and the underlying substrate. This process is repeated in layer-by-layer fashion until growth is ceased and yields a quasi-one-dimensional nanowire.

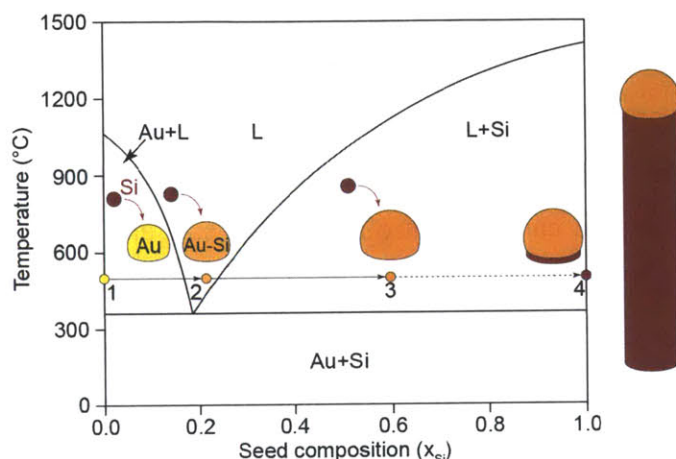


Figure 2-2. Vapor-liquid-solid (VLS) mechanism of nanowire growth. Binary AuSi phase diagram with schematic illustrations of the VLS mechanism. The seed particle begins as a solid Au particle (yellow; step 1). Si (red) from provided via gaseous precursors alloys with the seed and forms an AuSi alloy (light orange) once liquidus is reached (step 2). Further Si incorporation (step 3) yields a supersaturated AuSi alloy (orange) that drives formation of Si at the liquid/solid interface (step 4). Step 4 is repeated layer-by-layer to produce a quasi-one-dimensional Si nanowire (right).

The example above for Au-assisted Si nanowires provides a general description of the VLS process, but there are many important exceptions in particle-mediated growth that differ from the above process. First, the temperature does not necessarily have to be above the eutectic in order to promote nanowire growth. Nanowires can also grow from solid seed particles.⁶⁵⁻⁶⁷ This vapor-solid-solid (VSS) process is otherwise the same in that a supersaturated alloy drives growth of solid material over an area confined by the seed particle.

Particle-mediated growth of compound semiconductors also differs from the elemental case. For Au-assisted Si, the seed is an alloy of the seed metal and the material that composes the nanowire, and growth of Si is driven by supersaturation of Si in Au-Si. For compounds, the alloy is generally composed of the seed metal and the elements that form the compound, not of the metal and the compound itself. In the case of Au-assisted GaN growth, Ga alloys with Au but N is insoluble in both Au and Ga.⁶⁸⁻⁷⁰ It instead arrives at the vapor/liquid/solid triple-phase

boundary (TPB) and then diffuses along the liquid/solid interface to the site of reaction (Figure 2-3).⁶¹

For some compound semiconductors, it is possible to grow “self-assisted” nanowires, in which the seed metal is one of the constituent elements in the compound being grown. For example, GaAs nanowires can be grown using Ga seed particles.⁷¹ This process eliminates the risk of introducing impurities than can arise from using foreign metals as seeds,⁷² but it also limits the range of conditions that can be used to grow nanowires in order to avoid consuming the seed metal during growth.⁷³

2.2. Fundamentals of particle-mediated nanowire growth

In order to fabricate nanowires with the desired structure, morphology, and composition, it is necessary to understand and control the fundamental processes that occur during nanowire growth. This section describes the basic steps that take place during nanowire growth and how the rate-limiting step can be determined by analyzing the growth rate as a function of diameter. Additionally, nucleation is discussed in detail, including how the shape of the liquid/solid interface can affect nucleation. Finally, criteria for seed material selection are discussed.

2.2.1. Fundamental processes

As illustrated in Figure 2-3, particle-mediated growth involves the following processes:

1. Decomposition of precursors. Some precursors (e.g. metallic Ga for GaN) may already be present in their elemental form, but others (e.g. trimethylgallium and NH_3 for GaN) have to decompose to form elemental adatoms. Notably, decomposition may occur at various points during the growth process, including during precursor injection prior to arrival at the substrate or on the surface of the substrate, nanowire, or seed particle.
2. Transport of precursors/adatoms to the seed particle. Transport occurs through diffusion of both vapor-phase precursors and adsorbed adatoms.
3. Incorporation of the elemental adatoms into the seed particle.
4. Diffusion of elemental precursors through the seed.
5. Reaction at the liquid/solid (seed/nanowire) interface.

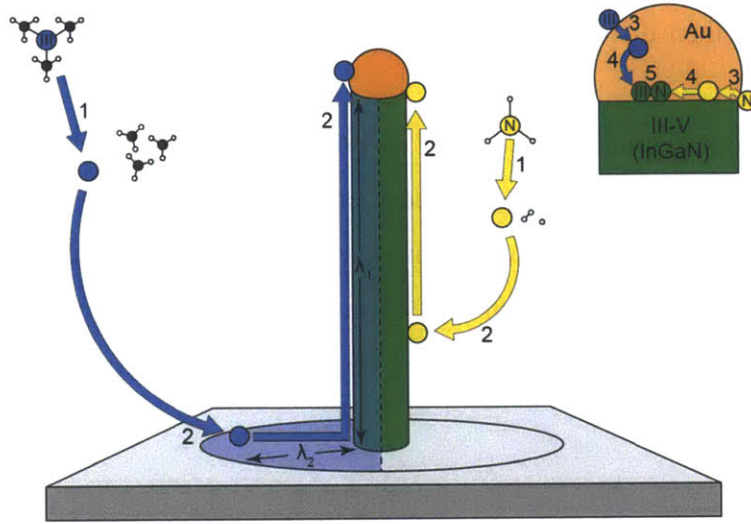


Figure 2-3. Fundamental processes in III-V nitride nanowire growth. Schematic illustration of the fundamental processes that occur during III-V nitride nanowire growth. The III, N, C, and H elements are represented by blue, yellow, black, and white circles, respectively. The substrate, nanowire, and seed are represented in gray, green, and orange, respectively. Precursor decomposition (step 1) is indicated here as occurring prior to arrival at the substrate, although it may actually occur on the substrate, nanowire, or seed surface. Both vapor and adatom diffusion (step 2) are shown. The adatom collection zone (semi-transparent blue) is dependent upon the diffusion length of III source along the substrate (λ_2) and nanowire (λ_1). Steps 3-5 are illustrated on the right and correspond to incorporation into the seed (step 3), diffusion to the site of reaction (step 4), and kinetic reaction at the seed/nanowire interface (step 5).

Analyzing the nanowire growth rate as a function of diameter helps to provide insight into which processes are rate-limiting. The diameter-dependent growth rate has been analyzed for a variety of materials under different growth conditions, and steps 2 and 5 have consistently been observed as the rate-limiting processes in nanowire growth.⁷⁴⁻⁷⁹

In the case of reaction-limited growth, one might expect the growth rate (v_{rxn}) to be independent of diameter based on the following equation.

$$v_{rxn}^{1/n} = K_{rxn} \left(\frac{\Delta\mu^0}{k_B T} \right) \quad (2-1)$$

Here, n is an empirical constant with a well-accepted value of 2,^{74,80} K is a kinetic coefficient independent of $\Delta\mu$, $\Delta\mu^0$ is the change in chemical potential for the bulk material (i.e. nanowire diameter $\rightarrow \infty$), k_B is the Boltzmann constant, and T is the growth temperature.⁸¹ However, experimental observations indicate that the growth rate tends to increase with diameter during reaction-limited growth. Multiple authors have attributed this result to the Gibbs-Thomson

effect,⁷⁵⁻⁷⁷ in which constituents of smaller particles have higher chemical potentials due to the increased surface-to-volume ratio. Therefore, thinner nanowires would grow slower than thicker ones because of the reduced driving force for nanowire growth. In this case, the growth rate (v_{GT}) can be expressed as,

$$v_{GT} = K_{GT} \left(\frac{\Delta\mu^0}{k_B T} - \frac{4\Omega\gamma}{k_B T d} \right)^2 \quad (2-2)$$

where Ω is the atomic volume of the source material in the crystal and γ is the surface energy of the nanowire.⁸¹

Transport of precursors to the seed occurs by diffusion of both vapor and adatoms. Because vapor transport is much more rapid than surface adatom transport, diffusion-limited growth is generally dictated by adatom diffusion. The equation for the growth rate in this case is given by,

$$v_{ad} = K_{ad} \left(\frac{\Delta\mu^0}{k_B T} - \frac{4\Omega\gamma}{k_B T d} \right)^2 \left(\frac{2(\lambda_1 + \lambda_2)}{d} - \frac{4\lambda_2^2}{d^2} \right) \quad (2-3)$$

where λ_1 and λ_2 are the portions of the diffusion length ($\lambda = \lambda_1 + \lambda_2$) along the nanowire sidewalls and the substrate, respectively (Figure 2-3).⁸¹ When $\lambda_1 \gg \lambda_2$, the growth rate is proportional to $1/d$. When $\lambda_1 \gg \lambda_2$, the growth rate is instead proportional to $1/d^2$.^{74,79}

One issue with the Gibbs-Thomson model is that the growth rate expression assumes continuous growth on a rough interface. Nanowire growth generally proceeds by layer-by-layer growth in which each new layer needs to be nucleated. Nucleation occurs relatively slowly in comparison to subsequent ledge filling, so reaction-limited growth models should account for nucleation-limited growth. Kashchiev presented a model for nucleation-mediated growth on a two-dimensional island, given as follows,

$$v_{NM} = \frac{a_1 d^2}{1 + a_2 d^2} \quad (2-4)$$

Here, a_1 ($\text{nm}^{-1} \text{min}^{-1}$) and a_2 (nm^{-2}) describe the rates of mononuclear and polynuclear growth, respectively.⁸² The d^2 term originates from the assumption that the nucleation probability increases with the area over which nucleation can occur, although it is possible that nucleation may occur preferentially at the perimeter.^{38,60} A model that accounts for preferential perimeter nucleation may more accurately describe the fundamental nanowire growth mechanism in many cases.

2.2.2. Nucleation and the liquid/solid interface

Nanowires have been observed to be able to grow faster than their thin-film counterparts with fewer stacking defects.⁸³ Because it enables greater growth rates, the seed particle has commonly been referred to as a catalyst. Notably, the chemical potential of the constituent elements decreases from the vapor to liquid to solid phases. Thus the reduction in chemical potential from vapor to solid in film growth is greater than the reduction in chemical potential from liquid to solid in nanowire growth. The higher growth rate of nanowires versus films, despite a lower reduction in chemical potential for the reacting species, can be explained by the reduced energy of the nucleus. Interfacial energies for liquid/solid interfaces are generally less than those for vapor/solid interfaces,⁸⁴⁻⁸⁶ In a nanowire, a nucleus creates new liquid/solid interfaces rather than new vapor/solid interfaces, yielding a lower energy nucleus. Thus the reduced nucleation barrier would explain why nanowires can grow faster than films despite lower supersaturation, while growth at low supersaturation also minimizes stacking defects.^{87,88}

It is often assumed that the nanowire interface is flat (Figure 2-4a,b) and that nucleation occurs at the vapor/liquid/solid triple-phase boundary (TPB),^{5,89-94} and this assumption has been used to explain structural and morphological changes in nanowires.^{5,92-94} Wacaser *et al.* suggested that nucleation should occur preferentially at the TPB because of its relatively high supersaturation.⁶⁰ There is a reduction in constituent chemical potential at each point between the vapor, liquid, and solid phases, so the supersaturation will be higher between the vapor and solid phases at the TPB than between the liquid and solid phases at the liquid/solid interface. In this case, the change in free energy of a homoepitaxial nucleus (ΔG) on the liquid solid/interface of a growing nanowire can be expressed as follows,

$$\Delta G_{nuc} = n\Delta\mu + A_{vs}\sigma_{vs} + A_{ls}\sigma_{ls} \quad (2-5)$$

where n is the number of atoms in the nucleus, $\Delta\mu$ is the change in chemical potential, and A and σ are the areas and surface energies of vapor/solid (vs) and liquid/solid (ls) interfaces. However, the energy of the liquid/solid interface (σ_{ls}) is generally less than the energy of the vapor/solid interface (σ_{vs}). For $\sigma_{ls} < \sigma_{vs}$, a nucleus would actually have lower energy away from the TPB.

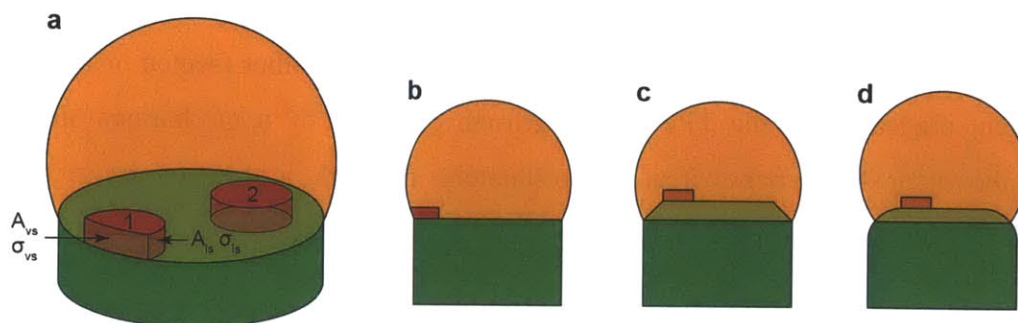


Figure 2-4. Liquid/solid interface morphology during nanowire growth. (a) Flat liquid/solid interface between a liquid seed (orange) and solid nanowire (green). Nuclei 1 and 2 (red) correspond to nucleation at and away from the TPB, respectively. These nuclei create new facet areas (A) with vapor/solid (vs) and liquid/solid (ls) interfaces, which have different surface energies (σ). (b-d) Three different potential liquid/solid interface morphologies: flat (b), faceted (c), and rounded (d). Semi-transparent areas indicate portions of the nanowire that are enveloped by the seed particle. Nuclei show potential preferential nucleation sites for each morphology.

Recent experimental^{7,95,96} and theoretical⁹⁷⁻¹⁰⁰ studies indicate that the liquid/solid interface may be either faceted (Figure 2-4c)^{7,95-98} or rounded (Figure 2-4d)⁹⁹ at some length scale near the perimeter of the liquid/solid interface. Notably, separate authors have performed *in situ* TEM studies of nanowires in different materials systems and observed faceted morphologies in which the size of the edge facet fluctuated cyclically with each new monolayer.^{7,95,96} In each case, the edge facets grew quickly until a new monolayer was nucleated, at which point material from the edge facets dissolved back into the seed (Figure 2-5). Oh *et al.* observed the liquid/solid interface of growing Al_2O_3 nanowires with atomic resolution and reported a cyclic process illustrated in Figure 2-5a.⁹⁶ They observed edge facets around the entire perimeter of the liquid/solid interface, each of which appeared atomically sharp and grew layer-by-layer, maintaining the same inclination angle. As soon as these facets were filled such that the upper liquid/solid interface made contact with the TPB, a new monolayer was nucleated. This result does indicate that nucleation at the TPB may be preferential and provides a mechanism by which non-flat liquid/solid interfaces can make contact between the upper surface and the TPB.

However, other authors have observed a different cyclic process in multiple nanowire materials including Ge, Si, and GaP.^{7,95} In these studies, the angle of the edge facet fluctuated during growth, and the facet was never completely filled before a new monolayer was nucleated. In other words, no contact was made between the upper liquid/solid surface and the TPB (Figure 2-5b). However, while individual facets were observed to display this behavior, these facets

were not observed around the entire liquid/solid interface. The other facets could be flat, which would allow nucleation at the TPB. Alternatively, they may be either faceted or rounded, which could prevent nucleation at the TPB unless growth proceeds by a mechanism similar to that described above for Al_2O_3 nanowires. Unfortunately, the dark contrast of the seed particle in these studies would have prevented a full view of such interface structures.

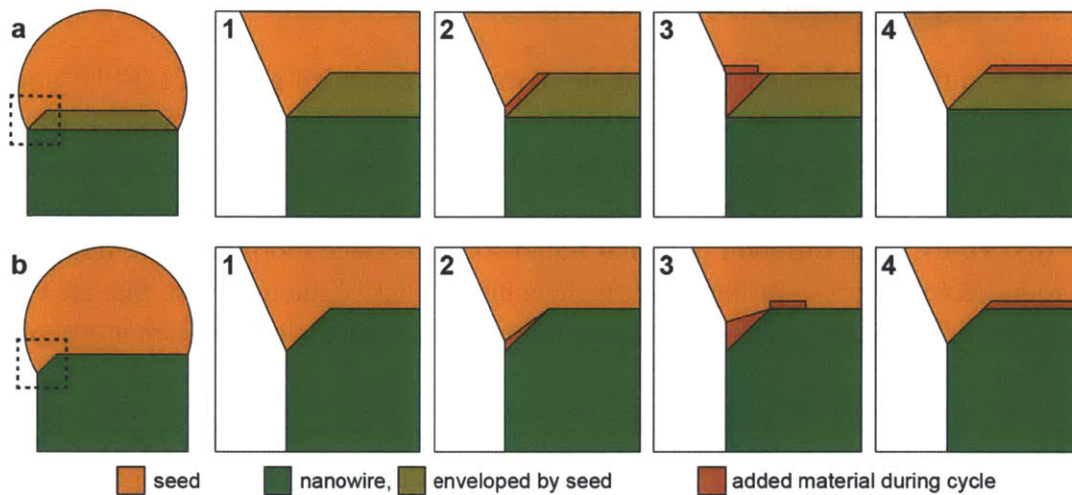


Figure 2-5. Growth mechanisms for faceted liquid/solid interfaces. (a) Growth mechanism observed in [96] for Al_2O_3 nanowires. Edge facets are present around the entire perimeter of the liquid/solid interface (left). (b) Growth mechanism observed in [7,95] for Ge, Si, and GaP nanowires. One large edge facet is present at the perimeter of the liquid/solid interface (left). Steps 1-4 show magnified views of the dashed regions and represent (1) the initial interface morphology, (2) rapid growth along the edge facet, (3) nucleation of a new monolayer on the upper liquid/solid surface, and (4) simultaneous ledge growth and reformation of the edge facet by dissolution of the nanowire.

The structure of the liquid/solid interface has significant consequences, including the preferred nucleation site. This significantly affects models of nanowire growth and explanations of certain phenomena, including the mechanism of twinning.⁷ In addition, periodic dissolution of nanowire material may limit the achievable sharpness of heterointerfaces,⁷ and the presence of rough facets may affect the incorporation of dopants.⁴ Therefore, further investigations into the liquid/solid interface structure and its role in nanowire growth can help provide a better foundation for understanding observed growth phenomena.

2.2.3. Seed material

The seed metal has a significant impact on many aspects of nanowire growth. The most basic consideration in seed particle selection is the phase diagram for the seed metal and the alloying element(s). Seed metals are often chosen such that the alloy will liquefy at the temperatures used for nanowire growth. For elemental nanowires of uniform composition, phase information is generally readily available. For compound semiconductor alloys, ternary phase diagrams are not always available. Seed particle selection for compound semiconductors is further complicated by the fact that the alloy is generally composed of the seed metal and a nonstoichiometric combination of the constituent elements of the nanowire, rather than an alloy of the seed particle with the compound itself. Furthermore, it is possible to promote nanowire growth with solid seed particles.⁶⁵⁻⁶⁷ In fact, Ross *et al.* grew SiGe axial heterostructure nanowires using AlAu seeds and found that more abrupt heterojunctions could be generated by operating below the eutectic temperature with solid seed particles.¹⁰¹ Even when seed metals have very similar phase diagrams, they do not necessarily produce similar results in nanowire growth. For example, the phase diagrams of Au-In and Ag-In are similar at the temperatures used for nanowire growth, but have yielded very different results in the growth of InN nanowires.¹⁰² Another important consideration is the solubility of the seed metal in the nanowire, as incorporation of metal impurities can erode nanowire properties.^{72,103}

Surface energy is another important consideration for the seed metal, as the seed metal affects the surface energies at the vapor/liquid and liquid/solid interfaces, thereby affecting the energy of a nucleus (see Equation 2-5) and consequently the nanowire growth rate.¹⁰⁴ Additionally the crystallographic orientation can be affected,⁶³ as the preferred orientation will minimize total energy, which includes the energy of the liquid/solid interface. While the seed particle attributes described above are known to impact nanowire growth, no model presently exists for predicting the viability of particular seed-nanowire combinations. Therefore, suitable seed metals have been largely been determined by trial and error.

2.3. Nanowire architectures

In order to fabricate nanowires with desired architectures, it is necessary to not only understand the fundamental processes in nanowire growth, but also how they can be altered with various growth parameters including temperature, pressure, and precursor flow rates. The

following section describes current understanding of how certain nanowire characteristics – specifically crystallographic growth direction, tapering, composition, and diameter – can be affected by various growth parameters during particle-mediated growth.

2.3.1. Crystallographic growth direction

The crystallographic growth direction is determined by maximizing the reduction in energy going from droplet to nanowire (ΔG), which can be described as follows.

$$\Delta G = n\Delta G_f + (A_{vl,2}\sigma_{vl,2} - A_{vl,1}\sigma_{vl,1}) + (A_{ls,2}\sigma_{ls,2} - A_{ls,1}\sigma_{ls,1}) + A_{vs,2}\sigma_{vs,2} + A_{ss,2}\sigma_{ss,2} + \Delta G_{strain} \quad (2-6)$$

Thus the growth direction is dependent upon the formation energy of the nanowire (ΔG_f), the strain energy (ΔG_{strain}) resulting from lattice mismatch between the nanowire and the substrate, as well as the areas (A) and surface energies (σ) of all vapor/liquid (vl), liquid/solid (ls), vapor/solid (vs) and solid/solid (ss) interfaces before (1) and after (2) nanowire formation (Figure 2-6).

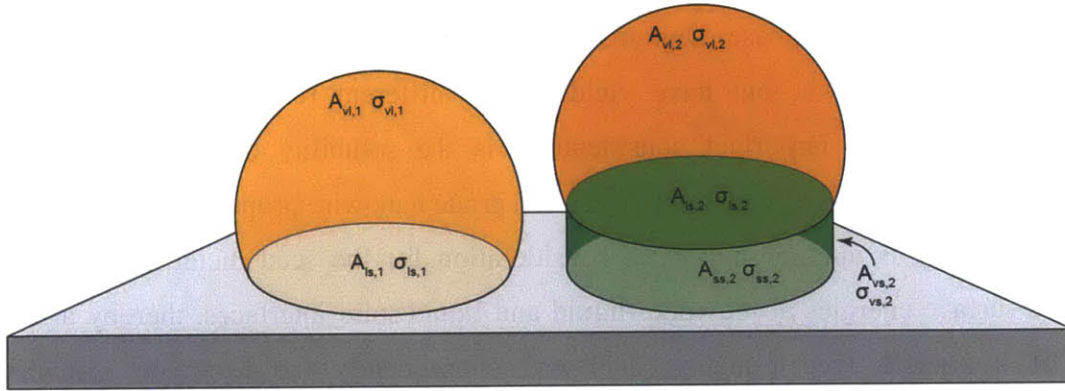


Figure 2-6. Surface energies affecting growth direction. Schematic illustrations of the seed before nanowire growth (left) and the seed and nanowire after nanowire growth (right). Labels indicate the areas (A) and surface energies (σ) of the vapor/liquid (vl), liquid/solid (ls), vapor/solid (vs), and solid/solid (ss) interfaces before (1) and after (2) nanowire formation.

Because particle-mediated growth presents so many factors that affect the growth direction, a variety of nanowire orientations can be achieved by controlling growth conditions.⁶² Two the most significant factors are the choice of seed and substrate materials. The seed metal has a significant impact on ΔG , σ_{vl} , and σ_{ls} . Kuykendall *et al.* observed that GaN nanowires grew preferentially in the m and a directions when seeded by Au and Ni, respectively.⁶³ The size of the seed particles can also have a significant impact on the preferential growth direction, because

it affects the relative areas of all the surfaces. Although Si nanowires tend to grow in the [111] direction, multiple authors have found that Si nanowires with diameters < 20 nm grow in the [110] direction.^{105,106}

The choice of substrate affects σ_{ls} , σ_{ss} , and ΔG_{strain} . By using (100) γ -LiAlO₂ and (111) MgO substrates, Au-seeded GaN nanowires could be grown in the c and m directions, respectively.⁶⁴ Notably, the crystallographic orientation of the nanowire affects faceting and, consequently, surface energy (σ_{vs}). In this case, the cross-sections of c -GaN and m -GaN nanowires are hexagonal and triangular, respectively.

Growth conditions such as temperature and pressure can also affect the orientation of nanowires. Shan *et al.* observed that CdSe nanowires grew in the [110] versus [111] direction when grown at 480°C versus 500°C, respectively.¹⁰⁷ Others found that the preferential growth direction of Si nanowires could be changed from [111] to [112] by increasing the system pressure.¹⁰⁸ Furthermore, the growth direction could be modified during growth by varying the pressure, producing kinked nanowires.¹⁰⁹ Unlike the effects of material selection, the impacts of changes in growth conditions are often more difficult to explain and therefore predict. For example, temperature indiscriminately affects nearly every kinetic process occurring during nanowire growth, as well the thermodynamic properties of the seed, nanowire, and substrate. Thus it is not impossible to provide a single analytical explanation for the effect of temperature on nanowire growth direction.

The crystallographic growth direction in III-V nitrides is particularly important due to spontaneous polarization in the [0001] c -direction (Figure 2-7a) arising from the lack of centrosymmetry in the unit cell. When heterojunctions are formed along this direction, the strain between the layers of different composition yields piezoelectric polarization.¹¹⁰ In very thin layers, including the MQW structures used in GaN-based LEDs, this polarization yields significant band bending and a consequent spatial separation of electrons and holes (Figure 2-7b), reducing the probability of radiative recombination. The issue, called the quantum-confined Stark effect (QCSE),³⁶ is particularly significant in InGaN because of the large lattice mismatch between GaN ($a = 3.2$ Å, $c = 5.2$ Å) and InN ($a = 3.5$ Å, $c = 5.7$ Å).

The QCSE can be minimized by orienting heterojunctions along nonpolar orientations orthogonal to the c -direction, including the [11-20] a -direction and [1-100] m -direction (Figure 2-7c). Nitride films are generally c -oriented due to preferential c -directional growth and lower

mismatch with available substrates.³⁷ Some progress has been made in fabricating semipolar (non-[0001] directions that are not nonpolar) and nonpolar GaN-based films, but these advancements have been largely based upon prohibitively expensive, low-area GaN templates.¹¹¹ Anisotropic GaN nanowires grow preferentially in the [0001] direction, in which case only radial heterostructures can be fabricated to have nonpolar-heterojunctions. Particle-mediated nanowire growth, however, has produced GaN nanowires grown in the c , m , and a directions.^{63,64} The growth direction has been controlled largely based on the choice of seed metal⁶³ and substrate.⁶⁴ While these different growth directions have been achieved with GaN, axial InGaN heterostructures have only been reported in the c -direction.

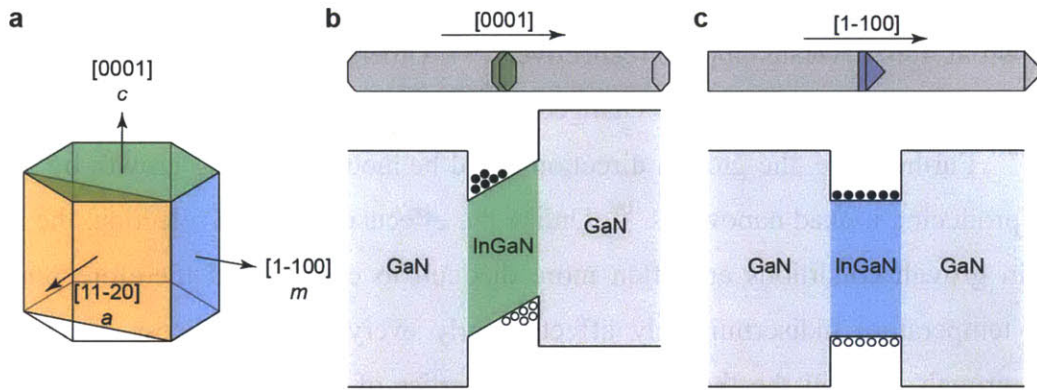


Figure 2-7. Nitride crystallography. (a) Crystallographic planes in the unit cell of III-V nitrides. The c -direction (green) is polar, while the a - and m -directions (orange and blue, respectively) are nonpolar. (b,c) GaN nanowires with embedded InGaN quantum wells (top) and corresponding band diagrams (bottom) for c -oriented (b) and m -oriented (c) nanowires. The color of the InGaN quantum wells corresponds to the orientation in (a). The band diagrams illustrate the overlap between electrons (black) and holes (white).

2.3.2. Tapering

During nanowire growth, film growth of a “shell” can occur simultaneously on the sidewalls of the nanowire “core”, yielding a tapered morphology (Figure 2-8). Although the tapered morphology can potentially have some benefits, including improved light trapping,²⁹ it can also complicate control of the dopant profile⁴² and composition⁴³ of the nanowire.

Tapering can be minimized in a variety of ways. The most common strategy to minimize radial shell growth is to operate at reduced growth temperatures.^{112,113} As discussed previously,

nanowires lower the driving force required to promote semiconductor growth. Thus nanowires can be grown at lower temperatures than films. During Ge nanowire growth using GeH_4 and H_2 , Musin *et al.* effectively passivated the nanowire sidewalls by introducing methylgermane.¹¹⁴ Although Ge nanowires usually taper above 300°C , they were able to grow untapered Ge nanowires above 475°C . Xu *et al.* recently found that tapering on GaAs nanowires could be minimized by increasing nanowire density, which can be attributed to effective consumption of precursors by the seed particles.¹¹⁵

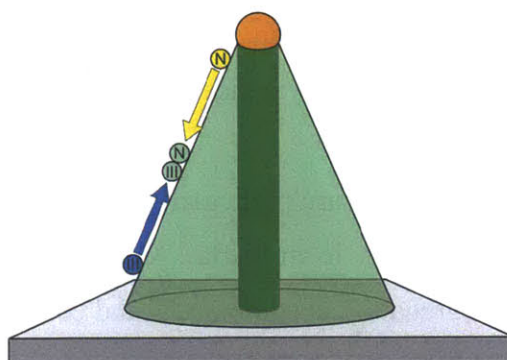


Figure 2-8. Tapered nanowire. (a) Tapered III-V nitride nanowire in which axial nanowire growth (solid green) occurs through the seed (orange), while radial film deposition (semi-transparent green) occurs by reaction of III (blue) and N (yellow) adatoms before they reach the seed.

2.3.3. Nanowire junctions and heterostructures

Spatial variations in composition are the basis of electronic and optoelectronic devices. Variations in low concentrations of dopant atoms are required to create p/n junctions and generate built-in electric fields to control the flow of current. More significant changes in composition can yield a variety of unique properties. For LEDs, lower bandgap MQW layers are embedded within a higher bandgap material so that electrons and holes fall into the wells, providing spatial confinement to promote radiative recombination. Also, high electron mobility transistors can be created via modulation doping, in which layers of different composition and doping levels yield an interfacial layer in which the Fermi energy lies above the conduction band edge, yielding an accumulation of “electron gas” that has metallic behavior with extremely high conductivity.⁴⁹ Nanowires allow heterojunctions to be formed axially or radially (Figure 1-1), depending on the preferred architecture for the particular application.

For particle-mediated nanowires, abrupt axial heterojunctions are sometimes difficult to achieve because of the “reservoir effect,” in which a graded heterojunction results from a gradual change in the composition of the seed despite abrupt changes in precursor flows.¹¹⁶ Wen *et al.* were able to achieve abrupt Si/Ge heterojunctions using solid AlAu seed particles, which have low solubility of Si and Ge and therefore minimize the reservoir effect.¹⁰¹ Dick *et al.* achieved abrupt InAs/GaAs heterojunctions by first pulsing trimethylgallium (TMG) to steadily drive In out of the alloy without promoting incorporation of Ga into the nanowire. Then a continuous TMG flow was used to grow GaAs, yielding an abrupt InAs/GaAs junction.¹¹⁷ In III-V nanowires, the reservoir effect is less significant when the V element is varied at the junction, because the seed alloy holds significant concentrations of III elements but very low concentrations of V elements.¹¹⁸

Heterostructures composed of InGaN are particularly challenging to fabricate, largely due to the significant miscibility gap ($\sim 10\text{-}90\%$ In in $\text{In}_x\text{Ga}_{1-x}\text{N}$)¹¹⁹ and strain ($\sim 10\%$ lattice mismatch) between GaN and InN. Phase segregation is common,¹²⁰ and compositions near the center of the miscibility gap have rarely been achieved. Notably, the one report of tunability across nearly the entire composition spectrum of InGaN was produced using nanowires.¹²¹ However, the authors used a halide process that produces HCl gas during growth, and little control was demonstrated over the nanowire morphology, which included significant tapering. Additionally, no similar reports have been made since, motivating the use of other techniques to fabricate InGaN alloys.

A variety of factors affect the composition of semiconductor alloys. A significant factor is the relative flux of precursors (e.g. trimethylindium versus trimethylgallium for InGaN).¹²² The composition of InGaN also depends largely upon the growth temperature. Yoshimoto *et al.* found that InGaN thin films contained significantly more In at lower temperatures,¹²² which is likely a consequence of the low stability of InN at higher temperatures.¹²³ As discussed above, the composition of the seed particle alloy has a substantial effect on the composition of the nanowire. In addition, the nanowire diameter can affect the composition. Zhang *et al.* found that the Ge composition in SiGe nanowires increased with diameter due to differences in the diameter-dependent growth rates of Si and Ge nanowires.¹²⁴ With limited reports of particle-mediated ternary InGaN nanowires, there is little known about how such growth parameters affect the composition of these alloys.

2.3.4. Diameter modulation

Changes in the diameter along the nanowire axis can impart unique properties to nanowires and nanowire arrays. For example, the light-trapping effect of nanowire arrays can be enhanced by using dual-diameter nanowires that are thin at the top and thick at the base.¹⁸ The thin-diameter tips reduce reflection off of the top surface, while the thick-diameter bases increase the absorption of light that penetrates into the interstices of the array. Theoretical work by Zianni indicates that nanowires with controlled diameter modulations can yield very high ZT values, the thermoelectric figure of merit that describes the ratio between electron and phonon conduction.⁴⁸ By modulating the diameter, phonon scattering can be increased without significantly affecting electron conduction. For nanowires with diameters below the Bohr exciton radius, the bandgap increases as diameter decreases.⁴⁷ In this quantum-confined regime, the nanowire bandgap can be tuned via diameter, either as an alternative or in addition to changes in nanowire composition. Furthermore, thin-diameter notches could be placed periodically along the nanowires to serve as preferential sites for controlled fracture, thereby increasing throughput in nanowire fabrication.

Many different methods have been reported to control the diameter of nanowires with uniform width, yet while unintentional changes in nanowire diameter have commonly been observed,^{67,125,126} few have demonstrated controlled modulation of the diameter during growth. The initial diameter of nanowires can be controlled by the use of colloids with known diameter,⁶¹ the thickness of seed films,³⁸ electron beam lithography,¹²⁷ or the size of pores in a template.¹⁸ Fan *et al.* synthesized Ge nanowires with thick bases and thin tips by performing a two-step anodization of an alumina template.¹⁸ Template-free approaches are desirable in order to reduce cost, fabricate diameter-modulated nanowires over large areas, and modulate the diameter cyclically between thick and thin. The diameter of SiC nanowires was changed by varying the pressure during growth,¹²⁸ but the mechanism for these changes was unclear, and the technique is not applicable for other precursors and materials systems. The diameter of Ge nanowires was controlled by using trimethyltin to prevent shell deposition in selected regions.¹²⁹ However, the use of a shell to achieve diameter modulation can have significant limit control over doping⁴² and composition.⁴³ Additionally, the applicability of this technique to other materials is unclear, and the potential introduction of impurities from the foreign material could erode nanowire properties. Therefore a need remains for a template-free method of fabricating diameter-modulated nanowires that is applicable across a variety of materials systems.

Chapter 3: Experimental Methods

The experimental techniques and the foundation for the theoretical models used for the investigations in this thesis are explained in this chapter. Chemical vapor deposition (CVD) techniques, including metalorganic chemical vapor deposition (MOCVD) were used to fabricate GaN, InN, InN/InGaN, and GaAs nanowires. Electron microscopy tools were used extensively to characterize the structure, morphology, and composition of the nanowires. Details of the processes, equipment, and settings used are described below. Additionally methodologies and assumptions are described for data acquisition and modeling of the following: the composition of the nanowire and seed particle, the three-dimensional shape of the seed particle, and the evolution of diameter along the nanowire axis.

3.1. Synthesis of III-V nitride nanowires

Nitride nanowires including GaN, InN, and InN/InGaN heterostructures were synthesized by a combination of CVD and MOCVD techniques using metal colloids and films to seed growth. Details of the experimental setup, growth conditions, and substrate preparation are described below.

3.1.1. *Experimental setup*

Nitride nanowires were grown in a hot-walled horizontal-flow chemical vapor deposition system as shown in Figure 3-1. All components in the reaction chamber are made of quartz, except the stainless steel load plate. The furnace has three independently-controlled temperature zones (load, center, and end). Growth temperatures varied from 500–950°C, and system pressures varied between 50–760 Torr. The carrier was N₂, H₂, or a combination of both. In all cases, NH₃ was used as the V source. Both carrier gas and NH₃ were delivered through the background line.

The system is equipped for use with both metallic (Ga, In) and metalorganic (trimethylgallium, trimethylindium) precursors as the III sources. Trimethylgallium (TMG) and trimethylindium (TMI) are delivered by bubbling carrier gas (N₂ or H₂) through bubblers to separate injection lines connected to tube injectors that carry the gas from the load zone to the center reaction zone where the substrates are placed (Figure 3-1). The temperature and pressure

of the bubblers, as well as the flow rate of carrier gas, were all used to control the flux of metalorganic precursors. When Ga was used, it was placed in a crucible with an independently controlled temperature, and carrier gas was flown over the crucible through a tube injector. When In was used, it was placed in the reaction zone either on or next to the growth substrates.

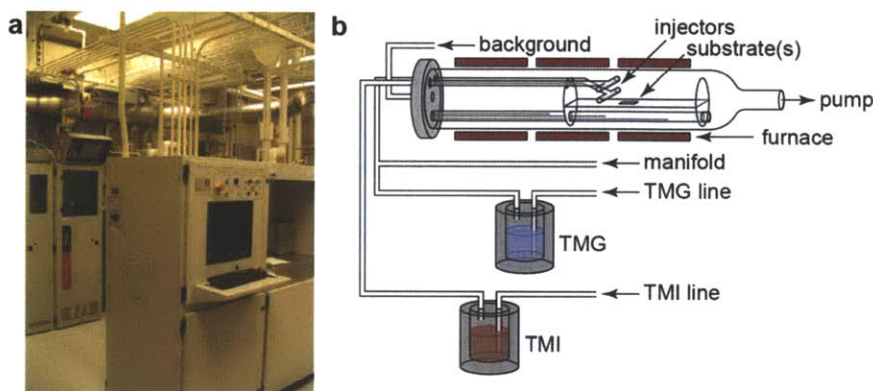


Figure 3-1. Chemical vapor deposition system for nitride nanowire growth. (a) Picture of the chemical vapor deposition system used for all III-V nitride nanowire growths. (b) Schematic illustration of the reaction furnace, quartzware, and gas injection lines.

All growths contained the following segments. First, growths began by pumping the system for about 20 min down to approximately 150 mTorr, then ceasing pumping to ensure that the rate of rise in pressure was no more than 20 mTorr/min. All gas lines were then purged with nitrogen, and the system pressure was increased to the pressure used for growth. The system was then heated to the growth temperature under a nitrogen atmosphere. Hydrogen was introduced briefly prior to growth to reduce any potential oxides on the surface. Unless otherwise noted, the III & V sources were introduced simultaneously to initiate growth. When fluxes of the III & V sources were varied during growth, the flow of carrier gas through the background line was adjusted to keep the total flow rate of gas constant. Unless otherwise noted, a nitrogen environment was used during cooling.

The quartzware was routinely cleaned by first heating it to 850°C for 3 hours in atmosphere, then placing it in concentrated phosphoric acid (J.T. Baker, 85% o-H₃PO₄) until clean. It was then rinsed with deionized (DI) water and dried with compressed air.

3.1.2. Substrate preparation

Substrates that were used included (0001) *c*-sapphire, (10-12) *r*-sapphire, *c*-GaN on *c*-sapphire (*c*-GaN/*c*-sapphire), and (11-20) *a*-GaN on *r*-sapphire (*a*-GaN/*r*-sapphire). GaN films on sapphire were 2–5 μm thick. Substrates were cleaved from 2" wafers to approximately 0.5 cm \times 1 cm, sonicated for 10 min each in acetone, methanol, and deionized water, and then stored in ethanol until seed deposition.

An electron-beam evaporator was used to deposit Au and Ni films ranging from 1-5 nm thick. The pressure during deposition exceeded no more than 1×10^{-5} Torr, and the deposition rate ranged from 1–4 $\text{\AA}/\text{s}$.

For colloid deposition, substrates were first coated with 20 μL of poly-L-lysine for 10 min to help the colloids to adhere to the substrate. The substrates were then rinsed with DI water and dried with compressed air. An aqueous solution of 60 nm Au colloids (BBI Solutions, 3×10^{-4} M Au) was diluted with equal parts DI water, and the substrates were coated with 20 μL of the diluted solution for 10 min. The substrates were then rinsed with DI water, dried with compressed air, and kept in a desiccator until being used for growth.

3.1.3. GaN nanowire growth

For the GaN nanowires used in the development nucleation-mediated growth model, the CVD setup shown in Figure 3-2a was used. Gold films with thicknesses of 1–3 nm were deposited onto *a*-GaN/*r*-sapphire substrates, which were placed 2 cm downstream from the injector. Nanowires were fabricated at 900°C and atmospheric pressure. The carrier gas was a mixture of N_2 and H_2 varied between 0–60% H_2 . A quartz crucible containing Ga (Aldrich, 99.999%) was kept at 950°C. During growth, 500 sccm carrier gas and 50 sccm NH_3 were delivered through the background line, while 7 sccm N_2 was delivered through the Ga crucible injector. The growth time was 20–40 min.

For comparing Au and Ni seed particles, the MOCVD setup shown in Figure 3-2b was used. Films of Au and Ni with thicknesses of 1-5 nm were deposited onto *r*-sapphire substrates were deposited by electron beam evaporation. Growth was performed at 850°C and 100 Torr by flowing 400 sccm N_2 and 50 sccm NH_3 through the background line, as well as 0.85 sccm H_2 through the TMG bubbler and an another 150 sccm H_2 to carry the TMG through the injector line. The growth time was varied between 0.5–80 min.

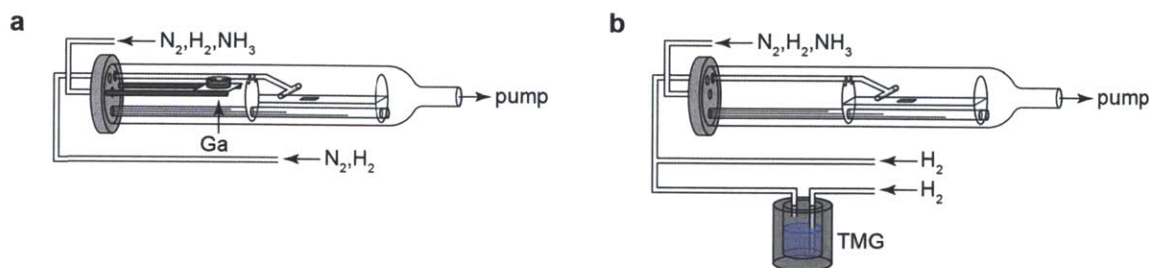


Figure 3-2. Setup for CVD and MOCVD GaN nanowire growth. (a,b) Schematic illustration of the quartzware setup, precursors, and gas injection for both CVD (a) and MOCVD (b) GaN nanowire growth.

For the diameter modulation studies, a setup similar to that in Figure 3-2b was used, except that the TMG injector was first coated with Ga prior to growth. To coat the injector, the system was heated to 860°C under a N₂ atmosphere before flowing 400 sccm N₂ and 20 sccm NH₃ through the background line, as well as 6 sccm H₂ through the TMG bubbler and another 150 sccm H₂ to carry the TMG through the injector line. After the injector coating, *r*-sapphire and *α*-GaN/*r*-sapphire substrates coated with 1 nm Au were loaded into the furnace and placed 1 cm from the injector head. Growths were performed at 835°C using 150 sccm H₂, 400 sccm N₂, and 50 sccm NH₃. H₂ was delivered through the injector line, while the remaining gases were delivered through the injector. The growth time varied from 15 min – 2 hr.

3.1.4. InN nanowire growth

Indium nitride was grown by both CVD (Figure 3-3a) and MOCVD (Figure 3-3b) techniques. In both cases, the quartzware was cleaned prior to each growth by flowing 250 sccm H₂ and 250 sccm N₂, heating the system to 950°C for 1 hr, and then cooling to 300°C before purging the system with N₂. For CVD growths, the *r*-sapphire and *α*-GaN/*r*-sapphire substrates were coated with 60 nm Au particles and placed 2–6 cm downstream from the TMG injector head. For MOCVD growths, the substrates were placed 2–6 cm downstream from the TMI injector head. For both CVD and MOCVD, the nanowires were nucleated at a temperature of 560°C. The standard growth temperature was 560°C, but growth temperatures were sometimes increased or decreased to between 520–650°C. The pressure varied between 50–400 Torr. The total flow of all gases was kept at 500 sccm, and N₂ was used as the carrier gas. The standard NH₃ flow was 300 sccm. For CVD growths, 5 ± 1 g In (Aldrich, 99.999%) was placed on or

near the substrates. For MOCVD growths, 100 sccm N_2 was bubbled through TMI and delivered through the TMI injector. The standard growth time was 1 hr.

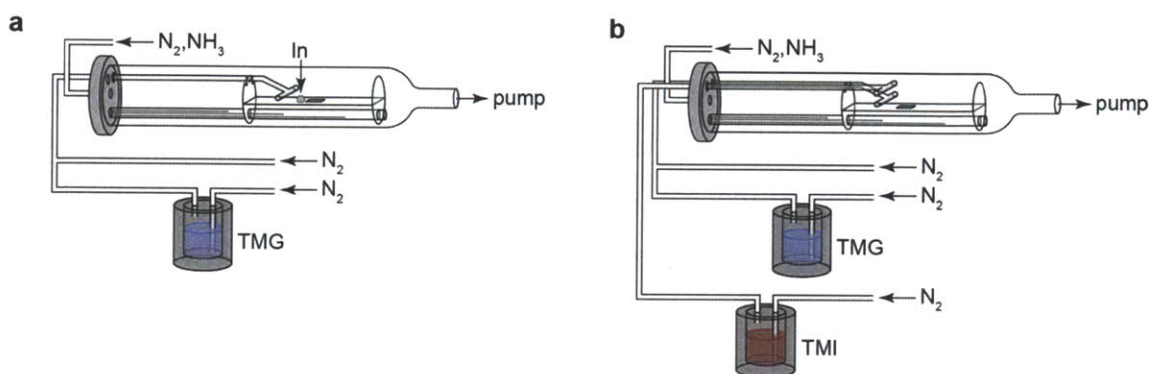


Figure 3-3. Setup for InN and InN/InGaN nanowire growth. (a,b) Schematic illustration of the quartzware setup, precursors, and gas injection for both InN and InN/InGaN nanowire growths for In (a) and TMI (b) sources.

3.1.5. Growth of InN/InGaN axial heterostructures

The conditions described above for InN were used as the basis for InN/InGaN axial heterostructures. Axial heterostructures were fabricated by introducing TMG during growth and keeping the total flow of gases constant. The TMG was delivered bubbling 0.2–10 sccm N_2 through TMG along with a total of 50 sccm N_2 through the injector line.

3.2. Synthesis of GaAs nanowires

Gallium arsenide nanowires were synthesized by MOCVD using Au colloids to seed growth. The fluxes of III and V precursors were varied during growth in order to modulate the nanowire diameter. Details of the experimental setup, growth conditions, and substrate preparation are described below.

3.2.1. Experimental setup & growth conditions

For GaAs nanowire growths, a cold-walled horizontal-flow MOCVD system (Thomas Swan CS62820) was used (Figure 3-4). Substrates are placed on a graphite susceptor that is heated by infrared emission from halogen lamps. This configuration allows the III and V precursors to be delivered to the substrate with minimal side reactions occurring away from the susceptor. All

growths were performed at 420°C and atmospheric pressure. Throughout heating, growth, and cooling, 15 slpm H_2 was delivered to the system. Once heated to 350°C, AsH_3 was introduced at a rate of 3.4 sccm to minimize decomposition at the surface of the GaAs substrates. In some cases, the substrates were annealed at 600°C for 10 min prior to growth and then cooled to 420°C. At 420°C, TMG was introduced to initiate growth. Growths proceeded for 5–8 min. For diameter modulation studies, the AsH_3 and TMG flows used during nucleation and growth varied within and between growths. At the end of growth, the TMG flow was ceased, and the system was allowed to cool. The H_2 and AsH_3 flows were generally kept on until the system cooled to 350°C, at which point N_2 was used instead.

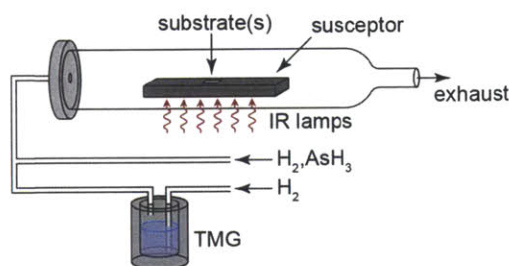


Figure 3-4. Chemical vapor deposition system for GaAs nanowire growth. Schematic illustration of the reaction furnace, graphite susceptor, and gas injection lines used for GaAs nanowire growths.

3.2.2. Substrate preparation

The substrates used for growth were (111)B GaAs and (111)A GaAs, which were cleaved from 2" wafers into approximately 0.5" × 1" substrates. The substrates were sonicated for 10 min each in acetone, methanol, and DI water. Aqueous solutions of gold colloids (BBI Solutions, 5-200 nm, 3×10^{-4} M Au) were diluted with DI water before deposition. Solutions with Au colloid diameters of 90, 60, 30, 10, and 5 nm were diluted with solution:DI water ratios of 1:1, 1:1, 1:5, 1:99, and 1:99. The 200 nm solution was not diluted. The substrates were coated with 20 μ L of the diluted solution for 10 min. The substrates were then rinsed with DI water, dried with compressed air, and kept in a desiccator until being used for growth.

3.3. Electron microscopy characterization

Electron microscopy is essential for characterizing the structure, morphology, and composition of nanowires. Because nanowires have diameters much smaller than the wavelength of light, traditional optical microscopy techniques cannot resolve them. The spatial resolution (δ_{opt}) of optical microscopy is given by the Rayleigh criterion,

$$\delta_{opt} = \frac{0.61\lambda}{NA} = \frac{0.61\lambda}{n \sin \theta} \quad (3-1)$$

where λ is the wavelength of light, NA is the numerical aperture, $n \cdot \sin \theta$, where n is the refractive index and θ is the semi-angle of collection).¹³⁰ For optical microscopy with visible light, λ is about 400–700 nm, and NA is usually less than 1. This technique does not offer the ability to resolve the diameter of the nanowire, let alone the nanoscopic features within the nanowire. To achieve better resolution, it is possible to image nanowires using an electron beam. The resolution (δ_{el}) of a transmission electron microscope is given by

$$\delta_{el} = 0.91(C_s \lambda_{el}^3)^{1/4} \quad (3-2)$$

where C_s is the coefficient of spherical aberration (which lies between 1 $\mu\text{m} - 1\text{mm}$),¹³¹ and λ_{el} is the wavelength of an electron.¹³²

$$\lambda_{el} = \frac{h}{\sqrt{2meV \left(1 + \frac{eV}{2mc^2}\right)}} \quad (3-3)$$

where h is the Planck constant, m is the mass of an electron, e is the charge of an electron, V is the accelerating voltage, and c is the speed of light.¹³² At the operating voltages used in scanning and transmission electron microscopy (1–300 kV), λ_{el} is around 1–10 pm. An electron beam can be generated by heating a filament (e.g. LaB₆) and/or operating that filament a high voltage to reduce the energy required to emit an electron. The beam can then be focused using electromagnetic lenses, which are analogous to the glass lenses used in optical microscopy. The resolution (δ_{el}) of scanning and transmission electron microscopy are around 1 nm and 0.1 nm, respectively. These techniques can therefore be used to resolve the smallest features of nanowires.

When a high-energy electron beam strikes a material, it produces a variety of signals that offer different information about the sample (Figure 3-5). Scanning electron microscopy (SEM) utilizes lower voltages (1–40 kV) and detects secondary and backscattered electrons that are

emitted from the surface of the sample. Therefore, SEM is used to detect surface morphology with nanometer resolution. Transmission electron microscopy (TEM) utilizes higher voltages (100's kV) to image thin samples and detects the electrons that pass through the sample. Consequently, TEM provides a two-dimensional projection of the material with atomic resolution. In both SEM and TEM, the electron beam can produce a variety of signals that give characteristic information about the sample, including infrared-ultraviolet light, X-rays, and Auger electrons. The high energy electron beam can excite electrons from the valence band to the conduction that can then relax back to valence band and emit infrared-ultraviolet light, a process called cathodoluminescence (CL). Detection of this light provides information about the material's band structure, as well as the presence of defects. Additionally, an incident high-energy electron can knock a core electron out of the nucleus of an atom. When another core electron relaxes into the missing electron's position, that electron's excess energy (about 1–20 keV) can yield high-energy X-rays, or that energy can be imparted to an outer electron that is then emitted with high energy, called an Auger electron. Because the energy of X-rays and Auger electrons are characteristic of the atoms from which they are emitted, detection of these signals using electron microscopy offers nanoscale resolution of the composition of the material.

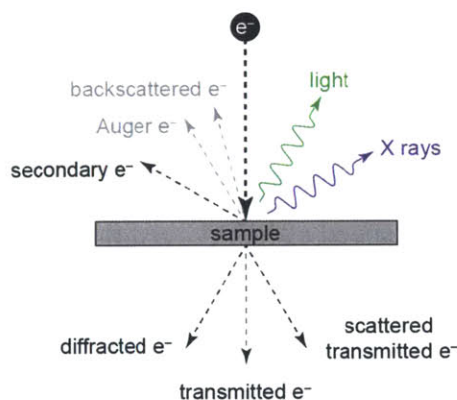


Figure 3-5. Signal production by high-energy electrons in electron microscopy. Schematic illustration depicting the detectable signals produced as a result of the high-energy electrons in electron microscopes interacting with the sample material. Secondary, backscattered, and Auger electrons are detected in SEM; transmitted and diffracted electrons are detected in TEM; scattered transmitted electrons are detected in STEM. Light and X-rays can be detected in any of these microscopes.

3.3.1. Scanning electron microscopy

As-grown nanowire arrays were analyzed using SEM to characterize their morphology – including diameter, length, tapering, and epitaxial orientation. In SEM, the emitted electrons are focused by a series of lens and apertures to form a probe that is around 1-10 nm wide (Figure 3-6). When this beam strikes the sample, secondary electrons are generated within a volume that is dependent upon both the operating voltage and the material composition. The beam is rastered over a selected area of the sample, and an electrically-biased Everhart-Thornley detector is used to collect secondary electrons. The image that is formed is based upon the quantity of electrons produced at a given point on the sample such that brighter regions indicate a greater emission of secondary electrons. Contrast from secondary electron detection is primarily a function of surface morphology, but is also dependent upon material composition. The instruments used to characterize nanowire samples for this thesis are a JEOL 6320F SEM and a Helios Nanolab 600 SEM operated at 1–5 kV in secondary electron mode. Additionally, in collaboration with Steven Boles at the Karlsruhe Institute of Technology, a FEI Nova NanoLAB 200 dual beam focused ion beam/scanning electron microscope equipped with a tungsten nanomanipulator probe (Kleindiek Nanotechnik GmbH) was used to test the mechanical properties of diameter-modulated GaN nanowires.

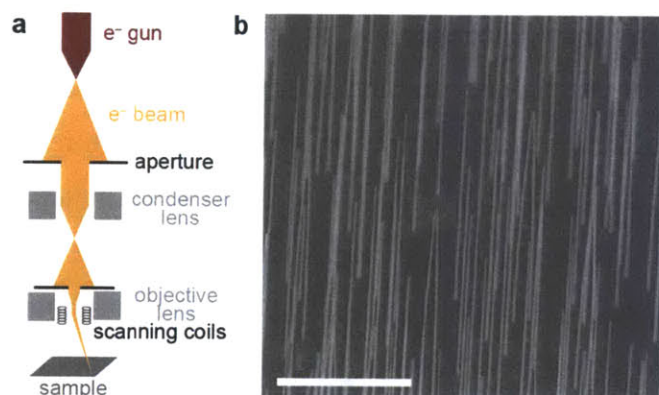


Figure 3-6. Scanning electron microscopy. (a) Schematic diagram of a scanning electron microscope adapted from [132]. (b) Plan-view (top) and cross-sectional (bottom) SEM images of *m*-GaN nanowire arrays. Scale bar represents 5 μm .

3.3.2. *Transmission electron microscopy*

Individual nanowires were characterized using TEM in order to provide detailed information about their structure and morphology – including the crystallographic growth direction, density of stacking faults, nanoscale morphological changes, and the diameter and length of segments formed under variable growth conditions. Very thin samples (about 1 μm or less) are needed for TEM, which relies upon the detection of high-energy electrons (100's kV) that are transmitted through the sample (Figure 3-7). Electrons from the emitter are formed into a parallel beam by the condenser lens. This electron beam passes through the sample, where some of the incident electrons are scattered elastically or inelastically. The objective lens focuses these electrons, and an objective aperture selects which regions of the beam are allowed to pass through to the intermediate and projection lenses magnify the image.

In standard bright-field imaging mode, the intermediate lens focuses the image formed by objective lens. In this case, the image that forms has contrast resulting from differences in the density of detected electrons. Scattered electrons are deflected away from the direction of the incident beam, producing “mass-thickness” contrast resulting from greater scattering from the heavier elements and thicker regions, which appear darker. Additionally, electrons can be scattered by diffraction resulting from the periodic arrangement of atoms in the material. This produces “diffraction contrast” that allows perturbations in the periodicity of the lattice – including stacking faults and dislocations – to be observed. Furthermore, selected area diffraction (SAD) patterns can be obtained by focusing the intermediate lens on the diffraction pattern formed in the back focal plane of the objective lens. High-resolution TEM (HR-TEM) allows the visualization of “phase contrast.” When crystalline materials are viewed along an appropriate zone axis of the crystal at very high magnification, the periodicity of the lattice is reflected by contrast that results from interference between the transmitted and scattered beams.

Nanowire samples were prepared on copper mesh grids with lacey carbon (Ted Pella) by one of two methods: (1) sonicating the as-grown sample in ethanol and pipetting the nanowire-containing solution onto a TEM grid or (2) mechanically swiping a TEM grid across the as-grown substrate. These samples were then imaged using a JEOL 2010 or JEOL 2010F TEM.

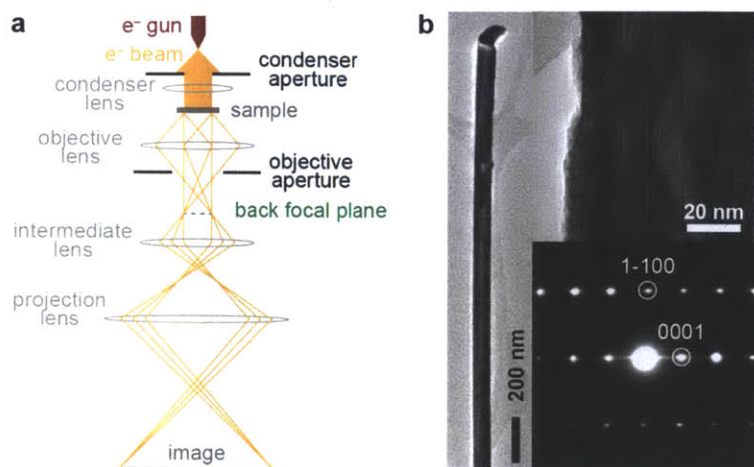


Figure 3-7. Transmission electron microscopy. (a) Ray diagram of a transmission electron microscope adapted from [132]. (b) TEM image (left), HR-TEM image (top right), and corresponding SAD pattern (bottom right) of an InN nanowire.

3.3.3. Scanning transmission electron microscopy

Scanning transmission electron microscopy (STEM) uses the same equipment as TEM, except the condenser lens converges the beam to a point instead of forming a parallel beam (Figure 3-8). Similar to SEM, the beam is rastered over the sample to produce an image. In dark-field STEM mode (DF-STEM), an annular detector is used to detect the scattered electrons. In comparison to TEM, STEM provides better mass contrast, enabling small differences in concentration to be visualized. Additionally, STEM can be coupled with other characterization techniques such as energy-dispersive X-ray spectroscopy (EDS), which provides a compositional map with nanometer resolution. In these studies, a JEOL 2010F STEM was operated at 200 kV with a 1 nm spot size and a 10 cm camera length.

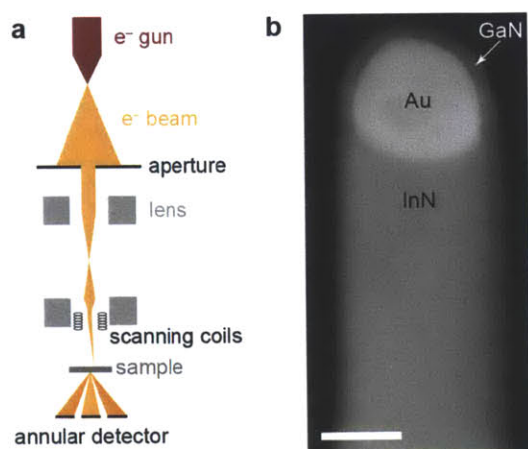


Figure 3-8. Scanning transmission electron microscopy. (a) Schematic diagram of a scanning transmission electron microscope adapted from [132]. (b) STEM image of an InN nanowire with a Au seed and GaN shell. Scale bar represents 100 nm.

3.3.4. Energy-dispersive x-ray spectroscopy

To assess the composition of individual nanowires, EDS was coupled with DF-STEM to detect the elemental composition with nanoscale resolution (Figure 3-9). As described previously, incident high-energy electrons can collide with core electrons in the sample, leaving an empty state. When an electron from a higher-energy orbital relaxes to fill that state, an X-ray can be emitted with a photon energy equal to the difference in energy between the two orbitals. Because the energies of core orbitals are element-specific, the energy of an X-ray photon provides a “fingerprint” of the element from which it was emitted. For these studies, a JEOL 2010F STEM was operated at 200 kV with a 1 nm spot size and 10 cm camera length.

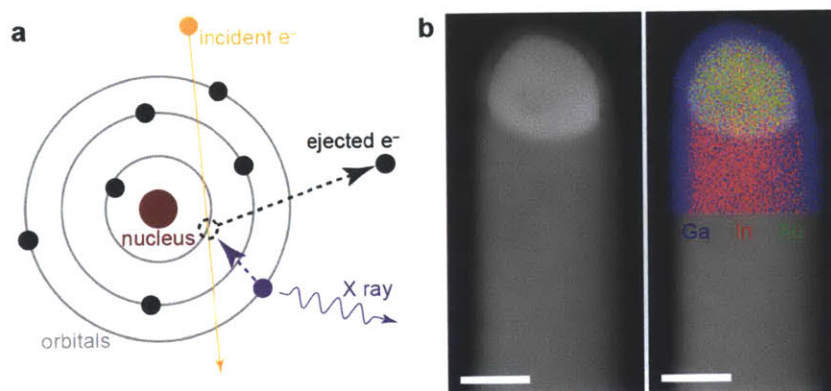


Figure 3-9. Energy dispersive X-ray spectroscopy. (a) X-ray generation by electron-beam irradiation. (b) STEM image of a Au-seeded InN nanowire with a GaN shell (left) and corresponding EDS map overlaid on the same STEM image (right). Scale bar represents 100 nm.

3.3.5. Electron tomography

While SEM provides information about surface morphology and TEM provides a two-dimensional projection with crystallographic information, it can nonetheless be challenging to fully understand the three-dimensional morphology of the nanowires. By taking multiple two-dimensional projections of the nanowires at different tilt angles, the three-dimensional shape of the nanowire can be reconstructed (Figure 3-10). This technique, called electron tomography, provides a detailed understanding of both surface morphology and crystallography. In particular, slices can be taken at different positions along the reconstructed nanowire to observe how the cross-sectional shape evolves during growth (Figure 3-10c).⁶¹ In these studies, electron tomography was performed using high-angle annular DF-STEM on a FEI Titan microscope operated at 200 kV. Images were taken in 1° increments between -67° and 67° . The images were aligned using a cross-correlation algorithm and three-dimensional reconstruction was carried out using the Simultaneous Iterative Reconstruction Technique, as well as total variation minimization. Electron tomography analysis was performed in collaboration with Georg Haberknecht at the French Alternative Energies and Atomic Energy Commission's Laboratory for electronics and information technologies (CEA-Leti).

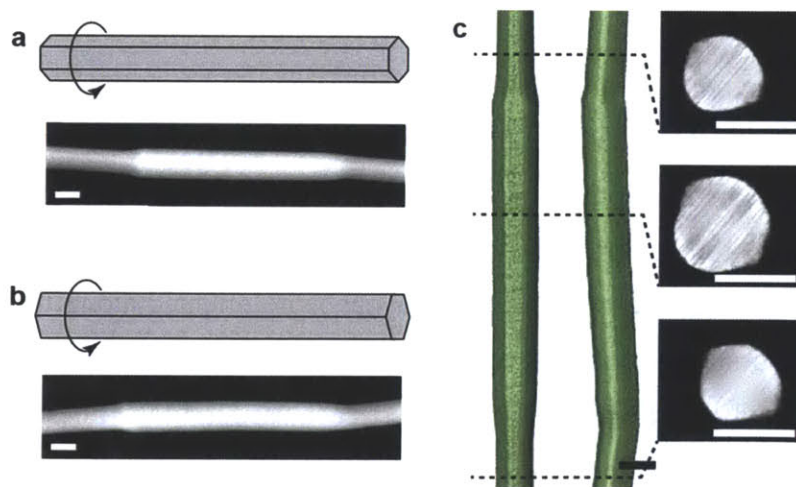


Figure 3-10. Electron tomography. (a,b) Schematic diagrams of GaAs nanowires with hexagonal cross-sections (top) and corresponding STEM image (bottom) for one orientation (a) and another after 90° rotation (b). (c) Tomographical reconstruction showing two orientations rotated by 90° and corresponding cross-sectional slices. Scale bar represents 100 nm.

3.4. Data analysis and modeling techniques

The following section describes data analysis and modeling techniques for EDS measurements and nanowire diameter evolution.

3.4.1. EDS measurements of seed particles and nanowires

Compositional information was obtained via EDS in STEM as described above in section 3.3.4. Spectra were collected and analyzed using INCA software. The spectra were corrected to account for false Cu and C signals originating from the TEM grid.

To calculate seed particle composition for InN and InN/InGaN nanowires (sections 5.2.1 and 6.1.2), the composition of both seed alloy and the neighboring oxide region were including in the measurements. The spectra were quantified from selected regions determined from the STEM image, Au signal map, and O signal map. The oxide region (determined to be In₂O₃ in the case of InN nanowires) is only present at the nanowire tip and is therefore presumed to form after growth as a result of remaining supersaturated III source in the Au-III seed alloy reacting with trace oxygen in the system. The presence of this oxide actually enables a better *ex situ* estimate of *in situ* seed composition, because the O traps the III source and ceases further nanowire growth. In the case of GaN nanowires with highly supersaturated seed particles (section 7.2.2), much of the remaining supersaturated Ga is extracted during the relatively long cooling phase (from 835°C for GaN versus 560°C for InN) to form GaN, instead of Ga₂O₃. The continued growth of GaN during cooling makes it difficult to differentiate between Ga originally present in the seed before cooling and Ga that continued to incorporate and promote growth during cooling.

To evaluate the cross-sectional shape and faceting of GaAs nanowires (section 8.2.2), hexagonal models and tomography results were used to model EDS linescan profiles. First, linescans were taken across the width of a GaAs nanowire oriented along the [110] zone axis, producing plots of the intensity of the Ga signal (I) versus position (x). First, hexagonal cross-sections which assumed {110} or {112} facets were each used to fit the linescan profile (a). The optimizing variables were the length of each facet (L), which was allowed to vary between facets, as well as the starting position (x_0) of the cross-section. To fit the linescan data, the following equation was used

$$I_{hex}(x) = \sum_i h(x) e^{-(x_i - x)^2 / (2D^2)} \quad (3-4)$$

where h is the height of the cross-section at a given position (x) and I_{hex} is the signal intensity, which accounts for spreading of the signals at each position (x_i) along the linescan assuming a spreading coefficient (D). The same spreading coefficient was used in all models. Next, I_{hex} was normalized using the following equation

$$I_{hex}^*(x) = \left(\frac{\sum_i I(x_i)}{\sum_i I_{hex}(x_i)} \right) I_{hex}(x) \quad (3-5)$$

which makes the total integrated intensity of the hexagonal model (I_{hex}^*) the same as the total integrated intensity of the linescan profile (I). The starting position and facet lengths were optimized to maximize the coefficient of determination, R^2 .

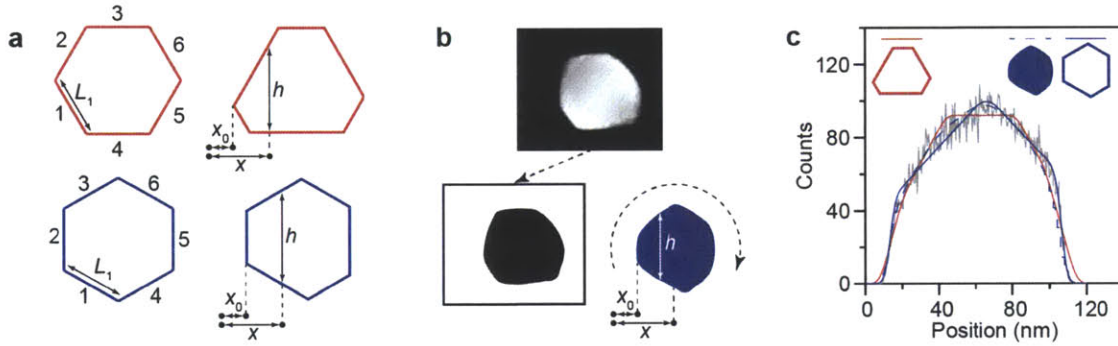


Figure 3-11. Models for cross-sectional EDS linescans. (a) Hexagonal models with $\{110\}$ (red) and $\{112\}$ (blue) facets. Both basic models (left) and optimized cross-sections (right) are shown, indicating facet length (L), position (x), starting position (x_0), and thickness (h). (b) Tomography cross-section image (top), binary image (bottom left), and rotated image assuming $\{112\}$ facets (bottom right). (c) EDS linescan profile (gray) and corresponding models using optimized shapes shown in (a) and (b). The inset indicates which line corresponds to which cross-section.

Next tomography cross-sections were fit to the linescan profile. Using ImageJ software, the cross-section images were first converted into binary images and then rotated such that the orientation of the facets corresponded to either $\{110\}$ or $\{112\}$ (Figure 3-11b). A plot of the thickness, h , was produced as a function of image position (x'), which was adjusted to be a function linescan position (x) as follows

$$x = ax' + x_0 \quad (3-6)$$

where a and x_0 are fitting parameters, and $h(x) = h(x')$. Because six different orientations are possible for each facet type ($\{110\}$ and $\{112\}$), the orientation that provided the best fit with the EDS profile was chosen. An intensity profile was produced from $h(x)$ using Equations 3-4 and 3-5, then fit to the linescan profile by optimizing a and x_0 .

Optimized models for a sample linescan profile are shown in Figure 3-11c.

3.4.2. Evolution of diameter along the nanowire axis

The axial evolution of nanowire diameter was modeled to evaluate the proposed mechanism of diameter evolution and the morphology of the liquid/solid interface (section 7.3.4). The flow rate of the V or III source was varied as a function of time, based on experimental results, and the diameter was calculated step-wise at each position along the nanowire, assuming that the force balance at the vapor/liquid/solid triple-phase boundary is upheld at all times. The step length (ΔL) was kept constant, and the extraction rate (E), incorporation rate (I), seed composition (x_{III}), amount of III source in the seed particle (n_{III}), volume (V), wetting angle (β), inclination angle (α), surface energies (σ), axial position (L), diameter (d), and growth time (t) were all calculated for each step (Figure 3-12).

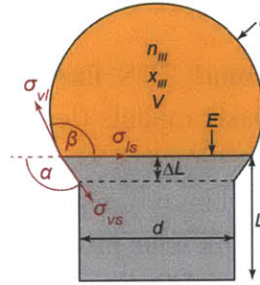


Figure 3-12. Model for nanowire diameter evolution. Schematic representation of the variables used in the nanowire diameter evolution model: incorporation rate (I), extraction rate (E), seed composition (x_{III}), number of III atoms (n_{III}), seed volume (V), length (L), step length (ΔL), diameter (d), wetting angle (β), inclination angle (α), and the surface energies of the vapor/liquid (σ_{vl}), liquid/solid (σ_{ls}), and vapor/solid (σ_{vs}) interfaces. The diagram represents the case of a flat liquid/solid interface.

To simplify the model, the extraction rate, incorporation rate, and surface energy of the seed were calculated based on empirical measurements. For a change in V flow, the extraction rate was assumed to be linearly dependent upon the NH_3 flux, while the incorporation rate and seed

surface energies were assumed to linearly be dependent upon the seed composition. These were calculated as follows

$$E = m_E F_V + b_E \quad (3-7)$$

$$I = m_I x_{III} + b_I \quad (3-8)$$

$$\sigma_i = m_\sigma x_{III} + b_\sigma \quad (3-9)$$

where F_V is the flow rate of the V precursor, and m and b are constants calculated from experimental measurements. For a change in III flow, the incorporation rate was assumed to be linearly dependent upon the Ga flux, while the extraction rate and seed surface energies were assumed to be linearly dependent upon the seed composition. In this case, these values were calculated as follows

$$E = m_E x_{III} + b_E \quad (3-10)$$

$$I = m_I F_{III} + b_I \quad (3-11)$$

$$\sigma_i = m_\sigma x_{III} + b_\sigma \quad (3-12)$$

where F_{III} is the flow rate of the III precursor. Different values of m and b were calculated for different nanowires.

In both cases, the following equations are used for the other parameters mentioned above

$$L_i = L_{i-1} + \Delta L \quad (3-13)$$

$$\Delta t_i = \frac{\Delta L A}{E_i \Omega_{NW}} \quad (3-14)$$

$$t_i = t_{i-1} + \Delta t_{i-1} \quad (3-15)$$

$$n_{III,i} = n_{III,i-1} + (I_i - E_i) \Delta t \quad (3-16)$$

$$x_{III,i} = \frac{n_{III,i}}{n_{III,i} + n_{Au}} \quad (3-17)$$

$$V_i = n_{III,i} \Omega_{III} + n_{Au} \Omega_{Au} \quad (3-18)$$

$$\alpha_i = \tan^{-1} \left(\frac{d_i - d_{i-1}}{2(L_i - L_{i-1})} \right) \quad (3-19)$$

$$d_i = (f(\beta_i)^3 V_i)^{1/3} \quad (3-20)$$

Where i is the step, Ω is atomic volume, A is the cross-sectional area of the nanowire, n_{Au} is the amount of gold in the seed, and $f(\beta)$ is an equation derived from Surface Evolver simulations describing the ratio between nanowire diameter and seed particle volume for a given wetting angle. The wetting angle, β , was calculated from force balance equations at the vapor/liquid/solid triple-phase boundary, which varied based on the assumed liquid/solid interface morphologies (flat, faceted, or rounded; see section 7.3.2). The diameter was optimized at each position such that force balance was maintained.

Chapter 4: Structural & morphological control of GaN nanowires

This chapter describes techniques that were developed to fabricate GaN nanowires with controlled structure and morphology. Both *c*- and *m*-oriented nanowires were grown by selecting substrates with appropriate epitaxial relationships. Tapering was minimized by reducing the Ga flux and increasing the nanowire density, enabling effective consumption of Ga precursors by the seed particles. The fundamental growth mechanism of GaN nanowires was explored by analyzing the growth rate as a function of diameter. A generalized nucleation-mediated growth model was developed to demonstrate that the rate-limiting step is nucleation at the perimeter of the liquid/solid interface. Using this model, a calculated reduction in the supersaturation was found to account for the reduction in GaN nanowire growth rate with increasing hydrogen content in the carrier gas. Next, GaN nanowires were grown using both Au and Ni films to elucidate the role of the seed material in nanowire growth. Given that nucleation was found to be the rate-limiting step, the high growth rate and low defect density in Ni-seeded nanowires was concluded to stem from a low seed/nanowire surface energy that reduces both the nucleation barrier and the probability of stacking fault formation.

4.1. Control of GaN nanowire growth direction and tapering

As discussed in Chapter 2, two very important characteristics of nanowires are the growth direction and tapering. The crystallographic growth direction is particularly important for III-V nitrides due to orientation-dependent spontaneous polarization. Tapering results from film deposition on the nanowire sidewalls and is generally undesirable for nanowire-based devices, because the differences in mechanisms between VLS growth and sidewall deposition yield spatial differences in nanowire properties. Here, we demonstrate control over both of these features. Both polar- and nonpolar-oriented GaN nanowires were grown by utilizing substrates with appropriate epitaxial relationships. When grown on *c*-sapphire and *r*-sapphire substrates, GaN nanowires grew in the *c*- and *m*-directions, respectively. Significant sidewall deposition led to tapered nanowire morphologies for high Ga fluxes and large inter-nanowire spacings, in both cases due to ineffective consumption of Ga precursors by the seed particles. For high Ga fluxes, the formation of Ga droplets slows diffusion and prevents Ga from reaching the seed before reacting with N species, yielding GaN film growth. For large inter-nanowire spacings, not

enough nanowires are present to consume all the Ga impinging on the substrate via particle-mediated axial growth, so excess Ga contributed to GaN film formation. By using a higher nanowire density and lower Ga flux, tapering was effectively minimized.

4.1.1. Control of crystallographic growth direction

As described in section 2.3.1, III-V nitrides have built-in polarization in the [0001] *c*-direction due to the arrangement of atoms within the unit cell. For LEDs, *c*-oriented heterojunctions induce the quantum-confined Stark effect,³⁶ in which a spatial separation of electrons and holes slows radiative recombination, reducing device efficiency. By orienting heterojunctions along nonpolar orientations, this effect can be minimized. In nanowires, this can be achieved by fabricating radial heterojunctions around *c*-oriented nanowires or axial heterojunctions along nonpolar-oriented nanowires, including the [1-100] *m*-direction and the [11-20] *a*-direction, although other potential nonpolar orientations do exist.¹³³

Here, we seek to fabricate GaN nanowires in both polar and nonpolar growth directions. Previous reports have demonstrated particle-mediated GaN nanowires grown in the *c*-, *m*-, and *a*-directions.^{63,64} Notably, Kuykendall *et al.* synthesized both *c*-GaN and *a*-GaN with Au seed particles using (111) MgO and (100) γ -LiAlO₂ substrates, respectively.⁶⁴ These substrates had been selected based on their lattice match with GaN. In this case, *c*-GaN matches well with (111) MgO, while *m*-GaN matches well with (100) γ -LiAlO₂. By comparison, sapphire substrates are cheaper and more widely available for GaN growth. We chose to use *c*-sapphire, which is known to produce *c*-oriented GaN films,³⁵ as well as *r*-sapphire, which produces *a*-oriented GaN films.¹³⁴

The *c*-sapphire and *r*-sapphire substrates were coated with 1 nm Au films using electron beam evaporation and then loaded into the growth chamber. GaN nanowires were grown at 900°C and atmospheric pressure using CVD with metallic Ga as the III-source, as described in section 3.1.3. The morphology and structure of the GaN nanowires were analyzed using SEM and TEM (Figure 4-1). As expected, *c*-sapphire produced polar-oriented nanowires (Figure 4-1a-e), while *r*-sapphire produced nonpolar-oriented nanowires (Figure 4-1f-j). Plan-view and cross-sectional SEM images show that the *c*-sapphire substrates produce vertical nanowires. Based on the epitaxial relationship between GaN and *c*-sapphire, vertical nanowires indicate *c*-directional growth (Figure 4-1d,e), which was confirmed by selected area diffraction (Figure

4-1c). In addition, some nanowires are observed to grow laterally along the substrate. Given that the vertical nanowires are *c*-oriented, the lateral nanowires should be nonpolar, and the six-fold symmetry of the lateral nanowires is consistent with nonpolar growth of either *a*- or *m*-oriented nanowires.

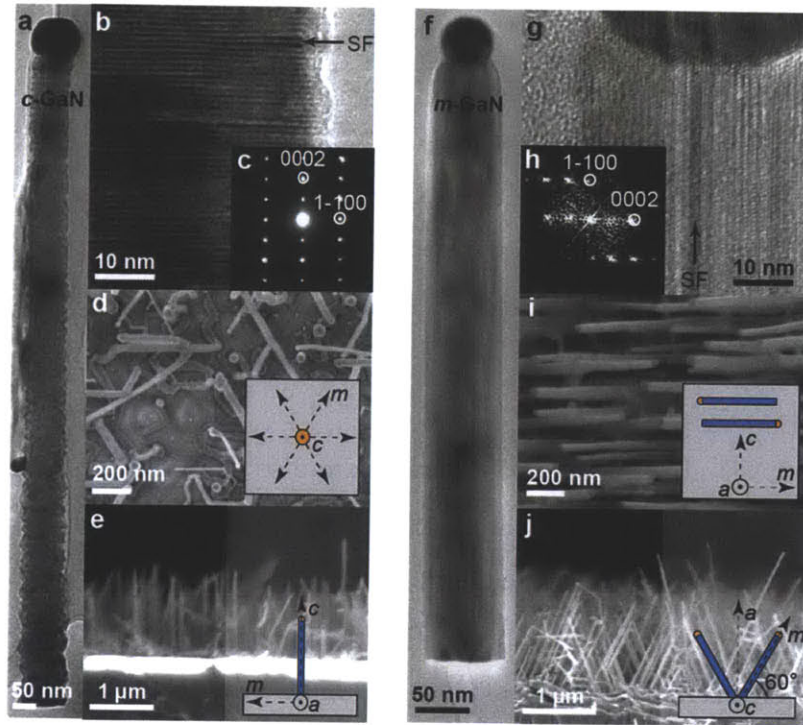


Figure 4-1. Controlling the growth direction of GaN nanowires. (a-j) SEM and TEM characterization of *c*-GaN nanowires grown on *c*-sapphire (a-e) and *m*-GaN nanowires grown *r*-sapphire (f-j). The morphology of individual nanowires is revealed by TEM images (a,f), while HR-TEM images (b,g) and corresponding SAD pattern/fast Fourier transform (c,h) show the stacking faults (SF) and their orientation, respectively. Top-down (d,i) and plan-view (e,j) SEM images show that *c*-GaN nanowires grow vertically from *c*-sapphire, while *m*-GaN nanowires grow at 60° angles from *r*-sapphire. Insets illustrate the crystallographic orientation of the nanowires.

The nanowires on *r*-sapphire grew inclined from the substrate at 60° angles (Figure 4-1i,j). Because of the epitaxial relationship between *r*-sapphire and GaN, vertical nanowires would correspond to *a*-GaN. Selected area diffraction indicates that the inclined nanowires are *m*-oriented (Figure 4-1h), which is consistent with the fact these nanowires which grow 30° from the normal, as the *a*- and *m*-directions are separated by 30° angles.

High-resolution TEM images of both *c*-GaN and *m*-GaN nanowires oriented along the [11-20] zone axis show planar defects along the *c*-plane (Figure 4-1b,g). These basal-plane stacking faults (BSFs) have commonly been observed in GaN films¹³⁵ and nanowires,¹³⁶ because the formation energy is only around 10 meV/unit cell.^{137,138} For *c*-GaN, the BSFs are orthogonal to the growth direction and occur randomly throughout the length of the nanowire during growth (Figure 4-1b). For *m*-GaN, the BSFs start at the base of the nanowire and continue to propagate along the length of the nanowire during growth (Figure 4-1g).

The ability to grow both *c*-GaN and *m*-GaN nanowires provides the ability to produce nonpolar-oriented heterojunctions in radial and axial heterostructures, respectively. However, the defects in these structures may inhibit device performance. The origin of these defects, and strategies for mitigating them, will be explored in more detail in section 4.3.

4.1.2. *Tapering minimization*

In addition to CVD-grown GaN, nanowires were also grown by MOCVD (section 3.1.3) using TMG instead of Ga as the III source. To grow *m*-GaN nanowires, *r*-sapphire substrates were used for the growth and were coated with 1 nm Au films. The GaN nanowires were grown at 835°C and 100 Torr. Initially, a significant amount of tapering was observed, which results from film deposition on the nanowire sidewalls (Figure 4-2a). Tapering is undesirable for a variety of reasons. First, it leads to a wider diameter at the nanowire base, which may offset some of the benefits of nanowires, for example inhibiting the efficient strain relaxation that allows dislocation-free growth. Furthermore, because film growth occurs by a different mechanism than nanowire growth, tapering leads to differences in composition⁴² and doping⁴³ between the VLS-grown core and the film shell. In other materials systems, tapering has most commonly been minimized by reducing the growth temperature.^{112,113} By this method, film deposition is minimized due to the fact that nanowires can grow at relatively high rates compared to films at low temperature. However, GaN nanowires have been observed to have higher resistivity and weaker luminescence as the growth temperature decreases, so a method of minimizing tapering at high temperature would be preferable.^{139,140}

Film deposition on nanowire sidewalls could be considered a result of excess Ga that is not effectively consumed by the seed during nanowire growth. To test this, the Ga flux was reduced from 2.1 to 0.4 sccm TMG. The resulting nanowires grew with minimal tapering (Figure 4-2b),

indicating that film growth was a consequence of excess Ga. Furthermore, when 60 nm Au colloids were used instead of 1 nm Au films, the resulting nanowires were highly tapered (Figure 4-2c). With fewer nanowires around to capture the available Ga, excess Ga resulted in film deposition. This explanation is consistent with the results of Borgstrom *et al.*, who found that the growth rate of GaP nanowires was dependent upon the inter-nanowire spacing due to competition for available Ga precursors.¹⁴¹ In fact, our GaN nanowires grew faster using sparse colloids than using dense particles via Au films. Conversely, the dense nanowire arrays grown at high Ga fluxes have lower axial growth rates than those grown at lower Ga fluxes. For high Ga fluxes, the thick shells consume most of the Ga before it reaches the seed. Excess amounts of Ga can produce Ga droplets on the substrate, which have much lower diffusivities than Ga adatoms,^{142,143} and therefore are less likely to reach the seed particle before being consumed by film growth.

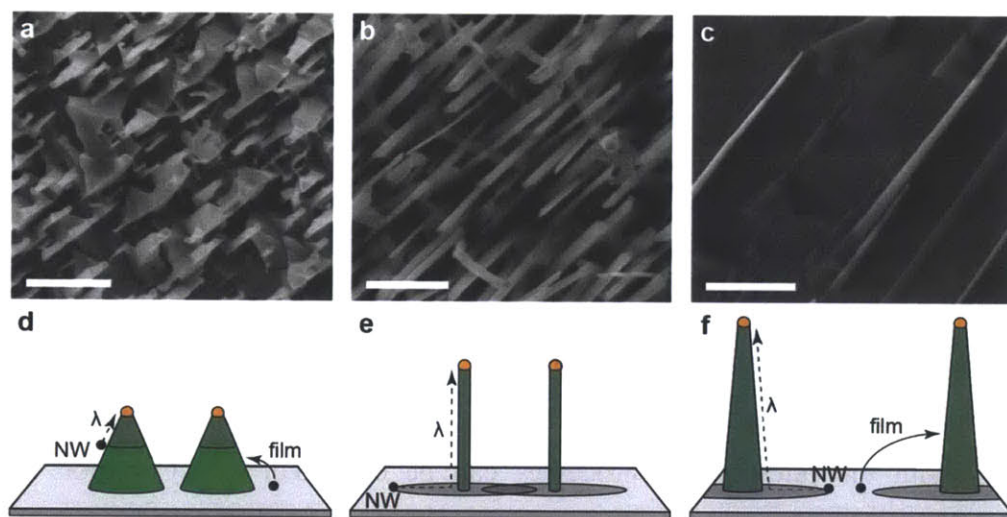


Figure 4-2. Tapering control in GaN nanowires. (a-c) SEM images of *m*-GaN nanowires grown using a 1 nm Au film and 2.1 sccm TMG (a), 1 nm Au film and 0.4 sccm TMG (b), and 60 nm Au colloids and 0.4 sccm TMG (c). (d-f) Schematic illustrations demonstrating simultaneous nanowire (“NW”) and sidewall (“film”) growth under the conditions in (a-c), respectively. Shaded regions illustrate the collection zone in which Ga precursors (black circles) contribute to nanowire growth. Ga precursors landing outside of the collection zone contribute to film growth. The size of the collection zone is defined by the diffusion length (λ) of the Ga precursor. All scale bars represent 500 nm.

Film deposition at both high Ga flux and large inter-nanowire spacing can be explained as follows. For temperatures at which film growth can occur readily, excess Ga not collected by the

seed for nanowire growth contributes to film growth (Figure 4-2d-f). When nanowires are close enough that they compete for Ga, film deposition is avoided (Figure 4-2e). This occurs when the collection zones overlap, where the collection zone is defined by the diffusion length of the precursor. In the case of colloids, the inter-nanowire distance was increased, reducing overlap of collection zones (Figure 4-2f). The reduced competition between nanowires for available Ga led to an increased growth rate, but excess Ga not collected by the nanowires led to tapering. Notably, similar results have since been reported by Xu *et al.* when growing GaAs nanowires at different nanowire spacings.¹¹⁵ In the case of high Ga fluxes, the reduced diffusivity of Ga resulted in less Ga reaching the nanowires before being consumed in film growth, which resulted in less Ga available for each nanowire and consequently reduced the growth rate (Figure 4-2d).

In addition to minimizing tapering in these GaN nanowires, these results provide a general method for achieving non-tapered nanowires at higher growth temperatures, specifically by reducing both the Ga precursor flux and inter-nanowire spacing. This finding is significant, because resulting nanowire properties can be dependent upon the growth temperature. For GaN nanowires, optical and electronic properties can degrade as the growth temperature decreases.^{139,140,144} For example, much lower lasing thresholds were obtained for GaN nanowires growth at 950°C versus 775°C.²⁷ In other nanowire systems, higher growth temperatures may enable superior epitaxy¹⁴⁵ and crystal phase purity.^{92,146}

4.2. Nucleation-mediated growth model

By investigating the nanowire growth rate as a function of diameter, fundamental information about the rate-limiting processes can be extracted.⁷⁴⁻⁷⁹ Common rate-limiting processes during nanowire growth include adatom diffusion and the reaction at the liquid/solid interface. Other potential rate-limiting processes are described in section 2.2.1. When the growth rate decreases as the diameter increases, the rate-limiting step is generally adatom diffusion.^{74,79} On the other hand, when the growth rate increases with diameter, the rate-limiting step is usually the reaction at the liquid/solid interface.⁷⁵⁻⁷⁷ By fitting the experimental data with theoretical models that describe the growth rate as a function of diameter, it is possible to extract further information about growth conditions, including the supersaturation^{38,76,147,148} and the diffusion length of precursors.^{76,149-151}

We investigated the growth rate of GaN nanowires as a function of both diameter and carrier gas composition. The nanowires were grown for 20 min at 900°C and atmospheric pressure using CVD, as described in section 3.1.3. In separate growths, the fraction of H₂ in the carrier gas was varied from 0 to 0.6, with the remainder being N₂. Using Au films, the nanowires grow with a range of diameters. For each growth, both 1 and 3 nm thick Au films were used to achieved a broader range of nanowire diameters. The films were deposited on 2 μm thick *α*-GaN films on *r*-sapphire. The *α*-GaN templates have a couple benefits in comparison to *r*-sapphire substrates. First, the *α*-GaN films are more conductive than *r*-sapphire, which is more ideal for carrying current in device applications. Second, the epitaxy of the nanowires with the substrate is superior, which provides a more reliable measurement of nanowire growth rate between different nanowires.

4.2.1. Diameter-dependent growth rate

The GaN nanowires grown with different film thicknesses and carrier gas compositions are shown in Figure 4-3. For all conditions, the nanowires grow at 60° angles relative to the substrate. This orientation is consistent with those with those depicted in Figure 4-1f-j, where SAD confirmed *m*-directional growth. As expected, the nanowires grown with 3 nm Au films have larger average diameters and lower areal densities than those grown with 1 nm Au films (Figure 4-3i). Additionally, increased H₂ fractions also increase the average diameter and

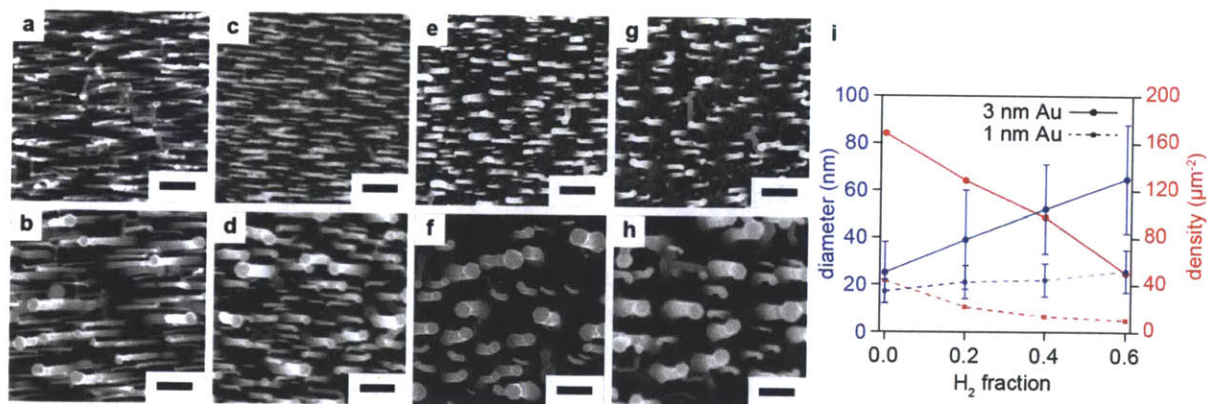


Figure 4-3. GaN nanowires grown using different carrier gas composition. (a-h) GaN nanowires grown using carrier gas H₂ fractions of 0 (a,b), 0.2 (c,d), 0.4 (e,f), and 0.6 (g,h) with 1 nm (a,c,e,g) and 3 nm (b,d,f,h) Au films. (i) Diameter (d ; blue) and areal density (ρ ; red) as a function of H₂ fraction. Images adapted from [38]. Scale bars represent 200 nm.

reduce the areal density. This effect can be attributed to increased Au particle agglomeration as the H_2 fraction in the carrier gas increases, which is consistent with previous observations of Au particle agglomeration on SiO_2 .¹⁵²

The growth rate of the GaN nanowires as a function of diameter and hydrogen fraction is plotted in Figure 4-4a,b. The increase in growth rate with increasing diameter is indicative of reaction-limited growth (see section 2.2.1). This diameter dependence is commonly attributed to the Gibbs-Thomson effect, which is described in Equation 2-2. In order to fit the data, the equation can be re-written as follows,

$$v_{GT} = \left(F_1 - \frac{F_2}{d} \right)^2 \quad (4-1)$$

Where v is the growth rate and d is the diameter. F_1 and F_2 are fitting parameters defined by

$$F_1 = \sqrt{K_{ls}} \frac{\Delta\mu_{ls}}{k_B T} \quad (4-2)$$

and

$$F_2 = \sqrt{K_{ls}} \frac{4\gamma_{ls}\Omega_s}{k_B T} \quad (4-3)$$

for growth limited by the reaction at the liquid/solid (ls) interface, where K is a kinetic coefficient, $\Delta\mu_{ls}$ is the change in chemical potential for the bulk material (i.e. nanowire diameter $\rightarrow \infty$), k_B is the Boltzmann constant, T is the growth temperature, Ω is the atomic volume of the

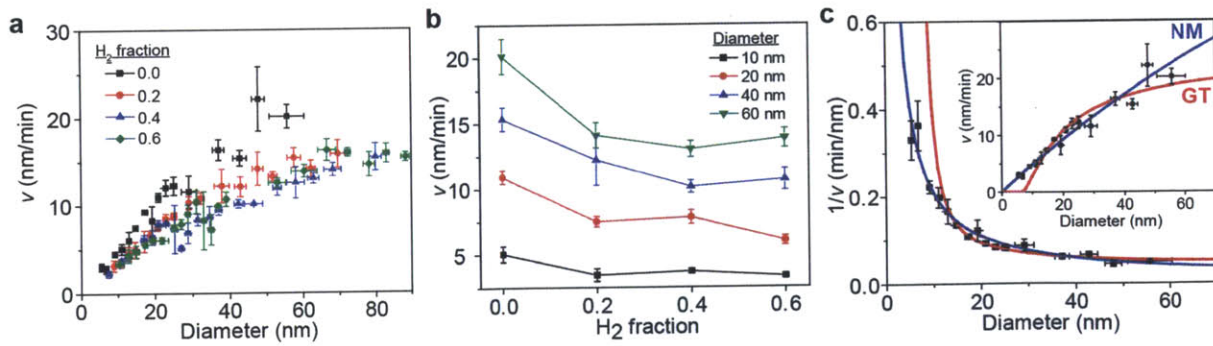


Figure 4-4. Diameter-dependent growth rate of GaN nanowires. (a) Growth rate (v) vs. nanowire diameter for different H_2 fractions in the carrier gas. (b) Growth rate vs. H_2 fraction for different nanowire diameters. (c) Fitting of the data from nanowires grown with N_2 carrier gas using the Gibbs-Thomson (“GT”) and nucleation-mediated (“NM”) growth models. Figure shows data plotted as $1/v$ vs. diameter. Inset shows the same data plotted as v vs. diameter. Figures adapted from [38].

source material in the crystal, γ is the surface energy at the liquid/solid interface.⁸¹ Figure 4-4c shows the fitting of this model for the nanowires grown using N₂ carrier gas. This model provides only a reasonable fit to the data ($R^2 = 0.845$) and is particularly inaccurate for the thinnest nanowires. Therefore, the Gibbs-Thomson effect may not account for the observed diameter-dependence of the growth rate.

As described in section 2.2.1, the Gibbs-Thomson model above is based upon an assumption of continuous on growth on a rough interface, but *in situ* nanowire growth studies demonstrate that the liquid/solid interface is smooth, and layer-by-layer growth proceeds by nucleation and subsequent ledge growth for each monolayer (Figure 4-5).¹⁵³ With each new layer, either one or multiple nuclei can form before the monolayer is filled via ledge growth. These two cases represent mononuclear and polynuclear growth, respectively. Because ledge filling proceeds rapidly relative to nucleation,¹⁵³ mononuclear growth becomes more dominant as the nanowire diameter decreases due to the reduction in available nucleation sites.⁸² Dubrovskii and Sibirev have developed a detailed model that includes contributions from the Gibbs-Thomson effect, adatom diffusion, and nucleation-mediated growth.¹⁵⁴ However, this complex model relies on multiple physical values that are unknown for nanowire systems and serve as fitting parameters. Alternatively, Kashchiev has demonstrated that a relatively simple model for growth of crystals of finite size can be applied to fit the diameter-dependent growth rate of GaAs nanowires.¹⁴⁸ This model is described in Equation 2-4, where the d^2 term originates from the assumption that nucleation is equally probable across the area of the crystal, which is proportional to d^2 .

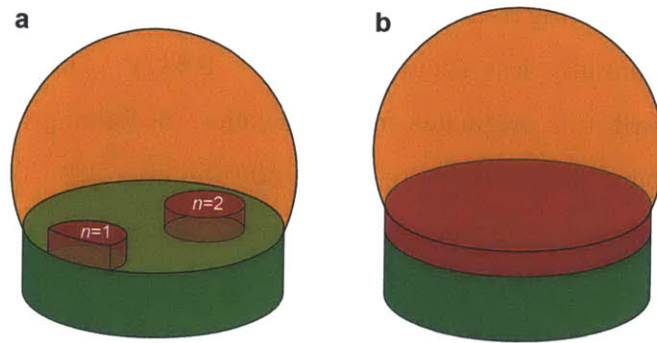


Figure 4-5. Nucleation-mediated nanowire growth. (a) Nuclei at the perimeter ($n = 1$) and interior ($n = 2$) illustrating situations where nucleation probability is proportional the circumference and area of the liquid/solid interface, respectively. (b) Subsequent and rapid ledge filling yields a new monolayer after a stable nucleus has formed.

For nanowires, growth may occur preferentially around the perimeter of the liquid/solid interface.⁶⁰ In this case, the probability of mononuclear growth would increase as the circumference of the liquid/solid interface increases, which is proportional to d . Hence we generalized Kashchiev's model as follows

$$v_{NM} = \frac{a_3 d^n}{1 + a_4 d^n} \quad (4-4)$$

where a_3 and a_4 represent the rates of polynuclear and mononuclear growth, respectively, while n is a geometrical factor that depends on whether nucleation probability is proportional to area ($n = 2$) or circumference ($n = 1$), as depicted in Figure 4-5. The rates of mononuclear and polynuclear growth can be expressed as functions of the supersaturation, $\Delta\mu$,

$$a_3 = A e^{\Delta\mu/k_B T} e^{-B/\Delta\mu} \quad (4-5)$$

$$a_4 = C(1 - e^{-\Delta\mu/k_B T})^{-2/3} e^{-2B/3\Delta\mu} \quad (4-6)$$

where A, B, and C are independent of $\Delta\mu$.⁸²

To determine the geometrical factor, n , Equation 4-4 can be rewritten as

$$\frac{1}{v_{NM}} = \frac{1}{a_3 d^n} + \frac{a_4}{a_3} \quad (4-7)$$

Where a_3 , a_4 , and n are used as fitting parameters and assumed to be independent of diameter. For the nanowires grown in N_2 (Figure 4-4c), the fit was optimized for $n = 0.96$ and very closely matches the experimental data ($R^2 = 0.953$). A similar power dependence ($n \approx 1$) was calculated for the nanowires grown under different carrier gas compositions. Furthermore, under the assumption that $n = 2$ and leaving a_3 and a_4 as fitting parameters, the nucleation-mediated growth model provided a substantially less accurate fit ($R^2 = 0.847$). This result indicates that the diameter-dependent growth rate originates from nucleation-mediated growth and that nucleation occurs preferentially around the perimeter of the liquid/solid interface. To our knowledge, this is the first direct experimental evidence of preferential nucleation at the perimeter of the liquid/solid interface.

It should be noted that the perimeter corresponds to the edge of the upper liquid/solid interface, which may or may not be the same as the vapor/liquid/solid triple-phase boundary (TPB). Even before our experimental results discussed above, it has been suggested in literature that nucleation occurs preferentially at the TPB, and this assumption has been used to explain

structural and morphological changes in other nanowire materials systems.^{5,92-94} This explanation largely hinges upon the assumption that the interface is flat with sharp edges (Figure 4-6a,b),⁸⁹⁻⁹¹ in which case the edge of the upper liquid/solid interface and the TPB are equivalent. However, recent studies suggest that the edges may be faceted (Figure 4-6c) or rounded (Figure 4-6d) at some length scale, which could result in nucleation occurring away from the TPB. While it is possible that contact between the upper liquid/solid surface and the TPB may occur temporarily,⁹⁶ it is also likely that no contact is made (see section 2.2.2).⁷ In the absence of such contact, it is still possible that the perimeter of the upper surface could serve as a preferential site for nucleation (Figure 4-6c,d) either be due to inhibited movement of atoms in the nucleus at the perimeter or due to higher supersaturation near rough edge facets.⁹⁵ Thus, for our GaN nanowires, nucleation could occur preferentially around the perimeter of the liquid/solid interface ($n = 1$) regardless of its morphology.

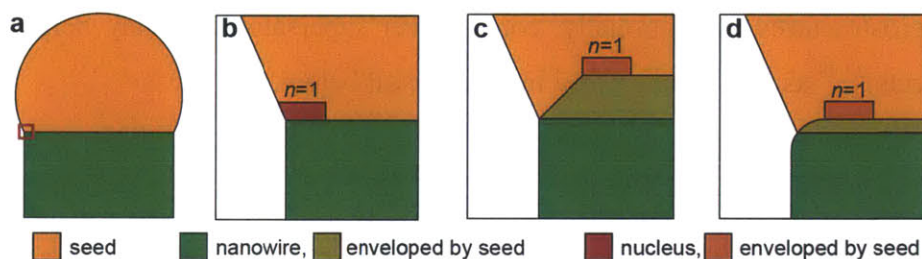
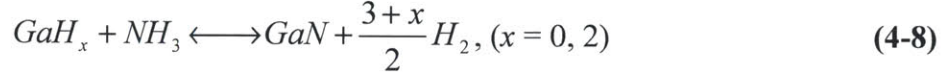


Figure 4-6. Liquid/solid interface morphology. (a) Illustration a seed particle on the tip of a nanowire. (b-d) Magnified views of the red box in (a) for flat (b), faceted (c), and rounded (d) liquid/solid interface morphologies. Red nuclei correspond to preferential perimeter nucleation ($n = 1$).

4.2.2. Effect of hydrogen

As described above, the growth rate of the GaN nanowires decreases as the fraction of H_2 in the carrier gas increases. Using Equations 4-4–4-6, it is possible to extract the supersaturation $\Delta\mu$ as a function of the composition of the carrier gas. The data in Figure 4-7 were fit using these equations assuming that $n = 1$ and the kinetic constants A , B , and C are not affected by H_2 . As shown in Figure 4-7e, the calculated supersaturation decreases as the H_2 composition in the carrier gas increases. The lower supersaturation is consistent with the observed reduction in growth rate and can be understood by considering the net chemical reaction that takes place. At

temperatures between 830°C and 1030°C, GaH₂ is more stable than Ga in the presence of H₂.¹⁵⁵ Here, H₂ is supplied by the carrier gas and/or decomposition of NH₃. Thus at 900°C, a mixture of Ga and GaH₂ reacts with NH₃ to form GaN and H₂:



Once the amount of H₂ in the system exceeds that necessary to saturate the amount of GaH₂, the excess H₂ promotes the reverse reaction. Thus the supersaturation and growth rate decrease as the H₂ composition in the carrier gas increases. A similar reduction in growth rate with H₂ has also been observed in GaN film growth.¹⁵⁶

These results are significant for multiple reasons. The ability to extract the supersaturation makes this model useful in probing fundamental phenomena of nanowire growth. Furthermore, by tuning the composition of the carrier gas, it is possible to control the growth rate of GaN nanowires, which can be particularly important for controlling the length of thin segments in nanowire heterostructures. Additionally, control over supersaturation may help in minimizing structural defects,^{87,88} as will be discussed in more detail below.

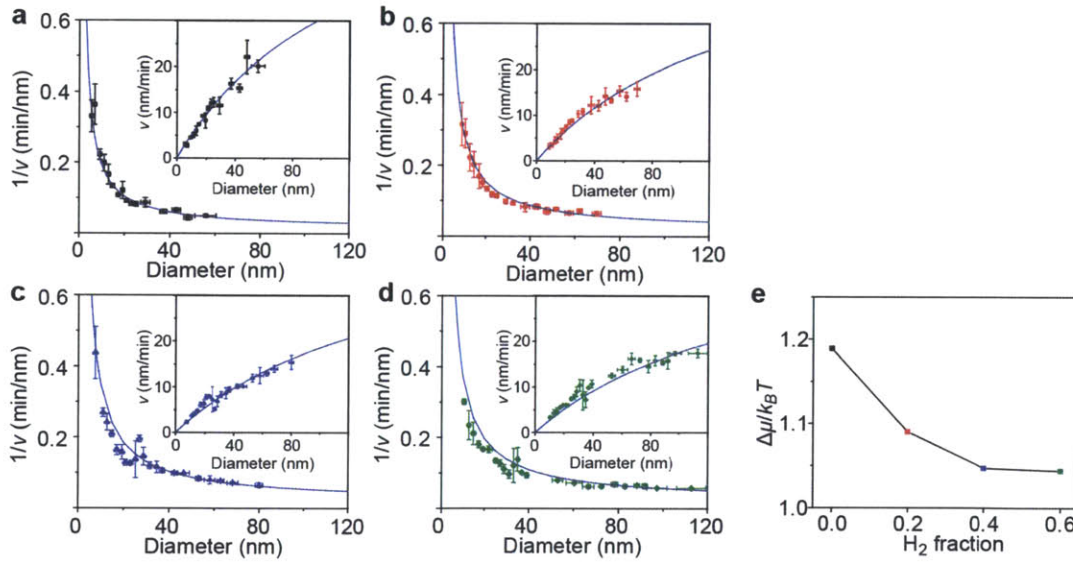


Figure 4-7. Hydrogen-driven reduction in supersaturation. (a-d) Diameter-dependence of the growth rate (v) of nanowires grown using carrier gas H₂ fractions of 0 (a), 0.2 (b), 0.4 (c), and 0.6 (d). Figures show the data plotted as $1/v$ vs. diameter. Insets show the same data plotted as v vs. diameter. The data were fit using Equations 4-4–4-6, assuming $n = 1$ using the same kinetic constants: $A = 5.249 \text{ min}^{-1}$, $B = 4.075 \text{ eV}$, and $C = 0.0645 \text{ nm}^{-1}$. Figures from [38].

4.3. Defect minimization through seed material selection

The composition of the seed material can have a significant effect on nanowire growth, including the nanowire orientation and growth rate,⁶³ as well as optical properties.^{72,104} GaN nanowires have been synthesized using multiple different seed particles, including Au, Ni, and Fe.^{63,64} Here, we directly compare nanowires grown by Au and Ni seed particles under otherwise identical growth conditions. Nanowires seeded by Ni are found to grow faster and with fewer structural defects than Au-seeded nanowires due to differences in the composition and surface energies of the seed particle. These results highlight the importance of seed material in nanowire growth and demonstrate that appropriate seed particle selection can yield nanowires with superior properties.

4.3.1. Morphology

Films of Au and Ni were deposited onto *r*-sapphire substrates with thicknesses of 1 nm and 5 nm by electron beam evaporation. The GaN nanowires were grown by MOCVD at 850°C and 100 Torr for 25 min using TMG as the III source, as described in section 3.1.3. As shown in Figure 4-8, the Au-seeded nanowires grew epitaxially from the substrate in the same orientation as *m*-directional nanowires observed previously, and the diameter increased as the film thickness increased. By comparison, the Ni-seeded nanowires showed no clear epitaxial relationship, and the diameter of the nanowires did not vary significantly as the film thickness increased. Furthermore, the Ni-seeded nanowires were much thinner (20-40 nm) and grew significantly faster (12 $\mu\text{m/hr}$) than the Au-seeded nanowires (40-100 nm; 3 $\mu\text{m/hr}$), consistent with previous reports.¹⁵⁷

While Au-seeded GaN nanowires are generally believed to grow from a liquid Au-Ga alloy,¹³⁶ Ni-seeded GaN nanowires may grow from a solid Ni-Ga alloy.¹⁵⁸ To form a liquid alloy at 850°C, the composition of the Au-Ga seed must exceed just 12% Ga,¹⁵⁹ while the composition of the AuNi seed must exceed 76% Ga.¹⁶⁰ *Ex situ* EDS measurement of the seed particles after growth indicate that the seed particles contain $13 \pm 6\%$ Ga and $45 \pm 21\%$ Ga for the Au and Ni seed particles, respectively. However, these *ex situ* measurements do not necessarily reflect the actual composition during growth. In fact, a high degree of necking was observed that the tip of both Au-seeded GaN nanowires, indicating that a significant amount of Ga was extracted during

cooling to form GaN.⁸⁴ Given the similarity between the measured composition and the Au-Ga liquidus, it is likely that this extraction ceased upon seed particle solidification. Thus the actual Ga composition was likely higher than the measured composition. Because the Ni-Ga alloy forms many intermetallic compounds at 850°C, it is unlikely that a significant amount of Ga was extracted during cooling. Measurements of seed particle composition in other III-V nanowires grown by solid seed particles indicate that intermetallic compounds tend to remain relatively stable during cooling. Therefore, based on the measured seed composition, the Ni-Ga alloy was likely solid during growth. Because Ni-Ga alloys form many intermetallic compounds at 850°C, extraction of Ga during cooling may be minimized due to the formation of stable alloys.⁶⁷ Nonetheless, some necking was also observed for Ni-seeded nanowires, so the possibility of VLS growth from a liquid Ni-Ga alloy cannot be ruled out.

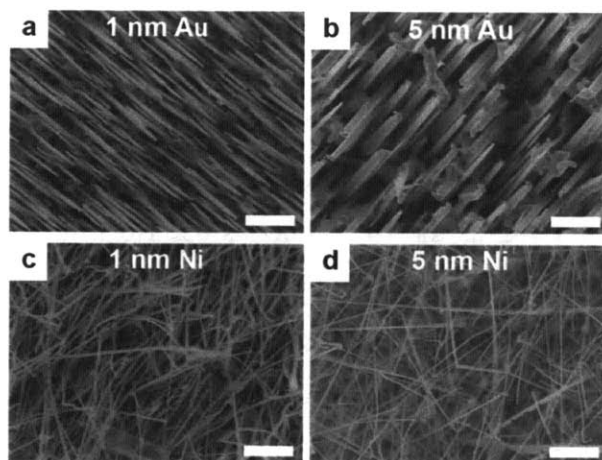


Figure 4-8. Morphology of Au-seeded and Ni-seeded nanowires. (a,b) GaN nanowires grown using Au films with 1 nm (a) and 5 nm (b) thicknesses. (c,d) GaN nanowires grown using Ni films with 1 nm (a) and 5 nm (b) thicknesses. Figures from [104].

The observation that GaN nanowires may grow faster from solid (Ni) seed particles than liquid (Au) seed particles is quite curious. Kodambaka *et al.* performed *in situ* TEM observations of the growth of Ge nanowires seeded by Au particles and varied temperature both above and below the eutectic to form liquid and solid seeds, respectively.¹⁶¹ In this case, they observed that the nanowires grew faster when the seed was liquid. However, this may have been in part due to the higher temperature of the liquid particle compared to the solid particle. Furthermore, analysis of the growth rate of Si nanowires seeded by solid particles indicated that

precursor decomposition or Si crystallization was the rate-limiting step, rather than diffusion through the seed.¹⁶² As demonstrated above, the rate-limiting step for GaN nanowires grown by Au seed particles is nucleation at the seed/solid interface, so GaN nanowires seeded by Ni seed particles could grow faster as long as another step (e.g. diffusion through the seed) does not impede faster nucleation. A rough estimate of the required concentration gradient (ΔC) for Ga diffusion through solid Ni-Ga can be obtained from the following¹⁶³

$$\Delta C = \frac{\rho v r}{D} \quad (4-9)$$

where ρ is the density of Ga ($5.1 \times 10^{22} \text{ cm}^{-3}$), v is the nanowire growth rate ($12 \text{ } \mu\text{m h}^{-1}$), and r is the seed radius (15 nm), and D is the diffusivity of Ga in Ni-Ga ($1.5 \times 10^{-10} \text{ cm}^2 \text{ s}^{-1}$ at 850°C).¹⁶⁴ From this, $\Delta C \approx 2 \times 10^{20} \text{ cm}^{-3}$, which would require a relative concentration gradient of less than 1% within a $\text{Ni}_{0.5}\text{Ga}_{0.5}$ particle. Thus, it is feasible that solid Ni-Ga could promote faster nanowire growth than liquid Au-Ga.

Nucleation could occur at a faster rate for Ni versus Au for a couple of reasons: (1) a higher supersaturation driving GaN growth and/or (2) a lower energy barrier for nucleation. While the *ex situ* measurements indicate that the composition of Ga may be higher for Ni versus Au seed particles, the supersaturation is not purely a function of the Ga composition in the seed and is dependent upon the state of both Ga and N before and after the formation of GaN. If the Ni seeds provide a lower barrier for nucleation, this would be the result of lower surface energies surrounding the nucleus that forms for each new monolayer, specifically a lower seed/nanowire surface energy. The effect of both supersaturation ($\Delta\mu$) and seed/nanowire interface energy (σ_{ls}) can be understood from Equation 2-5, which expresses the change in free energy as a result of forming a nucleus (ΔG_{nuc}) and is modified below assuming a circular nucleus with radius r and height h .

$$\Delta G_{nuc} = \frac{\pi r^2 h}{\Omega_{NW}} \Delta\mu + 2\pi r h \sigma_{ls} \quad (4-10)$$

Here, Ω_{NW} is the atomic volume of the nanowire. Based on this equation, the critical radius and free energy are as follows.

$$r_{crit} = -\Omega_{NW} \frac{\sigma_{ls}}{\Delta\mu} \quad (4-11)$$

$$\Delta G_{nuc,crit} = -\pi h \Omega_{NW} \frac{\sigma_{ls}^2}{\Delta \mu} \quad (4-12)$$

Thus r_{crit} and $\Delta G_{nuc,crit}$ decrease with greater supersaturation ($\Delta \mu$ more negative) and lower σ_{ls} . Thus either could explain the observed increase in growth rate for Ni-seeded versus Au-seeded GaN nanowires.

4.3.2. Structure

The structure of the GaN nanowires synthesized using both Au and Ni seed particles was characterized using TEM, as shown in Figure 4-9. Both Au- and Ni-seeded nanowires grew preferentially in the $[1-100]$ m -direction, as confirmed by selected area diffraction (SAD). Notably, the Au-seeded nanowires were observed to contain a significant quantity of basal-plane stacking faults (BSFs), which are located within $[0001]$ planes and extend along the length of the nanowire (Figure 4-9c). However, these defects were rarely observed in Ni-seeded nanowires (Figure 4-9f).

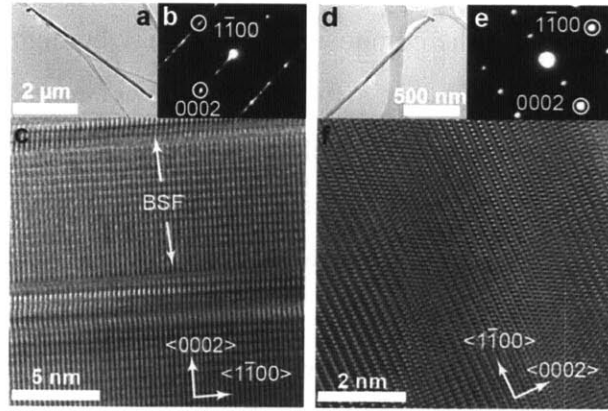


Figure 4-9. Structure of Au-seeded and Ni-seeded nanowires. (a-f) TEM analysis of Au-seeded (a-c) and Ni-seeded (d-f) GaN nanowires including TEM images (a,d), corresponding SAD patterns (b,e), and lattice-resolved HR-TEM images (c,f) indicating the presence or absence of stacking faults. Figures from [104].

To clarify the origin and distribution of these stacking faults, cross-sectional TEM was performed and revealed that the stacking faults in Au-seeded nanowires are primarily isolated in the thicker portion of the nanowire cross-section (Figure 4-10a). Furthermore, TEM analysis of multiple nanowires demonstrates that the position of the first BSF is proportional to the size of

the cross-section (Figure 4-10b,c). In other words, for nanowires with larger diameters, the first BSF appears further from the corner of the nanowire. Stacking faults in GaN films have been attributed to strain relaxation or surface steps on the substrate.¹³⁵ Given that the Au-seeded nanowires are thicker, one might suspect that strain is responsible for these stacking faults. However, BSFs are observed even in Au-seeded nanowires with the thinnest diameters, which are less than the average diameter of the Ni-seeded nanowires. Furthermore, strain-induced BSFs would be expected to occur with a frequency that increases with the absolute nanowire diameter, but instead occur at a position relative to the overall diameter of the nanowire. These BSFs cannot be attributed to surface steps either, because the BSFs would be expected occur randomly across the nanowire cross-section.

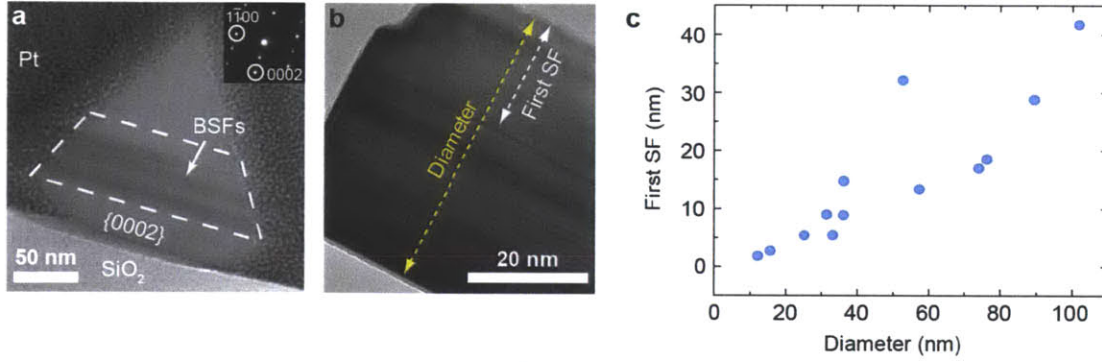


Figure 4-10. Distribution of stacking faults in Au-seeded nanowires. (a) Cross-sectional TEM image of a Au-seeded GaN nanowire. Dashed area indicates region containing stacking faults. (b) Au-seeded GaN nanowire indicating the measurement of diameter (yellow dashed line) and position of the first stacking fault (white dashed line). (c) Position of the first stacking fault as a function of diameter for multiple nanowires with different diameters. Figures from [104].

The energy of forming a one-atom stacking fault (ΔG_{SF}) along a ledge during the first monolayer of a nanowire can be expressed as follows

$$\Delta G_{SF} = \Delta\mu + s^2(\sigma_{SF} - \sigma_{ls}) \quad (4-13)$$

where σ_{SF} is the energy of the stacking fault, and s is the sidewall width of cubic atom (Figure 4-11). Thus greater supersaturation (more negative $\Delta\mu$) makes stacking fault formation more energetically favorable, while reduced σ_{ls} makes stacking fault formation less energetically favorable. In fact, multiple authors have demonstrated that an increase in supersaturation produces a higher density of stacking defects in nanowires.^{87,88} It is worth noting that Johansson

et al. observed in the growth of GaP nanowires that, under certain conditions, a high supersaturation favored the hexagonal wurtzite structure over the cubic zincblende structure, the latter being the stable phase for bulk GaP. While experimental observations by Johansson *et al.* with GaP nanowires and suggest that the hexagonal phase may be more preferred in nanowires grown at higher supersaturation,⁸⁷ a theoretical model developed by Dubrovskii *et al.* demonstrates that this applies only to materials in which the stable bulk phase is cubic,¹⁶⁵ whereas the stable bulk phase for GaN is the hexagonal wurtzite structure. Thus a higher saturation would be expected to induce a higher density of stacking faults in GaN nanowires.

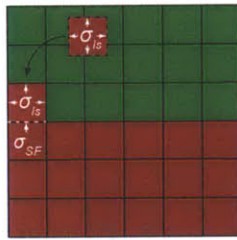


Figure 4-11. Surface energy of stacking fault formation. Schematic representation of an adatom before and after attaching to a ledge and creating a stacking fault. One facet with energy σ_{ls} is replaced by a faceted with energy σ_{SF} . Green and red represent the substrate and nanowire material, respectively.

Thus a lower seed/nanowire surface energy (σ_{ls}) for Ni-Ga/GaN versus Au-Ga/GaN would explain both the increase in growth rate and the decrease in stacking fault density for Ni-seeded nanowires. The lack of a clear epitaxial relationship between the Ni-seeded nanowires and the *r*-sapphire substrate indicates that an incoherent interface may be present between the nanowires and the substrate, although it is possible that significant bending for long and thin nanowires obscures potential epitaxy. For non-epitaxial nanowire growth, the energy penalty for forming an incoherent interface is not significant enough to prevent nanowire formation. A significant reduction in surface energy going from a Ni-Ga/sapphire to Ni-Ga/GaN interface could offset the increase in surface energy from the creation of an incoherent GaN/sapphire interface. In fact, Ni is commonly used in ohmic contacts for GaN and is suspected to stabilize the GaN surface,¹⁶⁶ indicating a low surface energy at the Ni/GaN interface.

Based on the analysis above, the distribution of defects in Au-seeded nanowires can be understood as follows. Because of the greater seed/nanowire interfacial energy, BSFs form at the initial stage of nanowire nucleation. Then, Ga is depleted from the seed particle as ledge

growth proceeds, reducing the local supersaturation and therefore the density of BSFs in the thinner regions of the nanowire cross-section.

We therefore conclude that differences in seed/nanowire surface energy are primarily responsible for the observed morphological and structural differences between Au-seeded and Ni-seeded GaN nanowires. The lower seed/nanowire surface energy in Ni-seeded nanowires allows energetically favorable growth of non-epitaxial nanowires despite suitable epitaxial orientations, promotes higher growth rates by lowering the energy of nuclei on the seed/nanowire surface, and produces nanowires with fewer structural defects by increasing the relative energy penalty of stacking fault formation. The results of this work highlight the importance of seed particle selection in nanowire growth and demonstrate that seed particle alloys with low seed/nanowire interfacial energies can promote rapid nanowire growth with minimal structural defects.

4.4. Summary

GaN nanowires were grown with control over important structural and morphological characteristics including the crystallographic growth direction, tapering, length, and defect density. By selecting appropriately lattice-matched substrates, nanowires were grown in both polar and nonpolar growth directions on sapphire substrates (*c*-GaN on *c*-sapphire and *m*-GaN on *r*-sapphire, respectively). This enables the fabrication of both radial and axial heterostructures with nonpolar-oriented junctions by using *c*-GaN and *m*-GaN nanowires, respectively. The significant tapering observed at high Ga fluxes and large inter-nanowire spacings was both attributed to incomplete Ga collection of impinging Ga precursors on the substrate. Tapering was minimized by operating at low Ga fluxes and high nanowire densities. This strategy can be used in other materials systems as well to enable the growth of non-tapered nanowires at higher temperatures.

The growth mechanism of GaN was determined by evaluating the growth rate as a function of nanowire diameter. A generalized nucleation-mediated growth model was developed and compared with the Gibbs-Thomson model. In addition to providing a substantially better fit to the observed data, this nucleation-mediated model indicated that nucleation occurs preferentially around the perimeter of the liquid/solid interface. Using this same model, the reduction in

supersaturation as a result of increased H_2 content in the carrier gas was calculated and explained the consequent reduction in nanowire growth rate.

We then investigated the role of the seed particle during nanowire growth by directly comparing Au-seeded and Ni-seeded nanowires. Nanowires grown using Ni were found to grow faster and with fewer defects than those grown using Au. Given that the growth rate was found to be limited by nucleation, we conclude that a low surface energy between the Ni-Ga alloy and the GaN nanowire enables rapid nucleation at low supersaturation, which both enhances the growth rate and minimizes the probability of stacking fault formation. This study highlights the importance of seed particle selection in nanowire growth and provides guidelines for choosing seed materials that will produce nanowires with high structural quality.

Chapter 5: InN/InGaN axial heterostructure nanowires

Building upon the techniques that were developed in the previous chapter to control nanowire structure and morphology, this chapter explores strategies for controlling the composition of III-V nitride nanowires. Many III-V nitride-based devices rely upon spatial variations in composition. However, compositional control is quite challenging in $\text{In}_x\text{Ga}_{1-x}\text{N}$ due to the large miscibility gap, which ranges between about $0.1 < x < 0.9$ at relevant growth temperatures.¹¹⁹ Consequently, there have been limited reports of InGaN synthesized well within the miscibility gap,^{121,167,168} yet there is much benefit to be gained from using nanowires for nitride-based devices,^{27,169,170} particularly those grown in nonpolar directions.³⁷ Therefore, we investigate the formation of *m*-directional InN/InGaN heterostructures by particle-mediated growth.

Here, we study the incorporation of Ga into InN nanowires to produce InN/InGaN axial heterostructures by introducing TMG during InN nanowire growth. The effects of different growth parameters are investigated and optimized including flow rate, pressure, and temperature with the best results achieved using high-flux TMG pulses and elevated system pressure. Using this strategy, InN/InGaN axial heterostructures are produced, and changes in nanowire composition are accompanied by changes in nanowire diameter. The mechanism of these Ga-driven morphological changes is elucidated using a combination of electron tomography and EDS. To our knowledge, this is the first demonstration of III-V nitride axial heterostructure nanowires grown in a nonpolar direction.

5.1. Ga incorporation into InN nanowires

Studies on the growth of InGaN films have shown significant effects of precursor flow rates, temperature, and pressure on film composition,^{122,123} but there have been limited reports of particle-mediated InGaN nanowires. We therefore investigated the effects of these parameters during the growth of InN/InGaN axial heterostructures, which were formed by pulsing TMG during InN nanowire growth. The range of viable TMG flows was limited by the formation of a Ga-rich shell, preventing higher TMG flows that would enable InGaN formation in the nanowire core. Elevated growth pressures and temperatures inhibited this sidewall deposition, enabling higher TMG flows. However, because sidewall deposition was likely minimized by a reduction

in the local supply of Ga, no significant increase in InGa_N formation was observed. By using high-flux TMG pulses for short durations, InN/InGa_N axial heterostructures were formed with minimal sidewall deposition.

5.1.1. InN nanowire basis

Indium nitride nanowires were grown by both CVD and MOCVD techniques, using solid In and TMI as the III source, respectively. For CVD InN nanowires, solid In (~5 mg) was placed on or near the growth substrates. For MOCVD InN nanowires, 100 sccm of N₂ was delivered through the TMI bubbler. Substrates used included 2-5 μm thick *a*-Ga_N and *c*-Ga_N films on *r*-sapphire and *c*-sapphire, respectively. Unless otherwise noted, all InN and InGa_N growths described below were performed at 560°C and 100 Torr for 1h using solid In as the III source and 60 nm Au colloids to seed nanowire growth.

The majority of nanowires grew in the [1-100] *m*-direction on *a*-Ga_N substrates, while the majority grew in the [0001] *c*-direction on *c*-Ga_N substrates, similar to the results for Ga_N nanowires. Figure 5-1 shows both *m*-InN and *c*-InN nanowires, which have triangular and hexagonal cross-sections, respectively.⁶¹ The SAD patterns confirm their orientation, and the HR-TEM images reveal that both types of nanowires have *c*-plane stacking faults similar to those in Au-seeded Ga_N nanowires. These stacking faults extend axially along the length of the nanowire and radially along individual monolayers for *m*-InN and *c*-InN nanowires, respectively. Attempts were made to grow InN nanowires with other seed metals, including Ni, but nanowire growth was not observed. Other authors have also found difficulties growing InN nanowires with metals other than Au.¹⁰² Nonetheless, these nanowires provide a suitable platform for investigating the incorporation of Ga to form InGa_N. For InN/InGa_N axial heterostructures, we

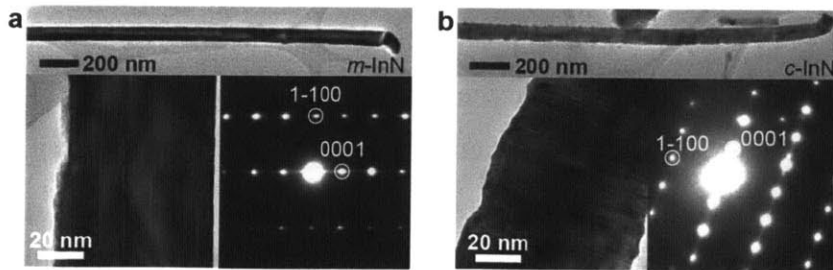


Figure 5-1. Structure of InN nanowires. (a,b) Structure of *m*-InN (a) and *c*-InN (b) nanowires including bright-field TEM images (top), HR-TEM images with visible *c*-plane stacking faults (left), and corresponding SAD patterns (right) indicating orientation along the [11-20] zone axis.

focus primarily on nanowires grown on α -GaN substrates due to the benefits of nonpolar-oriented heterojunctions for nanowire-based devices.³⁷

5.1.2. TMG flux

To produce InGaN segments, TMG was introduced during the growth of InN nanowires. Two different methods were used: (1) pulsed TMG flow for a few seconds and (2) continuous TMG flow for a few minutes. In both cases, Ga incorporation was limited at lower TMG flows, while higher TMG flows produced a Ga-rich shell around the InN core (Figure 5-2). The formation of the shell was so significant that it actually coated the seed particle as well (see Figure 5-2b). The HR-TEM image in Figure 5-2e reveals that the shell is somewhat rough but still single-crystalline, and the corresponding SAD pattern is consistent with heteroepitaxy between single-crystalline InN and GaN layers. To confirm that the coating around the seed formed during nanowire growth, InN nanowires were grown for 10 and 30 min prior to introducing TMG. The resulting nanowires grown for just 10 min were much shorter, indicating that the seed was coated upon introduction of TMG, consequently causing nanowire growth to cease. While GaN is generally grown at much higher temperatures, thin films have been grown at temperatures around 600°C and below,¹⁷¹⁻¹⁷⁴ but activated processes were generally employed to overcome the large kinetic barrier at low temperatures.^{171,172} Notably, Nagata *et al.* produced GaN microcrystals at 600°C using liquid Ga droplets to promote nucleation.¹⁷³ Thus, the GaN shells may have formed due to Ga droplet formation above a threshold TMG flow.^{142,143} As further evidence, shell growth was accompanied by the formation of isolated Ga-rich nanostructures across the substrate, indicating potential nucleation from Ga droplets (Figure 5-2e). Additionally, the roughness of the shell is consistent with the presence of Ga droplets.¹⁷⁵

For 2 s TMG pulses, flows as high as 0.30 sccm TMG could be used prior to shell formation, but 4 s pulses at the same flow produced GaN shells. With continuous TMG flow, shell formation occurred for even the lowest TMG flows used, although shell formation at 0.02 sccm TMG was low enough that it did not cease growth (Figure 5-2a). However, some Ga incorporation was observed using pulsed TMG flow (Figure 5-2c). For the nanowire in Figure 5-2c, EDS measurements indicate at least 10% Ga incorporation (i.e. $x = 0.10$ within the

$\text{In}_x\text{Ga}_{1-x}\text{N}$ region).[†] When TMI was used as the III precursor, the flow was just 0.15 sccm TMI, only half of the highest TMG pulse flow, so significantly higher TMG/TMI ratios are needed to promote InGaN formation in these particle-mediate nanowires compared to InGaN films at similar temperatures.^{122,123} This is also clear from the fact that the shell is Ga-rich while the core is In-rich. The need for such a high TMG flux could be a consequence of thermodynamic barriers inhibiting Ga incorporation into the Au-In alloy. Dick *et al.* reported that TMG pulses drove In out of Au-In seed particles during the growth of InAs/GaAs axial heterostructure nanowires,¹¹⁷ indicating that mixing of Ga and In in Au-In-Ga alloys may not be thermodynamically favorable under certain conditions.

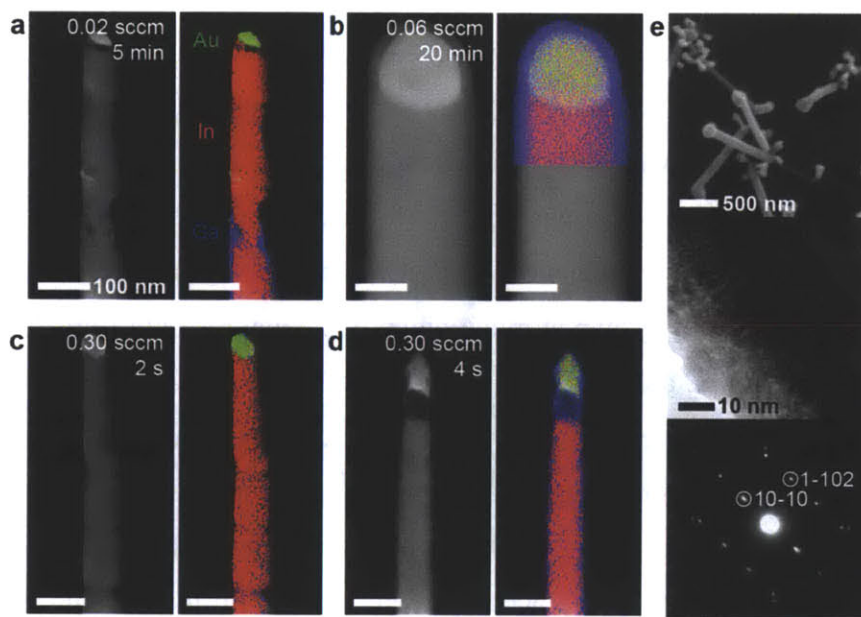


Figure 5-2. Effect of TMG flux on axial InGaN growth and radial GaN growth. (a-d) STEM images (left) and corresponding EDS maps (right) for InN-InGaN heterostructures grown using different TMG flows: (a) 0.02 sccm for 5 min \times 2 (2 pulses); (b) 0.06 sccm for 20 min; (c) 0.30 sccm for 2 s \times 4; (d) 0.30 sccm for 4 s \times 4. Green, red, and blue correspond to Au, In, and Ga respectively. (e) SEM image of InN-GaN core-shell nanowires and small Ga-rich nanostructures grown on a SiO_x/Si substrate (top), HR-TEM image of the InN core and GaN shell from the substrate above (center), and corresponding SAD pattern indicating orientation along the $[-24-23]$ zone axis. Scale bars in (a-d) represent 100 nm.

[†] The composition within the first InGaN segment was measured to be 9.8% Ga based on the maximum Ga/In signal ratio from an EDS linescan. However, this results in an underestimate of the actual Ga concentration due to the fact that signal spreading reduces the measured peak Ga composition.

5.1.3. Pressure

Because Ga-rich shell formation puts a ceiling on the allowable flow of TMG, we varied the growth conditions in order to inhibit shell formation. First, we varied the system pressure and found that higher pressures allow greater TMG flows without inducing shell formation. Figure 5-3 shows nanowires grown at different system pressures and TMG flows. For nanowires grown at 100 Torr with 4 s pulses of 0.30 sccm TMG, shell formation occurred (Figure 5-3a). However, no shell formation was observed at 400 Torr even when the flow was doubled to 0.60 sccm TMG (Figure 5-3b). While many authors have reported reduced GaN growth rates at higher system pressures,¹⁷⁶⁻¹⁷⁸ these studies were generally performed at high temperatures in the mass-transport-limited regime in which the growth rate is limited by vapor-phase diffusion of Ga species, which is inhibited at higher pressures. At lower temperatures, GaN growth should be reaction-limited due to the significant kinetic barrier to GaN formation. Because shell formation here is suspected to occur due to the presence of liquid Ga droplets, higher system pressures likely inhibit Ga droplet formation. Notably, indium-rich conditions have been shown to inhibit the formation of Ga droplets,¹⁷⁵ and In droplet formation increased at higher pressures in the growth of InAlN/AlN/GaN heterostructures,¹⁷⁹ indicating greater In surface coverage with increased pressure. Therefore, we suggest that higher pressures increase the ratio of In to Ga adatoms on the substrate, which inhibits Ga droplet formation and therefore GaN shell formation.

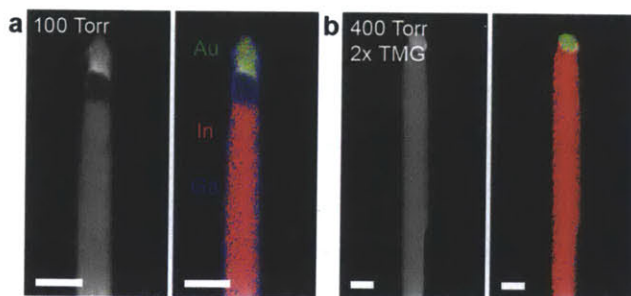


Figure 5-3. Effect of system pressure. (a,b) STEM images (left) and corresponding EDS maps (right) for nanowires grown at 100 Torr using 0.30 sccm TMG pulses (a) and 400 Torr with 0.60 sccm TMG pulses (b). Green, red, and blue correspond to Au, In, and Ga respectively. Scale bars represent 100 nm.

While a significant amount of Ga incorporation into the nanowire core was observed for the nanowire grown at 100 Torr in Figure 5-2c, no significant Ga incorporation into the nanowire

core was observed at 400 Torr even when each TMG pulse contained 4 times as much TMG (Figure 5-3b). The fact that higher TMG fluxes at higher pressures did not produce greater Ga incorporation than lower TMG fluxes at lower pressures may also be a consequence of greater surface coverage by In versus Ga adatoms, which could reduce the supply of Ga reaching the seed particle. Thus greater In versus Ga surface coverage at higher pressure is consistent with the observed reductions in both GaN shell formation and InGaN formation in the nanowire core.

5.1.4. Temperature

The growth temperature can have significant consequences on the formation of InGaN. For example, Yoshimoto *et al.* found that the TMI/TMG ratio required to produce InGaN films with high In content decreased as the temperature decreased.¹²² Here, we found that the kinetics of nanowire growth were notably different at different growth temperatures. After initial InN growth at 560°C and 100 Torr, the growth temperature was changed, and TMG was then pulsed to produce a marker indicating the onset of growth at a different temperature. The growth rates of different segments could then be compared (Figure 5-4). Segments grown at 540°C grew 51% faster than those grown at 560°C. However, segments grown at 520°C and 600°C grew 11% and 62% slower, respectively, than segments grown at 560°C. Thus the nanowire growth rate initially increases with temperature, then decreases again. The initial increase could be associated with the increased In vapor pressure, a reduced kinetic barrier for InN formation, and/or increased NH₃ cracking,¹⁸⁰ which is less than 1% efficient at 500°C but reaches a near maximum of about 4% by 600°C.[‡] It could also be associated with the phase of the seed particle, which should be liquid at 560°C, but may be solid at 520°C.¹⁸¹ The decreased growth rate above 540°C may be driven by greater In desorption at higher temperatures¹⁸² and/or increased H₂ from increased NH₃ cracking.¹⁸³ Here, InN etching was observed when H₂ was introduced during nanowire growth. The relatively slow growth rate of InN at 600°C may also be the result of the reduced stability of InN at higher temperatures. Dissociation of InN can occur below 600°C, generally limiting growth to below 650°C.^{184,185} Here, InN etching was observed at 625°C. These differences in nanowire growth kinetics at different temperatures could have an effect on shell formation, as well as Ga incorporation into the nanowire.

[‡] Note: These values do not consider any potential catalytic effect that Au may have on NH₃ cracking.

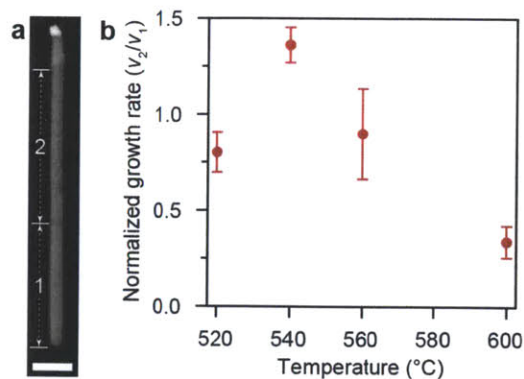


Figure 5-4. Effect of temperature on growth rate. (a) STEM image of an InN-InGaN nanowire grown at 540°C in which TMG pulses were used as markers to indicate segments grown at 560°C (segment 1) and another temperature (segment 2). (b) Growth rate measurements of nanowires similar to the one shown in (a) grown with different segment 2 temperatures. The growth rate of segment 2 (v_2) is normalized with respect to the growth rate of segment 1 (v_1). Scale bar represents 200 nm.

Figure 5-5 shows nanowires grown at 520-600°C at 400 Torr with both continuous and pulsed flows. Although no shell formation was observed for pulsed TMG flow (Figure 5-5d-f), shell formation increased as temperature decreased for continuous TMG flow (Figure 5-5a-c), particularly between 560°C and 520°C. This trend may seem counterintuitive, as shell formation is generally greater at elevated temperatures. In fact, nanowires are often grown at lower temperatures to avoid tapering resulting from shell deposition.^{112,113} Furthermore, when core-shell nanowires are grown, the growth temperature is commonly raised between core growth and shell deposition.^{103,186} However, as discussed previously, shell formation at these low temperatures is likely a consequence of Ga droplet formation. Therefore, the decrease in shell formation at elevated temperatures is likely due to increased desorption of Ga, which has been shown to reduce droplet formation within the specific temperature region studied here.¹⁴²

The effect of temperature on Ga incorporation into the nanowire is not entirely clear. Again, no axial InGaN formation was observed using continuous TMG flow (Figure 5-5a-c). For pulsed TMG flow at 400 Torr, InGaN formation was only observed at 600°C. However, while the nanowire in Figure 5-5f has an $\text{In}_{1-x}\text{Ga}_x\text{N}$ disc with at least $x = 0.12$, only one of the four different TMG pulses produced significant InGaN formation. Therefore, variations in the amount of Ga pulsed may have a greater effect than temperature between 560-600°C. At 520°C, the introduction of TMG caused the seed particle to separate into multiple different particles,

essentially ceasing axial growth in the case of both continuous and pulsed TMG flow (Figure 5-5a,d).

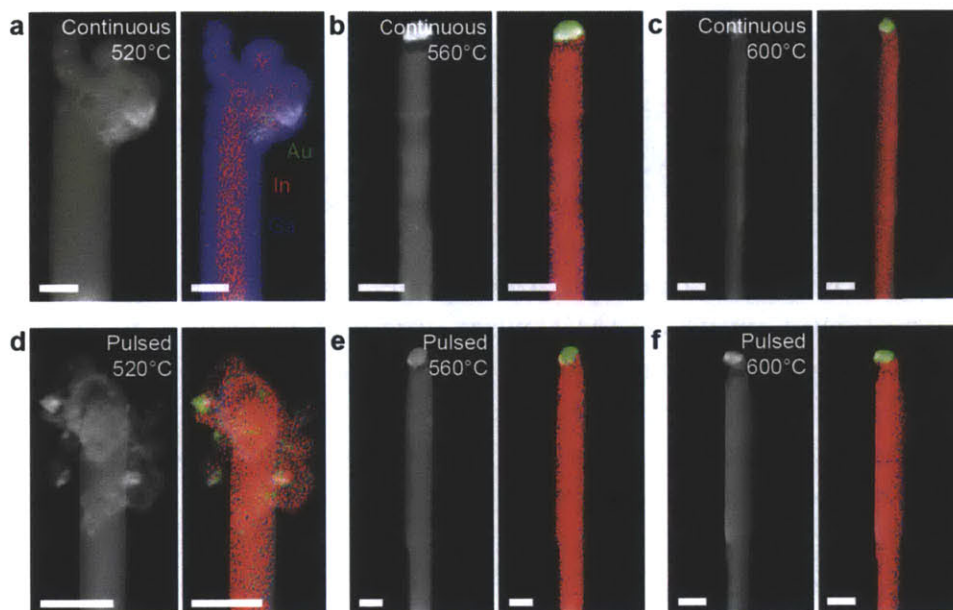


Figure 5-5. Effect of temperature on InGaN formation. (a-f) STEM images (left) and corresponding EDS maps (right) of nanowires grown at 400 Torr with upper segments grown at 520°C (a,d), 560°C (b,e), and 600°C (c,f). For (a-c), a continuous flow of 1 sccm TMG was used for 15 min. For (d-f), multiple 4 s pulses with 0.60 sccm TMG were used. Scale bars represent 100 nm.

5.1.5. Seed particle composition

Axial InN/InGaN heterostructures with compositions as high as $x = 0.16$ within the $\text{In}_{1-x}\text{Ga}_x\text{N}$ discs were achieved using pulsed TMG flow,⁶¹ but under no conditions was a detectable amount InGaN formed within the core using continuous TMG flow. Clearly a higher Ga flux was required, although it is not clear whether the brief TMG pulses significantly affect only the concentration of Ga in the vapor/adatom phase or if they affect the composition of the seed particle as well. To investigate this, we used STEM-EDS to measure the *ex situ* composition of seed particles of nanowires grown with continuous and pulsed TMG flow that did not have shells around the seed. For continuous TMG flow, no Ga was detected in the seed particle. For pulsed TMG flow, the measured seed composition was as high as 7% Ga. This indicates that a high Ga flux is needed to drive Ga incorporation into the seed and that particle-mediated InGaN

formation will not occur without a certain threshold concentration of Ga within the seed particle. Even when Ga-rich shells deposited around the nanowire, the core remained In-rich. Therefore, Ga incorporation into the nanowire core is likely limited by the composition of Ga in the seed.

Both the liquid- and vapor-phase concentrations of Ga may be important in determining the composition of the nanowire. Notably, Dick *et al.* were able to achieve abrupt junctions in InAs/GaAs axial heterostructure nanowires by pulsing TMG prior to continuous TMG flow, whereas they produced graded junctions when switching immediately from continuous TMI flow to continuous TMG flow due to residual In in the seed particle.¹¹⁷ In their case, the Ga pulses drove Ga into and In out of the seed without forming InGaAs. Before continuous TMG flow, the composition of Ga in the seed particle was significant, but the vapor/adatom-phase Ga concentration was low enough to prevent InGaAs formation. Once continuous TMG was used, the composition of In in the seed was low enough that pure GaAs formed instead of InGaAs, creating an abrupt InAs/GaAs junction.

In our case, a high vapor/adatom-phase Ga concentration was required to drive Ga into both the seed particle and the nanowire. A continuous low-flux TMG flow did not produce any measured Ga incorporation into either the seed or the nanowire. However, high-flux pulses of TMG were enough to induce InGaAs formation even with a relatively low composition of Ga in the seed. On the other hand, Ga could be detected in the seed particle even when InN was grown for 10 min after the last TMG pulse, indicating that the vapor/adatom-phase Ga concentration was then too low for InGaAs to form. However, the flux and duration of the TMG flow were limited by the formation of Ga droplets, which facilitated GaAs shell formation.

5.2. InN/InGaAs axial heterostructures

Given that TMG pulses were proven effective in producing InN/InGaAs axial heterostructures, we further explored this technique and the resulting nanowire composition and morphology. The intermittent TMG pulses during growth produced thin-diameter regions along the nanowires, and EDS was used to confirm that the InGaAs discs are located in these thin-diameter regions. Furthermore, electron tomography was used to produce a three-dimensional model of these nanowires from which cross-sections could be extracted. From the tomography and EDS results, we explain how the cross-section evolves when TMG is introduced during InN nanowire growth.

5.2.1. Structure & composition

InN/InGaN axial heterostructure nanowires were grown by pulsing TMG quasi-periodically during growth (Figure 5-6a). As shown in the TEM images and corresponding SAD patterns in Figure 5-6b, the resulting nanowires grew preferentially in the nonpolar *m*-direction with a “caterpillar” morphology containing multiple thin-diameter regions along the nanowire. Interestingly, the diameter change appears uniform when viewed along the [0001] zone axis, but non-uniform when viewed along the [11-20] zone axis. The EDS profile in Figure 5-7a shows that Ga is isolated within the thin-diameter regions of these nanowires, indicating that the TMG pulses lead to a reduction in nanowire diameter associated with the formation of InGaN.

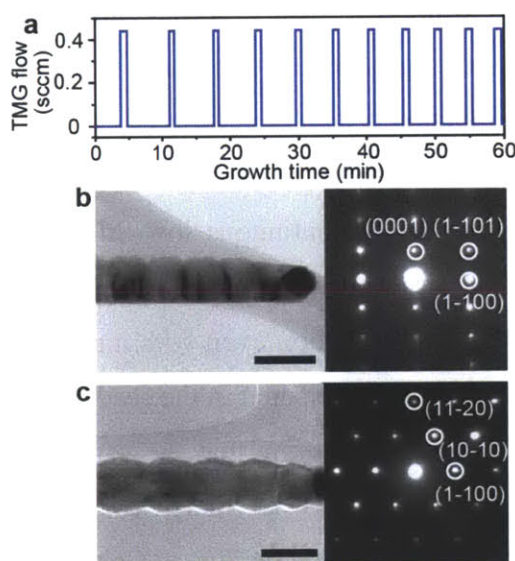


Figure 5-6. Morphology of caterpillar-shaped InN-InGaN heterostructures. (a) Variation of TMG flow with time during growth of caterpillar-shaped InN/InGaN axial heterostructure nanowires. (b,c) Bright-field TEM images (left) and corresponding SAD patterns (right) of the nanowires taken along the [11-20] (b) and [0001] (c) zone axes. All scale bars represent 100 nm.

Changes in nanowire diameter are associated with changes in seed particle volume and wetting angle. For example, assuming a constant wetting angle, an increase in seed particle volume would yield an increase in nanowire diameter.^{61,84,90} Therefore, we compared the seed particle composition of two different nanowires (Figure 5-7b). One nanowire was finished with an InGaN segment, while the other was finished with a 10-min InN segment that followed an InGaN segment. The Au composition was higher for the thinner InGaN segment ($66 \pm 4\%$) than

the thicker InN segment ($54 \pm 6\%$), indicating that the total composition of III source (In and Ga) was lower in the thin diameter regions. Therefore, the diameter changes are driven at least in part by the changes in seed particle volume.

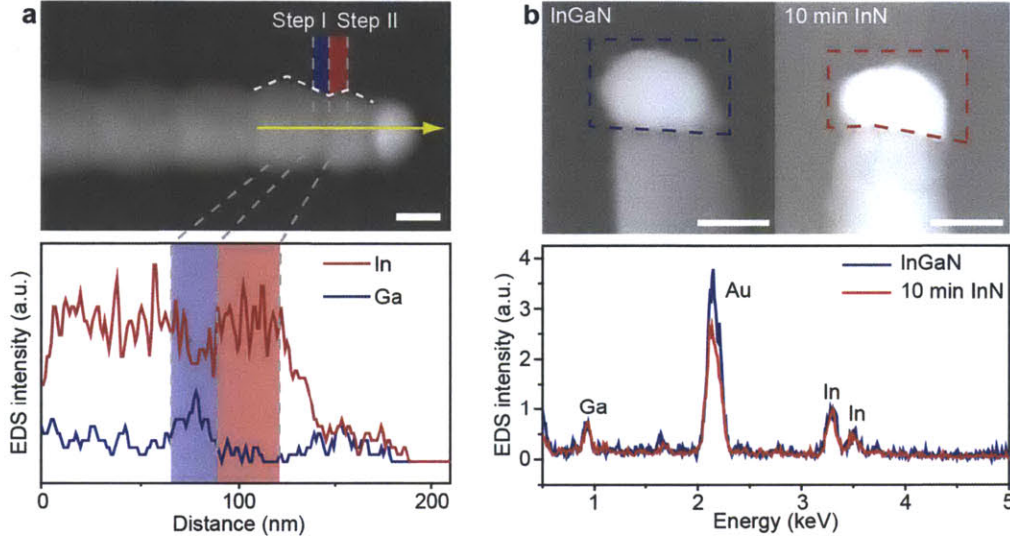


Figure 5-7. Composition of InN-InGaN heterostructures and seed particles. (a) DF-STEM image (top) of a *m*-directional caterpillar-shaped InN/InGaN nanowire taken along the [0001] zone axis and EDS linescan profiles (bottom) of In and Ga taken along the yellow arrow. The regions corresponding to Steps I and II of the cross-sectional shape evolution are indicated by red and blue, respectively, which also correspond to regions with greater In (red) and Ga (blue) content, respectively. (b) DF-STEM images of an InN/InGaN axial heterostructure nanowire finished with an InGaN segment (left) and another finished with a 10 min InN segment following an InGaN segment. The dashed regions correspond to the seed particle regions with Au and oxide. EDS spectra (bottom) were collected from within the dashed regions and normalized to the In peaks. All scale bars represent 50 nm.

5.2.2. Cross-section evolution

To further evaluate the Ga-driven morphological changes in these nanowires, electron tomography was performed to reconstruct the three-dimensional shape of these nanowires (Figure 5-8). From this model, we were able to extract cross-sectional slices at specific positions along the nanowire (Figure 5-8g-i). Using SEM, TEM, and SAD analysis (Figure 5-8c-e and Figure 5-6b), we were able to index the orientation of the nanowire and the facets of the cross-section. At position 1 (Figure 5-8f,g), the nanowire has a truncated triangular

geometry with two upper $\{11-22\}$ facets and a lower $\{0001\}$ that are truncated at the corners by the same planes of the same family ($\{11-22\}$ and $\{0001\}$).

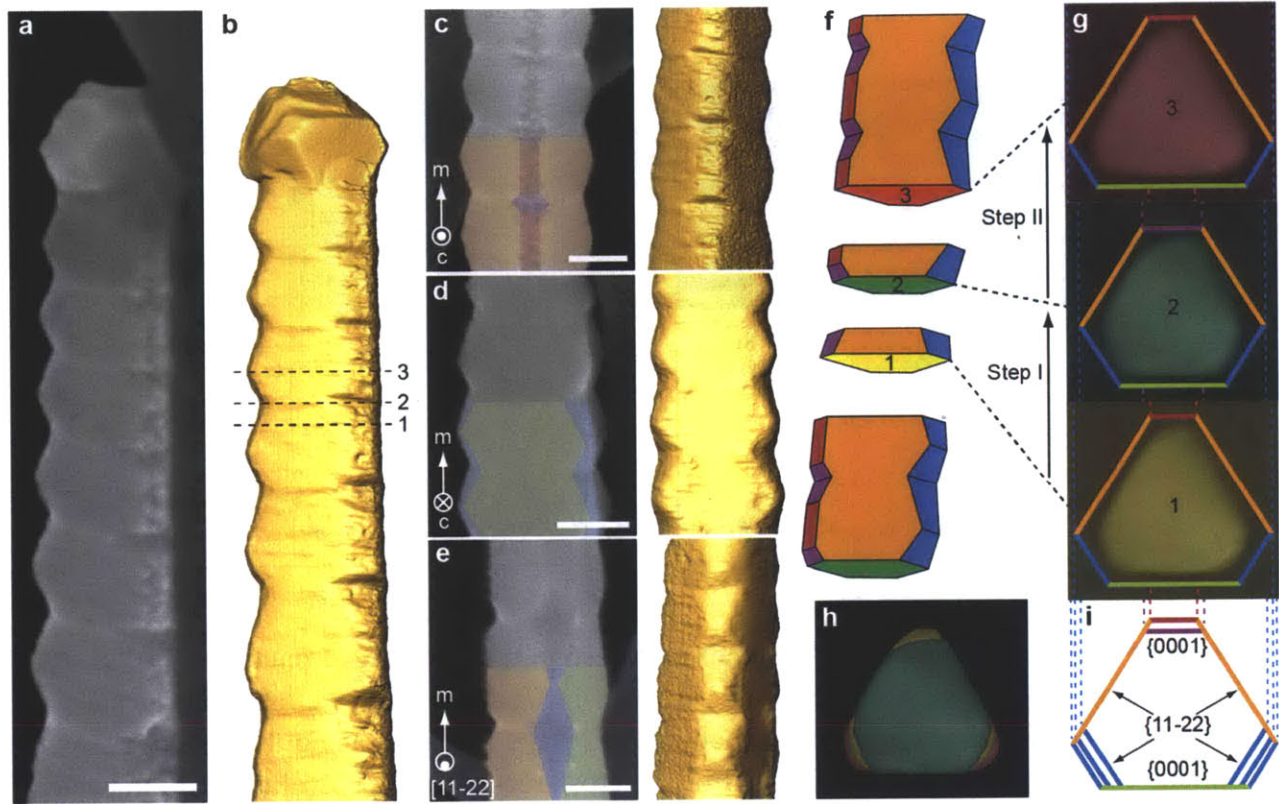


Figure 5-8. Tomography of caterpillar-shaped InN-InGaN heterostructures. (a) SEM image of a caterpillar-shaped InN/InGaN axial heterostructure lying on a lacey carbon TEM grid. (b) Tomography reconstruction with the same orientation as in (a). (c–e) SEM images (left) and corresponding tomography reconstruction (right) of caterpillar-shaped InN/InGaN nanowires taken along two $\langle 0001 \rangle$ directions and one $\langle 11-22 \rangle$ direction, described by insets and supported by diffraction patterns (Figure 5-6). Colors represent different facets defined in (i). (f) Reconstructed model of the nanowire morphology using the same facet color scheme as in (c–e). (g) Cross-sections at positions 1, 2 and 3 extracted from the tomography results at the positions labeled in (b) and illustrated in (f). Colors of cross-sections and facets correspond to those in (c–f). The facet inclination in the upper left corner of the reconstructed cross-sections is an artifact resulting from the limited tilt range of the tomography series. (h) Overlaid cross-sections shown in (g) emphasize the evolution during steps I & II. (i) Identification of the nanowire facets and their two-step evolution. The “upper” $\{0001\}$ and $\{11-22\}$ facets are shown in red/purple and orange, respectively. The “lower” $\{0001\}$ and $\{11-22\}$ facets are shown in green and blue, respectively. All scale bars represent 50 nm.

This cross-section evolves from wide (position 1) to narrow (position 2) to wide again (position 3) repeatedly throughout growth (see Figure 5-8f-i). In step I, moving from position 1 to 2, the lower corner $\{11-22\}$ facets broaden steadily causing a diameter reduction along the $\langle 11-22 \rangle$ directions. Simultaneously, the upper $\{0001\}$ facet broadens abruptly and causes a $\langle 0001 \rangle$ -directional diameter reduction, yielding a highly truncated cross-section that is almost hexagonal. In step II, moving from position 2 to 3, the upper $\{0001\}$ facet quickly shrinks, increasing the diameter along the $\langle 0001 \rangle$ direction, and then stabilizes. Simultaneously, the lower $\{11-22\}$ facets shrink, increasing the diameter along the $\langle 11-22 \rangle$ directions, and continue to do so until reaching position 3, at which they begin to broaden again.

The two-step evolution of the cross-section can be understood by considering the changes in surface energy and volume that occur as a result of introducing Ga into the system. The abrupt reduction in diameter that occurs during Step I should occur upon the introduction of Ga into the system. As described previously, EDS results indicate that InGa₂N forms within the thin-diameter regions (Figure 5-7a). Measurements of the *ex situ* seed particle composition (Figure 5-7b) indicate that the seed particle volume is lower in the thin-diameter regions, which may explain the reduction in nanowire diameter. In fact, studies by Dick *et al.* suggest that the introduction of Ga can drive In out of Au-In seeds.¹¹⁷ This could be a consequence of reduced In solubility as Ga is introduced (thermodynamic factors) or Ga adatoms inhibiting In transport to the seed (kinetic factors). Regardless, the introduction of Ga reduces the seed particle volume and drives the reduction in nanowire diameter, which occurs primarily by broadening of the upper $\{0001\}$ facet (Figure 5-8f-i) and results in a significant reduction in diameter along the $\langle 0001 \rangle$ direction. The most stable facets for InN and GaN have been observed to be (000-1) and (0001), respectively.^{187,188} We therefore suggest the upper (0001) facet is stabilized as Ga is introduced, while the lower facet is (000-1). Z-contrast tomography shows that InGa₂N forms in very narrow discs within the thinnest regions of the nanowire (Figure 5-9a), indicating that the upper (0001) facet begins to broaden even before InGa₂N forms, so this facet broadening is not necessarily associated with InGa₂N formation. Additionally, nanowires grown under similar conditions with lower-flux TMG pulses show significant $\langle 0001 \rangle$ -directional diameter reductions even when little Ga is incorporated into the nanowire (Figure 5-9b), indicating that (0001) facet broadening is not dependent on the composition of the nanowire. Furthermore, InGa₂N formation appears to follow the facet broadening rather than precede it. First-principles calculations

suggest that In adatoms can destabilize (0001) GaN surfaces,¹⁸⁹ so it is reasonable that Ga adatoms would also destabilize (0001) InN surfaces, which may explain why the (0001) facet broadening occurs even without substantial InGaN formation.

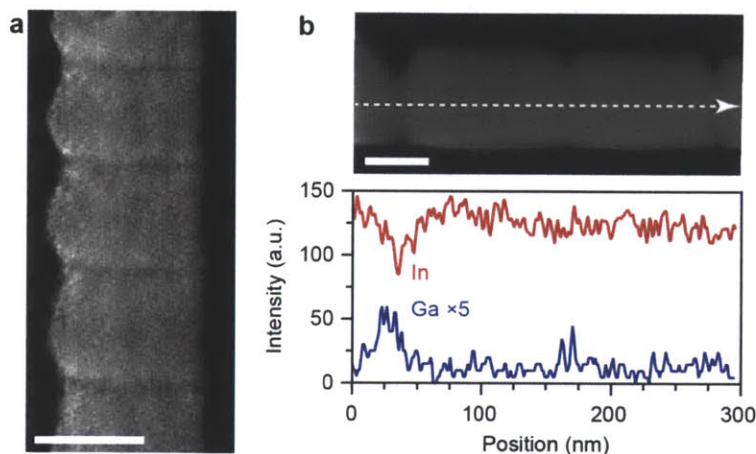


Figure 5-9. Diameter and composition changes in InN-InGaN heterostructure. (a) Slice along the tomographically reconstructed nanowire in Figure 5-8. The darker contrast in the thin-diameter regions indicates greater Ga content. (b) Linescan along a nanowire from a separate growth in which the Ga content varies between TMG pulses. The EDS profile (bottom) was obtained along the dashed line in the STEM image above it.

Next, in step II following InGaN formation, the composition of III source in the seed particle increases again, causing an increase in seed particle volume and therefore nanowire diameter. The $\langle 0001 \rangle$ -directional diameter increase is achieved by a rapid reduction in the width of the upper $\{0001\}$ facet, while the $\langle 11\bar{2}2 \rangle$ -directional diameter increase is achieved by gradual contraction of the lower $\{11\bar{2}2\}$ facets. After point 3, these lower $\{11\bar{2}2\}$ facets begin to broaden again resulting in a gradual $\langle 11\bar{2}2 \rangle$ -directional diameter reduction. Notably, the polarity of the upper and lower $\{11\bar{2}2\}$ facets is opposite. Therefore, the broadening and contraction of the lower $\{11\bar{2}2\}$ facets is likely a consequence of changes in the relative abundance of different III and V adatoms, which affects the relative stability of facets of different polarity within the same family.^{189,190} Close inspection of the nanowire in Figure 5-8b shows that the duration of the $\langle 11\bar{2}2 \rangle$ -directional diameter increase is similar after each TMG pulse, while the duration of the $\langle 11\bar{2}2 \rangle$ -directional diameter reduction decreases as the time between pulses decreases. Therefore, we suggest that lower $\{11\bar{2}2\}$ facet contraction occurs

gradually until residual Ga that remains after the TMG pulse is sufficiently removed. Then the lower {11-22} facets expand again until the next TMG pulse.

While the exact geometry of the seed particles and the composition-dependent surface energies would need to be considered to quantitatively describe the shape evolution of these InN/InGaN axial heterostructure nanowires, the measured nanowire and seed particle composition indicate a Ga-driven nanowire diameter reduction associated with a decrease in seed particle volume. Meanwhile, changes in the lengths of different nanowire facets indicate that the introduction of different III species can significantly modify the facet surface energies, resulting in changes in nanowire cross-section. Facet surface energies could also potentially be controlled by growth temperature and pressure,¹⁹¹ allowing control over the relative sizes of different nanowire facets.

5.3. Summary

Nonpolar-directional InN/InGaN axial heterostructure nanowires were synthesized by pulsing TMG during InN nanowire growth. Significant Ga incorporation into the seed particle could only be achieved through the use of high TMG flows. However, excessive TMG resulted in the formation of a Ga-rich shell that coated the nanowire and seed particle, ceasing axial nanowire growth. Axial heterostructures were formed without significant shell formation by using brief high-flux TMG pulses. Operation at higher system pressure and temperature inhibited shell formation and allowed higher TMG fluxes to be utilized. Nonetheless, less Ga incorporation into the nanowire was observed at the higher pressure, which was likely due to a reduction in the peak concentration of Ga resulting from greater TMG spreading in the injector line. Also, the stability of InN decreases at higher temperatures. Therefore, moderate pressure and temperature were used to achieve InN/InGaN axial heterostructures with up to 16% Ga at 100 Torr and 560°C.⁶¹ In addition to constituting the first demonstration of nonpolar-oriented III-V nitride axial heterostructure nanowires, these studies reveal the complexity of ternary nanowire synthesis via particle-mediated growth, in which the composition of the III element in both the vapor/adatom phase and seed phase has a significant impact on nanowire composition.

Quasi-periodic TMG pulses produced “caterpillar”-shaped structures with repeated asymmetric diameter changes. Measurements of both nanowire and seed particle composition via EDS indicate that Ga is isolated within the thin-diameter regions of the nanowire and that the

diameter reduction is a consequence of reduced seed particle volume. Electron tomography was used to reconstruct a three-dimensional model of a nanowire from which multiple cross-sectional slices along the nanowire were extracted. The nanowire diameter and cross-sectional shape were found to evolve by changes in the relative length of different $\{11\bar{2}2\}$ and $\{0001\}$ facets, which we explained to be the result of facet surface energy modification by the introduction of Ga.

In addition to constituting the first demonstration of nonpolar-oriented III-V nitride axial heterostructure nanowires, these results demonstrate the effects that changes in facet surface energy and seed particle volume can have on nanowire structure. In particular, the ability to controllably modulate the nanowire diameter via changes in seed particle composition could offer opportunities to fabricate unique nanowire architectures that are more optimally designed for specific functional nanowire-based devices. In the following chapters, both experimental and theoretical aspects of diameter modulation are explored in detail.

Chapter 6: Growth of diameter-modulated GaN & InN nanowires

While we observed nanowire diameter changes during the growth of InN/InGaN heterostructures, we now consider the intentional modulation of diameter in binary GaN and InN nanowires, which could have a variety of applications. Diameter-modulated nanowires can be used to enhance light trapping in photovoltaics by using thin-diameter tips to minimize reflection and thick-diameter bases to maximize absorption.¹⁸ Nanowires have been demonstrated to be promising materials for thermoelectrics by inhibiting phonon conduction while maintaining high electronic conductivity,^{17,192} and theoretical work has demonstrated the controlled variations in diameter could significantly increase phonon scattering.⁴⁸ Additionally, in thin nanowires with radial quantum confinement, variations in diameter could be used to change the bandgap of the material either as an alternative to or in conjunction with compositional control over the bandgap. Furthermore, changes in the nanowire diameter could be used to selectively alter the mechanical properties of different nanowire regions.

Diameter changes have commonly been observed during particle-mediated nanowire growth,^{67,125,126} but there have been limited reports of intentional diameter modulation. Fan et. al generated dual-diameter Ge nanowires by using an anodized alumina template in which a two-step anodization process was used to vary the width of the pores in which the nanowires were grown.¹⁸ To eliminate the need for such templates, as well as allow for multiple diameter changes along the nanowire, the diameter can instead be altered by changing the composition of the seed particle during growth.^{61,67,128} In the absence of a template, the diameter (d) of the nanowire is dependent upon both the volume (V) of the seed particle and the wetting angle (β) between the seed particle and the nanowire. For cylindrical nanowires, this can be expressed as follows.⁹⁰

$$d = 2 \left(\frac{3V}{\pi} \right)^{1/3} \frac{(1 + \cos(\beta))^{1/2}}{(1 - \cos(\beta))^{1/6} (2 + \cos(\beta))^{1/3}} \quad (6-1)$$

Changes in the composition of the alloying element(s) in the seed particle directly alter the volume of the seed volume while also affecting the composition-dependent surface energies that determine the wetting angle.

In the case of III-V nitrides, the group III elements (In,Ga,Al) alloy readily with the metal seed, but the group V source (N) is generally insoluble in the seed and III metals.^{68-70,193} Instead,

N enters at the vapor/liquid/solid (v/l/s) interface and diffuses along the l/s surface, where III-V solidification occurs (see Figure 2-3). Therefore, it should be possible to use the flow rates of the III and V precursors to control the rates of III source incorporation into and extraction out of the seed particle, respectively, thereby altering the seed particle composition and nanowire diameter.

We explore this flow-controlled approach by varying the flow of III & V precursors during nanowire growth. We achieve diameter modulation in InN and GaN nanowires by changing the fluxes of NH₃ and Ga, respectively. Measurements of seed particle composition indicate that these diameter changes are driven by changes in seed particle volume. Based on differences in segment growth rates, we conclude that the III and V sources can be used to alter the rates of III source incorporation and extraction, respectively. Using this technique, we fabricate GaN nanowires with thin-diameter notches and demonstrate that these regions can serve as sites for preferential nanowire fracture.

6.1. Modulation of InN diameter with the V source

We investigated diameter modulation in InN nanowires by adjusting the flux of the V source (NH₃) during growth while keeping the flux of the III source (In) constant. Reductions in V flow resulted in segments with reduced growth rates and wider diameters. The slower growth rate stems from a reduction in the rate of extraction of In out the Au seed particle, which leads to an accumulation of In within the seed, as confirmed by *ex situ* EDS measurements. These results demonstrate that template-free nanowire diameter modulation can be effectively achieved by a simple flow-controlled approach.

6.1.1. Diameter and growth rate changes in InN nanowires

The InN nanowires were synthesized by CVD at 560°C and 200 Torr using metallic In as the III source. The nanowires were grown on 2-5 µm thick films of *a*-GaN on *r*-sapphire and *c*-GaN on *c*-sapphire using 60 nm Au colloids as seed particles. Figure 6-1 shows SEM and TEM images of the InN nanowires grown using 300 sccm NH₃, which were removed from the growth substrate by sonication. These nanowires have either triangular or hexagonal cross-sections, while TEM images and their corresponding SAD patterns confirm that these grow along the [1-100] direction (*m*-InN) and [0001] direction (*c*-InN), respectively. The choice of substrate

has a significant impact on the preferential crystallographic orientation, as the majority of nanowires grown on *a*- and *c*-GaN grew in the *m*- and *c*-direction, respectively.

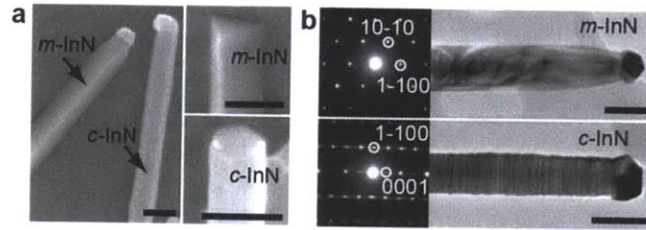


Figure 6-1. InN nanowires oriented in the *m*- and *c*-directions. (a) SEM images of *m*-InN and *c*-InN nanowires (left), as well as their corresponding triangular and hexagonal cross-sections, respectively (right). (b) TEM images (right) and corresponding SAD patterns (left) for *m*-InN (top) and *c*-InN (bottom) nanowires. All scale bars represent 100 nm.

To investigate diameter modulation in InN nanowires, we varied the flux of the V source (NH_3) during growth while keeping the flux of the III source (In) constant. Three different growths (I, II, & III) were performed, each consisting of an initial segment grown for 60 min at 300 sccm NH_3 followed three segments each consisting of a duration of both low (50 sccm) and high (300 sccm) NH_3 flow (Figure 6-2a-c). The resulting nanowires show distinct regions with larger and smaller diameters (hillocks and valleys, respectively). As shown in Figure 6-2d, the lengths of the hillocks and valleys were proportional to the durations of low and high NH_3 flow, respectively. Therefore, it can be concluded that a reduction in NH_3 flow causes nanowire diameter expansion, while resumption of high NH_3 flow causes contraction back to the original diameter. Furthermore, when the durations of high and low NH_3 flow were equal (growth I), the hillocks were $39 \pm 7\%$ shorter than the valleys, demonstrating that reduced NH_3 flow also reduces the growth rate.

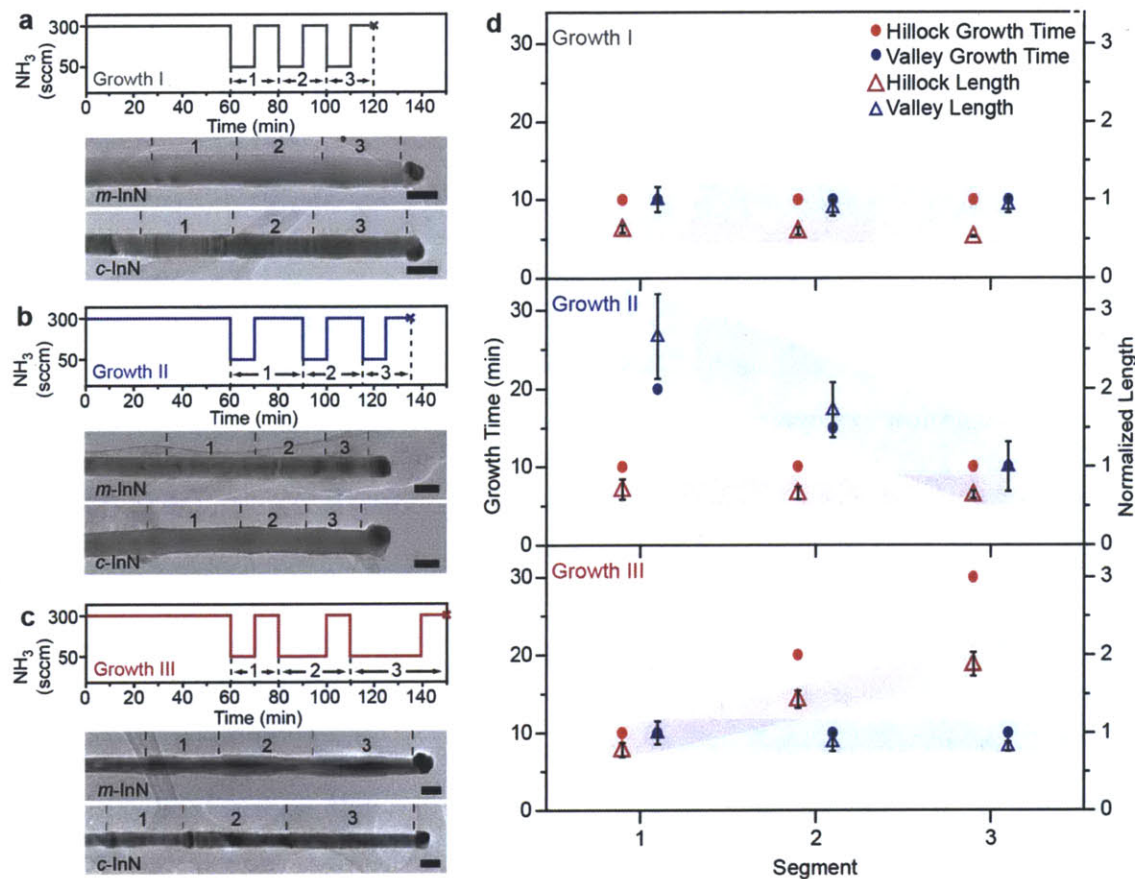


Figure 6-2. Diameter-modulated InN nanowires via V source reduction. (a-c) NH₃ flow as a function of time (top) for *m*-InN (middle) and *c*-InN (bottom) nanowires grown in growths I (a), II (b), and III (c). (d) Growth time and normalized length of hillocks and valleys for each of the 3 segments in growths I (top), II (middle), and III (bottom). All scale bars represent 100 nm.

6.1.2. Seed particle composition

As shown in Equation 6-1, changes in nanowire diameter can result from changes in either diameter or wetting angle. Given the slower growth rate of the nanowires during segments with low NH₃ flow, it makes sense that the reduced extraction rate of In out of the seed particle would cause an accumulation of In within it. To test this, we measured the composition of the Au-In seed particles after segments of both high and low NH₃ flow. For high NH₃ flow, the InN nanowires were grown for 60 min at 300 sccm NH₃. For low NH₃ flow, the initial 60-min segment was followed by a 30-min segment at 25 sccm NH₃. The composition of the Au-In alloys was measured using EDS coupled with STEM.

It is important to note that the *in situ* composition of the seed particle during growth can vary from the *ex situ* EDS measurements, because some of the supersaturated In can be extracted from the seed particle during post-growth cooling. However, for these InN nanowires, a localized In_2O_3 layer (bcc, Ia3, $a = 1.0117 \text{ nm}$)¹⁹⁴ was observed between the InN nanowire and the Au-In particle (Figure 6-3a,b), which we attributed to oxidized In formed during cooling through reaction with impurity oxygen or water vapor in the reactor. The presence of this oxide actually enables a better *ex situ* estimate of *in situ* seed composition, because the O traps the In and ceases further nanowire growth. Therefore, In present in both the seed alloy and the neighboring oxide region were including in the EDS measurements. For volume calculations, only Au and In were taken into account, as the oxygen in the oxide was not present during growth, and N has negligible solubility in Au. The error of the measurements reported above includes small compositional differences between different nanowires as well as the limitations in defining the precise interface between the nanowire and the seed particle regions. In some cases, there was overlap between the seed particle and the nanowire, but the small amount of extra In included here was found to have a minimal overall effect on the measured composition.

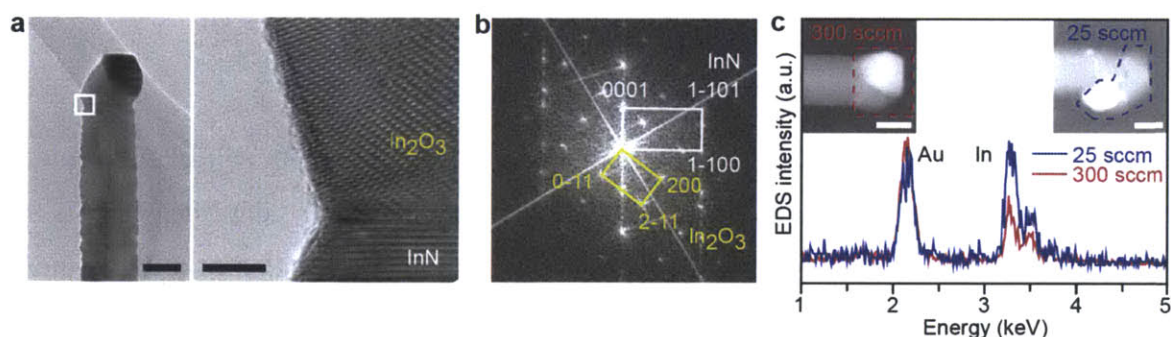


Figure 6-3. Au-In seed particle composition. (a) TEM image of the tip of an InN nanowire (left) and a lattice-resolved HR-TEM image (right) from the area indicated by the white box showing an In_2O_3 region between the nanowire and the Au-In seed. (b) Fast Fourier transform (FFT) produced from the HR-TEM image. Diffraction spots corresponding to InN and In_2O_3 are indicated in white and yellow, respectively. (c) EDS profiles of seed particles measured after high (red) and low (blue) NH_3 flow. The spectra were obtained from the nanowires shown in the STEM images in the insets, as indicated by the dashed regions.

From EDS measurements of multiple nanowires, the seed particles were found to have greater In composition ($71 \pm 6\%$) after lower NH_3 flow than after higher NH_3 flow ($50 \pm 7\%$), indicating a larger seed particle volume for the wide diameter regions (Figure 6-3c). Taking into

account the molar volumes of liquid In and Au at 560°C,¹⁹⁵ the compositional changes reported above would correspond to a $93 \pm 55\%$ volume expansion of the seed particle and a $24 \pm 12\%$ increase in diameter, assuming no change in wetting angle. These measurements are in agreement (within the error of measurement) with the measured increase in nanowire diameter of $34 \pm 9\%$ (measured from more than 25 nanowires). Based on Equation 6-1, an *in situ* wetting angle change of 6° would account for the small difference between the measured diameter change and the values estimated from EDS. While measuring *in situ* seed composition and accounting for changes in wetting angle would yield a more precise calculation, our results clearly demonstrate that reduced NH₃ flow induces increased seed particle volume and consequent nanowire diameter expansion.

6.1.3. Mechanism of V-flow-induced diameter modulation

According to Equation 6-1, the nanowire diameter remains unchanged when (1) the wetting angle of the seed particle is at equilibrium and (2) the rate of III-source incorporation into the seed particle is balanced by the extraction rate of III-source out of the seed particle by reaction with N-source (seed particle volume is constant). Assuming a flat liquid/solid interface, the equilibrium wetting angle can be calculated as follows:

$$\sigma_{vl} \cos \beta = \sigma_{vs} \cos \alpha - \sigma_{ls} \quad (6-2)$$

where σ_{vl} , σ_{vs} , and σ_{ls} are the surface energies at the vapor/liquid, vapor/solid, and liquid/solid interfaces, respectively, and α is the inclination angle of the nanowire sidewall, which is 90° at steady state (Figure 6-4). (The validity of Equation 6-2 and the assumption of a flat liquid/solid interface will be discussed further in section 7.3, but this equation is qualitatively sufficient for the purpose of this analysis.) The rate of III-source incorporation into the seed particle with the difference in chemical potential between the vapor (v) and liquid (l) phases.⁶⁰

$$\Delta\mu_{v,l}^{III} = \mu_l^{III} - \mu_v^{III} \quad (6-3)$$

The extraction of III source out of the seed particle occurs by reaction of III source in the liquid with N. Therefore the extraction rate is dependent upon the supersaturation of both the III and N sources between their respective phases and the solid (s) nanowire phase.

$$\Delta\mu_{l,s}^{III} = \mu_s^{III} - \mu_l^{III} \quad (6-4)$$

$$\Delta\mu_{p,s}^N = \mu_s^N - \mu_p^N \quad (6-5)$$

Because N is insoluble in Au and the III metals,⁶⁸⁻⁷⁰ the reference phase (*P*) for N may be either the *v*/*l*/*s* triple phase line or the *l*/*s* interface, depending on where nucleation occurs.

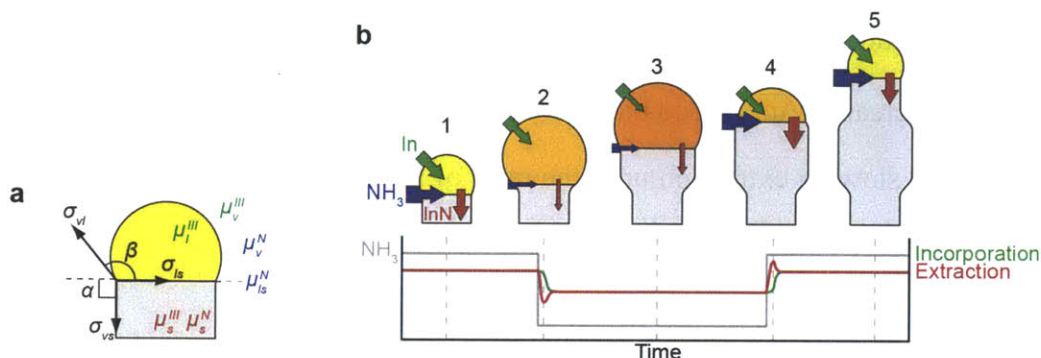


Figure 6-4. Mechanism of InN nanowire diameter evolution. (a) Illustration describing the terms in Equations 6-2–6-5, including the relevant chemical potentials (μ) of the III source and N, as well as the relationship between the wetting angle (β), the inclination angle (α), and the surface energies (σ) of the vapor (*v*), liquid (*l*), and solid (*s*) regions. (b) Schematic depiction of the mechanism of InN nanowire diameter evolution (top) and a graph of the corresponding NH_3 flow, incorporation rate, and extraction rate throughout the 5-step process (bottom). The sizes of the green, blue, and red arrows illustrate the rates of In incorporation, N incorporation, and InN solidification, respectively. Green and blue squares connected to the arrows indicate the supplied fluxes of In and NH_3 , respectively. All representations, including object sizes and graphical values, are intended to illustrate relative quantities and do not necessarily reflect actual values proportionately.

Based on the equations above, the mechanism of InN nanowire diameter modulation depicted in Figure 6-4b can be understood as follows. Under constant 300 sccm NH_3 flow, the nanowire grows at steady state with constant diameter (step 1). When the NH_3 flow is reduced to 50 sccm, the rate of In extraction out of the seed particle suddenly decreases while the rate of In incorporation into the seed particle remains high (red and green lines in Figure 6-4b, respectively). This imbalance leads to an accumulation of In within the seed particle, increasing its volume. Consequently, β exceeds its equilibrium value, and α increases to maintain the force balance in Equation 6-2, resulting in diameter expansion (step 2). As the concentration of In in the seed particle continues to increase, μ_l^{III} increases. This simultaneously decreases $\Delta\mu_{v,l}^{III}$ (Equation 6-3) and increases $\Delta\mu_{l,s}^{III}$ (Equation 6-4), which slows the incorporation rate and speeds up the extraction rate, respectively. Eventually these rates become balanced, β returns to equilibrium, and a larger steady-state diameter is obtained (step 3).

A similar process occurs when the NH_3 flow is increased back to 300 sccm. The extraction rate suddenly increases while the incorporation rate remains low, which reduces both the seed particle volume and wetting angle. This reduction in β causes a corresponding reduction in α , which leads to a reduced diameter (step 4). The reduction in In composition lowers μ_l^{III} , which simultaneously increases $\Delta\mu_{v,l}^{\text{III}}$ (Equation 6-3) and decreases $\Delta\mu_{l,s}^{\text{III}}$ (Equation 6-4), speeding up incorporation and slowing extraction until the rates of incorporation and extraction are balanced. Eventually, the original steady-state diameter is obtained (step 5).

6.2. Diameter modulation of GaN nanowires with the III source

The results of the diameter modulation studies with InN nanowires demonstrate that the nanowire diameter can be tuned by adjusting the flow of the V precursor, which alters the extraction rate of the III source out of the seed particle. To demonstrate that the nanowire diameter can also be tuned using the III precursor, we varied the flux of Ga during the growth of GaN nanowires. The nanowire diameter and growth rate both decreased upon reduction of the Ga flux, which was attributed to a lower composition of Ga in the seed particle as a consequence of the reduced driving force for Ga incorporation.

6.2.1. Ga-induced changes in diameter and growth rate

GaN nanowires were synthesized by MOCVD at 835°C and 100 Torr using a setup similar to that in section 4.3 except the Ga flux was controlled by the flow of H_2 through a Ga-coated quartz tube injector (see section 3.1.3). In this case, we utilize our observation in section 4.2.2 that H_2 inhibits growth of GaN to minimize Ga consumption within the injector, thereby achieving better control over the Ga flux. To maintain a reasonable growth rate, N_2 carrier gas was also used but not delivered through the injector. As with previous GaN studies, *r*-sapphire substrates coated with 1 nm Au films produced GaN nanowires orientated in the [1-100] *m*-direction.

The flux of Ga was varied during growth by changing the flow rate of H_2 through the Ga-coated injector between 0–150 sccm as described in Figure 6-5a. As the flux of Ga was reduced, both the nanowire diameter and growth rate decreased accordingly. A reduction from 50 to 10 sccm H_2 reduced the nanowire diameter by $13 \pm 5\%$ (Figure 6-5c) and the growth rate by $65 \pm$

9%. This effect was reversible, as the same nanowire diameter was restored when the flow was increased back to 50 sccm. Notably, the diameter could be continuously tuned with the Ga flux such that the diameter decreased incrementally from 150 to 50 to 10 sccm. Also, brief cessations of the injector flow generated short, thin-diameter regions along the GaN nanowire.

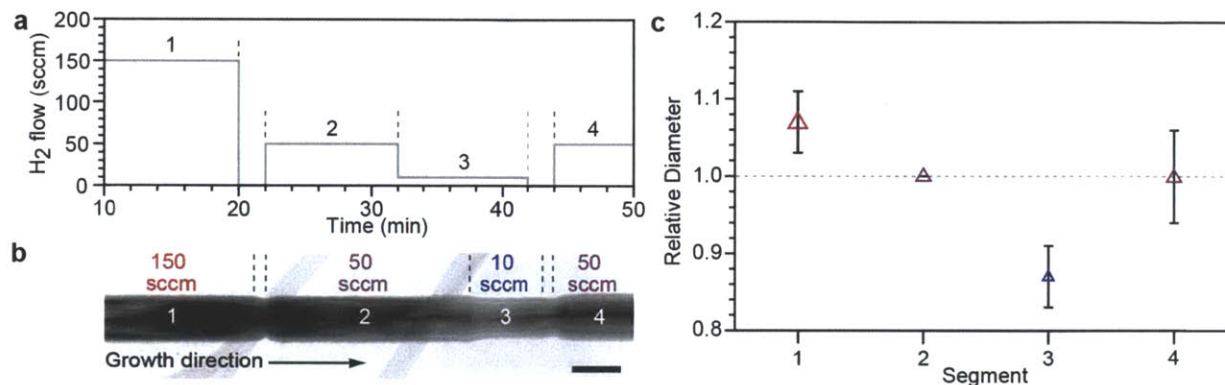


Figure 6-5. Diameter-modulated GaN nanowires using via III source reduction. (a) Flow rate of H_2 through the Ga-coated quartz tube injector during nanowire growth. (b) TEM image of a GaN nanowire taken along the $[0001]$ zone axis. Segments 1–4 corresponding to the flows described in (a). (c) Average diameter of each nanowire segment normalized to the diameter of segment 2. Scale bar represents 100 nm.

As indicated by SEM images in which the GaN facets are clearly visible (Figure 6-6a,b), the triangular cross-section of the nanowire is maintained throughout growth even as the diameter changes, but the diameter changes are anisotropic. The triangular m -GaN cross-section is known to be bounded by one $\{0001\}$ facet and two $\{11\bar{2}2\}$ facets. The TEM images and SAD patterns in Figure 6-6c,d confirm that the SEM images in Figure 6-6a,b are viewed along the $[0001]$ and $[11-20]$ zone axes, respectively. Thus it is clear that the $\{0001\}$ facet remains flat during diameter modulation, while the $\{11-22\}$ facets incline (α changes) to accommodate the changes in diameter. These anisotropic changes are likely due to differences in surface facet energies. It is important to note that α in Equation 6-2 is coupled with the value of σ_{vs} , which is different for the two $\{11\bar{2}2\}$ facets versus the $\{0001\}$ facet. In order to achieve a certain change of the $\sigma_{vs} \cos \alpha$ term in Equation 6-2, the deviation of α from 90° should be significant with low σ_{vs} , but negligible with high σ_{vs} . Therefore, an inclined facet deviating from the $\{0001\}$ plane would likely have a relatively high increase in σ_{vs} compared to the flat $\{0001\}$, while the inclined

facets deviating from the $\{11\bar{2}2\}$ planes likely have a relatively low increase in σ_{vs} . This would explain why the $\{11\bar{2}2\}$ incline to accommodate diameter changes while the $\{0001\}$ facet remains stable throughout the growth.

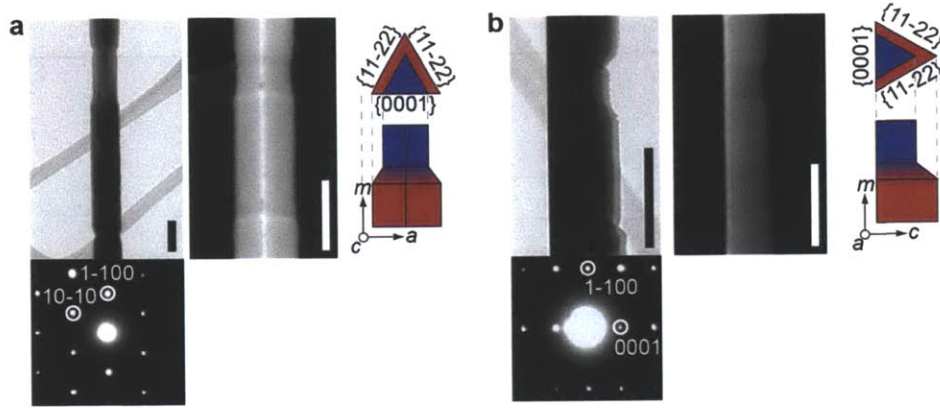


Figure 6-6. Anisotropic diameter evolution in GaN nanowires. (a,b) GaN nanowires viewed along the $[0001]$ c -axis (a) and $[11-20]$ a -axis. The TEM images and corresponding SAD patterns (left) confirm the orientation of the SEM images (center). The diagrams on the right schematically illustrate the changes in nanowire diameter and morphology in cross-sectional (top) and zone axis (bottom) views. Red and blue indicate wide and narrow diameters, respectively. All scale bars represent 100 nm.

6.2.2. Mechanism of III-flow-induced diameter modulation

For these GaN nanowires, the mechanism of diameter evolution is illustrated in Figure 6-7 and can be understood as follows. The initial Ga flux is high and constant, resulting in a large steady-state diameter (step 1). When the Ga flux is reduced, the incorporation rate suddenly decreases while the extraction rate remains high, consequently decreasing the seed particle volume. This results in a reduced wetting angle and a corresponding reduction in α (Figure 6-4), which leads to a reduced nanowire diameter (step 2). As the Ga composition in the seed continues to decrease, the incorporation rate increases with increasing $\Delta\mu_{v,l}^{III}$ (Equation 6-3), while the extraction rate decreases with decreasing $\Delta\mu_{i,s}^{III}$ (Equation 6-4). These rates eventually become balanced, β remains constant, and a new steady-state is reached at a thinner nanowire diameter (step 3). Upon restoration of high Ga flux, the incorporation rate suddenly increases while the extraction rate remains low, which leads to Ga accumulation in the seed, increasing the

seed particle volume and nanowire diameter (step 4). The increasing Ga composition in the seed particle causes a reduction in the incorporation rate and an increase in the extraction rate until these rates are equal, yielding a large steady-state diameter once again (step 5).

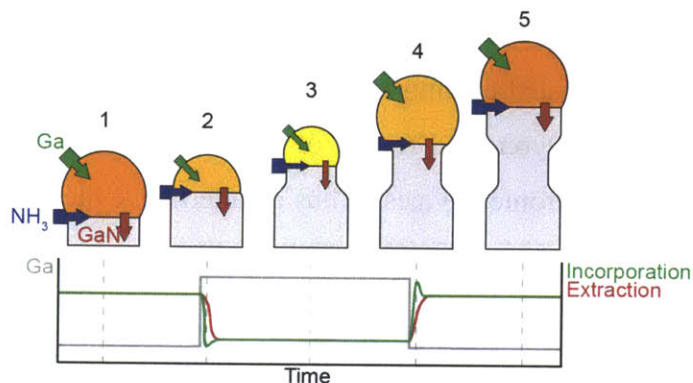


Figure 6-7. Mechanism of GaN nanowire diameter evolution. Schematic depiction of the mechanism of GaN nanowire diameter evolution (top) and a graph of the corresponding Ga flow, incorporation rate, and extraction rate throughout the 5-step process (bottom). The sizes of the green, blue, and red arrows illustrate the rates of Ga incorporation, N incorporation, and GaN solidification, respectively. Green and blue squares connected to the arrows indicate the supplied fluxes of Ga and NH_3 , respectively. All representations, including object sizes and graphical values, are intended to illustrate relative quantities and do not necessarily reflect actual values proportionately.

6.3. Diameter modulation for controlled fracture

Diameter-modulated nanowires with short, thin-diameter regions could be used to promote preferential fracture at specific points along the nanowire, which may have a variety of useful applications including enhanced yield during transfer printing (Figure 6-8a),^{196,197} separation of free-standing nanowire-templated films (Figure 6-8b),¹⁹⁸ and fundamental studies of the mechanical properties of nanowires. Additionally, these structures could be used to increase the throughput of nanowires synthesized by high-temperature batch processing techniques including chemical vapor deposition and molecular beam epitaxy, reducing both the time to fabricate each nanowire and the costs associated with expensive epitaxial growth substrates (Figure 6-8c). In this case, periodic thin-diameter notches along the nanowire could be used to induce preferential fracture and allow multiple nanowires to be grown from each individual seed. There are a variety of nanowire applications that do not require the nanowires to be affixed epitaxially to the

original growth substrate. In particular, there is interest in fabricating nanowire-based flexible electronics, solar cells, displays, and sensors.^{196,199-201} However, the substrates are often incompatible with the conditions used during nanowire growth. Thus the nanowires need to be grown on another substrate and then transferred to the flexible one. Notably, Weisse *et al.* demonstrated preferential fracture in Si nanowires via pore formation.²⁰² However, the cracks were formed during metal-assisted etching by delamination of Ag, which produced pores in the nanowires that often extend beyond the region of preferential fracture and can therefore have deleterious effects on optoelectronic devices. Thus an alternative method of preferential fracture is desired.

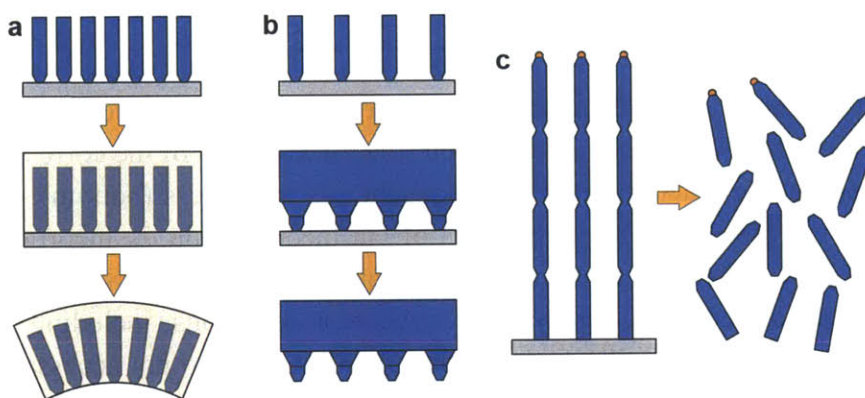


Figure 6-8. Applications of controlled fracture in nanowires. (a) Transfer of nanowires from the growth substrate to a flexible substrate using a polymer mold. (b) Separation of nanowire-templated films to produce free-standing films. (c) Multiple nanowires produced from a single seed to increase throughput.

Using the flow-controlled diameter modulation technique developed above, we fabricated GaN nanowires with thin-diameter notches placed periodically along the nanowire by reducing the Ga flow during growth. Preferential fracture at thin-diameter regions was demonstrated by bending tests in SEM using a tungsten nanomanipulator probe. The mechanism of nanowire fracture and potential strategies controlled fracture of large-area nanowire arrays are also discussed.

6.3.1. Producing thin-diameter notches

Thin-diameter notches were created along GaN nanowires by periodically reducing the Ga flow during growth. Like the diameter-modulated GaN nanowires described above, these

nanowires were grown at 835°C and 100 Torr with the flux of Ga controlled by the flow rate of H₂ through a Ga-coated quartz tube injector. An initial 30 min GaN segment with 50 sccm H₂ through the injector was followed by 3 cycles each consisting of 5 min at 1 sccm H₂ followed by 10 min at 50 sccm H₂. The resulting nanowires had 3 thin-diameter notches separating the 4 segments (Figure 6-9). SEM and TEM images show that these nanowires have the same anisotropic diameter changes as those described above, in which the {0001} facet remains flat while the {11 $\bar{2}2$ } facets incline to accommodate diameter changes. The diameter of the notch was $16 \pm 4\%$ thinner than the diameter of the segments. Notably, when the nanowires were transferred to TEM grids by mechanically swiping the grid across the growth substrate, it was difficult to find nanowires on the grid with all four segments still intact. Furthermore, thin-diameter regions were generally visible where this fracture occurred, indicating that these notches may serve as sites for preferential fracture.

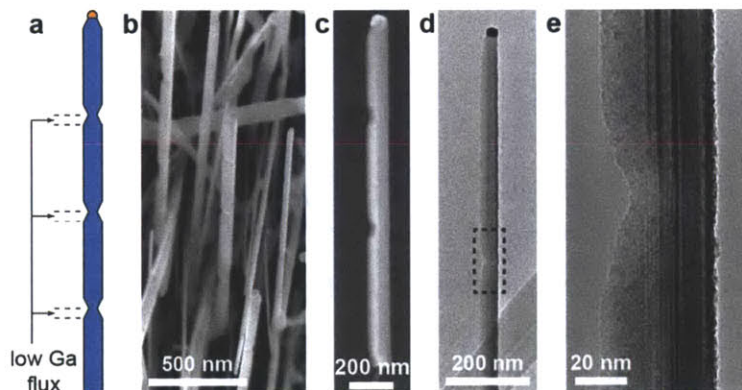


Figure 6-9. Notched GaN nanowires. (a) Schematic illustration of the notched nanowires, which contain 4 segments separated by 3 notches that were formed by reducing the Ga flux. (b) SEM image of the array of the as-grown nanowire array. (c) SEM image of a nanowire with the upper 3 segments intact after transfer to a Si substrate. (d) TEM image of a notched GaN nanowire viewed along the [11-20] zone axis. (e) Magnified view of the dashed region in (d) showing the morphology of the notch.

Based on our previous observation in section 4.2.2 that H₂ reduces the growth of GaN nanowires, we also grew notched nanowires in which we varied the carrier gas flow during notch formation, as well as the duration of the flow. In this case, the segments were grown for 3 min each with 50 sccm H₂ through the Ga-coated injector, and the notches were grown with no Ga flow for 3 and 5 min for both N₂ and H₂ carrier gas (Figure 6-10). For N₂ carrier flow, the length

of the notches increased with time, indicating that some Ga continues to be supplied when the flow is shut off, perhaps by diffusion of Ga from the walls of the injector. For H_2 carrier flow, only very subtle notches can be seen (Figure 6-10b). Furthermore, the lengths of the segments grown prior to these notches are significantly shorter than the other segments, which were all grown under the same conditions. Thus it is likely that etching occurs when H_2 carrier gas is used after the Ga supply is shut off. While this is undesirable, these results do demonstrate that it may be possible to improve the sharpness of the notch geometry by finely tuning the composition of H_2 in the carrier gas.

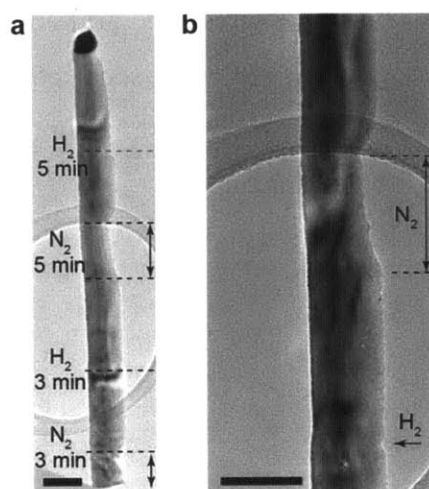


Figure 6-10. Notched GaN nanowire with variable carrier gas composition. (a) TEM image of a notched GaN nanowire in which the carrier gas composition and the duration of growth was varied between notches. (b) Magnified view of notches in (a). Scale bars represent 100 nm.

6.3.2. Preferential fracture

To examine whether these notches can serve as sites for preferential fracture, bending tests were performed in collaboration with Steven Boles at the Karlsruher Institute of Technology. Analysis was performed on four notched nanowires from the growth described in Figure 6-9, as well as four nanowires grown without diameter modulation. The nanowires were transferred from the original growth substrate to Si substrates with a native oxide layer. These tests were performed under SEM observation, and videos of the tests were recorded. The nanowires were bent by pushing on the ends of the nanowires with a tungsten probe. The attractive forces between the nanowire and the substrate were sufficient to hold the nanowires in place. All four

diameter-modulated nanowires tested were observed to fracture preferentially at the thin-diameter regions (Figure 6-11a,b). The aspect ratio between the segments and the notches had some variability between nanowires, and even notches with relatively low aspect ratios ($d_{notch}/d_{segment} > 0.9$) induced preferential fracture. For the straight nanowires, two of the four nanowires tested fractured, and the others showed significant bending without fracturing.

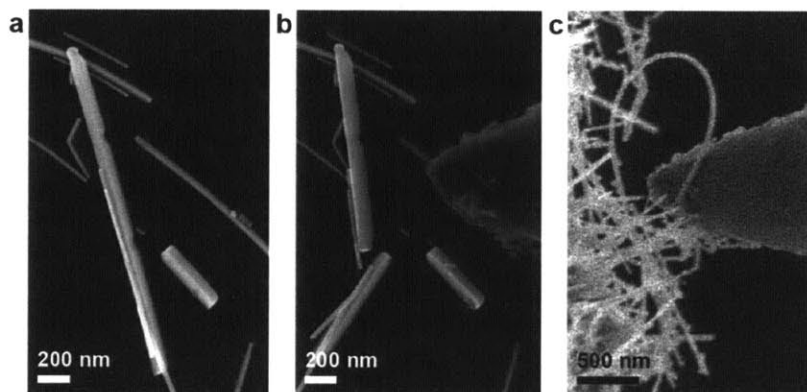


Figure 6-11. Bending tests of notched GaN nanowires. (a,b) SEM images of a notched GaN nanowire before (a) and after (b) the bending test, demonstrating preferential fracture at the thin-diameter notch. Nanowires are on a SiO_x/Si substrate after being transferred from the original growth substrate. (c) Video frame taken during bending of a straight GaN nanowire. In this case, the nanowire was protruding from the edge of the original growth substrate.

These bending tests clearly demonstrate that thin-diameter notches provide sites where fracture occurs preferentially, and this proof of concept warrants further investigation. First, the underlying mechanism of preferential fracture is not entirely clear. While very sharp cracks in materials concentrate applied stresses at the crack tip, these notches are not known to initially contain a very sharp crack tip. Also, thinner nanowires are known to be highly flexible,²⁰³ so fracture in the thinner regions is quite interesting. A likely explanation is that stress concentrates in the thinner regions as a consequence of the lower flexibility in the wider regions, which induces bending primarily at the notch. Eventually, this concentrated stress results in the formation of a crack, which then propagates readily across the nanowire. Further tests with quantitative measurements will provide insight into the mechanism and degree of stress concentration in the notched regions. Additionally, insight into how material properties and notch geometry affect preferential fracture will help aid in guiding the synthesis of notched nanowires.

Additionally, in order for this technique to be useful in applications, preferential fracture must be able to be induced over large-area nanowire arrays. When a Si substrate was swiped over the growth substrate, preferential fracture at the notches could be observed, but not all notches induced fracture. For example, in Figure 6-11a three of the four original segments are present, and the lowest segment fractured at the notch. Also, fracture sometimes occurred away from the notches. Many techniques have been developed to transfer nanowires from one substrate to another,^{196,200,204} and some of these may also be applicable in inducing preferential fracture. As mentioned previously, Weisse *et al.* induced preferential fracture in Si nanowires at regions that were highly porous.²⁰² In addition, they were able to effectively remove these nanowires at the notches with high yield using multiple methods, including embedding the nanowires in PMMA and PDMS, as well as removing the nanowires using adhesive tape. Applying similar techniques to notched nanowires with optimized geometries could enable their use a variety of applications.

6.4. Summary

A particle-mediated template-free approach to nanowire diameter modulation was effectively demonstrated using both InN and GaN nanowires by varying the flow of the V and III precursor, respectively, during nanowire growth. For InN nanowires, a reduction in the flow of the V source (NH_3) led to segments with thicker diameters and slower growth rates. *Ex situ* measurements of seed particle composition via EDS indicate that the seed particle composition was greater during growth of segments with larger diameter. Based on these measurements, the calculated changes in seed particle volume were found to account for the majority of the observed changes in nanowire diameter. Here, the reduced V source flow slowed the rate of extraction of the III element (In) out of the seed particle, which both reduced the nanowire growth rate and led to accumulation of In within the seed particle that increased the seed particle volume and, consequently, the nanowire diameter. For GaN nanowires, a reduction in the flow of the III element (Ga) also produced segments with slower growth rates, but with thinner diameters. The nanowire diameter and growth rate were continuously tuned by incremental changes in Ga flow. Here, the reduced III flow slowed the rate of Ga incorporation into the seed. The consequent reduction in Ga composition resulted in a slower growth rate due to the reduced driving force for GaN formation and a thinner diameter due to the reduction in seed particle

volume. This flow-controlled approach provides a versatile technique for producing diameter-modulated nanowires in compound semiconductor materials, enabling new opportunities to more optimally design complex nanowire architectures for specific device applications.

Using this approach, we were able to fabricate GaN nanowires with short, thin-diameter notches by reducing the flow of Ga periodically during growth. Bending tests observed *in situ* demonstrated that the nanowires fractured preferentially at the thin-diameter notches, which likely occurs due to stress concentration originating from greater curvature in the thin-diameter regions. These nanowires demonstrate a very intriguing proof of concept and open up new areas of research including quantification of the mechanical properties of diameter-modulated nanowires and strategies for controlled fracture of notched nanowire arrays over large areas. These notched nanowires could potentially be used in a variety of applications, including yield enhancement during transfer printing and increased throughput from nanowire growth.

Chapter 7: Modeling diameter-modulated nitride nanowires

The flow-controlled diameter modulation technique developed in Chapter 6 provides a versatile template-free tool for synthesizing diameter-modulated nanowires. However, the potential for fabricating nanowires with arbitrary diameter ratios is unclear. Furthermore, while we focused previously on volume-driven diameter changes, there may be potential to achieve larger diameter ratios via changes in wetting angle, which are driven by changes in the surface energies at the vapor/liquid/solid triple-phase boundary (TPB).

To explore the potential and limitations for template-free particle-mediated nanowire diameter modulation, we develop a theoretical approach that incorporates changes in the volume, wetting angle, and three-dimensional morphology of the seed particle to understand and guide nanowire diameter modulation. The model is applied to our experimental results for InN and GaN nanowires in order to understand the origin of the diameter changes for those nanowires. The analysis is further extended to evaluate the general potential and limitations for diameter modulation in other materials systems. Additionally, the model is applied to evaluate the shape of the liquid/solid interface, which has significant implications for nanowire synthesis and understanding of fundamental nanowire growth mechanisms.

7.1. Theoretical model

Models were developed to assess nanowire diameter modulation in InN and GaN nanowires. The methods for calculating wetting angle and modeling three-dimensional seed particle geometry are described below. In addition, the difference between nominal input wetting angles and actual output wetting angles in the Surface Evolver models is discussed, as well as the impact of liquid/solid interface morphology on the Surface Evolver models.

7.1.1. Calculation of wetting angle

To model nanowire diameter modulation, the following equation was used when nanowires were assumed to be cylindrical,

$$\frac{d}{V^{1/3}} = \left(\frac{24}{\pi} \right)^{1/3} \frac{(1 + \cos(\beta))^{1/2}}{(1 - \cos(\beta))^{1/6} (2 + \cos(\beta))^{1/3}} \quad (7-1)$$

where d is the nanowire diameter, V is the seed particle volume and β is the wetting angle between the vapor/liquid and liquid/solid surfaces (Figure 7-1).⁹⁰ The wetting angle was calculated from measured values of d and V . The values of d were directly measured from TEM images using Digital Micrograph. The values of V were calculated from EDS measurements of the composition of the seed particle. In the case of III-V nitride nanowires synthesized using Au seed particles, nitrogen is insoluble in Au and the III metals used,⁶⁸⁻⁷⁰ so only the composition of the III element is considered when calculating the volume of the seed.

$$V = n_{Au} \Omega_{Au} + \frac{x_{III}}{1 - x_{III}} n_{Au} \Omega_{III} \quad (7-2)$$

Here, n_{Au} is the number of Au atoms, Ω is the atomic volume of liquid metal at the growth temperature,¹⁹⁵ and x_{III} is the composition of the III element (In or Ga) in the seed particle.

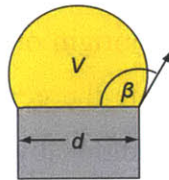


Figure 7-1. Wetting angle of the seed particle. Diagram illustrating the relationship between nanowire diameter (d), seed particle volume (V), and the wetting angle (β) between the seed particle and the nanowire.

The amount of gold (n_{Au}) remains constant throughout growth and can be determined from known original seed particle sizes or by a combination of TEM and EDS measurements.^{NL2} For InN nanowires, Au colloids of known diameter were used, so n_{Au} was calculated assuming the volume of a sphere with a 60 nm diameter. Au films were used for GaN nanowires, so the volume of gold could not be assumed. Instead, n_{Au} was calculated assuming the following,

$$V = \frac{4\pi}{3} \left(\frac{A_{seed}}{\pi} \right)^{3/2} \quad (7-3)$$

where A_{seed} is the area of the seed particle measured using Image J software.

7.1.2. Surface Evolver for non-cylindrical nanowires

To model nanowire diameter modulation in InN and GaN nanowires, Surface Evolver software was used to account for the three-dimensional geometry of the seed particle. The

program minimizes the energy of a surface according to given constraints. The constraints imposed here were the volume of the seed particle, shape of the nanowire cross-section (either round, hexagonal, or triangular) and the relative energies of the vapor/liquid (σ_{vl}) and liquid/solid (σ_{ls}) interfaces. These energies correspond to a nominal wetting angle (β) as follows.

$$\beta = \cos^{-1} \left(-\frac{\sigma_{ls}}{\sigma_{vl}} \right) \quad (7-4)$$

The software uses a triangular mesh, which is optimized iteratively. After the shape converges to a particular solution, the size of the mesh is decreased to improve resolution (Figure 7-2a). The accuracy of the model is accurate, as the input wetting angle matches the measured output wetting angle for circular cross-sections (Figure 7-2b).

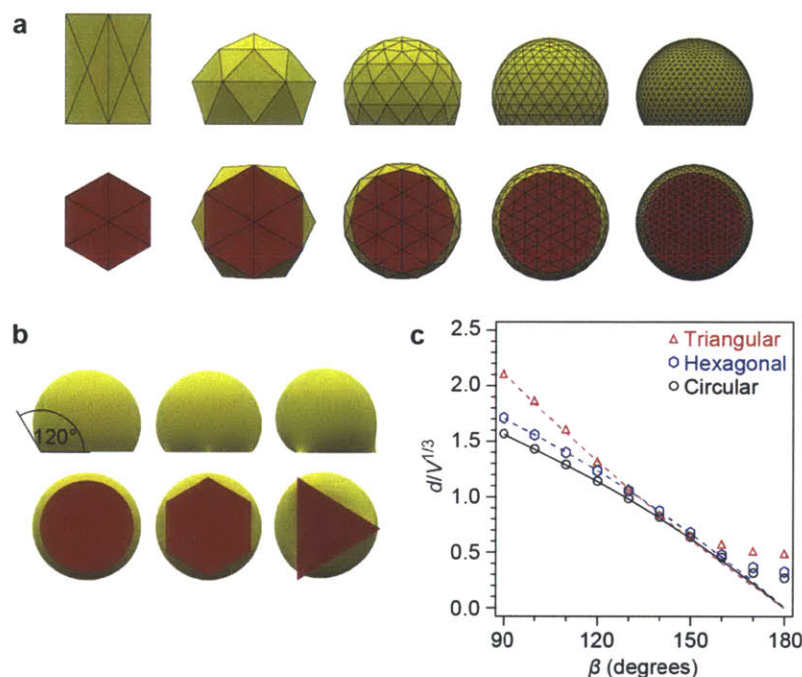


Figure 7-2. Surface Evolver model. (a) Surface Evolver step-wise evolution, from left to right, of a seed particle (yellow) on a nanowire with a circular cross-section (red) showing side (top) and bottom (bottom) views. Black lines illustrate the triangular mesh. (b) Side (top) and cross-sectional (bottom) views of Surface Evolver models for circular, hexagonal, and triangular cross-sections with an input wetting angle (β) of 120° , which is consistent with the measured output wetting angle for the circular cross-section. (c) $f(\beta)$ as a function of wetting angle (β) for the nanowire cross sections described in (a). Black solid line was calculated using Equation 7-1, whereas dashed lines were fitted to the data using quadratic functions.

For non-cylindrical nanowires, Equation 7-1 was modified to create a generalized expression for the relationship between d and V .

$$\frac{d}{V^{1/3}} = f(\beta) \quad (7-5)$$

The values of $d/V^{1/3}$ were calculated between 90° – 180° in 10° increments using Surface Evolver models for circular, hexagonal, and triangular cross-sections and plotted as a function of β (Figure 7-2c). From this plot, $f(\beta)$ was determined empirically by fitting the data using quadratic equations. For $\beta \geq 160^\circ$, the Surface Evolver model was not as accurate due to difficulties in the finite triangular mesh converging upon the very small diameters at such high wetting angles. Therefore, the fit ignored values for $\beta \geq 160^\circ$ and logically assumed that $d = 0$ for $\beta = 180^\circ$.

7.1.3. Model accuracy

The accuracy of this approach is supported in multiple ways. First, as shown in Figure 7-3, the actual output wetting angle (β^* ; measured from Surface Evolver images) for a cylindrical cross-section was the same as the input nominal wetting angle (β ; represents the ratio between surface energies as described by Equation 7-4). Second, for non-cylindrical geometries, $\beta^* > \beta$ at edges while $\beta^* < \beta$ at corners (Figure 7-3). This variation in contact angle around non-cylindrical nanowires is consistent with *in situ* nanowire growth studies reported in literature,^{7,205} and this model accurately reproduces reported seed particle shapes in these studies (Figure 7-4).

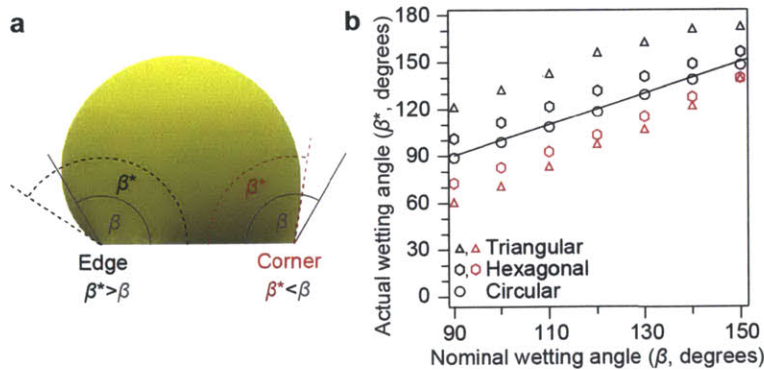


Figure 7-3. Actual versus nominal wetting angle. (a) Illustration of nominal wetting angle (β ; solid gray lines) and actual wetting angle (β^*) at both the edges (dashed black lines) and corners (dashed red lines) for a seed particle on a triangular cross-section. (b) Comparison of actual wetting angle at edges (black) and corners (red) as measured from Surface Evolver images to nominal wetting angle.

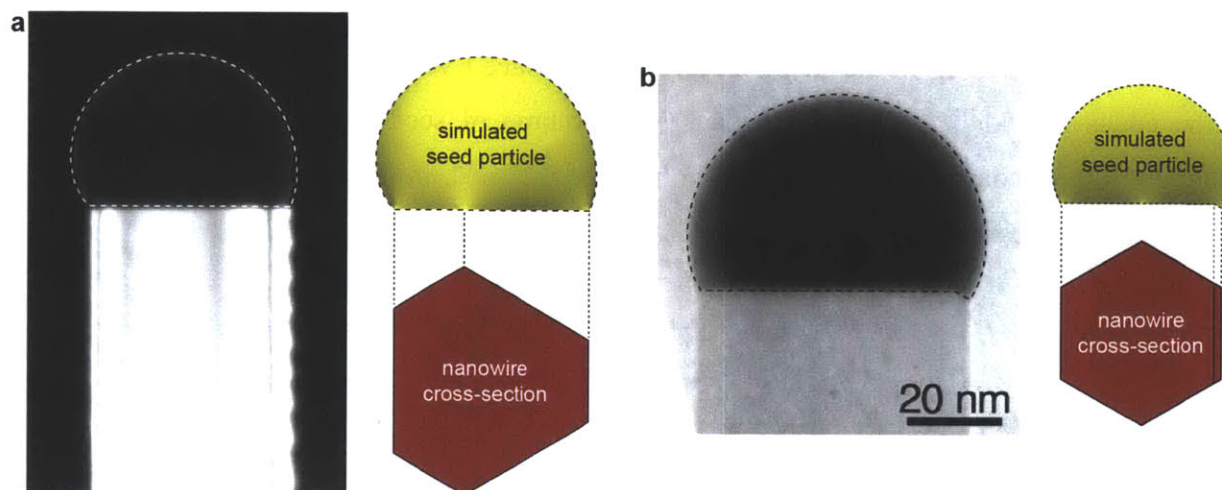


Figure 7-4. Comparison of Surface Evolver model with *in situ* TEM studies. (a) Si nanowire seeded by a Au-Si seed particle (left). Simulated seed particle morphology (top right) and corresponding cross-sectional geometry (bottom right). (b) Si nanowire seeded by a Au-Ga-Si seed particle (left). Seed particle morphology (top right) and corresponding cross-sectional geometry (bottom right), which is a hexagonal cross-section with an extra tilted facet at the liquid/solid interface. The dashed lines in the micrographs of (a) and (b) indicate the simulated boundaries of the seed particles, which are consistent with the geometry reported by the authors. Micrographs in (a) and (b) adapted from [205] and [7], respectively.

The discrepancy between the nominal wetting angle (β) input into the Surface Evolver model and the actual wetting angle (β^*) output by Surface Evolver is evaluated in Figure 7-5 for triangles with different degrees of curvature. The effect of line tension was considered here based on reported values for other materials ($1 \times 10^{-9} \text{ J/m}^2$ for Si)²⁰⁶ but was found to have a minimal effect and was therefore neglected in our model. It is important to note that some values for “corner” wetting angles reported in this work were in some cases actually measured at inflection points (Figure 7-5a) to reflect the rounded corners that would likely be observed in real structures. There are multiple reasons to expect that actual wetting angles at the corners would more closely resemble the measurements at the inflection points. First, a high degree of curvature in the liquid, as sometimes observed in Surface Evolver models near sharp corners, is energetically unfavorable in the case of nanoscale particles used for nanowire growth. Also, measurements at inflection points are more consistent. Figure 7-5c illustrates that, when inflection points are observed near the corner of a sharp triangle, measurements at the inflection points follow a clear and consistent trend, but measurements at the corner do not. As corner curvature increases, the measurements between corner and inflection points become more

similar, and eventually inflection points disappear (Figure 7-5d). Notably, while the real shape of the seed may differ from the shape predicted by Surface Evolver at the corners, discrepancies at the edges should be minimal. Because the volume of seed material near the corners is relatively low in comparison to the total volume of the seed, minor variations in these regions should not significantly affect the overall calculation of $d/V^{1/3}$.

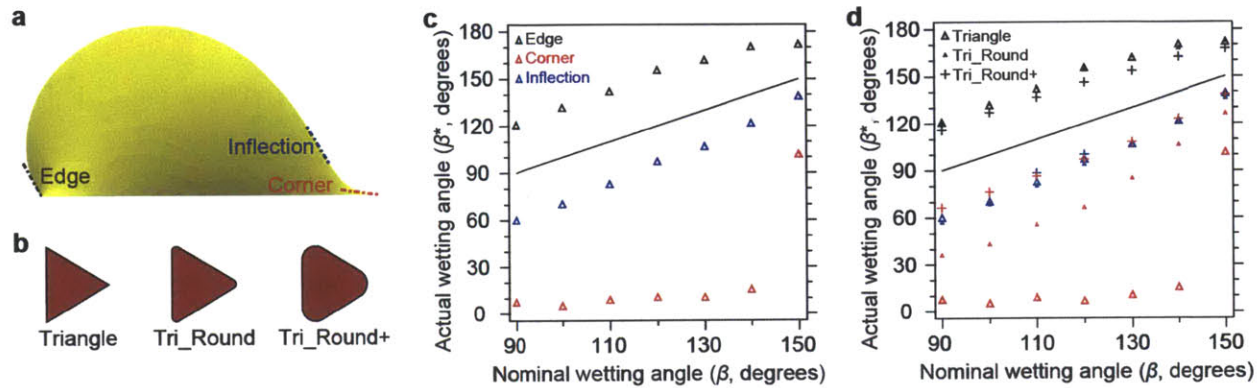


Figure 7-5. Effect of nanowire corner curvature on measured wetting angle. (a) Illustration of measurements of the contact angle of the seed particle at the edge and corner of a triangular cross-section, as well as the inflection point on the seed particle. (b) Triangular cross-sections with different degrees of curvature at the corners. (c) Actual wetting angle (β^*) at edge, corner, and inflection points for a triangular cross-section measured from Surface Evolver images as described in (a) as a function of the nominal wetting angle (β) used to produce the Surface Evolver model. Black line represents $\beta^* = \beta$. (d) Same as (c), except includes data from triangular cross-sections with rounded corners illustrated in (b).

7.1.4. Liquid/solid interface morphology

Because some nanowires have been observed to have a single tilted facet at the edge of the liquid/solid interface, as in Figure 7-4, we investigated the effect that this would have on the validity of our Surface Evolver model. We compared the results for a flat hexagonal cross-section with those for a hexagonal cross-section that contains one tilted facet at the edge of the liquid/solid interface, as shown in Figure 7-6. It is apparent that there is little effect of this additional facet on either seed morphology or $f(\beta)$. Thus the presence of such a facet would have minimal effect on our calculations for diameter-modulated InN and GaN nanowires.

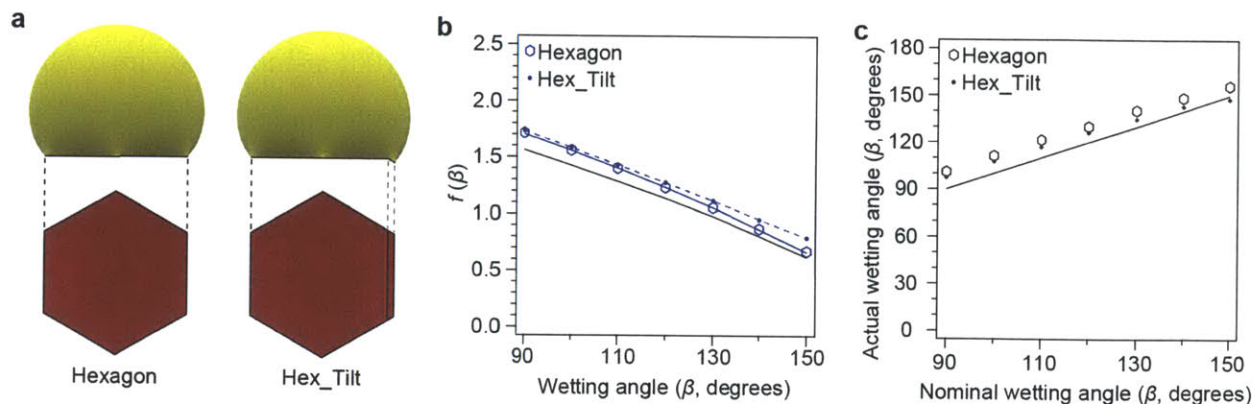


Figure 7-6. Effect of extra tilted facet at liquid/solid interface edge on seed morphology. (a) Comparison of a flat hexagonal cross-section with one that has an extra tilted facet inclined at 30° . (b) Ratio of nanowire diameter to seed particle volume as a function nominal wetting angle. Solid black line represents Equation 7-1. Solid and dashed blue lines indicate $f(\beta)$ for the flat and tilted cross-sections, respectively, which were fit empirically with quadratic equations. (c) Comparison of actual wetting angle (β^*) at edges and corners as measured from Surface Evolver images to nominal wetting angle (β) input into the Surface Evolver model. Black line represents $\beta^* = \beta$. See Figure 7-5 for more details.

7.2. Factors affecting diameter modulation

Experimental results from diameter-modulated InN and GaN nanowires were analyzed using the model described above. Furthermore, diameter modulation maps were constructed that illustrate different combinations of changes in seed composition and wetting angle that can be used to achieve specific diameter ratios. For InN nanowires, changes in nanowire diameter were driven primarily by changes in seed particle volume. Nonetheless, somewhat larger diameter ratios were achieved in triangular nanowires due to greater contributions from changes in wetting angle. For GaN nanowires, diameter ratios in excess of 2 were achieved due to large changes in seed particle volume, as well as significant contributions from changes in wetting angle.

7.2.1. InN nanowires and the role of cross-sectional geometry

Diameter-modulated InN nanowires were fabricated by the same technique described in Chapter 6, initially flowing 300 sccm NH_3 and then reducing the flow to 25 sccm NH_3 to produce an increase in diameter. The diameter in the thin (d_1) and thick (d_2) regions were measured from TEM images, while the volume (V) was calculated from EDS measurements of seed particle composition using Equation 7-2. Based on these measurements, $f(\beta)$ was calculated

from Equation 7-5, and the nominal wetting angle (β) was determined using Surface Evolver (Figure 7-2b). We compared the results for [0001] *c*-InN and [1-100] *m*-InN nanowires, which have hexagonal and triangular cross-sections, respectively.⁶¹ Furthermore, we evaluated the “cylindrical assumption” used in Equation 7-1 by using average measurements from *c*- and *m*-InN nanowires and assuming a circular cross-section. The results of these calculations are summarized in Table 7-1.

Table 7-1. Parameters for thin (d_1) and thick (d_2) segments of diameter-modulated InN nanowires with different cross sections.

	units	Circular		Hexagonal		Triangular	
		Thin	Thick	Thin	Thick	Thin	Thick
d	Nm	74 ± 6	99 ± 10	74 ± 4	96 ± 6	75 ± 8	105 ± 12
x_{In}	at.%	50 ± 7	71 ± 6	49 ± 6	71 ± 7	50 ± 9	72 ± 2
V	nm ³	2.9×10^5	5.5×10^5	2.9×10^5	5.4×10^5	2.9×10^5	5.6×10^5
β	°	121	115	127	123	128	122
$f(\beta)$	-	1.13	1.22	1.12	1.18	1.14	1.27
$(V_2/V_1)^{1/3}$	-		1.24		1.24		1.25
$f(\beta_2)/f(\beta_1)$	-		1.08		1.05		1.12

Furthermore, we evaluated different possible combinations of changes in diameter and wetting angle to achieve different diameter ratios (d_2/d_1) using the following equation:

$$\frac{d_2}{d_1} = \left(\frac{V_2}{V_1} \right)^{1/3} \frac{f(\beta_2)}{f(\beta_1)} \quad (7-6)$$

Note that the parameters $(V_2/V_1)^{1/3}$ and $f(\beta_2)/f(\beta_1)$ correspond to the separate contributions from changes in seed particle volume and wetting angle, respectively, to the changes in nanowire diameter (see Figure 7-7a). To produce the diameter modulation maps in Figure 7-7b-d, we used experimental measurements from the thin-diameter regions to determine d_1 , V_1 , and $f(\beta_1)$. Then, we calculated the changes in wetting angle and composition necessary to achieve particular diameter ratios using Equation 7-6. For comparison, we plotted our experimental results on top of the diameter modulation maps.

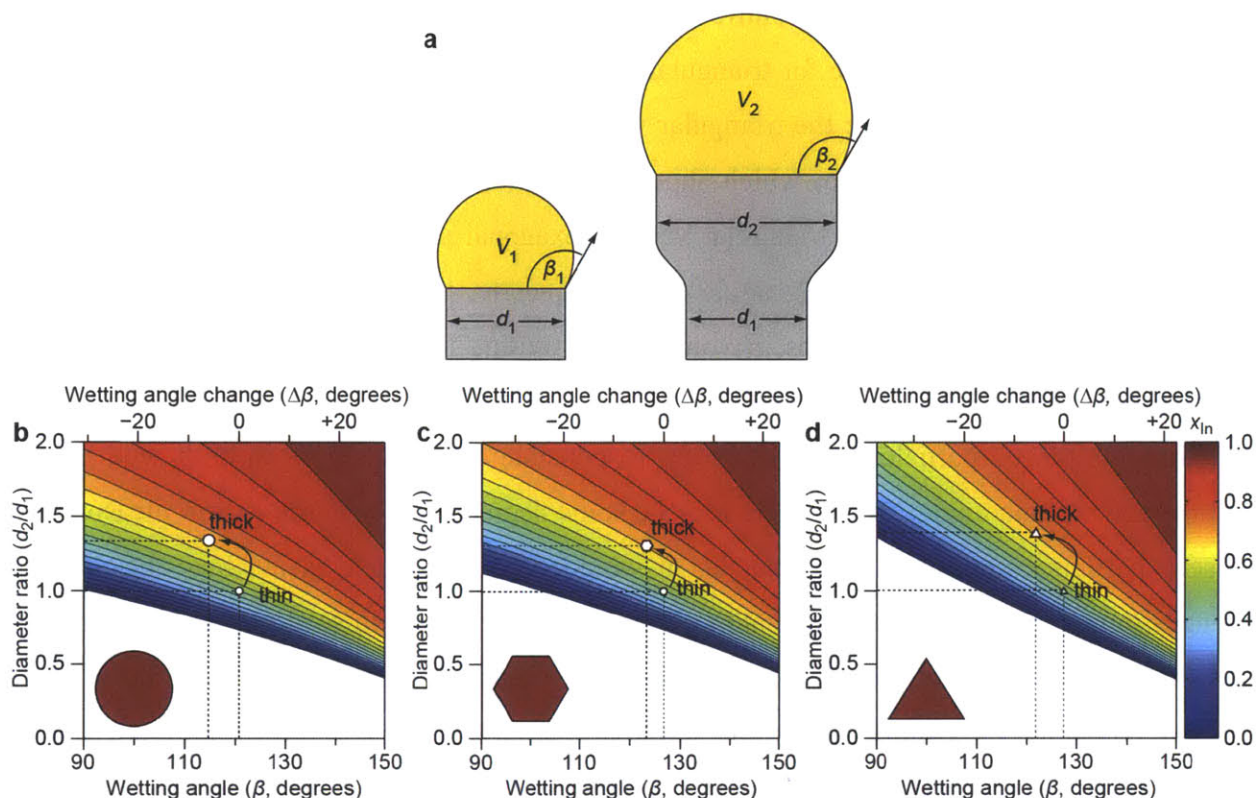


Figure 7-7. Diameter modulation maps of InN nanowires with different cross-sections. (a) Relevant parameters for diameter modulation, shown here for cylindrical nanowires (gray) and corresponding seed particles (yellow) before (left) and after (right) diameter modulation. Diagrams illustrate the diameter (d), volume (V), and wetting angle (β_1) for both the thin (1) and thick (2) segments. (b–d) Diameter modulation maps for circular (b), hexagonal (c), and triangular (d) cross sections. Points on the map indicate experimentally measured values from the thin-diameter (small symbols) and thick-diameter (large symbols) segments of InN nanowires. Top axis indicates the change in wetting angle ($\Delta\beta$) from the thin to the thick segment.

The results demonstrate the importance of accounting for the cross-sectional shape of the nanowire and the associated three-dimensional shape of the seed particle. First, while the calculated wetting angles for the hexagonal and triangular InN nanowires were very similar ($\beta_1 = 127^\circ$ and 128° , respectively), the assumption of a circular geometry yielded a much lower wetting angle ($\beta_1 = 121^\circ$). Additionally, the triangular *m*-InN nanowires yielded a slightly larger average diameter ratio ($d_2/d_1 = 1.40 \pm 0.09$) than for the hexagonal *c*-InN nanowires ($d_2/d_1 = 1.30 \pm 0.06$) despite both having very similar seed particle volumes and wetting angles. In both cases, the change in diameter was driven primarily by an increase in seed particle volume (25% and 24% volume-driven diameter increase for triangular and hexagonal nanowires, respectively).

However, the lesser but notable contribution from changes in wetting angle (12% and 5% wetting-driven diameter increase for triangular and hexagonal nanowires, respectively) accounts for the larger diameter ratio for the triangular versus hexagonal nanowires. This difference can be understood from Figure 7-2b, which shows that similar changes in wetting angle produce greater changes in diameter for triangular versus hexagonal nanowires. Notably, this effect is most significant at smaller wetting angles. Consequently, triangular nanowires yield greater diameter ratios for similar changes in volume and wetting angle compared to hexagonal and circular nanowires (Figure 7-7b-d).

Changes in seed particle composition are responsible for the changes in both seed particle volume and wetting angle. While there may be some degree of error in the *ex situ* measurement of seed particle composition, we find that it would be unreasonable to attribute the diameter changes to changes in wetting angle alone, as significant changes in seed particle composition, and therefore volume, are necessary to produce the observed diameter changes. To illustrate this, we compared the changes in volume alone (i.e. assuming $\Delta\beta = 0$) and wetting angle alone (i.e. assuming $\Delta V = 0$) that would have been necessary to produce the observed changes in nanowire diameter. Table 7-2 shows these calculations for hexagonal InN nanowires. For the latter assumption in which $\Delta V = 0$, the required changes in wetting angle (and therefore surface energy, σ) would need to be significant despite a minimal change in composition. Therefore, it is clear that the diameter changes were driven primarily by changes in seed particle volume.

Table 7-2. Required changes in volume and wetting angle for observed changes in diameter of hexagonal InN nanowires

		Thin	Thick		
			exp.	$\Delta\beta = 0$	$\Delta x = 0$
d	nm	74 ± 4	96 ± 6	96	96
x_{In}	at.%	49 ± 6	71 ± 7	74	49
V	nm ³	2.9×10^5	5.4×10^5	6.3×10^5	2.9×10^5
B	°	127	123	127	107
$f(\beta)$	-	1.12	1.18	1.12	1.46
$(V_2/V_1)^{1/3}$	-		1.24	1.30	1.00
$f(\beta_2)/f(\beta_1)$	-		1.05	1.00	1.30

7.2.2. GaN nanowires and the role of seed particle composition

In the case of InN nanowires, the maximum observed diameter ratio was 1.5, but significantly higher diameter ratios should be achievable by the flow-controlled diameter modulation approach. In fact, we produced diameter ratios in excess of 2 with GaN nanowires, which were fabricated in the same manner as those in Chapter 6. The nanowires were grown at 850°C using 1 nm Au films on [1-102] *r*-sapphire substrates, and diameter modulation was achieved by reducing the Ga flux during growth, producing an average diameter ratio of 1.9 ± 0.2 between the thick and thin segments. Figure 7-8a shows a GaN nanowire with a diameter ratio of 2.2. The diameter modulation map in Figure 7-8b was produced using Equation 7-6 based on measured values of diameter (d_1) and composition (x_{Ga}) from the thin-diameter region of the GaN nanowires. Equations 7-2 and 7-5 were used to calculate V_1 and $f(\beta_1)$, respectively, while β_1 was determined using the fitting equation in Figure 7-2b for a triangular cross-section in accordance with our previous observations.^{61,104}

The composition of the seed was measured in the same manner as for InN nanowires, described previously in section 6.1.2.⁶¹ However, because thin films were used instead of colloids with known diameters, the calculation of seed particle volume was instead based upon the measured area of the seed particle using Equation 7-3, which is a similar approach to that reported by Wallentin *et al.*⁹¹ The measured composition of Ga in the thin-diameter region was 28 at.% Ga, according to *ex situ* EDS measurements. However, reliable measurements of the seed particle composition were difficult to obtain for the thick-diameter regions due to the high Ga supersaturation, which led to significant extraction of Ga from the seed during the relatively long cooling period for GaN versus InN (growth temperatures of 850 versus 560°C, respectively) to form GaN, instead of Ga₂O₃. The continued growth of GaN during cooling makes it difficult to differentiate between Ga originally present in the seed before cooling and Ga that continued to incorporate and promote growth during cooling. This post-growth Ga extraction was evident from a large degree of necking at the tip of the nanowire. In the absence of reliable EDS measurements, the composition and wetting angle of the seed particle in the thick-diameter regions was instead extracted using the diameter modulation map in Figure 7-8b.

[The greater diameter modulation in GaN versus InN nanowires was due in part to the lower group-III seed composition (x_{III}) in the thin-diameter regions (28 at.% Ga versus 50 at.% In, respectively). As shown in Figure 7-8c, a lower thin-diameter seed composition allows greater

volume-driven diameter changes for the same thick-diameter seed composition. Nonetheless, to achieve a diameter ratio of 2.2 with a constant wetting angle, the thick-diameter seed particle composition would need to be about 93 at.% Ga. Such a high composition is unlikely because of the significant amount of Ga that must be incorporated into the seed particle (Figure 7-8c, inset) despite the fact that the extraction rate of Ga out of the seed particle increases as the Ga composition increases (section 6.2).

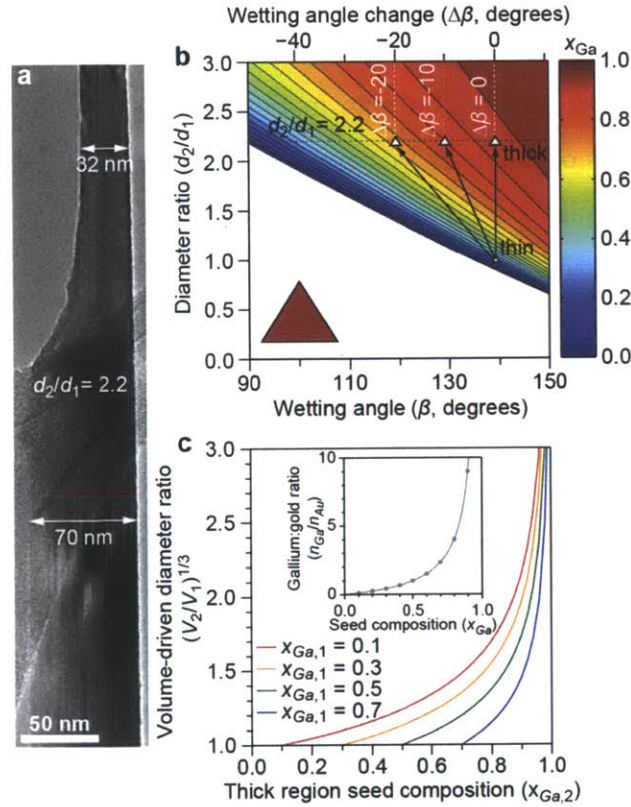


Figure 7-8. GaN nanowires with large diameter ratios. (a) TEM image of a GaN nanowire with a diameter ratio of 2.2. (b) Diameter modulation map for GaN nanowires based on measurements from thin-diameter region. Points on map indicate measured conditions in thin-diameter region (small triangles), as well conditions in the thick-diameter region (large triangles) for a diameter ratio of 2.2 assuming a change in wetting angle ($\Delta\beta$) of 0, -10, and -20°. (c) Volume changes $(V_2/V_1)^{1/3}$ as a function of thick-diameter composition ($x_{Ga,2}$) for different thin-diameter compositions ($x_{Ga,1}$) assuming only volume changes, without any contribution from changes in wetting angle. Inset shows molar ratio of Ga to Au (n_{Ga}/n_{Au}) in the seed particle as a function of Ga composition.

To estimate the seed composition in the thick-diameter region, we calculated the required seed particle composition for a different thick-diameter wetting angles. For a change in wetting

angle ($\Delta\beta$) of -10° and -20° , the required thick-diameter seed composition would be 85 and 73 at.% Ga, respectively (Figure 7-8b and Table 7-3). As shown in the inset of Figure 7-8c, nearly 5 times less total Ga is required to reach $x_{Ga} = 0.93$ versus $x_{Ga} = 0.73$, which is similar to the thick-diameter composition for InN nanowires ($x_{In} = 0.71$). Therefore the calculated seed particle composition is much more reasonable for significant changes in wetting. Thus the low composition in the thin-diameter region not only allows large changes in volume with composition but also greater changes in wetting angle due to the changes in the composition-dependent surface energies that define it.

Table 7-3. Parameters for diameter-modulated GaN nanowires

		Thin	Thick		
			$\Delta\beta = 0^\circ$	$\Delta\beta = -10^\circ$	$\Delta\beta = -20^\circ$
d	nm	31.8	69.7	69.7	69.7
x_{In}	at.%	28 ± 4	93	85	73
V	nm ³	5.1×10^4	5.4×10^5	2.6×10^5	1.4×10^5
β	°	139	139	129	119
$f(\beta)$	-	0.86	0.86	1.09	1.34
$(V_2/V_1)^{1/3}$	-		2.19	1.72	1.40
$f(\beta_2)/f(\beta_1)$	-		1.00	1.27	1.56

7.3. Morphology of the liquid/solid interface

In this section, the model above is extended beyond diameter modulation and applied to evaluate the liquid/solid interface morphology and surface energy. As stated previously, the wetting angle of the seed particle depends on the surface energies of the seed particle and nanowire. In this section, we calculate these surface energies for our InN and GaN nanowires assuming three different potential liquid/solid interface morphologies. Although a flat liquid/solid interface has been commonly assumed in many nanowire investigations, the force balances are not upheld for our nanowires, and a relatively low liquid/solid interface energy is calculated. However, when a faceted or rounded interface morphology is assumed, the forces are in equilibrium, and the calculated liquid/solid interface energy is consistent with expected values. Additionally, the evolution of the nanowire diameter is modeled for each interface morphology. An accurate fit with experimental results is obtained when a faceted or rounded interface is assumed.

7.3.1. Potential morphologies

We consider three different liquid/solid interface morphologies in our analysis (Figure 7-9). Although the liquid/solid (l/s) interface has often been assumed to be flat with sharp corners (Figure 7-9b),⁸⁹⁻⁹¹ recent theoretical⁹⁷⁻¹⁰⁰ and experimental^{7,95,96} reports have challenged this assumption. Oh *et al.* performed *in situ* TEM analysis of growing Al_2O_3 nanowires via Al seed particles and observed a faceted interface morphology (Figure 7-9c) with atomic-scale resolution.⁹⁶ Although those nanowires were observed to have a similar structure at each facet, other authors performing *in situ* TEM nanowire growths have observed a faceted morphology at just one facet, while the l/s interface morphology at the other facets was unclear.^{7,95} Some theoretical studies have suggested that the interface morphology should be faceted,^{97,98} while another has suggested that the corners should be rounded at some length scale (Figure 7-9d) because high facet curvature should be unfavorable.⁹⁹ Therefore flat, faceted, and rounded interface morphologies are all considered in the analysis below.

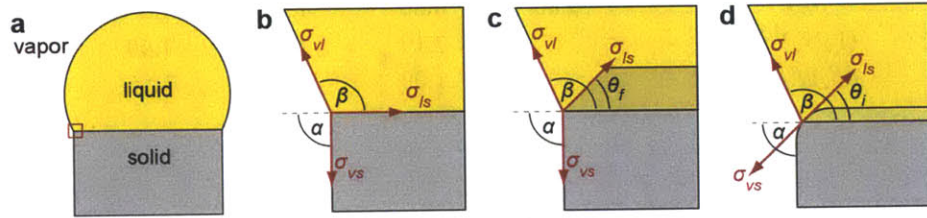


Figure 7-9. Surface energies and force balances at the triple-phase boundary for different liquid/solid interface morphologies. (a) Macroscopic view of a cylindrical nanowire and seed particle. (b–d) Models for calculating surface energies for different nanoscopic morphologies near the vapor/liquid/solid interface, zoomed in at red box in (a): flat with a sharp corner (b), faceted with a sharp corner (c), or inclined along a rounded corner (d). Shaded areas between the nanowire and seed particle indicate the portions of the nanowire that are encapsulated within the seed particle. Figures show the steady-state case in which $\alpha = 90^\circ$.

7.3.2. Force balances

It is possible to extract the l/s interfacial energy (σ_{ls}) by knowing the nominal wetting angle (β), the energies of the vapor/solid (σ_{vs}) and vapor/liquid (σ_{vl}) interfaces, and the force balance at triple-phase boundary (TPB; red box in Figure 7-9a), which depends on the morphology of the

triple-phase boundary. The force balances for flat, faceted, and rounded interfaces are illustrated in Figure 7-9b-d and evaluated below.

For a flat liquid/solid interface, the force balance along l/s surface is as follows

$$\sigma_{ls} = \sigma_{vs} \cos(\alpha) - \sigma_{vl} \cos(\beta) \quad (7-7a)$$

where α is the inclination angle between the vapor/solid (v/s) and l/s interfaces (Figure 7-9b). When the diameter remains constant during steady-state growth, $\alpha = 90^\circ$, and Equation 7-7a reduces to

$$\sigma_{ls} = -\sigma_{vl} \cos(\beta) \quad (7-7b)$$

This condition is only met when $\beta \geq 90^\circ$ and $\sigma_{vl} > \sigma_{ls}$. Additionally, the force balance along the vapor/solid interface can be written as

$$\sigma_{vs} = \sigma_{vl} \cos(\beta - \alpha) + \sigma_{ls} \cos(\alpha) \quad (7-8a)$$

When $\alpha = 90^\circ$, the condition is only met when $\sigma_{vl} \geq \sigma_{vs}$.

$$\sigma_{vs} = \sigma_{vl} \sin(\beta) \quad (7-8b)$$

For InN and GaN nanowires seeded by Au particles, $\sigma_{vl} < \sigma_{vs}$, indicating that Equation 7-8b cannot be satisfied. A similar criterion was developed by Nebol'sin and Shchetinin from energetic considerations assuming a flat l/s interface, suggesting that $1.41\sigma_{vl} \geq \sigma_{vs}$ for stable nanowire growth,²⁰⁷ a condition that is also not upheld here. Therefore, it is likely that the l/s interface is not flat, contrary to the common assumption for nanowire growth models.

For the faceted interface morphology, we assume that all edges are faceted at some length scale with an inclination angle of θ_f (Figure 7-9c). In this case, the force balances along the l/s and v/s surfaces at the TPB are, respectively:

$$\sigma_{ls} = \sigma_{vs} \cos(\alpha - \theta_f) - \sigma_{vl} \cos(\beta - \theta_f) \quad (7-9)$$

$$\sigma_{vs} = \sigma_{vl} \cos(\beta - \alpha) + \sigma_{ls} \cos(\alpha - \theta_f) \quad (7-10)$$

The values of θ_f and σ_{ls} can be determined by solving Equations 7-9 and 7-10 together such that both conditions are met.

For the rounded interface morphology, we assume that the edge of the seed particle intersects the rounded corner at some inclination angle (θ_i) such that $0^\circ \leq \theta_i \leq 90^\circ$ (Figure 7-9d). The force balance here takes the standard form of Young's equation:

$$\sigma_{ls} = \sigma_{vs} + \sigma_{vl} \cos(\beta - \theta_i) \quad (7-11)$$

The value of σ_{ls} was calculated such that the minimum total surface energy for σ_{ls} occurs at the measured value of β . Notably, for all conditions here, total surface energy was minimized when $\theta_i = 90^\circ$. However, θ_i may be less than 90° as σ_{vl} approaches σ_{vs} .

7.3.3. Surface energies

Using the equations above, it is possible to calculate σ_{ls} for each of the interface morphologies in Figure 7-9. The values of β and σ_{vs} are determined from our experimental data and literature,^{189,208} respectively, for our InN and GaN nanowires. The value of σ_{vs} is assumed to be independent of facet orientation. To calculate σ_{vl} , we account for the migration of low-surface-energy elements to the liquid surface by solving the following equation

$$\sigma_{Au-i} = \sigma_{Au} + \frac{RT}{1.091N_A^{1/3}\bar{V}_{Au}^{2/3}} \ln\left(\frac{1-x_i^s}{1-x_i}\right) = \sigma_i + \frac{RT}{1.091N_A^{1/3}\bar{V}_{Au}^{2/3}} \ln\left(\frac{x_i^s}{x_i}\right) \quad (7-12)$$

where σ is vapor/liquid surface energy,¹⁹⁵ R is the gas constant, T is temperature, i is either In or Ga, N_A is Avogadro's number, \bar{V} is the molar volume,¹⁹⁵ and x_i^s is the concentration of element i at the liquid surface.²⁰⁹ Because Equation 7-8b is not upheld, only Equation 7-7b was used to calculate σ_{ls} for the flat interface, considering that perhaps the v/s force balance may not need to be upheld since the seed is not in contact with the nanowire sidewall.

The calculated values of σ_{ls} for both InN and GaN nanowires are shown in Table 7-4. For InN, the calculated value of σ_{ls}/σ_{vs} for liquid Au-In on solid InN for the flat, faceted, and rounded interfaces is approximately 23%, 70%, and 66%, respectively. While there is a lack of reported data for σ_{ls}/σ_{vs} for liquid In on InN, this value was determined to be about 70% for liquid Si on solid SiC⁸⁶ and 60% for liquid Ga on solid GaAs.⁸⁵ While calculated values of σ_{ls} for the faceted and rounded interfaces are consistent with expected values based on reported results from elemental liquids on compound semiconductors, the values for the flat interface seem quite low. Interestingly, the values of σ_{ls} also remained relatively constant between the thin and thick regions for both the faceted and rounded models.

Because of the similarities in calculated surface energy, we cannot distinguish between the faceted and rounded models from this analysis. However, based on both the force balance and calculated surface energies, our results do suggest that the l/s interface is either faceted or rounded, but not flat. Because Equation 7-7b requires that $\sigma_{vl} \geq \sigma_{vs}$, a condition that is rarely upheld even in other materials systems, it is generally unlikely that a flat liquid solid interface

would be stable. Furthermore, because similar wetting angles have been observed in other materials with similar σ_{vl} and σ_{vs} , the flat interface model would generally yield unreasonably low values calculated value for σ_{ls} .

Table 7-4. Surface energies during diameter-modulated InN and GaN nanowire growth.

		<i>c</i> -InN		<i>m</i> -InN		<i>m</i> -GaN	
		thin	thick	Thin	Thick	Thin	thick $\Delta\beta = -20^\circ$
β	$^\circ$	127	123	128	122	139	119
σ_{vs}	J/m ²	1.40	1.40	1.40	1.40	2.00	2.00
σ_{vl}	J/m ²	0.59	0.55	0.59	0.55	0.88	0.68
σ_{ls}^{flat}	J/m ²	0.35	0.30	0.36	0.29	0.67	0.33
σ_{ls}^{facet}	J/m ²	0.99	0.98	1.00	0.97	1.58	1.45
σ_{ls}^{round}	J/m ²	0.92	0.94	0.93	0.93	1.43	1.41

7.3.4. Nanowire diameter evolution

The mechanism of diameter modulation and *l/s* interface morphology were further evaluated by modeling the evolution of nanowire growth stepwise and comparing it to experimental results for InN nanowires. The step length (ΔL) was kept constant, and the extraction rate (E), incorporation rate (I), seed composition (x_{III}), volume (V), wetting angle (β), inclination angle (α), surface energies (σ), axial position (L), diameter (d), and time (t) were all calculated for each step (see section 3.4.2). To simplify the model, the extraction rate, incorporation rate, and surface energy of the seed were calculated based on empirical measurements. For InN nanowires, these values were calculated as follows

$$E = \left(\frac{v_2 - v_1}{N_2 - N_1} \right) N + \left[v_2 - \left(\frac{v_2 - v_1}{N_2 - N_1} \right) N \right] = m_E N + b_E \quad (7-13)$$

$$I = \left(\frac{v_2 - v_1}{x_{III,2} - x_{III,1}} \right) x_{III} + \left[v_2 - \left(\frac{v_2 - v_1}{x_{III,2} - x_{III,1}} \right) x_{III,2} \right] = m_I x_{III} + b_I \quad (7-14)$$

$$\sigma_i = \left(\frac{\sigma_{i,2} - \sigma_{i,1}}{x_{III,2} - x_{III,1}} \right) x_{III} + \left[\sigma_{i,2} - \left(\frac{\sigma_{i,2} - \sigma_{i,1}}{x_{III,2} - x_{III,1}} \right) x_{III,2} \right] = m_\sigma x_{III} + b_\sigma \quad (7-15)$$

where v is the measured growth rate for the thin (1) and thick (2) regions of InN nanowires, N is the flow rate of NH₃, i represents either the vapor/liquid (*vl*) or liquid/solid interface (*ls*), and

both m and b are constants calculated from experimental measurements. Put simply, the extraction rate was assumed to be directly dependent upon the NH_3 flux, while the incorporation rate and seed surface energies were assumed to be dependent upon the seed composition.

For GaN, the extraction rate, incorporation rate, and surface energies were calculate as follows

$$E = \left(\frac{v_2 - v_1}{x_{III,2} - x_{III,1}} \right) x_{III} + \left[v_2 - \left(\frac{v_2 - v_1}{x_{III,2} - x_{III,1}} \right) x_{III} \right] = m_E x_{III} + b_E \quad (7-16)$$

$$I = \left(\frac{v_2 - v_1}{H_2 - H_1} \right) H + \left[v_2 - \left(\frac{v_2 - v_1}{H_2 - H_1} \right) H \right] = m_I H + b_I \quad (7-17)$$

$$\sigma_i = \left(\frac{\sigma_{i,2} - \sigma_{i,1}}{x_{III,2} - x_{III,1}} \right) x_{III} + \left[\sigma_{i,2} - \left(\frac{\sigma_{i,2} - \sigma_{i,1}}{x_{III,2} - x_{III,1}} \right) x_{III,2} \right] = m_\sigma x_{III} + b_\sigma \quad (7-18)$$

where H is the flow rate of H_2 through the Ga-coated quartz tube injector. Different values of m and b here were calculated here based on measurements of GaN nanowires assuming a wetting angle change of 20° from the thick to thin region (Figure 7-8b and Table 7-3). In this case, the incorporation rate was assumed to be directly controlled by the Ga flux, while the extraction rate and surface energies were assumed to be dependent upon the seed composition.

For both GaN and InN nanowires, the model was applied using each of the three l/s interface morphologies in Figure 7-9 assuming that the the force balance of the seed particle was upheld at all times, and the results of the theoretical model were compared to results from actual nanowires (Figure 7-10). For the faceted and rounded interface models, the results of the model fit well the observed nanowire diameter evolution for both single (Figure 7-10a) and multiple (Figure 7-10b) changes in NH_3 flux for InN nanowires, as well as a reduction in Ga flux for GaN nanowires (Figure 7-10c). However, the flat interface model produced a relatively slow diameter evolution that provided a poor fit with experimental observations, particularly in Figure 7-10c. These results further indicate that the l/s interface is likely not flat. While nanowires with faceted or rounded l/s interfaces can readily accommodate changes in seed particle volume and wetting angle, nanowires with flat interfaces would not be able to respond as rapidly. Additionally, these results provide strong evidence in support of the proposed diameter evolution model described in Chapter 6.

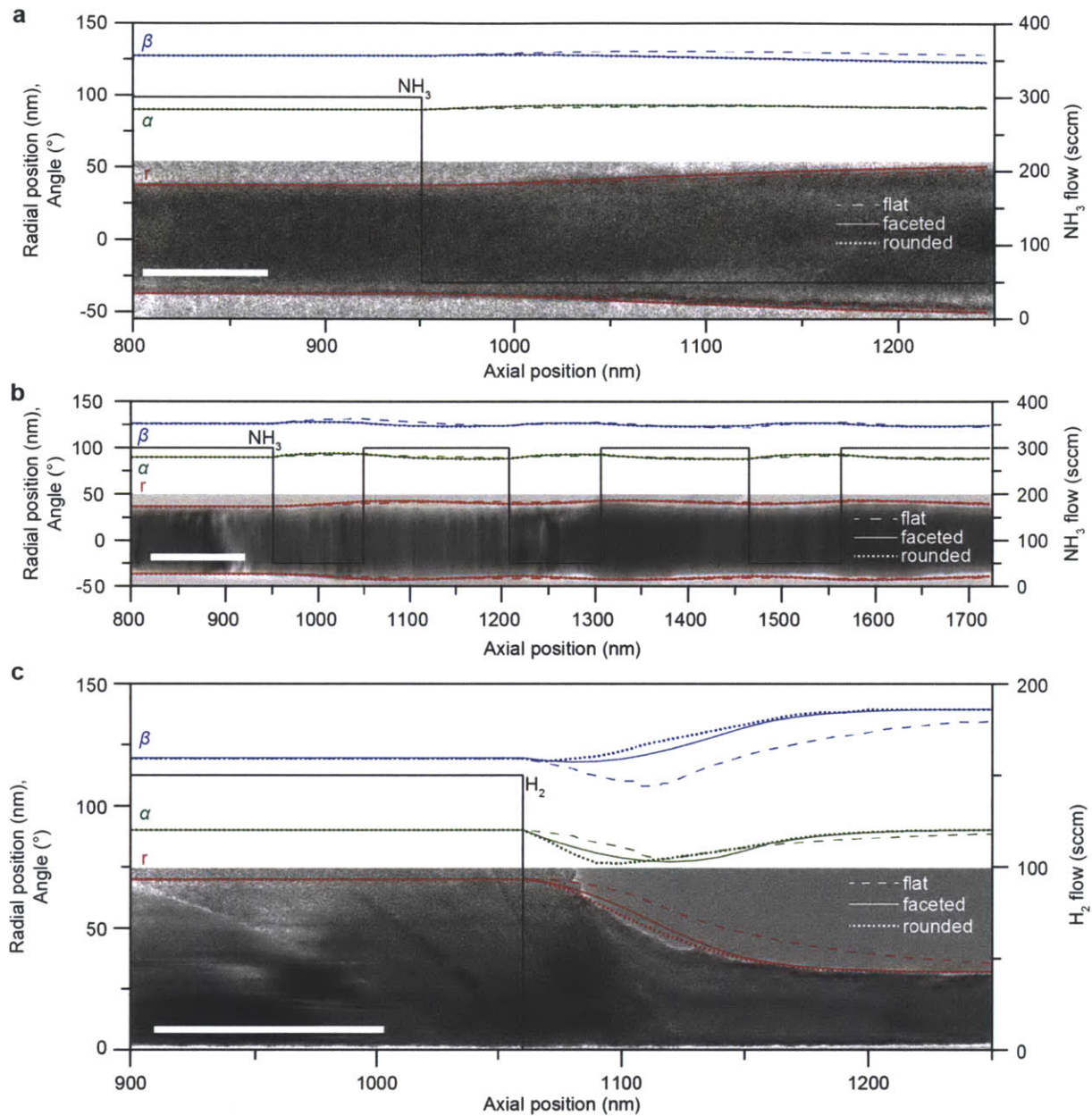


Figure 7-10. Evolution of III-V nitride nanowire diameter via varied precursor flux. (a–c) Plot of nanowire diameter evolution for a triangular *m*-InN nanowire with a single reduction in NH_3 flow (a), a hexagonal *c*-InN nanowire with multiple variations in NH_3 flow (b), and a triangular *m*-GaN nanowire with a single reduction in Ga flux (c). In (c) the Ga flux was controlled by the H_2 flow through the Ga-coated injector. TEM images provide a comparison of the model with experimental results. Images were scaled to match the diameter used in the model. Scale bars represent 100 nm.

7.4. Opportunities, limitations, and the role of materials selection

Based on the analysis above, general guiding principles for template-free modulation of nanowire diameter can be developed. First, greater diameter ratios are possible for seed materials that can promote nanowire growth over a large range of supersaturation, which results in large changes in seed particle volume. However, as discussed previously, adding large amounts of alloying elements into an already highly supersaturated seed particle is challenging due to the high extraction rate of those elements out of the seed particle, limiting the upper achievable seed composition. Consequently, achieving large diameter ratios in excess of 2 requires significant changes in wetting angle. In the case of GaN nanowires, the large variation in seed composition produced significant changes in both seed volume and wetting angle, resulting in diameter ratios as high as 2.2.

Using the l/s interface models developed in section 7.3, it is possible to evaluate how seed material selection can be used to achieve greater wetting-driven diameter ratios. According to the flat interface model in Figure 7-9b, a large thin-diameter wetting angle resulting from a lower ratio of σ_{vl}/σ_{ls} would make the nanowire diameter more sensitive to changes in surface energy (Figure 7-11a). Thus, selecting seed materials with lower surface energy (σ_{vl}) would facilitate greater changes in nanowire diameter. However, assuming constant σ_{ls} for the faceted and rounded interface models (Figure 7-11b), greater reductions in σ_{vl} with increasing composition of the alloying precursor element should yield greater changes in nanowire diameter. Because the analysis in section 7.3 indicates that the interface is likely not flat, it is therefore reasonable to suggest that selection of seed materials with high σ_{vl} that form alloys in which σ_{vl} decreases more linearly with composition would produce greater changes in nanowire diameter. This is consistent with the fact that changes in wetting angle had a greater contribution to the observed diameter changes for GaN nanowires than for InN nanowires. Additionally, it is worth noting that it may be possible to use foreign elements to alter interfacial energies.^{19,21} Of course other factors must also be considered in seed material selection, including other potential effects on nanowire structure and morphology. For example, as described in section 4.3, Ni seeds can substantially reduce stacking fault density versus Au-seeded GaN nanowires.

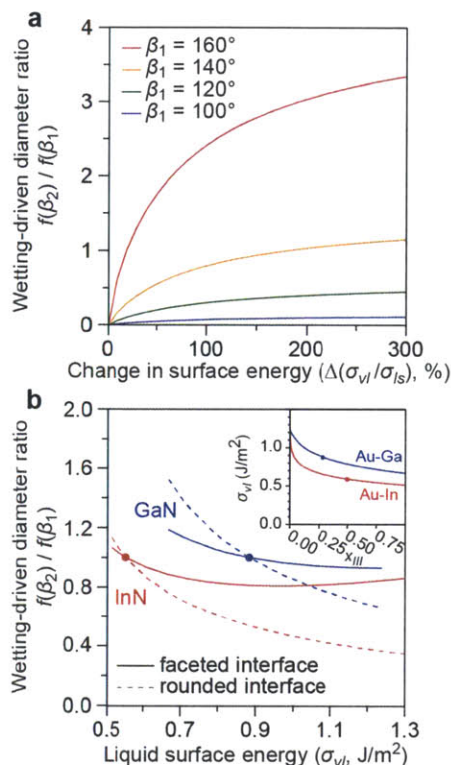


Figure 7-11. Contributions of changes in surface to changes in nanowire diameter. (a) Changes in nanowire diameter as a function of relative surface energy for different thin-diameter wetting angles, assuming a flat liquid/solid interface. $f(\beta_2)/f(\beta_1)$ indicates diameter ratio that would be expected from changes in surface energy alone, without any contribution from changes in seed volume. (b) Changes in nanowire diameter as a function of σ_{vl} for triangular InN and GaN nanowires, assuming a faceted or rounded interface with constant σ_{ls} . Inset shows the change in the surface energy of the seed particle as a function of composition for Au-In and Au-Ga alloys, according to Equation 7-12. Dots correspond to values in thin-diameter region.

Different materials systems may require different strategies for achieving diameter modulation. Because of the low solubility of N in the seed particle,⁶⁸⁻⁷⁰ the III-V nitride system offers a unique ability to separately tune the rates of incorporation of alloying elements into the seed particle and extraction out of the seed particle by modulating the flux of III and V precursors, respectively.⁶¹ Nonetheless, while the solubility of the V element in the seed particle may not be negligible for other III-V materials, the III source is generally the predominant alloying precursor,¹¹⁷ so modulation of incorporation and extraction rates with precursor fluxes should still be possible. However, for elemental nanowires such as Si, other strategies may need to be used to achieve diameter modulation, such as adjusting the seed particle composition via temperature.²¹⁰ In some materials systems, defects such as twins may preferentially form under

certain conditions,⁹² which may place limits on the range of conditions that can be used without diminishing material performance.

The discussion thus far has centered on liquid seed particles, but the seed remains solid in many cases.^{41,65,66} Caroff *et al.* reported InAs/InSb axial heterostructures with a 40% greater diameter for the InSb segment than the InAs segment, which had seed compositions of 67 and 30 at.% In, respectively. The calculated volume changes alone accounted for a 35% increase in diameter, indicating that the diameter changes were driven primarily by changes in seed particle volume. While continuous diameter modulation should be possible for solid solutions, compound-forming alloys might limit the nanowire diameter to a discrete range of values. However, in order to model the diameter modulation potential using Equation 7-6, different models that account for changes in the three-dimensional shape of solid seed particles would be necessary to determine $f(\beta)$.

7.5. Summary

Experimental results from diameter-modulated InN and GaN nanowires were analyzed using a theoretical model that was developed to include the effects of changes in the volume, wetting angle, and three-dimensional morphology of the seed particle on nanowire diameter. The accuracy of the model was confirmed via comparison with *in situ* TEM studies by other authors. The shape of the nanowire cross-section can significantly impact the dependence of nanowire diameter on wetting angle, particularly for low wetting angles. As demonstrated with GaN nanowires, large diameter ratios require significant changes in both the volume and wetting angle of the seed particle. Therefore, for large diameter ratios, seed metals should be chosen that can promote nanowire growth over a large range of nanowire composition and result in significant reductions in seed surface energy as the composition of alloying elements in the seed increases.

The information extracted from these models allowed calculation of the liquid/solid surface energy. The calculated surface energy was dependent upon the assumed morphology of the liquid/solid interface near the TPB. Under the assumption of a flat interface with sharp corners, the force balance at the TPB was not upheld, very low liquid/solid surface energies were calculated, and the nanowire could not readily change diameter to accommodate changes in seed particle volume and surface energy. On the other hand, both faceted and rounded TPB morphologies allow stable seed particles at reasonable liquid/solid surface interface energies.

Furthermore, the modeled evolution of nanowire diameter is consistent with experimental results. While the faceted and rounded models could not be differentiated from these studies, the models developed here can be paired with *in situ* TEM investigation to provide clarity into the nanoscopic structure of the liquid/solid interface near the TPB, which has significant implications for particle-mediated nanowires, including the fundamental growth mechanism, the sharpness of heterointerfaces, the mechanism of twinning, and dopant incorporation.^{4,7}

The model developed here not only explains experimental results with InN and GaN nanowires, but also provides a general foundation for guiding the synthesis of diameter-modulated nanowires in other materials systems. Although elemental nanowires may require alternative diameter modulation strategies, the flow-controlled technique developed in Chapter 6 may be a feasible method of achieving nanowire diameter modulation in a variety of compound semiconductors. In the following chapter, we evaluate the general applicability of the flow-controlled approach by using the same diameter modulation technique with GaAs nanowires.

Chapter 8: Diameter modulation of GaAs nanowires

The experimental demonstration of the diameter modulation technique described in Chapter 6 and the theoretical model developed in Chapter 7 provide a foundation for the fabrication of diameter-modulated nanowires in both III-V nitride and other materials systems. However, as mentioned previously, N is insoluble in Au seed particles that were used in those studies,⁶⁸⁻⁷⁰ which allowed the group III and N precursors to control the rates of III source incorporation into the seed particle and extraction out of the seed particle, respectively. In other III-V nanowire materials, the solubility of the V source (e.g. As, P, Sb) is generally low but not necessarily negligible. For example, Au seed particles may hold up to 3% As.²¹¹ However, the composition of the III elements in the seed is generally much greater than the V elements, so it is possible that our flow-controlled approach could be applied to other compound semiconductor nanowires and yield similar trends in diameter and growth rate with changes in the III and V flows.

To investigate the potential of the flow-controlled diameter modulation technique in other materials systems, we varied the flux of both the III and V precursors (TMG and AsH₃, respectively) during the growth of GaAs nanowires, which have a variety of electronic and optoelectronic applications including high electron mobility transistors,²¹² solar cells,²¹³ and lasers.²¹⁴ We successfully induced diameter modulation in these GaAs nanowires, and the trends in both diameter and growth rate are consistent with those observed for InN and GaN nanowires. Three different types of [111]B-oriented GaAs nanowires were obtained on the same substrate with discrete differences in diameter and growth rate. Electron tomography shows that these nanowires have different cross-sectional shapes, which likely stem from differences in the composition and/or phase of the seed particle. By varying the nanowire diameter, substrate orientation, and growth conditions, nanowires of each type were preferentially obtained.

8.1. Diameter modulation with both the III & V sources

Diameter modulation along GaAs nanowires was achieved by varying the flux of both III and V precursors during growth. Consistent with the previous results for InN nanowires, a reduced V flux produced segments with wider diameters and slower growth rates. An increased III flux also produced segments with wider diameters, but with faster growth rates, consistent with the previous results for GaN nanowires. Furthermore, larger diameter ratios were achieved by

varying the flux of both the III and V precursors during growth. Some limitations in the allowable III and V fluxes were observed, such that excessively high V/III ratios induced shell formation on some nanowires, while excessively low V/III ratios yielded a high density of twinning defects.

8.1.1. Diameter modulation with the III & V sources

The GaAs nanowires were synthesized using a cold-walled horizontal-flow MOCVD reactor (see section 3.2) at 420°C and atmospheric pressure. Gold colloids (90 nm) were deposited onto (111)B GaAs substrates, which were then heated under H₂ (15 slpm) and AsH₃ (3.4 sccm) flow. Growth was initiated by the introduction of TMG (0.36 sccm) at a V/III ratio of 9.5. Diameter modulation was achieved by varying the flux of the III and V precursors during growth.

To examine the applicability of the flow-controlled approach developed in Chapter 6 to Au-seeded GaAs nanowires, we varied the flux of the V and III precursors in separate growths. First, an initial 3-min segment at standard AsH₃ and TMG flows (3.4 sccm AsH₃ and 0.36 sccm TMG) was followed by three 1-min segments with 1.1, 3.4, and 0.7 sccm AsH₃, respectively. Consistent with the results for InN nanowires in section 6.1, a reduction in V flow produced segments with wider diameters and slower growth rates (Figure 8-1a). In the next growth, an initial 3-min segment with standard flows (3.4 sccm AsH₃ and 0.36 sccm TMG) was followed by three 1-min segments with 1.1, 0.36, and 1.8 sccm TMG, respectively. As with the GaN nanowires section 6.2, an increased III flux yielded segments with wider diameters and faster growth rates (Figure 8-1b). Because the diameter changes in these nanowires are relatively small (<25%), the SEM images in Figure 8-1 have been stretched in the radial direction to help visualize the diameter expansion. These results confirm that the flow-controlled approach developed for III-V nitride nanowires is applicable in other particle-mediated compound semiconductor nanowires. While the solubility of As in Au is not necessarily negligible, Ga is still the predominant alloying element in Au.^{117,211,215} Thus the same trends in diameter and growth rate are observed with GaAs nanowires as with InN and GaN nanowires, because the III and V sources can still be used to alter the rates of III source incorporation into and extraction out of the seed particle, respectively.

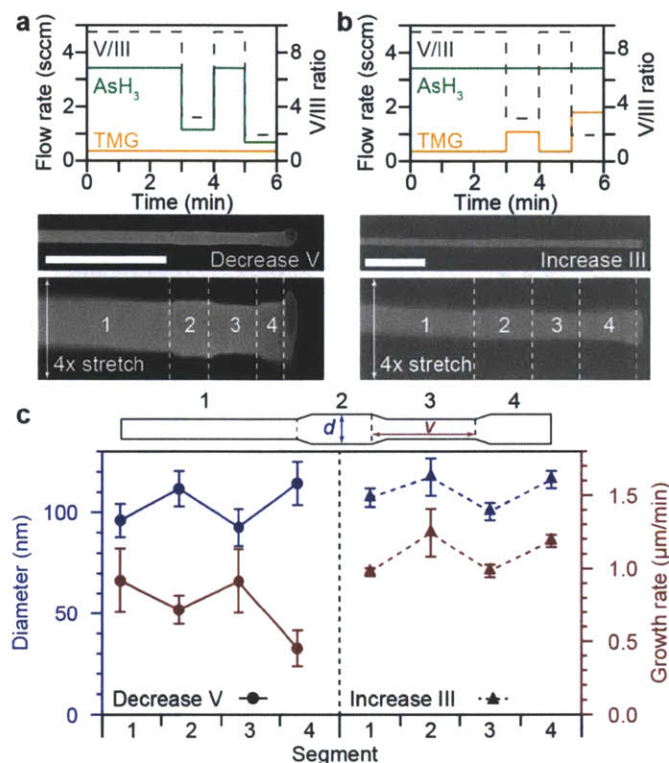


Figure 8-1. Diameter-modulated GaAs nanowires. (a,b) Precursor flow rates (top) and SEM images (bottom) of corresponding SEM images of GaAs nanowires with diameter modulations produced via changes in AsH₃ (a) and TMG (b) flow during growth. One axis of the lower SEM images is stretched to help visualize the changes in diameter. (c) Diameter (d) and growth rate (v) of different segments of individual nanowires as a result of decreasing the V flow and increasing the III flow for the growths in (a) and (b), respectively. The schematic illustrates the measurement of segment diameter and growth rate. Scale bars represent 1 μm.

Notably, we did attempt to measure the *ex situ* seed particle composition in order to assess the relative contributions from changes in both volume and wetting angle. However, reliable measurements could not be obtained. Whether cooled with or without AsH₃ flow, the measured composition of both Ga and As in the Au seed was generally <1%.

To achieve larger diameter modulation, we varied both the III and V precursors in the same growth. In this case an initial 2 min segment at 3.4 sccm AsH₃ and 0.36 sccm TMG was followed by a segment with reduced AsH₃ flow (0.7 sccm AsH₃ and 0.36 sccm TMG for 2 min), then another with reduced TMG flow while maintaining the low AsH₃ (0.7 sccm AsH₃ and 0.07 sccm TMG for 2 min). The resulting nanowires are shown in Figure 8-2. Again, the trends in diameter (d) and growth rate (v) are consistent with expectations (Figure 8-2c). Furthermore, while the diameter ratio between the first and second segments by reducing the AsH₃ flow (d_2/d_1

$= 1.24 \pm 0.07$) was similar to that obtained previously ($d_4/d_3 = 1.25 \pm 0.09$ in Figure 8-1a), the diameter ratio between the second and third segments was significantly greater ($d_2/d_3 = 1.50 \pm 0.13$), indicating that variations in both the V and III flows can be used to achieve greater diameter ratios between different segments.

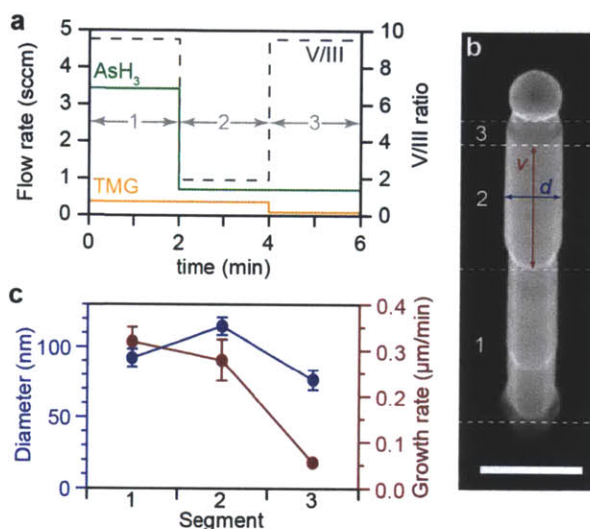


Figure 8-2. Diameter-modulated GaAs nanowires with V and III variation in a single growth. (a) Precursor flow rates during growth. (b) SEM image of a corresponding GaAs nanowires on the growth substrate at a 45° viewing angle. (c) Diameter (d) and growth rate (v) of each segment, as indicated in (b). Scale bar represents 200 nm.

8.1.2. The role of the III & V sources in nanowire growth

These diameter-modulated GaAs nanowires not only demonstrate the universality of the flow-controlled approach to diameter modulation for particle-mediated compound semiconductor nanowires, but also highlight the importance of the fluxes of both the III and V precursors during nanowire growth. Authors commonly report the V/III ratio as an important parameter in nanowire growth. For example, changes in the V/III ratio have been attributed to differences in tapering^{83,216} and the density of stacking defects.⁹² In fact, a high density of twins was observed here when a V/III ratio < 1 was used (Figure 8-3a), consistent with observations by Joyce *et al.* that the density of twin-plane defects in GaAs nanowires increases as the V/III ratio decreases.¹¹³ In the growth shown in Figure 8-1a, a V/III ratio of 2 was obtained by decreasing the V flux, and no twins were observed within that segment. On the other hand, when a V/III ratio of 2 was

obtained by increasing the III flux (Figure 8-1a), some nanowires were found to contain twins within that segment (Figure 8-3b). Thus both the relative and absolute flows of precursors are important in controlling the nanowire structure. Notably, while defects may be introduced under certain conditions, the results shown in Figure 8-2 demonstrate that it is possible to achieve significant diameter modulation within a relatively narrow range of V/III ratios by changing the fluxes of both III and V precursors.

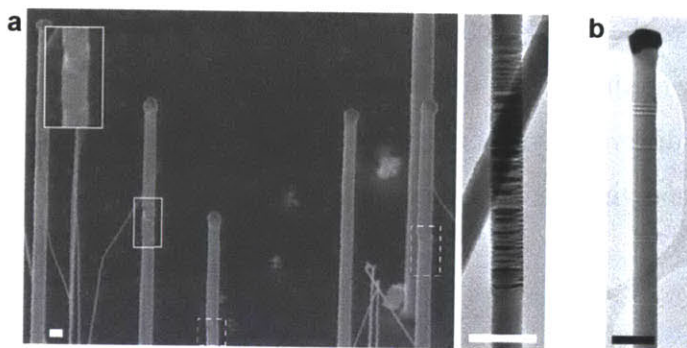


Figure 8-3. Defects resulting from low V/III ratios. (a) SEM (left) and TEM (right) images of GaAs nanowires with segments grown with a V/III ratio < 1 . White boxes indicate these segments, which have a high density of twinning defects, and the inset shows a magnified view of the segment indicated by the solid white line. (b) TEM image of a GaAs nanowire grown with a V/III ratio of 2 by increasing the III flow. Contrast along nanowires in both TEM images originates from twinning defects. All scale bars represent 200 nm.

The absolute flows of both the III and V precursors were shown here to each have a significant effect on both the nanowire diameter and the growth rate, rather than one precursor being limiting and dictating nanowire kinetics. The nanowires in Figure 8-1 were grown using the same sequence of V/III ratios, but the V/III ratio was decreased in one growth by a reduction in V flow (Figure 8-1a) and, in the other, by an increase in III flow (Figure 8-1b), resulting in a decreased versus increased growth rate, respectively. Additionally, the first and third segments in Figure 8-2 were grown using the same V/III ratio, but a five-fold reduction in the flow of both precursors resulted in a $17 \pm 6\%$ decrease in diameter and an $83 \pm 1\%$ decrease in growth rate. These results demonstrate that the absolute flows of both the III and V precursors have a significant effect on growth kinetics, and the V/III ratio cannot be considered independently of the absolute source fluxes. Thus both absolute and relative precursor flows must be considered in the growth, optimization, and diameter modulation of III-V nanowires.

8.2. Variations between different nanowires

It is important to note that the nanowires described above represent just one type of nanowire observed during the growth of diameter-modulated GaAs nanowires. In fact, three different types of [111]B-oriented nanowires showed distinct differences in diameter modulation behavior. In this section, the structure, morphology and growth kinetics of each of these nanowires are discussed and compared. Three-dimensional reconstructions of a nanowire of each type were generated using electron tomography, and cross-sections were extracted along each nanowire to assess the cross-sectional shape and evolution during diameter modulation. Differences in diameter modulation, growth rate, and cross-sectional shape between the different nanowires suggest that differences in seed particle composition and phase are largely responsible for the differences in nanowire diameter modulation.

8.2.1. Nanowire types

The diameter-modulated GaAs nanowires described above were grown on GaAs (111)B substrates and grew preferentially in the vertical [111]B direction, consistent with results from other authors.^{113,217} However, in this case, three different types of nanowires with distinct differences in nanowire morphology were observed to grow vertically from the (111)B substrate. Sample nanowires of each type from the same growth as in Figure 8-1a are shown in Figure 8-4. Here, the wide-diameter segments were produced by reductions in the V flow rate. Type A (“DM”) nanowires have moderate diameter ratios ($d_{thick}/d_{thin} = 1.25 \pm 0.09$) and grow at a relatively slow growth rate (Figure 8-4a). Type B (“straight”) nanowires show no observable diameter modulation and grow at a relatively fast growth rate (Figure 8-4b). Type C (“kinked DM”) nanowires have large diameter ratios ($d_{thick}/d_{thin} = 1.94 \pm 0.36$), grow at a similar rate to the straight nanowires, and produce kinks during each change in flow (Figure 8-4c). Changes in the V flux produced the same trends in diameter and growth rate for both Type A and C nanowires. The diameter modulation and growth rate behavior for each of these three types is summarized in Figure 8-4d. It is important to note that the nanowires described in Figure 8-1 and Figure 8-2 represent only the Type A DM nanowires. We also note that some nanowires grew non-vertically and/or were highly kinked, but only vertical [111]B nanowires are considered in the following discussion.

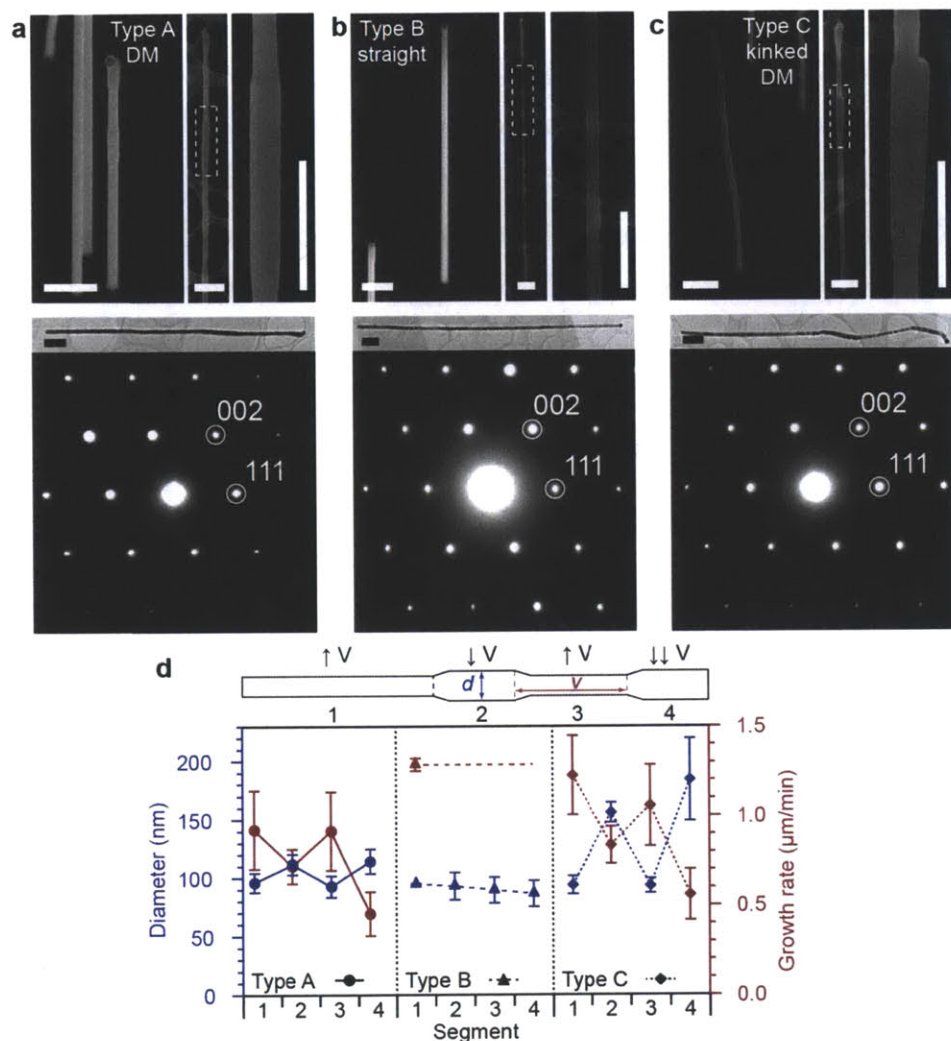


Figure 8-4. Variable diameter modulation between different GaAs nanowires. (a-c) SEM images (top) and TEM images with corresponding diffraction patterns (bottom) for Type A DM (a), Type B straight (b), and Type C kinked DM (c) nanowires. The SEM images show as-grown nanowires viewed at a 45° inclination angle (left), nanowires after transfer to TEM grids (center), and magnified views (right) of the regions indicated by dashed white lines. (d) Diameter (d) and growth rate (v) of specific nanowire segments. Schematic indicates the measurement of segment diameter and growth rate, as well as the flow rate during each segment ($\uparrow V$, $\downarrow V$, and $\downarrow\downarrow V$ correspond to 3.4, 1.1, and 0.7 sccm AsH_3 , respectively). Scale bars represent 500 nm.

Of [111]B-oriented nanowires, only Type A, B, and C nanowires were observed, with the exception of some highly kinked nanowires. Notably, no difference in the relative nanowire density or inter-nanowire spacing between different nanowire types was observed. Thus, the observed differences in diameter modulation upon each reduction in AsH_3 flow were not based on fluctuations in local conditions near the nanowires, but must have instead been based upon

fundamental differences between each type of nanowire. Notably, the Type A nanowires grew relatively slowly even during the first segment before any change in AsH₃ flux. Thus, we suspect that the nanowire type is determined during nucleation. Furthermore, because the nanowires grow in the same [111]B direction, there must be inherent differences in the seed particle and/or cross-sectional shape that explain the observed differences in behavior. Differences in seed particle composition and/or phase would affect the surface energy and supersaturation of the seed,²¹¹ while differences in faceting could affect adatom diffusion.²¹⁸

8.2.2. Cross-sectional shape for different nanowire types

To probe the cross-sectional shape and its evolution during diameter modulation, electron tomography was performed on a nanowire of each type to produce a three-dimensional reconstruction of each nanowire from which the cross-sectional shape could be extracted (Figure 8-5). Electron tomography analysis was performed in collaboration with Georg Haberfehlner at CEA-Leti. The cross-section of the Type A DM nanowire has a hexagonal shape with six facets that are maintained throughout diameter evolution, although the relative length of each facet varies (Figure 8-5a).[§] On the other hand, the Type B straight nanowire has a truncated hexagonal shape, and a hexagonal cross-section is restored at the very tip of the nanowire upon cooling (Figure 8-5b). The Type C kinked DM nanowire also has a unique cross-sectional shape, and the diameter expansion in the kinked DM nanowires is asymmetric, as the cross-section expands preferentially in specific directions (Figure 8-5c). The geometry and faceting of these facets cross-sections are analyzed in detail below.

To further assess the cross-sectional morphology and index the facets of the cross-sections captured via tomography, we performed EDS linescans at different positions along nanowires of each type (Figure 8-6).^{**} To provide a basis for indexing the crystallographic orientation of facets, each nanowire was oriented along the [110] zone axis during linescan acquisition. The Ga signals from these linescans were fit using four different models, where applicable: (1) hexagonal cross-section with {110} facets, (2) hexagonal cross-section with {112} facets, (3) projections of the cross-sections obtained via tomography with defined {110} facets, and (4)

[§] In addition to the tomography results, EDS linescans of multiple Type 1 nanowires indicate well-defined facets throughout the nanowires.

^{**} These nanowires were not the exact same nanowires used for tomography, but the general shape of the cross-section should be similar for different nanowires of the same type.

cross-sectional projections with defined $\{112\}$ facets. For the hexagonal cross-sections, the angle between each facet was fixed at 120° , but the relative length of each facet was allowed to vary. For the tomography cross-sections, the cross-sections were rotated such that (1) the projection intensity provided a good fit with the EDS linescan intensity, and (2) the orientation of reference facets (Figure 8-5) corresponded to $\{110\}$ or $\{112\}$ facets (see section 3.4.1).^{††} The $\{110\}$ and $\{112\}$ facets were chosen based on commonly observed facets in $[111]$ B-oriented III-V nanowires.^{92,186,219-224}

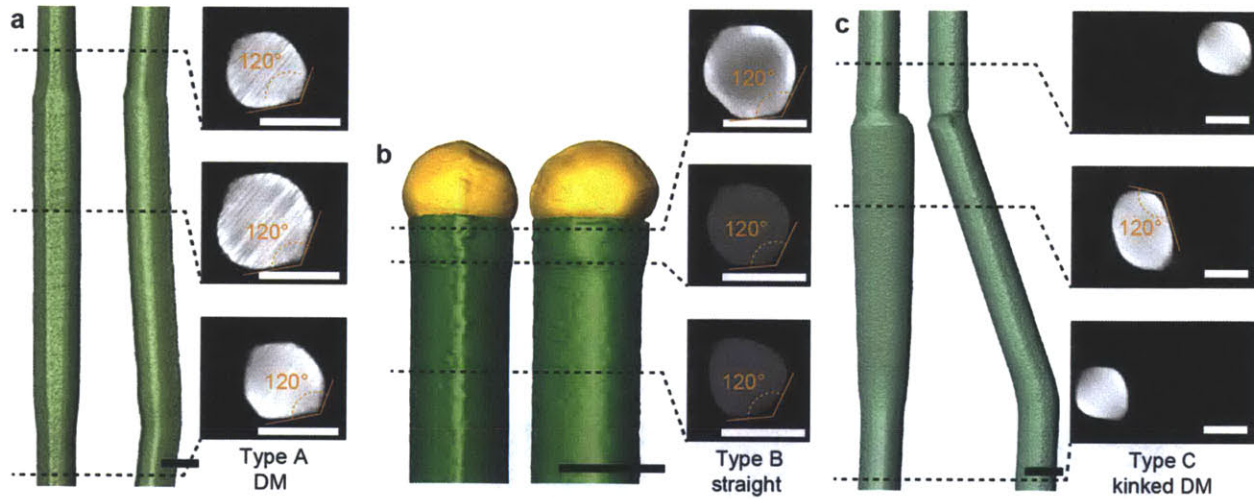


Figure 8-5. Cross-section-dependent diameter modulation. (a-c) Tomography reconstructions (left) rotated by 90° with respect to one another and cross-sections (right) extracted from 3 positions along each nanowire for a Type A DM (a), Type B straight (b), and Type C kinked (c) nanowire. The positions of the cross-sectional slices along the nanowires are indicated by dashed black lines. Orange lines indicate reference facets used for EDS. Scale bars equal 100 nm.

For all nanowire types, linescans near the base of the nanowire indicate a hexagonal cross-section with well-defined $\{112\}$ facets (Figure 8-6), which is the most commonly observed facet orientation for Au-seeded GaAs nanowires.^{92,219,221,222,224} Linescans at multiple positions along the Type A DM nanowire indicate retention of this well-defined cross-section, although with a shift in the relative lengths of different facets (Figure 8-6a and Figure 8-7a). The $\{112\}$ model matches very well with the EDS profile, and the difference between the $\{112\}$ tomography projection and the EDS profile can be attributed to differences in the lengths of particular facets.

^{††} For the tomography cross-section, there are 6 different configurations separated by 60° rotations in which the well-defined facets correspond to $\{112\}$ facets, as well as 6 configurations that correspond to $\{110\}$ facets. For a given facet type, the configuration which best corresponded to the observed EDS profile was chosen.

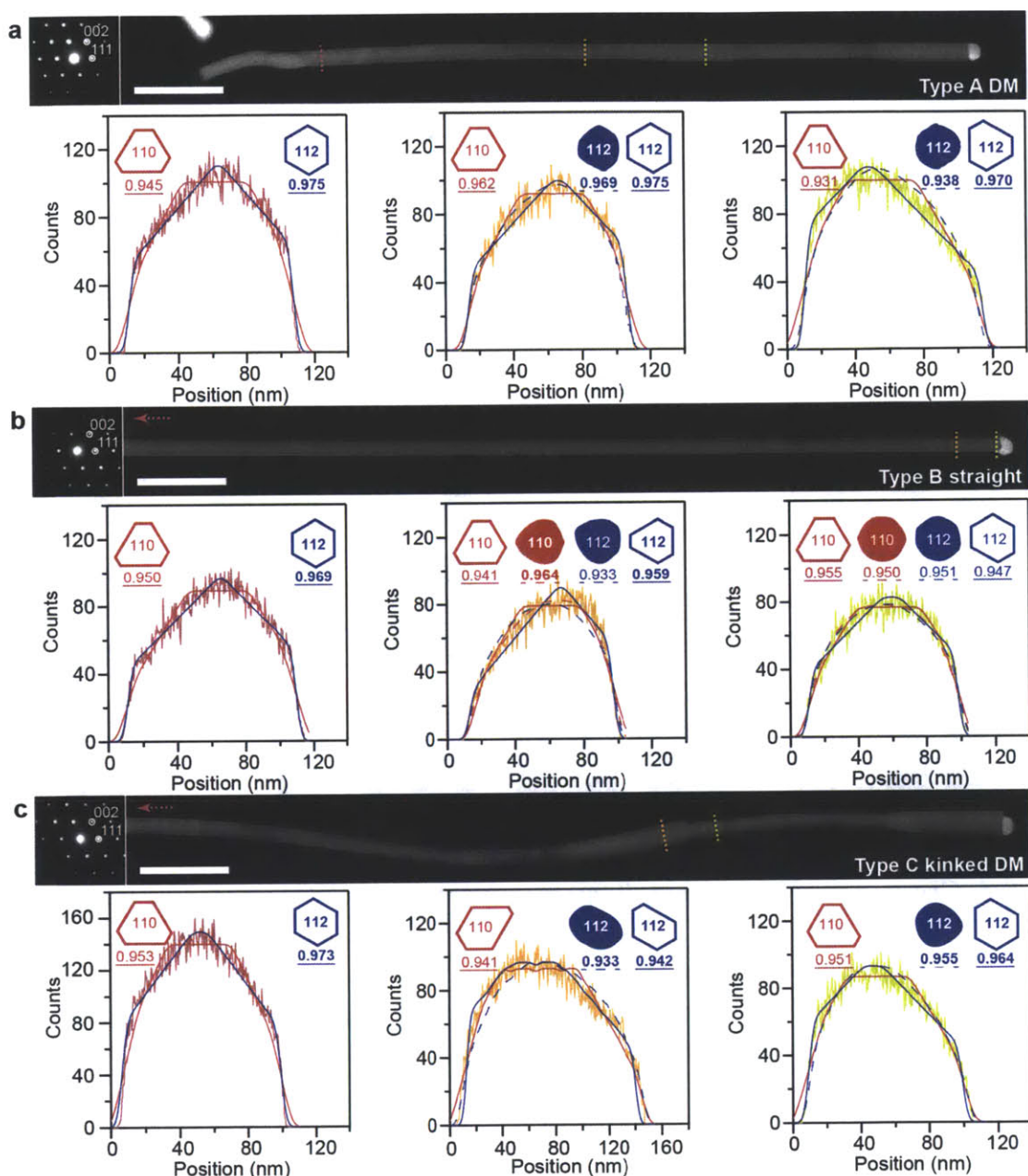


Figure 8-6. Cross-section evolution. (a-c) STEM images (top), corresponding SAD patterns (top left), and EDS linescan profiles (bottom) for Type A DM (a), Type B straight (b), and Type C kinked DM (c) nanowires. Linescan positions are indicated by red, orange, and yellow dashed lines. In (b,c), the locations of the first linescan are taken from the base region of the nanowire to the left of the STEM images, as indicated by the red arrows. The color the Ga signal in each EDS profile corresponds the color indicated on the STEM image. The insets show modeled hexagonal cross-sections (outline) and tomography cross-sections from Figure 8-5 (filled) with corresponding linescans indicated by solid and dashed lines, respectively. Profiles assuming $\{110\}$ and $\{112\}$ facets are indicated by red and blue, respectively. The numbers indicate the R^2 value for each cross-section. Best fits are indicated in bold. Scale bars represent 500 nm.

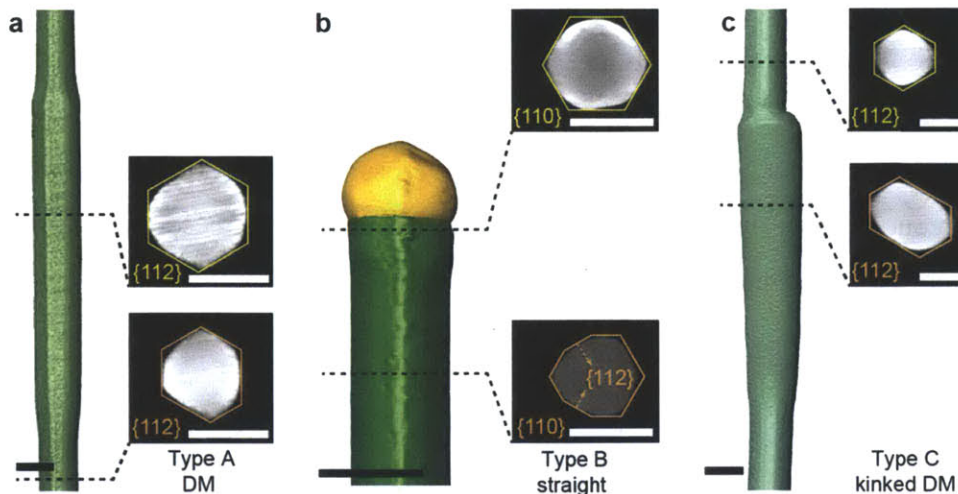


Figure 8-7. Facet orientation. (a-c) Tomography reconstructions (left) and cross-sectional slices with facet indices (right) for a Type A DM (a), Type B straight (b), and Type C kinked (c) nanowire. The cross-sections, line color (orange and yellow), and orientation (i.e. [110] vertical) correspond to those used in Figure 8-6. Scale bars represent 100 nm.

For the Type B straight nanowire, tomography results in Figure 8-5b show that the cross-section goes from truncated hexagonal near the tip of the nanowire (corresponding to low V flow) to hexagonal directly below the seed (corresponding to the end of growth and cooling). For the truncated cross-section, the hexagonal models for the EDS profile do not necessarily reflect the actual facets of the real cross-section (Figure 8-6b, center). In fact, while the {112} hexagonal model provides a better fit than the {110} hexagonal model, the {110} tomography projection provides a better fit than the {112} tomography projection. In this case, the overall shape of the {110} tomography projection is qualitatively more similar to the {112} hexagonal model than the {110} hexagonal model. Because the facets clearly start out as {112} at the base of the nanowire (Figure 8-6b, left), this analysis indicates that the cross-section evolves during growth such that the defined facets in the truncated cross-section are {110}, which then become more defined after the TMG flow is cut off at the end of growth (Figure 8-7b). However, because of the high degree of rounding in the hexagonal cross-section at the tip of the nanowire (Figure 8-6b, right), tomography projections with {110} and {112} facets both provide a very similar fit to the EDS linescan profile. It is therefore difficult to unequivocally claim that the facets of Type B nanowires evolve from {112} to {110} during growth, although the EDS analysis of the truncated cross-section does support that notion. Furthermore, Tambe *et al.* reported GaAs nanowires with multiple {112} and {110} facets, yielding a cross-section similar

to the truncated shape observed here.²²⁵ Those results also suggest that the predominant facets in the truncated tomography cross-section are $\{110\}$. Regardless, even with $\{112\}$ -type facets present, the unique truncated hexagonal shape of the cross-section differentiates Type B straight nanowires from the others. Notably, EDS linescans across Type B nanowires grown without any changes in precursor flow during growth show the same trends as these linescans here (Figure 8-8), indicating that the truncated hexagonal cross-section is inherent to these nanowires and is not a consequence of changes in precursors flows.

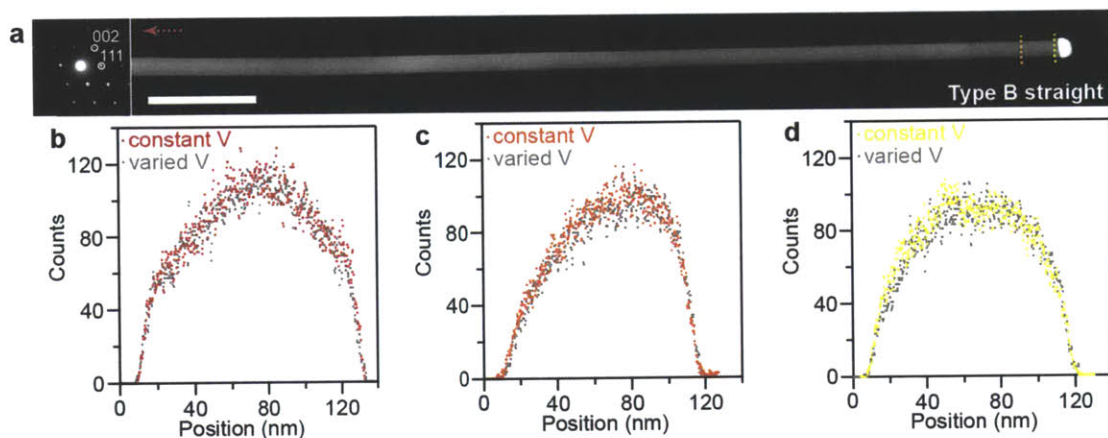


Figure 8-8. Type B straight nanowires with no change in AsH_3 flow. (a) STEM image (right) and corresponding SAD pattern (right) of a Type B straight nanowire grown with no change in AsH_3 . (b-d) EDS linescan profiles at the base (b), near the tip (c), and just below the seed (d). The red, orange, and yellow profiles correspond to the linescans indicated by dashed lines in the STEM image. The gray profiles were taken from the nanowire in Figure 8-6b. The red arrow indicates that the linescan in (b) was taken at the base of the nanowire. Scale bar represents 500 nm.

The models of the EDS linescans along the Type C nanowire allow more facile indexing of the facets obtained via tomography. The actual cross-sectional shapes and the theoretical models for $\{112\}$ -type facets match are qualitatively similar and provide a reasonable fit with the EDS profile (Figure 8-6c). Thus it is clear that the diameter expands and contracts by elongation and shortening, respectively, of $\{112\}$ -type facets (Figure 8-7c).

8.2.3. Origin of differences in cross-sectional shape

While the tomography and EDS results indicate distinct differences in the cross-sectional shape and evolution between the different types of $[111]\text{B}$ -oriented GaAs nanowires, the

underlying origin of these differences is less clear. Differences in cross-sectional shape could potentially arise from disparities in the presence of stacking defects or the composition of the seed particle. Stacking defects are an unlikely explanation for these results, because differences in cross-sectional shape and growth rate are present prior to any change in flow, and no twins were observed in this region. In fact, twins were rarely observed at all in these nanowires except occasionally at the beginning of kinks in Type C kinked DM nanowires. Furthermore, the fact that each individual nanowire displays the same of behavior (i.e. only Type A, B, or C) during all changes in flow indicates discrete differences between the seed particles.

Therefore, these results suggest the different nanowire types are driven by differences in seed particle composition and/or phase. In fact, in the absence of variations in seed composition and/or phase between nanowires, it seems unlikely that different nanowires would maintain such discrete differences in cross-sectional shape, diameter, and growth rate throughout growth. The steady-state seed particle composition is affected by the chemical potential of precursors in different phases (i.e. μ_v , μ_s , and μ_n for the vapor/adatom, seed, and nanowire phases; Figure 8-9a,b).^{60,61} While variations in the local supply (e.g. as a result of variations in inter-nanowire spacing) of precursors can lead to differences in the local $\Delta\mu_v$, these have been shown to produce a continuous spectrum of nanowire growth rates, rather than discrete differences.¹⁴¹ Differences in $\Delta\mu_n$ are minimal, because all types grow in the [111]B direction and initially have well-defined {112} facets. While the facet structure evolves differently for each nanowire type, affecting facet surface energy (σ_{vs} ; Figure 8-9a,b) differences in growth rate are observed even in the initial base region where the facet structure is similar. Furthermore, the nanowire facets can readily evolve during growth to minimize total energy,^{61,89,92} so there must be a driving force for maintaining these differences in cross-sectional shape. Because differences in the vapor, adatom, and nanowire phases cannot explain the observed results, there must be discrete differences in the seed particle phase affecting μ_s and therefore the growth rate and diameter.

At 420°C, bulk Au-Ga alloys are only fully liquid between 22-40% Ga and greater than 84% Ga (Figure 8-9c),¹⁵⁹ and the presence of As raises the temperature of the liquidus,²²⁶ so it is possible that the seeds of some nanowires may be liquid while others may be solid. Differences in cross-sectional shape have been observed in the growth of solid-seeded versus liquid-seeded Ge nanowires,²²⁷ and Au-seeded GaAs nanowires have been reported to grow from both liquid²¹¹ and solid⁶⁵ Au alloys in different studies. Even to reach the liquidus, the seed particle must first

undergo a phase transitions from solid Au to solid Au_7Ga_2 to liquid Au-Ga.¹⁵⁹ For solid Au seeds, there may be differences in the composition of the intermetallic alloy, which could explain differences in growth rates and diameter changes between different nanowire types. As discussed earlier for Au-seeded versus Ni-seeded GaN nanowires, differences in interfacial energies and the chemical potential of III and V elements in different seed particles can significantly affect growth kinetics (Figure 8-9a,b).

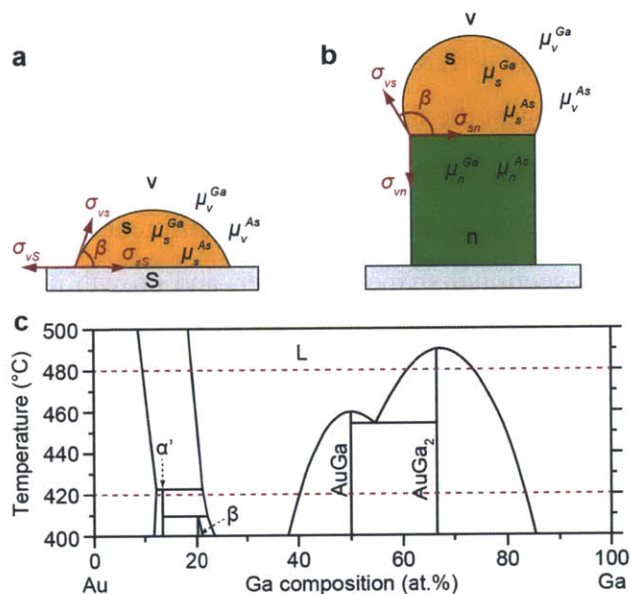


Figure 8-9. Parameters affecting GaAs nanowire growth. (a,b) Surface energies (σ) and chemical potentials (μ) for the vapor (v), seed (s), substrate (S), and nanowire (n) phases before (a) and after (b) nanowire nucleation. The wetting angle (β) is determined by the surface energies. (c) Binary Au-Ga phase diagram between 400–500°C, adapted from [159]. The β and L phases correspond to Au_7Ga_2 and liquid, respectively, while α' is another solid phase. Red dashed lines correspond to 420°C and 480°C.

Interestingly, there is initially no significant difference in diameter between the three types of nanowires prior to diameter modulation (Figure 8-4d) despite the high likelihood of differences in seed composition and/or phase, which would affect both the volume and wetting behavior of the seed particle. Therefore, the compositional differences may be small and/or the three-dimensional shape of the seed particle varies between the different nanowire types. Even with small differences in composition, the seed may remain either a liquid or in a particular solid phase due to the energy barrier in nucleating a new solid phase. As noted above, the seed particle has to go through phase transitions prior to reaching the liquidus. Also, multiple solid

phase transitions have been observed in Ni-Ga alloys prior to GaN nucleation.²²⁸ Here, it is possible that some seeds nucleate GaAs nanowires in one phase, while other seeds do not nucleate them until another phase has formed. Then, after nanowire formation, there may be a larger barrier to seed phase transitions due to the formation of a stable interface between the seed and nanowire. In fact, Adhikari *et al.* observed that liquid AuGe alloys could remain liquid when the temperature was reduced well below the bulk eutectic temperature, indicating some seed particle hysteresis may be present.¹¹² Due to the high surface-to-volume ratio of the seed particles and the energy penalty associated with creating interfaces, phase changes are likely to occur throughout the entire nanoparticle. Seed particle hysteresis may therefore allow certain phases to exist over a large range of composition. For example, at 420°C in the bulk Au-Ga phase diagram, the liquid phase is present at least to some extent between 14–50% Ga, as well as between 67–100% Ga. Furthermore, it is possible that changes in the wetting and shape of the seed particle may contribute significantly to the observed diameter changes such that significant diameter changes occur for relative small changes in seed particle composition. For example, As has a very low surface energy ($\sim 0.14 \text{ J m}^{-2}$ at 420°C),²²⁹ and low-energy elements tend to migrate to the surface to reduce surface energy,²⁰⁹ so small changes in the As concentration could significantly affect the surface energy of the seed particle.²²⁹

The shape of the liquid/solid interface may also vary between nanowires of different types. For example, an inclined facet similar to those observed in Ge, Si, and GaP nanowires may be present at the triple-phase boundary,^{95,101} and the orientation of this facet may vary between different nanowires, which could affect the incorporation of As and the growth rate of the nanowires. It is possible that this effect could be present as a consequence of differences in seed particle phase.

8.3. Control of nanowire type

As stated above, each individual [111]B nanowire distinctly displayed only Type A, B, or C behavior throughout all changes in V flow. Because no individual nanowire was observed to contain segments with different behavior, there must be fundamental differences between each of the three types. In fact, differences in the cross-sectional shape were observed between nanowires of different types. Furthermore, differences in the behavior of nanowires of different nanowire types are present prior to variations in precursor flows, including the growth rate. Thus

the nanowire type is presumably determined during nucleation and can therefore be controlled by varying parameters that affect nucleation.

Here, we vary the diameter, substrate orientation, and growth conditions, including V/III ratio during nucleation, pre-growth annealing, and nucleation temperature. Nanowires of each type could be preferentially obtained under different conditions. Type B straight nanowires were preferentially obtained by using 30-60 nm Au colloids and, for 90 nm colloids, by nucleating the nanowires at a higher temperature. Type A DM nanowires were preferentially obtained by using (111)A substrates. Type C nanowires were preferentially obtained by eliminating the pre-growth annealing procedure and nucleating at a high V/III ratio.

8.3.1. Diameter dependence

The size of the seed particle can have a significant effect on the initial formation of the nanowire because of the high surface-to-volume ratio of the nanoparticles. In fact, authors have observed that nanowires with different diameters sometimes grow preferentially in different directions.^{105,106,230} To investigate the effect of diameter on nanowire type, Au colloids with different diameters between 10-200 nm were dispersed on separate GaAs (111)B substrates.

Figure 8-10 shows nanowires grown with different sizes of Au colloids grown in two separate growths. Colloids with 200, 90, and 30 nm diameters were used in one growth (Figure 8-10a-e), while 90, 60, and 10 nm diameters were used in another (Figure 8-10f-j). The fraction of vertical [111]B nanowires (including Type A, B, and C nanowires) increases as the colloid diameter decreases from 200 to 90 nm (Figure 8-10d,i), then decreases as the colloid diameter drops below 60 nm. For 60 nm Au colloids, the fraction nanowires that are vertical [111]B exceeds 99%. For colloids >60 nm, the fraction of vertical [111]B nanowires is limited by kinking, which increases as the diameter increases, consistent with reports by other authors.^{127,230,231} For colloids <60 nm, nearly all nanowires grow straight, but some grow preferentially in non-[111]B (i.e. non-vertical) directions. At 30 nm, the fraction of vertical [111]B nanowires still exceeds 90%, but a much more significant amount of non-vertical growth is evident at 10 nm. Unfortunately, quantification of the results for 10 nm Au colloids was challenging due to limited SEM resolution at such thin diameters, the high density of nanowires, and significant nanowire bending (Figure 8-10h). Nonetheless, increased non-vertical growth is readily apparent. Other authors have reported a significant change in the preferential growth

direction below a particular nanowire diameter,^{105,106,230} which is likely driven by the changes in surface-to-volume ratio, as well as the relative surface area of different seed particle and nanowire interfaces.

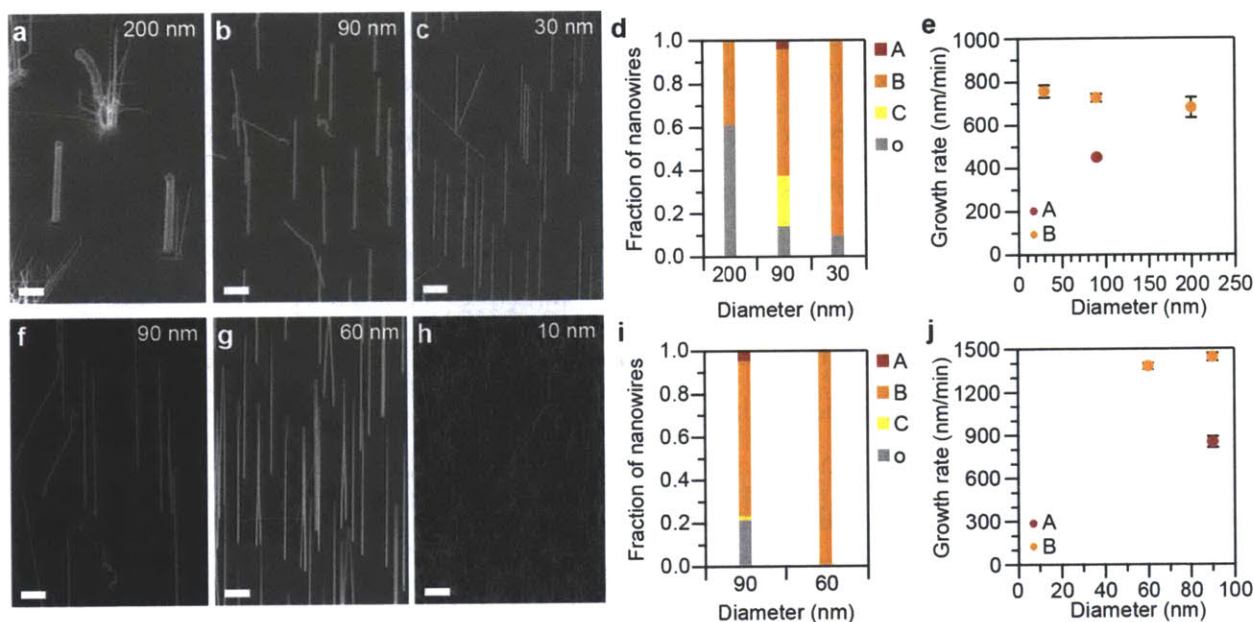


Figure 8-10. Diameter dependence of nanowire type. (a-e) GaAs nanowires grown using 200 (a), 90 (b), and 30 (c) nm Au colloids and their corresponding orientation (d) and growth rate (e). (f-j) Another growth using 90 (f), 60 (g), and 10 (h) nm Au colloids and the corresponding nanowire orientation (i) and growth rate (j). All SEM images are at 45° viewing angles. The histograms (d,i) indicate the fraction of nanowires that are Type A DM (red), Type B straight (orange), and Type C kinked DM (yellow), as well as other nanowires (“o”; gray) that are either highly kinked or non-[111]B. The growth rate plots (e,j) show the nanowire growth rate as a function of colloid diameter for both Type A (red) and Type B (orange) nanowires. Data for 10 nm nanowires is not included because of difficulties in obtaining accurate measurements from SEM images. All scale bars represent 1 μ m.

Only the 90 nm Au colloids produced Type A DM and Type C kinked DM nanowires. For all other colloid sizes, nearly all vertical [111]B nanowires were Type B straight ones. While the size of the Au colloids and the inter-nanowire spacing varied for different colloid sizes and can affect growth kinetics,¹⁴¹ the growth rate of nanowires with different diameters was relatively constant (Figure 8-10e,j), indicating reaction-limited growth with minimal effect of inter-nanowire spacing. Thus it can be concluded that the difference in diameter modulation originates from the difference in colloid diameter. As further evidence, the only exception in

which Type A or C nanowires were observed with non-90-nm Au colloids was for 60 nm colloids in which some thick nanowires (resulting from colloid aggregation) were Type C kinked DM.

At relatively thin diameters (30–60 nm), the strong preference for Type B straight nanowires could be a consequence of a greater preference for a certain seed particle phase. The surface-to-volume ratio increases as seed volume decreases, which would lead to a greater preference for a phase with low surface energy at the vapor/liquid and/or liquid/solid interface (see Figure 8-9a,b). In fact, a low liquid/solid surface energy for the Type B nanowires would be consistent with the fact that they grow relatively fast compared to the other nanowires (Figure 8-10e,j), as was the case for Ni-seeded versus Au-seeded GaN nanowires (section 4.3).

For the 200 nm Au colloids, the lack of diameter-modulated nanowires (Types A and C) may originate from greater instabilities at larger diameters. Highly kinked nanowires are common with the 200 nm Au colloids, and the seed particles often break up into many smaller particles and produce a high density of thin nanowires. A very similar observation was made for InP nanowires with very large diameters.¹²⁷ It is possible that changes in flow induce instabilities in these nanowires that cause kinking, rather than diameter modulation. Also, the relatively large seed volume may allow multiple solid phases to be present, which could explain both the high degree of kinking and the separation of the seed into multiple particles. While the nucleation of a new phase within the seed generally results in a phase change for the entire particle, it is possible that multiple phases may coexist in larger particles. This could initially result in the production of many small seed particles formed by phase segregation^{††} prior to nanowire nucleation and then the generation of kinks after nucleation.

8.3.2. Substrate dependence

As demonstrated previously with GaN and InN nanowires, the orientation of the substrate can have a significant impact on the orientation of the nanowires that grow from it. Here, we compare the growth of nanowires on (111)A and (111)B GaAs substrates, which are Ga-terminated and As-terminated, respectively, and have been shown to affect nanowire orientation

^{††} It makes the most sense that these would be small liquid droplets forming before reaching the first liquidus (~12-21% Ga), because GaAs nanowires are less likely to have nucleated. A reduction in total surface energy could make separation energetically favorable. Additionally, these liquid droplets would be somewhat mobile and could randomly diffuse away from the larger particle.

in studies by other authors.²²³ For both substrates, 90 nm Au colloids were used. In this growth, the nanowires were first grown under a low V/III ratio, and diameter modulation was achieved by increasing the V flow, then decreasing it, then increasing it again. The plan-view SEM image in Figure 8-11a shows that the nanowires on the (111)A substrate grew preferentially in three directions at 120° angles relative to one another, indicating [111]B-oriented growth, which was confirmed by SAD (Figure 8-11e).²³² On (111)B GaAs substrates, nanowires also grow preferentially in the [111]B direction, which is instead vertically oriented from the substrate (Figure 8-11b).

The substrate was found to have a significant impact on diameter modulation. While (111)B substrates produced mostly Type B straight nanowires, (111)A substrates produced mostly Type A DM nanowires (Figure 8-11c). Figure 8-11d compares the diameters and growth rates of Type A DM nanowires on (111)A and (111)B substrates. The extent of the diameter modulation resulting from a reduction in AsH₃ flow was greater for (111)A versus (111)B substrates (1.30 ± 0.10 versus 1.19 ± 0.03 , respectively).

The nanowires on the (111)A substrates were concluded to be Type A DM based on the extent of their diameter modulation and lack of kinking, but the growth rates are also an important consideration. Interestingly, there seemed to actually be two groups of Type A DM nanowires on (111)A substrates with different diameter ratios and growth rates. The nanowires that grew slower had diameter ratios of 1.15 ± 0.05 and growth rates of 1.04 ± 0.07 μm/min in the high-AsH₃ segments, very similar to the Type A nanowires grown on (111)B substrates (1.19 ± 0.03 and 0.95 ± 0.08 μm/min, respectively). The nanowires that grew faster had diameter ratios of 1.33 ± 0.07 and growth rates of 1.42 ± 0.07 μm/min in the high-AsH₃ segments. In this case, the growth rate is very similar to the growth rate of Type B straight nanowires grown on (111)B substrates (1.44 ± 0.02 μm/min). Furthermore, the cross-sectional shape of the fast-growing Type A DM nanowires on (111)A substrates matches that of the type B straight nanowires on (111)A substrates (Figure 8-11e–h). Given the similarities in these growth rate and cross-sectional shape, as well as the absence of any Type B straight nanowires on (111)A substrates, it is likely that the fast-growing Type A DM nanowires on (111)A substrates grow from seed particles in the same phase as those for the Type B straight nanowires on (111)B substrates. The fast-growing nanowires represent 83% of the Type A DM nanowires on (111)A

substrates, indicating a similar preference for cross-sectional shapes on both (111)A and (111)B substrates.

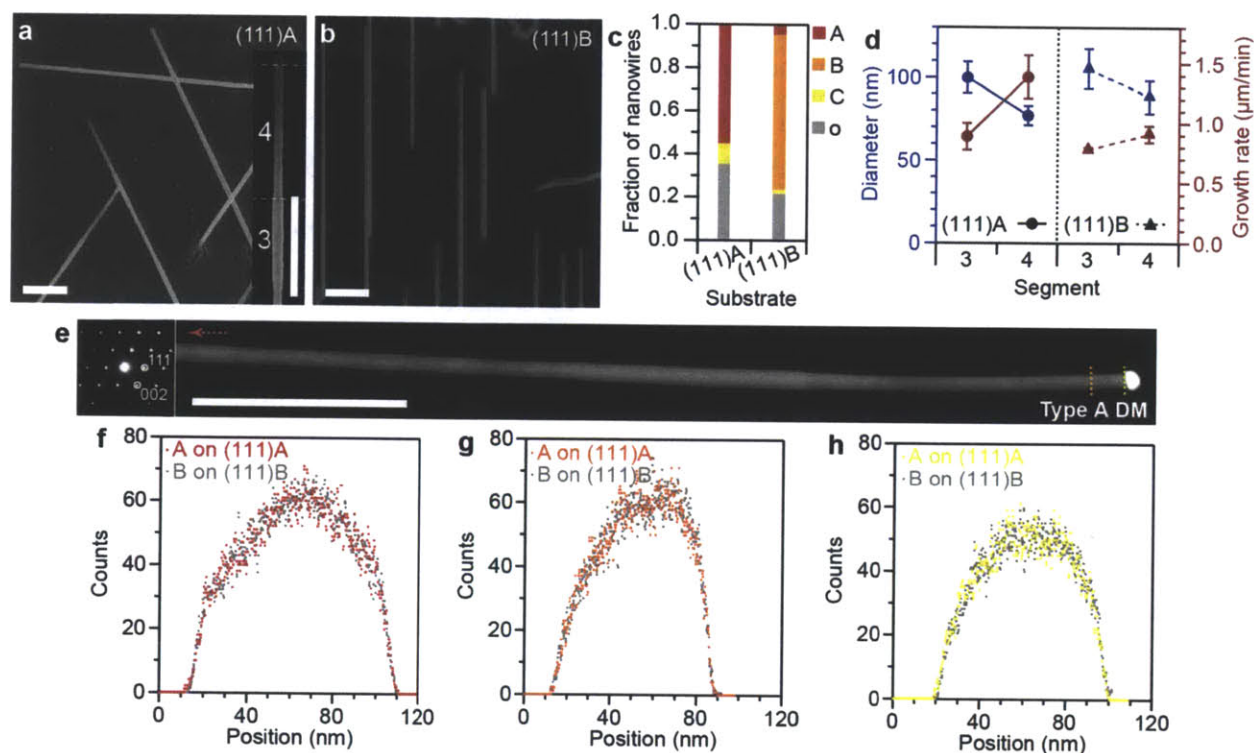


Figure 8-11. Substrate dependence of nanowire type. (a) Plan-view SEM images of GaAs nanowires grown on (111)A GaAs substrates. Inset shows magnified view of upper segments. (b) SEM images of GaAs nanowires grown on (111)B GaAs substrates at a 45° viewing angle. (c) Histogram indicating the fraction of nanowires that are Type A DM (red), Type B straight (orange), and Type C kinked DM (yellow), as well as other nanowires (“o”; gray) that are either highly kinked or non-[111]B. (d) Diameter (d) and growth rate (v) of specific nanowire segments of Type A DM nanowires on (111)A versus (111)B substrates. The segments labeled in the inset of (a) correspond to those represented in the histogram. (e) STEM image (right) and corresponding SAD pattern (left) of a fast-growing Type A DM nanowire. (f-h) EDS linescan profiles at the base (f), near the tip (g), and just below the seed (h). The red, orange, and yellow profiles correspond to the linescans indicated by dashed lines in the STEM image. The gray profiles were taken from the nanowire in Figure 8-6b. The red arrow indicates that the linescan in (f) was taken at the base of the nanowire. All scale bars represent 1 μm.

Thus it appears that the main difference between the nanowires grown on (111)A and (111)B substrates is that the fast-growing nanowires show significant diameter modulation on (111)A substrates, but no diameter modulation on (111)B substrates. For no diameter modulation to occur when the AsH_3 flow is reduced, the seed particle must be able to still receive enough As

such that the growth rate is unchanged, which is the case for the fast-growing nanowires on (111)B substrates. However, for the fast-growing nanowires on (111)A substrates, the reduction in AsH₃ flow reduces the growth rate by $36 \pm 6\%$, causing an increase in diameter. Simulations of As adatom diffusion on (111)A and (111)B surfaces indicate that As adatoms are more mobile on As-terminated (111)B surfaces, while they tend to form stronger surface bonds on Ga-terminated (111)A surfaces.²³³ Experimental results also suggest that As species bind strongly to Ga-rich surfaces.²³⁴ Therefore, we conclude that the effective supply of As to the seed must be more limited on Ga-terminated (111)A substrates, making them more sensitive to changes in As flow and resulting in more significant As-driven diameter modulation.

8.3.3. Dependence upon growth conditions

We also utilized growth conditions during nucleation to control the preferred nanowire type. Here, we compare nanowires grown on (111)B substrates using 90 nm colloids. We varied the pre-growth annealing procedure, the nucleation temperature, and the V/III ratio during nucleation, each of which have been shown to affect nanowire orientation.^{113,223,231} Parameters that can affect orientation could also affect nanowire type, as both the orientation and type are determined during the initial stages of growth. A 600°C annealing procedure under H₂ and AsH₃ flow is generally used to remove surface oxides. For comparison, we also grew un-annealed samples. Additionally, we nucleated nanowires at both 480°C and 420°C for 1 min, followed in both cases by growth at 420°C. Finally, the V/III ratio during nucleation was varied from 2 (low) to 10 (medium) to 60 (high). The low V/III ratio was achieved by using a lower AsH₃ flux, while the high V/III ratio was achieved by using a lower TMG flux.

An increase in the nucleation temperature from 420°C to 480°C increased the total fraction of vertical [111]B nanowires (Figure 8-12), particularly for the un-annealed samples (Figure 8-12c,d), for which the verticality increased from 31% to 83% (Figure 8-12e). This is consistent with multiple reports of increased nanowire verticality using an elevated nucleation temperature.^{113,235} Furthermore, nearly all of the vertical nanowires at 480°C were Type B straight nanowires.^{§§} Bulk Au-Ga alloys at 480°C are fully liquid throughout most of the compositional range (19-60% and >74%; Figure 8-9c), while the range of fully liquid

^{§§} For un-annealed substrates, 92% of observed [111]B nanowires were Type 2 straight. For annealed substrates, every measured [111]B nanowire was found to be Type 2 straight.

compositions is more limited at 420°C (23–41% Ga and >84% Ga; Figure 8-9c).¹⁸¹ Also, the supply of Ga is likely greater at higher 480°C versus 420°C due to more efficient Ga decomposition (~90% versus ~20%, respectively),²³⁶ further increasing the likelihood of the seed reaching the liquidus. Thus it is likely that the Type B straight nanowires correspond to liquid seed particles, while the Type A and Type C nanowires correspond to solid seed particles in different phases. When the temperature is reduced to 420°C for growth, the seeds may preferentially remain in the liquid phase even if the composition of the seed changes and/or would thermodynamically correspond to a solid phase at the lower temperature due to the energy barrier in nucleating a solid phase. In fact, seed particles have been observed to remain in the liquid phase even after being cooled well below the eutectic temperature.¹¹²

At 420°C, the greater preference for Type A DM and Type C kinked DM nanowires over Type B straight nanowires for un-annealed versus annealed samples is likely a consequence of the presence of native oxide layers on the GaAs substrate surface. The 600°C anneal removes these oxides. At 420°C, As oxides may decompose, but Ga oxides remain stable.⁶ The surface diffusion of adatoms would be different on oxide versus arsenide surfaces, therefore affecting the supply of precursors to the seed particle. Furthermore, the presence of oxides can alter the surface energy of the seed/substrate interface, which could affect the preferred phase of the seed particle.

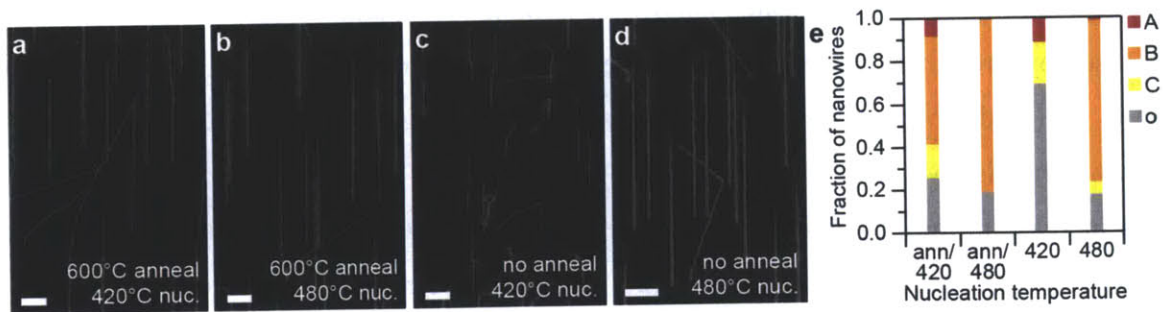


Figure 8-12. Dependence of nanowire type on nucleation temperature. (a-d) SEM images taken at 45° viewing angles of GaAs nanowires grown using 420°C nucleation after 600°C annealing (a), 480°C nucleation after 600°C annealing (b), 420°C nucleation without annealing (c), and 420°C nucleation without annealing (d). (e) Histogram indicating the fraction of nanowires that are Type A DM (red), Type B straight (orange), and Type C kinked DM (yellow), as well as other nanowires (“o”; gray) that are either highly kinked or non-[111]B. All scale bars represent 1 μm .

The effect of V/III ratio during nucleation was also investigated for both annealed and un-annealed samples. An increased V/III ratio during nucleation generally produced more diameter-modulated nanowires (Types A and C), as opposed to Type B straight nanowires (Figure 8-13). A similar effect has been observed in the growth of InP nanowires.²³¹ For annealed samples, the total fraction of all [111]B nanowires (Types A, B, and C) slightly decreased as the V/III ratio increased, but the effect was relatively small (Figure 8-13d). For un-annealed samples, kinking was a significant issue that resulted in a very high fraction of non-[111]B nanowires. However, an increased V/III ratio during nucleation not only produced more diameter-modulated nanowires (particularly Type C nanowires with high diameter ratios) but also significantly reduced the fraction of non-[111]B nanowires (Figure 8-13h).

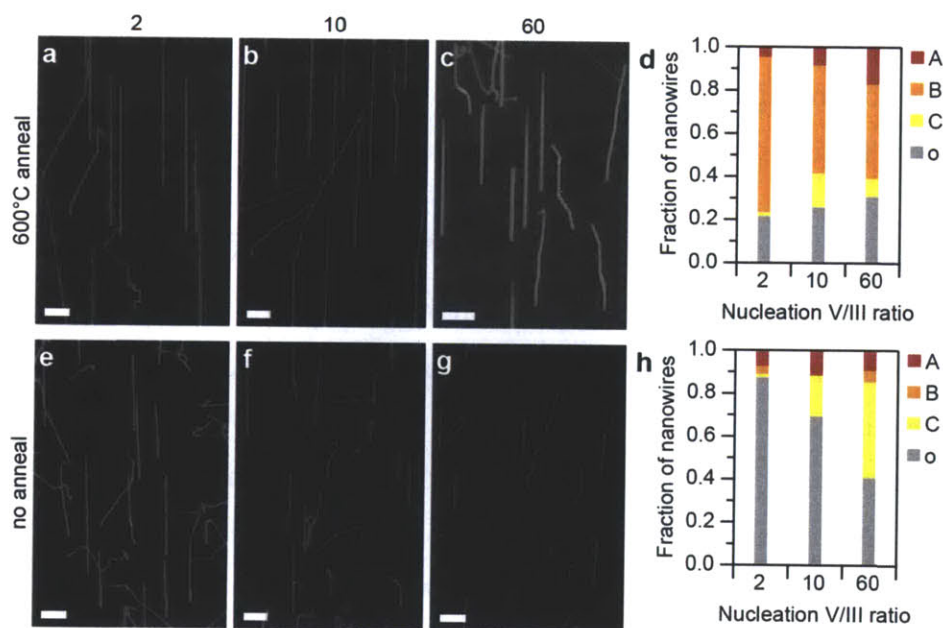


Figure 8-13. Dependence of nanowire type on V/III ratio during nucleation. (a-d) GaAs nanowires grown after 600°C annealing using low (a), medium (b), and high (c) V/III ratios during nucleation, as well as their corresponding orientation (d). (e-h) Nanowires grown without annealing using low (a), medium (b), and high (c) V/III ratios during nucleation, as well as their corresponding orientation (d). All SEM images are at 45° viewing angles. The histograms (d,h) indicate the fraction of nanowires that are Type A DM (red), Type B straight (orange), and Type C kinked DM (yellow), as well as other nanowires (“o”; gray) that are either highly kinked or non-[111]B. All scale bars represent 1 μm .

The preference for Type A and C nanowires over Type B nanowires at high V/III ratios may indicate that the composition of Ga in the seed is lower for Type A and C nanowires. However,

it is difficult to definitively identify the phase corresponding to each nanowire type. As stated previously, the preference for Type B straight nanowires at high nucleation temperatures does indicate the corresponding seed particles may be in the liquid phase due the limited amount of solid Au-Ga phases present at that temperature. The large change in diameter for the Type C nanowires, as well as the kinking that occurs, indicates that a phase change is likely. Even with a phase change with a large increase in Ga composition (e.g. AuGa to AuGa₂), volume changes would only account for a small portion of the diameter change, indicating that changes in surface energy and wetting angle are a significant factor in the diameter changes along Type C nanowires. Notably, the surface energy of As is very low ($\sim 0.14 \text{ J m}^{-2}$ at 420°C),²²⁹ so small changes in the As composition in the seed could have a significant impact on the wetting angle and, therefore, the nanowire diameter. Regardless of the specific phase, these results demonstrate that each type of diameter modulation behavior (DM, straight, and kinked DM) can be produced by controlling the initial conditions under which nanowires grow, indicating that the phase of the seed particle can be controlled during nucleation.

8.4. Summary

The flow-controlled diameter modulation approach developed in Chapter 6 was successfully applied to GaAs nanowires, demonstrating the general applicability of the technique for particle-mediated compound semiconductor nanowires. A reduction in the V flow led to a decrease in nanowire growth rate and increase in nanowire diameter, consistent with the previous results for InN nanowires. An increase in the III flow led to an increase in both diameter and growth rate, consistent with the previous results for GaN nanowires. Greater diameter ratios were achieved by modulating both the III and V source in the same growth.

The extent of diameter modulation varied between nanowires, and three distinct types of [111]B-oriented nanowires were observed: (1) nanowires with moderate diameter modulation with a relatively slow growth rate, (2) nanowires with no detectable diameter modulation and a relatively high growth rate, and (3) nanowires with significant diameter modulation that kinked upon changes in precursor flow. Electron tomography was performed on nanowires of each type, which were found to have differences in the cross-sectional shape. The differences in cross-sectional shape, diameter modulation, and growth rate between nanowires of different types indicated differences in the seed particle composition and phase.

Each type of diameter modulation behavior was preferentially produced by using multiple techniques to modify conditions during nucleation. Type B straight nanowires were obtained preferentially by using smaller Au colloids with diameters below 90 nm. For 90 nm Au colloids, the frequency of Type B straight nanowires was significantly increased by nucleating the nanowires at an elevated temperature (480°C) and then continuing growth at a lower temperature (420°C). Type A diameter modulation behavior was obtained preferentially by using (111)A instead of (111)B substrates. Notably, the high growth rate of these nanowires suggests that this was less of a consequence of more nanowires nucleating with the Type A seed particles and more due to diameter modulation occurring even for Type B seed particles, indicating a significant role of substrate adatom diffusion on diameter modulation. Finally, by operating at high V/III ratios without a pre-growth annealing procedure, the majority of [111]B nanowires obtained were Type C kinked DM nanowires with large diameter ratios.

These results have significant implications not only for nanowire diameter modulation, but for the general growth of III-V nanowires. By operating at the same V/III ratio but with different flows of the III & V precursors, differences in growth rate, diameter modulation, and defect densities were observed, which highlights the importance of the absolute III & V fluxes in optimizing III-V nanowire growth. The presence of different types of [111]B-oriented nanowires with discrete differences in diameter modulation, growth rate, and cross-sectional shape likely stems from variations in seed particle composition and phase between different nanowires, highlighting difficulties in obtaining uniform nanowire arrays with compound-forming seed alloys. However, different strategies were developed here to preferentially produce each of the three types of [111]B-oriented nanowires that were observed, suggesting that experimental techniques may be used to control the composition and phase of the seed particle.

Chapter 9: Conclusions

In this thesis, both experimental and theoretical investigations were employed to develop tools for controlling the structure, morphology, and composition of compound semiconductor nanowires, particularly III-V nitrides. The tools developed in this thesis provide a foundation for synthesizing nanowires with desired properties that are tailored for specific electronic and optoelectronic device applications.

9.1. Summary & implications of thesis work

Techniques were developed in Chapter 4 for controlling nanowire growth direction, tapering, and defect density in GaN nanowires. By using *c*-sapphire and *r*-sapphire substrates, GaN nanowires were grown preferentially in the polar *c*-direction and nonpolar *m*-direction, respectively. Thus, using growth substrates that are standard for GaN film growth, either *c*-GaN or *m*-GaN nanowires can be chosen for radial or axial heterostructures, respectively, with nonpolar-oriented heterojunctions. Film deposition on the nanowire sidewalls was minimized by reducing the Ga flux and increasing the density of nanowires. This technique could be used to enable growth of nanowires with uniform diameters at higher temperatures. Using straight taper-free *m*-directional GaN nanowires, the fundamental growth mechanism was elucidated by analyzing the diameter-dependent growth rate. A model was developed to demonstrate that growth was limited by monolayer nucleation and that nucleation occurs preferentially around the perimeter of the liquid/solid interface. The significance of nucleation in nanowire growth was illustrated by the fact that Ni-seeded nanowires grew faster than Au-seeded nanowires and contained a much lower density of stacking defects. These results indicate that rapid growth of defect-free nanowires can be enabled by choosing seed alloys with a low liquid/solid surface energy that reduces the energy barrier to nucleation.

Next, nonpolar-directional InN/InGaN axial heterostructure nanowires were fabricated in Chapter 5 by introducing TMG during InN growth. The allowable flux of TMG was limited by the formation of a GaN shell for higher and more prolonged TMG fluxes. Radial shell growth was effectively minimized by increasing system temperature and pressure, enabling greater TMG flows. However, likely due to reduction of the local supply of Ga at the seed, axial InGaN growth was also inhibited. Therefore, brief high-flux pulses were used at lower pressure to

produce InN/InGaN heterostructures with minimal GaN shell growth. The introduction of TMG induced axial changes in nanowire diameter and cross-sectional shape, which were analyzed using electron tomography and EDS and found to be a consequence of changes in seed particle volume and facet surface energy. In addition to constituting the first demonstration of nonpolar-oriented III-V nitride axial heterostructure nanowires, these results reveal the complexity of ternary nanowire growth using seed particles, as the composition of the III element in both the vapor/adatom phase and seed phase can have a significant impact on nanowire composition.

In Chapter 6, variations in the vapor-phase concentration of V and III precursors were used in the growth of binary III-V nitride nanowires to alter the seed particle composition and therefore nanowire diameter. A reduction in the V flux during InN growth produced segments with slower growth rates and larger diameters, while a reduction in the III flux also produced segments with slower growth rates, but larger diameters. Because of the low solubility of N in both Au and Ga, it does not alloy with the seed.^{69,70} Therefore, while the III flux controls the incorporation rate of III element incorporation into the seed particle, the V flux controls the extraction rate of III element extraction out of the seed. Measurements of seed particle composition indicate that an increase in nanowire diameter was associated with an increase in seed particle composition, which increases the volume of the seed particle. Additionally, nanowires were fabricated with thin-diameter notches that were shown to promote preferential fracture, which could be used advantageously in certain nanowire applications. This flow-controlled technique provides a practical template-free route to fabricating nanowires with tunable diameter changes, which have many potential applications in addition to controlled fracture.

Next in Chapter 7, the potential and limitations of template-free particle-mediated nanowire diameter modulation were explored using experimental results from InN and GaN nanowires as a basis. A model was developed that takes into account contributions of changes in seed particle volume, wetting angle, and three-dimensional morphology to changes in nanowire diameter. For InN nanowires, the diameter changes were found to be primarily driven by changes in seed particle volume. However, changes in wetting angle accounted for the fact that triangular nanowires had larger diameter ratios than hexagonal nanowires. Diameter ratios in excess of 2 were achieved with GaN nanowires due to significant changes in both seed particle volume and wetting angle. Furthermore, the model was used to assess the morphology and surface energy of the liquid/solid interface. Although the liquid/solid interface has commonly been assumed to be

flat, the force balance is not upheld, the calculated surface energy is quite low, and the nanowire diameter would evolve relatively slowly. However, either a faceted or rounded interface structure is feasible. In addition to explaining the results for InN and GaN, this model provides general guidelines for nanowire diameter modulation, including seed material selection. Furthermore, it can be applied in assessing fundamental growth phenomena. For example, by pairing this model with *in situ* TEM investigations, the nanoscopic shape of the liquid/solid interface can be elucidated.

Finally in Chapter 8, the flow-controlled diameter modulation approach was applied to GaAs nanowires to demonstrate the general applicability of the technique for compound semiconductor nanowires. The trends in growth rate and diameter with changes in III and V flow for GaAs nanowires were the same as those for InN and GaN nanowires. Furthermore, changes in both III and V flow were used in the same growth to produce more significant diameter ratios. Interestingly, three different types of vertically oriented [111]B GaAs nanowires were observed and had discrete differences in nanowire growth rate, diameter modulation, and cross-sectional shape. These discrepancies are likely due to variations in seed particle phase. By controlling conditions during nucleation, each type of diameter modulation behavior was produced preferentially. Together, these results demonstrate the general applicability of the flow-controlled diameter modulation strategy to compound semiconductor nanowires and highlight the importance of both relative and absolute fluxes of both the III and V precursors during growth. Additionally, the control of nanowire type suggests that, while compound-forming seed alloys may introduce further complexities into nanowire growth, they can also provide versatility in producing nanowires with desired structure and morphology.

9.2. Suggested future work

In addition to providing concrete strategies for tailoring nanowire structure, morphology, and composition, these studies also open up new questions that warrant further analysis. Below are three recommended avenues of research that would provide further insight into effective nanowire growth strategies.

9.2.1. *Alternative seed metals for III-V nitride axial heterostructures*

In the fabrication of InN/InGaN axial heterostructure nanowires, achieving high Ga composition in the InGaN discs was challenging due to the formation of a GaN shell at high Ga fluxes. Furthermore, formation of InGaN was only achievable using brief high-flux TMG pulses, limiting the ability to control the length of segments with different composition. The high flux of Ga required to form InGaN indicates that it is difficult to drive Ga into Au-In alloys, and other studies also indicate that Ga and In may not mix well in ternary Au-In-Ga seed particles.¹¹⁷ Therefore, an investigation into viable alternative seed metals for ternary InGaN nanowires would be useful. While GaN nanowires have been effectively grown with various metals including Au, Ni, and Fe,⁶³ synthesis of InN nanowires with metals other than Au has proven challenging. Attempts were made here to use Ni and Ag seed particles, but no nanowire growth was observed. Unfortunately, no known model exists for predicting the viability of a particular metal for seeding a specific nanowire material. Furthermore ternary phase diagrams for InGaM (where M is a metal) alloys are limited. However, by surveying effective seed metals used in synthesis of other nanowire materials and inspecting InM and GaM binary phase diagrams, some prospective candidates can be extracted. Notably, in this work, significant differences in nanowire growth were observed for colloids versus films. Thus it may be useful to investigate both dense and sparse nanowire growth for each chosen metal. For sparse nanowires, lithographic techniques could be used to deposit multiple metals in different regions of the same substrate.

9.2.2. *Quantitative fracture analysis of notched nanowires*

The bending tests of notched GaN nanowires provide a proof of concept that thin-diameter notches can be used to promote preferential fracture in nanowires, which could potentially be used for increasing throughput in commercial nanowire synthesis and/or facilitating transfer of nanowires from the growth substrate to foreign substrates. However, quantitative analysis of the fracture of notched nanowires would provide more insight into the extent of the effect of notches on nanowire mechanical properties and aid in the design of nanowires with ideal notch geometry. This analysis could include the dependence of fracture behavior on nanowire diameter, notch diameter, and nanowire/notch diameter ratio. Additionally, notched nanowires could be fabricated with other materials (e.g. GaAs) to clarify the role of inherent mechanical properties to

determine if this strategy for controlled fracture is more viable in some materials than others. Furthermore, once suitable materials and geometries have been identified from investigations of individual nanowires, a demonstration of controlled fracture of nanowire arrays would truly reveal the potential of this technique.

9.2.3. *Role of seed particle in phase in ternary alloy growth*

In Chapter 8, variations in the morphology between three different types of [111]B nanowires were attributed to differences in seed particle phase, and each of the three types of diameter modulation behavior were produced preferentially by controlling growth conditions. The same strategies used to control seed particle phase for diameter modulation could also be applied in the growth of axial heterostructures composed of ternary AlGaAs alloys. First, further insight into the exact phase of the seed particle for each nanowire type may be gained from improved analysis of seed particle composition. Cooling strategies have been shown to affect *ex situ* measurement of seed composition,²¹¹ so a study of cooling conditions on measured seed particle composition could enable identification of seed particle phase. Then GaAs/AlGaAs axial heterostructures can be grown by varying the Ga and Al precursor fluxes. The effects of seed particle phase on nanowire composition can then be evaluated. With knowledge of each phase, these effects can be related back to fundamental phenomena and provide insight into general strategies for controlling nanowire composition with a variety of seed and nanowire materials.

List of Abbreviations

<i>a</i> -	[11-20] direction or (11-20) plane
BSF	basal-plane stacking fault
<i>c</i> -	[0001] direction or (0001) plane
CEA-Leti	Commissariat à l'énergie atomique et aux énergies alternatives - Laboratoire d'électronique des technologies de l'information
CVD	chemical vapor deposition
DF	dark field
DI	deionized
EDS	energy dispersive X-ray spectroscopy
FFT	fast Fourier transform
HR	high resolution
LED	light emitting diode
<i>l/s</i>	liquid/solid (interface)
<i>m</i> -	[1-100] direction or (1-100) plane
MOCVD	metalorganic chemical vapor deposition
MQW	multiple quantum well
NW	nanowire
OPV	organic photovoltaic
PV	photovoltaic
QCSE	quantum-confined Stark effect
<i>r</i> -	[1-102] direction or (1-102) plane
SAD	selected area diffraction
sccm	standard cubic centimeters per minute
SEM	scanning electron microscope/microscopy
SF	stacking fault
STEM	scanning transmission electron microscope/microscopy
TEM	transmission electron microscope/microscopy
TMG	trimethylgallium
TMI	trimethylindium

TPB	triple-phase boundary
$v/l/s$	vapor/liquid/solid (interface)
v/s	vapor/solid (interface)
VLS	vapor-liquid-solid (growth mechanism)
VSS	vapor-solid-solid (growth mechanism)
VS	vapor-solid (growth mechanism)

References

1. Wu, J.; Walukiewicz, W.; Yu, K. M.; Shan, W.; Ager, J. W.; Haller, E. E.; Lu, H.; Schaff, W. J.; Metzger, W. K.; Kurtz, S. *Journal of Applied Physics*. "Superior radiation resistance of $\text{In}_{1-x}\text{Ga}_x\text{N}$ alloys: Full-solar-spectrum photovoltaic material system", **94** (2003) 6477-6482.
2. Park, Y. S.; Park, C. M.; Fu, D. J.; Kang, T. W.; Oh, J. E. *Applied Physics Letters*. "Photoluminescence studies of GaN nanorods on Si (111) substrates grown by molecular-beam epitaxy", **85** (2004) 5718-5720.
3. Dick, K. A. *Progress in Crystal Growth and Characterization of Materials*. "A review of nanowire growth promoted by alloys and non-alloying elements with emphasis on Au-assisted III-V nanowires", **54** (2008) 138-173.
4. Connell, J. G.; Yoon, K.; Perea, D. E.; Schwalbach, E. J.; Voorhees, P. W.; Lauhon, L. J. *Nano Letters*. "Identification of an intrinsic source of doping inhomogeneity in vapor-liquid-solid-grown nanowires", **13** (2013) 199-206.
5. Glas, F.; Harmand, J. C.; Patriarche, G. *Physical Review Letters*. "Why does wurtzite form in nanowires of III-V zinc blende semiconductors?", **99** (2007).
6. Frank, M. M.; Wilk, G. D.; Starodub, D.; Gustafsson, T.; Garfunkel, E.; Chabal, Y. J.; Grazul, J.; Muller, D. A. *Applied Physics Letters*. " HfO_2 and Al_2O_3 gate dielectrics on GaAs grown by atomic layer deposition", **86** (2005).
7. Wen, C. Y.; Tersoff, J.; Hillerich, K.; Reuter, M. C.; Park, J. H.; Kodambaka, S.; Stach, E. A.; Ross, F. M. *Physical Review Letters*. "Periodically changing morphology of the growth interface in Si, Ge, and GaP nanowires", **107** (2011).
8. Clark, T. E.; Nimmatouri, P.; Lew, K. K.; Pan, L.; Redwing, J. M.; Dickey, E. C. *Nano Letters*. "Diameter dependent growth rate and interfacial abruptness in vapor-liquid-solid Si/Si_{1-x}Ge_x heterostructure nanowires", **8** (2008) 1246-1252.
9. Bennett, S. E. *Materials Science and Technology*. "Dislocations and their reduction in GaN", **26** (2010) 1017-1028.
10. Moore, J. C.; Kasliwal, V.; Baski, A. A.; Ni, X.; Ozgur, U.; Morkoc, H. *Applied Physics Letters*. "Local electronic and optical behaviors of *a*-plane GaN grown via epitaxial lateral overgrowth", **90** (2007).
11. Van de Walle, C. G.; Neugebauer, J. *Journal of Applied Physics*. "First-principles calculations for defects and impurities: Applications to III-nitrides", **95** (2004) 3851-3879.
12. Sugahara, T.; Sato, H.; Hao, M.; Naoi, Y.; Kurai, S.; Tottori, S.; Yamashita, K.; Nishino, K.; Romano, L. T.; Sakai, S. *Japanese Journal of Applied Physics*. "Direct evidence that dislocations are non-radiative recombination centers in GaN", **37** (1998) L398-L400.
13. Bryllert, T.; Wernersson, L. E.; Lowgren, T.; Samuelson, L. *Nanotechnology*. "Vertical wrap-gated nanowire transistors", **17** (2006) S227-S230.
14. Colinge, J. P.; Lee, C. W.; Afzal, A.; Akhavan, N. D.; Yan, R.; Ferain, I.; Razavi, P.; O'Neill, B.; Blake, A.; White, M.; Kelleher, A. M.; McCarthy, B.; Murphy, R. *Nature Nanotechnology*. "Nanowire transistors without junctions", **5** (2010) 225-229.
15. Majumdar, A. *Science*. "Thermoelectricity in semiconductor nanostructures", **303** (2004) 777-778.
16. Hicks, L. D.; Dresselhaus, M. S. *Physical Review B*. "Thermoelectric figure of merit of a one-dimensional conductor", **47** (1993) 16631-16634.
17. Hochbaum, A. I.; Chen, R. K.; Delgado, R. D.; Liang, W. J.; Garnett, E. C.; Najarian, M.; Majumdar, A.; Yang, P. D. *Nature*. "Enhanced thermoelectric performance of rough silicon nanowires", **451** (2008) 163-U5.
18. Fan, Z. Y.; Kapadia, R.; Leu, P. W.; Zhang, X. B.; Chueh, Y. L.; Takei, K.; Yu, K.; Jamshidi, A.; Rathore, A. A.; Ruebusch, D. J.; Wu, M.; Javey, A. *Nano Letters*. "Ordered arrays of dual-diameter nanopillars for maximized optical absorption", **10** (2010) 3823-3827.
19. Kelzenberg, M. D.; Boettcher, S. W.; Petykiewicz, J. A.; Turner-Evans, D. B.; Putnam, M. C.; Warren, E. L.; Spurgeon, J. M.; Briggs, R. M.; Lewis, N. S.; Atwater, H. A. *Nature Materials*. "Enhanced absorption and carrier collection in Si wire arrays for photovoltaic applications", **9** (2010) 239-244.
20. Feldman, D.; Barbose, G.; Margolis, R.; Wiser, R.; Darghouth, N.; Goodrich, A. *Photovoltaic (PV) Pricing Trends: Historical, Recent, and Near-Term Projections* DOE/GO-102012-3839 U.S. Department of Energy: November 2012, 2012.
21. Andersson, B. V.; Herland, A.; Masich, S.; Inganäs, O. *Nano Letters*. "Imaging of the 3D nanostructure of a polymer solar cell by electron tomography", **9** (2009) 853-855.

22. van Bavel, S. S.; Sourty, E.; de With, G.; Loos, J. *Nano Letters*. "Three-dimensional nanoscale organization of bulk heterojunction polymer solar cells", **9** (2009) 507-513.
23. Huynh, W. U.; Dittmer, J. J.; Alivisatos, A. P. *Science*. "Hybrid nanorod-polymer solar cells", **295** (2002) 2425-2427.
24. Ren, S. Q.; Zhao, N.; Crawford, S. C.; Tambe, M.; Bulovic, V.; Gradecak, S. *Nano Letters*. "Heterojunction photovoltaics using GaAs nanowires and conjugated polymers", **11** (2011) 408-413.
25. Nduwimana, A.; Musin, R. N.; Smith, A. M.; Wang, X. Q. *Nano Letters*. "Spatial carrier confinement in core-shell and multishell nanowire heterostructures", **8** (2008) 3341-3344.
26. Ra, Y.-H.; Navamathavan, R.; Park, J.-H.; Lee, C.-R. *Nano Letters*. "Coaxial $\text{In}_x\text{Ga}_{1-x}\text{N}/\text{GaN}$ multiple quantum well nanowire arrays on Si(111) substrate for high-performance light-emitting diodes", (2013) Articles ASAP, dx.doi.org/10.1021/nl400906r.
27. Gradecak, S.; Qian, F.; Li, Y.; Park, H. G.; Lieber, C. M. *Applied Physics Letters*. "GaN nanowire lasers with low lasing thresholds", **87** (2005).
28. Kim, H. M.; Cho, Y. H.; Lee, H.; Kim, S. I.; Ryu, S. R.; Kim, D. Y.; Kang, T. W.; Chung, K. S. *Nano Letters*. "High-brightness light emitting diodes using dislocation-free indium gallium nitride/gallium nitride multiquantum-well nanorod arrays", **4** (2004) 1059-1062.
29. Diedenhofen, S. L.; Janssen, O. T. A.; Hocevar, M.; Pierret, A.; Bakkers, E. P. A. M.; Urbach, H. P.; Rivas, J. G. *ACS Nano*. "Controlling the directional emission of light by periodic arrays of hetero-structured semiconductor nanowires", **5** (2011) 5830-5837.
30. Chesin, J.; Zhou, X.; Gradecak, S., Light extraction in individual GaN nanowires on Si for LEDs. In *Proceedings of SPIE*, San Diego, 2012; Vol. 8467, p 846703.
31. Chu, S.; Wang, G. P.; Zhou, W. H.; Lin, Y. Q.; Chernyak, L.; Zhao, J. Z.; Kong, J. Y.; Li, L.; Ren, J. J.; Liu, J. L. *Nature Nanotechnology*. "Electrically pumped waveguide lasing from ZnO nanowires", **6** (2011) 506-510.
32. Henneghien, A. L.; Gayral, B.; Desieres, Y.; Gerard, J. M. *Journal of the Optical Society of America B*. "Simulation of waveguiding and emitting properties of semiconductor nanowires with hexagonal or circular sections", **26** (2009) 2396-2403.
33. Koleske, D. D.; Wickenden, A. E.; Henry, R. L.; Culbertson, J. C.; Twigg, M. E. *Journal of Crystal Growth*. "GaN decomposition in H_2 and N_2 at MOVPE temperatures and pressures", **223** (2001) 466-483.
34. Lei, T.; Ludwig, K. F.; Moustakas, T. D. *Journal of Applied Physics*. "Heteroepitaxy, polymorphism, and faulting in GaN thin-films on silicon and sapphire substrates", **74** (1993) 4430-4437.
35. LilienthalWeber, Z.; Sohn, H.; Newman, N.; Washburn, J. *Journal of Vacuum Science & Technology B*. "Electron microscopy characterization of GaN films grown by molecular-beam epitaxy on sapphire and SiC", **13** (1995) 1578-1581.
36. Miller, D. A. B.; Chemla, D. S.; Damen, T. C.; Gossard, A. C.; Wiegmann, W.; Wood, T. H.; Burrus, C. A. *Physical Review Letters*. "Band-edge electroabsorption in quantum well structures: The quantum-confined Stark effect", **53** (1984) 2173-2176.
37. Speck, J. S.; Chichibu, S. F. *MRS Bulletin*. "Nonpolar and semipolar group III nitride-based materials", **34** (2009) 304-312.
38. Lim, S. K.; Crawford, S.; Gradecak, S. *Nanotechnology*. "Growth mechanism of GaN nanowires: preferred nucleation site and effect of hydrogen", **21** (2010).
39. Tsivion, D.; Schwartzman, M.; Popovitz-Biro, R.; von Huth, P.; Joselevich, E. *Science*. "Guided growth of millimeter-long horizontal nanowires with controlled orientations", **333** (2011) 1003-1007.
40. Boulanger, J. P.; LaPierre, R. R. *Journal of Crystal Growth*. "Polytype formation in GaAs/GaP axial nanowire heterostructures", **332** (2011) 21-26.
41. Caroff, P.; Dick, K. A.; Johansson, J.; Messing, M. E.; Deppert, K.; Samuelson, L. *Nature Nanotechnology*. "Controlled polytypic and twin-plane superlattices in III-V nanowires", **4** (2009) 50-55.
42. Perea, D. E.; Hemesath, E. R.; Schwalbach, E. J.; Lensch-Falk, J. L.; Voorhees, P. W.; Lauhon, L. J. *Nature Nanotechnology*. "Direct measurement of dopant distribution in an individual vapour-liquid-solid nanowire", **4** (2009) 315-319.
43. Lim, S. K.; Tambe, M. J.; Brewster, M. M.; Gradecak, S. *Nano Letters*. "Controlled growth of ternary alloy nanowires using metalorganic chemical vapor deposition", **8** (2008) 1386-1392.
44. Kayes, B. M.; Atwater, H. A.; Lewis, N. S. *Journal of Applied Physics*. "Comparison of the device physics principles of planar and radial p-n junction nanorod solar cells", **97** (2005).
45. Singh, N.; Lim, F. Y.; Fang, W. W.; Rustagi, S. C.; Bera, L. K.; Agarwal, A.; Tung, C. H.; Hoe, K. M.; Omampuliyur, S. R.; Tripathi, D.; Adeyeye, A. O.; Lo, G. Q.; Balasubramanian, N.; Kwong, D. L., Ultra-

narrow silicon nanowire gate-all-around CMOS devices: Impact of diameter, channel-orientation and low temperature on device performance. In *2006 International Electron Devices Meeting*, San Francisco, 2006; Vol. 1-2, pp 294-297.

46. Calarco, R.; Marso, M.; Richter, T.; Aykanat, A. I.; Meijers, R.; Hart, A. V.; Stoica, T.; Luth, H. *Nano Letters*. "Size-dependent photoconductivity in MBE-grown GaN-nanowires", **5** (2005) 981-984.
47. Zhang, G. Q.; Tateno, K.; Sanada, H.; Tawara, T.; Gotoh, H.; Nakano, H. *Applied Physics Letters*. "Synthesis of GaAs nanowires with very small diameters and their optical properties with the radial quantum-confinement effect", **95** (2009).
48. Zianni, X. *Applied Physics Letters*. "Diameter-modulated nanowires as candidates for high thermoelectric energy conversion efficiency", **97** (2010).
49. Li, Y.; Xiang, J.; Qian, F.; Gradecak, S.; Wu, Y.; Yan, H.; Yan, H.; Blom, D. A.; Lieber, C. M. *Nano Letters*. "Dopant-free GaN/AlN/AlGaIn radial nanowire heterostructures as high electron mobility transistors", **6** (2006) 1468-1473.
50. Qian, F.; Gradecak, S.; Li, Y.; Wen, C. Y.; Lieber, C. M. *Nano Letters*. "Core/multishell nanowire heterostructures as multicolor, high-efficiency light-emitting diodes", **5** (2005) 2287-2291.
51. Hobbs, R. G.; Petkov, N.; Holmes, J. D. *Chemistry of Materials*. "Semiconductor nanowire fabrication by bottom-up and top-down paradigms", **24** (2012) 1975-1991.
52. Huang, Z. P.; Fang, H.; Zhu, J. *Advanced Materials*. "Fabrication of silicon nanowire arrays with controlled diameter, length, and density", **19** (2007) 744-+.
53. Huang, Z. P.; Geyer, N.; Werner, P.; de Boor, J.; Gosele, U. *Advanced Materials*. "Metal-assisted chemical etching of silicon: A review", **23** (2011) 285-308.
54. Li, Q. M.; Westlake, K. R.; Crawford, M. H.; Lee, S. R.; Koleske, D. D.; Figiel, J. J.; Cross, K. C.; Fatholouloumi, S.; Mi, Z. T.; Wang, G. T. *Optics Express*. "Optical performance of top-down fabricated InGaIn/GaN nanorod light emitting diode arrays", **19** (2011) 25528-25534.
55. Ikejiri, K.; Noborisaka, J.; Hara, S.; Motohisa, J.; Fukui, T. *Journal of Crystal Growth*. "Mechanism of catalyst-free growth of GaAs nanowires by selective area MOVPE", **298** (2007) 616-619.
56. Guo, W.; Zhang, M.; Banerjee, A.; Bhattacharya, P. *Nano Letters*. "Catalyst-free InGaIn/GaN nanowire light emitting diodes grown on (001) silicon by molecular beam epitaxy", **10** (2010) 3355-3359.
57. Noborisaka, J.; Motohisa, J.; Fukui, T. *Applied Physics Letters*. "Catalyst-free growth of GaAs nanowires by selective-area metalorganic vapor-phase epitaxy", **86** (2005).
58. Lymperakis, L.; Neugebauer, J. *Physical Review B*. "Large anisotropic adatom kinetics on nonpolar GaN surfaces: Consequences for surface morphologies and nanowire growth", **79** (2009).
59. Wagner, R. S.; Ellis, W. C. *Applied Physics Letters*. "Vapor-liquid-solid mechanism of single crystal growth", **4** (1964) 89-&.
60. Wacaser, B. A.; Dick, K. A.; Johansson, J.; Borgstrom, M. T.; Deppert, K.; Samuelson, L. *Advanced Materials*. "Preferential interface nucleation: An expansion of the VLS growth mechanism for nanowires", **21** (2009) 153-165.
61. Lim, S. K.; Crawford, S.; Habermann, G.; Gradecak, S. *Nano Letters*. "Controlled modulation of diameter and composition along individual III-V nitride nanowires", **13** (2013) 331-336.
62. Fortuna, S. A.; Li, X. L. *Semiconductor Science and Technology*. "Metal-catalyzed semiconductor nanowires: A review on the control of growth directions", **25** (2010).
63. Kuykendall, T.; Pauzaskie, P.; Lee, S. K.; Zhang, Y. F.; Goldberger, J.; Yang, P. D. *Nano Letters*. "Metalorganic chemical vapor deposition route to GaN nanowires with triangular cross sections", **3** (2003) 1063-1066.
64. Kuykendall, T.; Pauzaskie, P. J.; Zhang, Y. F.; Goldberger, J.; Sirbulu, D.; Denlinger, J.; Yang, P. D. *Nature Materials*. "Crystallographic alignment of high-density gallium nitride nanowire arrays", **3** (2004) 524-528.
65. Persson, A. I.; Larsson, M. W.; Stenstrom, S.; Ohlsson, B. J.; Samuelson, L.; Wallenberg, L. R. *Nature Materials*. "Solid-phase diffusion mechanism for GaAs nanowire growth", **3** (2004) 677-681.
66. Dick, K. A.; Deppert, K.; Martensson, T.; Mandl, B.; Samuelson, L.; Seifert, W. *Nano Letters*. "Failure of the vapor-liquid-solid mechanism in Au-assisted MOVPE growth of InAs nanowires", **5** (2005) 761-764.
67. Caroff, P.; Wagner, J. B.; Dick, K. A.; Nilsson, H. A.; Jeppsson, M.; Deppert, K.; Samuelson, L.; Wallenberg, L. R.; Wernersson, L. E. *Small*. "High-quality InAs/InSb nanowire heterostructures grown by metal-organic vapor-phase epitaxy", **4** (2008) 878-882.
68. Kuo, C. K.; Hsu, C. W.; Wu, C. T.; Lan, Z. H.; Mou, C. Y.; Chen, C. C.; Yang, Y. J.; Chen, L. C.; Chen, K. H. *Nanotechnology*. "Self-regulating and diameter-selective growth of GaN nanowires", **17** (2006) S332-S337.

69. Okamoto, H.; Massalski, T. B. *Bulletin of Alloy Phase Diagrams*. "The Au-N (gold-nitrogen) system", **5** (1984) 381-382.
70. Unland, J.; Onderka, B.; Davydov, A.; Schmid-Fetzer, R. *Journal of Crystal Growth*. "Thermodynamics and phase stability in the Ga-N system", **256** (2003) 33-51.
71. Krogstrup, P.; Popovitz-Biro, R.; Johnson, E.; Madsen, M. H.; Nygard, J.; Shtrikman, H. *Nano Letters*. "Structural phase control in self-catalyzed growth of GaAs nanowires on silicon (111)", **10** (2010) 4475-4482.
72. Cheze, C.; Geelhaar, L.; Jenichen, B.; Riechert, H. *Applied Physics Letters*. "Different growth rates for catalyst-induced and self-induced GaN nanowires", **97** (2010).
73. Rudolph, D.; Hertenberger, S.; Bolte, S.; Paosangthong, W.; Spirkoska, D.; Dobliger, M.; Bichler, M.; Finley, J. J.; Abstreiter, G.; Koblmüller, G. *Nano Letters*. "Direct observation of a noncatalytic growth regime for GaAs nanowires", **11** (2011) 3848-3854.
74. Seifert, W.; Borgstrom, M.; Deppert, K.; Dick, K. A.; Johansson, J.; Larsson, M. W.; Martensson, T.; Skold, N.; Svensson, C. P. T.; Wacaser, B. A.; Wallenberg, L. R.; Samuelson, L. *Journal of Crystal Growth*. "Growth of one-dimensional nanostructures in MOVPE", **272** (2004) 211-220.
75. Tchernycheva, M.; Sarte, C.; Ciril, G.; Travers, L.; Patriarche, G.; Harmand, J. C.; Dang, L. S.; Renard, J.; Gayral, B.; Nevou, L.; Julien, F. *Nanotechnology*. "Growth of GaN free-standing nanowires by plasma-assisted molecular beam epitaxy: structural and optical characterization", **18** (2007).
76. Froberg, L. E.; Seifert, W.; Johansson, J. *Physical Review B*. "Diameter-dependent growth rate of InAs nanowires", **76** (2007).
77. Plante, M. C.; LaPierre, R. R. *Journal of Crystal Growth*. "Growth mechanisms of GaAs nanowires by gas source molecular beam epitaxy", **286** (2006) 394-399.
78. Soci, C.; Bao, X. Y.; Aplin, D. P. R.; Wang, D. L. *Nano Letters*. "A systematic study on the growth of GaAs nanowires by metal-organic chemical vapor deposition", **8** (2008) 4275-4282.
79. Tomioka, K.; Motohisa, J.; Hara, S.; Fukui, T. *Japanese Journal of Applied Physics*. "Crystallographic structure of InAs nanowires studied by transmission electron microscopy", **46** (2007) L1102-L1104.
80. Chen, Z.; Cao, C. B. *Applied Physics Letters*. "Effect of size in nanowires grown by the vapor-liquid-solid mechanism", **88** (2006).
81. Lim, S. K. *III-V Nanowires: From Fundamental Growth Models to Novel Architectures*. Massachusetts Institute of Technology, Cambridge, 2011.
82. Kaschiev, D., *Nucleation: Basic Theory with Applications*. Oxford: Butterworth-Heinemann: 2000.
83. Joyce, H. J.; Gao, Q.; Tan, H. H.; Jagadish, C.; Kim, Y.; Fickenscher, M. A.; Perera, S.; Hoang, T. B.; Smith, L. M.; Jackson, H. E.; Yarrison-Rice, J. M.; Zhang, X.; Zou, J. *Nano Letters*. "Unexpected benefits of rapid growth rate for III-V nanowires", **9** (2009) 695-701.
84. Crawford, S.; Lim, S. K.; Gradecak, S. *Nano Letters*. "Fundamental insights into nanowire diameter modulation and the liquid/solid interface", **13** (2013) 226-232.
85. König, U.; Keck, W. *Journal of the Electrochemical Society*. "Contact angles between III-V melts and several substrates", **130** (1983) 685-686.
86. Nikolopoulos, P.; Agathopoulos, S.; Angelopoulos, G. N.; Naoumidis, A.; Grubmeier, H. *Journal of Materials Science*. "Wettability and interfacial energies in SiC-liquid metal systems", **27** (1992) 139-145.
87. Johansson, J.; Karlsson, L. S.; Dick, K. A.; Bolinsson, J.; Wacaser, B. A.; Deppert, K.; Samuelson, L. *Crystal Growth & Design*. "Effects of supersaturation on the crystal structure of gold seeded III-V nanowires", **9** (2009) 766-773.
88. Mohseni, P. K.; LaPierre, R. R. *Nanotechnology*. "A growth interruption technique for stacking fault-free nanowire superlattices", **20** (2009).
89. Algra, R. E.; Verheijen, M. A.; Borgstrom, M. T.; Feiner, L. F.; Immink, G.; van Enckevort, W. J. P.; Vlieg, E.; Bakkers, E. P. A. M. *Nature*. "Twinning superlattices in indium phosphide nanowires", **456** (2008) 369-372.
90. Schmidt, V.; Wittemann, J. V.; Senz, S.; Gosele, U. *Advanced Materials*. "Silicon nanowires: A review on aspects of their growth and their electrical properties", **21** (2009) 2681-2702.
91. Wallentin, J.; Ek, M.; Wallenberg, L. R.; Samuelson, L.; Deppert, K.; Borgstrom, M. T. *Nano Letters*. "Changes in contact angle of seed particle correlated with increased zincblende formation in doped InP nanowires", **10** (2010) 4807-4812.
92. Joyce, H. J.; Wong-Leung, J.; Gao, Q.; Tan, H. H.; Jagadish, C. *Nano Letters*. "Phase perfection in zinc blende and wurtzite III-V nanowires using basic growth parameters", **10** (2010) 908-915.
93. De Jong, E.; LaPierre, R. R.; Wen, J. Z. *Nanotechnology*. "Detailed modeling of the epitaxial growth of GaAs nanowires", **21** (2010).

94. Johansson, J.; Karlsson, L. S.; Svensson, C. P. T.; Martensson, T.; Wacaser, B. A.; Deppert, K.; Samuelson, L.; Seifert, W. *Nature Materials*. "Structural properties of (111)B-oriented III-V nanowires", **5** (2006) 574-580.
95. Gamalski, A. D.; Ducati, C.; Hofmann, S. *Journal of Physical Chemistry C*. "Cyclic supersaturation and triple phase boundary dynamics in germanium nanowire growth", **115** (2011) 4413-4417.
96. Oh, S. H.; Chisholm, M. F.; Kauffmann, Y.; Kaplan, W. D.; Luo, W. D.; Ruhle, M.; Scheu, C. *Science*. "Oscillatory mass transport in vapor-liquid-solid growth of sapphire nanowires", **330** (2010) 489-493.
97. Haxhimali, T.; Buta, D.; Asta, M.; Voorhees, P. W.; Hoyt, J. J. *Physical Review E*. "Size-dependent nucleation kinetics at nonplanar nanowire growth interfaces", **80** (2009).
98. Ryu, S.; Cai, W. *Journal of Materials Research*. "Molecular dynamics simulations of gold-catalyzed growth of silicon bulk crystals and nanowires", **26** (2011) 2199-2206.
99. Schwarz, K. W.; Tersoff, J. *Physical Review Letters*. "From droplets to nanowires: Dynamics of vapor-liquid-solid growth", **102** (2009).
100. Schwarz, K. W.; Tersoff, J. *Nano Letters*. "Elementary processes in nanowire growth", **11** (2011) 316-320.
101. Wen, C. Y.; Reuter, M. C.; Bruley, J.; Tersoff, J.; Kodambaka, S.; Stach, E. A.; Ross, F. M. *Science*. "Formation of compositionally abrupt axial heterojunctions in silicon-germanium nanowires", **326** (2009) 1247-1250.
102. Cai, X. M.; Ye, F.; Jing, S. Y.; Zhang, D. P.; Fan, P.; Xie, E. Q. *Applied Surface Science*. "A systematic study of chemical vapor deposition growth of InN", **255** (2008) 2153-2158.
103. Tambe, M. J.; Ren, S. Q.; Gradecak, S. *Nano Letters*. "Effects of gold diffusion on *n*-type doping of GaAs nanowires", **10** (2010) 4584-4589.
104. Zhou, X.; Chesin, J.; Crawford, S.; Gradecak, S. *Nanotechnology*. "Using seed particle composition to control structural and optical properties of GaN nanowires", **23** (2012).
105. Schmidt, V.; Senz, S.; Gosele, U. *Nano Letters*. "Diameter-dependent growth direction of epitaxial silicon nanowires", **5** (2005) 931-935.
106. Wu, Y.; Cui, Y.; Huynh, L.; Barrelet, C. J.; Bell, D. C.; Lieber, C. M. *Nano Letters*. "Controlled growth and structures of molecular-scale silicon nanowires", **4** (2004) 433-436.
107. Shan, C. X.; Liu, Z.; Hark, S. K. *Applied Physics Letters*. "CdSe nanowires with controllable growth orientations", **90** (2007).
108. Lugstein, A.; Steinmair, M.; Hyun, Y. J.; Hauer, G.; Pongratz, P.; Bertagnolli, E. *Nano Letters*. "Pressure-induced orientation control of the growth of epitaxial silicon nanowires", **8** (2008) 2310-2314.
109. Hyun, Y. J.; Lugstein, A.; Steinmair, M.; Bertagnolli, E.; Pongratz, P. *Nanotechnology*. "Orientation specific synthesis of kinked silicon nanowires grown by the vapour-liquid-solid mechanism", **20** (2009).
110. Takeuchi, T.; Sota, S.; Katsuragawa, M.; Komori, M.; Takeuchi, H.; Amano, H.; Akasaki, I. *Japanese Journal of Applied Physics*. "Quantum-confined Stark effect due to piezoelectric fields in GaInN strained quantum wells", **36** (1997) L382-L385.
111. Farrell, R. M.; Young, E. C.; Wu, F.; DenBaars, S. P.; Speck, J. S. *Semiconductor Science and Technology*. "Materials and growth issues for high-performance nonpolar and semipolar light-emitting devices", **27** (2012).
112. Adhikari, H.; Marshall, A. F.; Goldthorpe, I. A.; Chidsey, C. E. D.; McIntyre, P. C. *ACS Nano*. "Metastability of Au-Ge liquid nanocatalysts: Ge vapor-liquid-solid nanowire growth far below the bulk eutectic temperature", **1** (2007) 415-422.
113. Joyce, H. J.; Gao, Q.; Tan, H. H.; Jagadish, C.; Kim, Y.; Zhang, X.; Guo, Y. N.; Zou, J. *Nano Letters*. "Twin-free uniform epitaxial GaAs nanowires grown by a two-temperature process", **7** (2007) 921-926.
114. Musin, I. R.; Filler, M. A. *Nano Letters*. "Chemical control of semiconductor nanowire kinking and superstructure", **12** (2012) 3363-3368.
115. Xu, H. Y.; Wang, Y.; Guo, Y. N.; Liao, Z. M.; Gao, Q.; Jiang, N.; Tan, H. H.; Jagadish, C.; Zou, J. *Crystal Growth & Design*. "High-density, defect-free, and taper-restrained epitaxial GaAs nanowires induced from annealed Au thin films", **12** (2012) 2018-2022.
116. Clark, T. E.; Nimmatoori, P.; Lew, K. K.; Pan, L.; Redwing, J. M.; Dickey, E. C. *Nano Letters*. "Diameter dependent growth rate and interfacial abruptness in vapor-liquid-solid Si/Si(1-x)Ge(x) heterostructure nanowires", **8** (2008) 1246-1252.
117. Dick, K. A.; Bolinsson, J.; Borg, B. M.; Johansson, J. *Nano Letters*. "Controlling the abruptness of axial heterojunctions in III-V nanowires: Beyond the reservoir effect", **12** (2012) 3200-3206.
118. Harmand, J. C.; Glas, F.; Patriarche, G. *Physical Review B*. "Growth kinetics of a single InP_{1-x}As_x nanowire", **81** (2010).

119. Matsuoka, T. *Applied Physics Letters*. "Calculation of unstable mixing region in wurtzite $\text{In}_{1-x-y}\text{Ga}_x\text{Al}_y\text{N}$ ", **71** (1997) 105-106.
120. El-Masry, N. A.; Piner, E. L.; Liu, S. X.; Bedair, S. M. *Applied Physics Letters*. "Phase separation in InGaN grown by metalorganic chemical vapor deposition", **72** (1998) 40-42.
121. Kuykendall, T.; Ulrich, P.; Aloni, S.; Yang, P. *Nature Materials*. "Complete composition tunability of InGaN nanowires using a combinatorial approach", **6** (2007) 951-956.
122. Yoshimoto, N.; Matsuoka, T.; Sasaki, T.; Katsui, A. *Applied Physics Letters*. "Photoluminescence of InGaN films grown at high temperature by metalorganic vapor phase epitaxy", **59** (1991) 2251-2253.
123. Matsuoka, T., Progress in MOVPE-growth of GaN to InN. In *Proceedings of SPIE*, San Jose, 2008; Vol. 6900, pp S9000-S9000.
124. Zhang, X.; Lew, K. K.; Nimmatoori, P.; Redwing, J. M.; Dickey, E. C. *Nano Letters*. "Diameter-dependent composition of vapor-liquid-solid grown $\text{Si}_{1-x}\text{Ge}_x$ nanowires", **7** (2007) 3241-3245.
125. Chiamonte, T.; Tizei, L. H. G.; Ugarte, D.; Cotta, M. A. *Nano Letters*. "Kinetic effects in InP nanowire growth and stacking fault formation: The role of interface roughening", **11** (2011) 1934-1940.
126. Poole, P. J.; Dalacu, D.; Wu, X.; Lapointe, J.; Mnaymneh, K. *Nanotechnology*. "Interplay between crystal phase purity and radial growth in InP nanowires", **23** (2012).
127. Martensson, T.; Borgstrom, M.; Seifert, W.; Ohlsson, B. J.; Samuelson, L. *Nanotechnology*. "Fabrication of individually seeded nanowire arrays by vapour-liquid-solid growth", **14** (2003) 1255-1258.
128. Wang, H. T.; Xie, Z. P.; Yang, W. Y.; Fang, J. Y.; An, L. N. *Crystal Growth & Design*. "Morphology control in the vapor-liquid-solid growth of SiC nanowires", **8** (2008) 3893-3896.
129. Musin, I. R.; Boyuk, D. S.; Filler, M. A. *Journal of Vacuum Science & Technology B*. "Surface chemistry controlled diameter-modulated semiconductor nanowire superstructures", **31** (2013).
130. Born, M.; Wolf, E., *Principles of Optics*. 7th ed. ed.; Cambridge University Press: Cambridge, 1999.
131. Lentzen, M. *Microscopy and Microanalysis*. "Progress in aberration-corrected high-resolution transmission electron microscopy using hardware aberration correction", **12** (2006) 191-205.
132. Williams, D. B.; Carter, C. B., *Transmission Electron Microscopy: A Textbook for Materials Science*. Plenum Press: New York City, 1996.
133. Romanov, A. E.; Baker, T. J.; Nakamura, S.; Speck, J. S. *Journal of Applied Physics*. "Strain-induced polarization in wurtzite III-nitride semipolar layers", **100** (2006).
134. Li, D. S.; Chen, H.; Yu, H. B.; Zheng, X. H.; Huang, Q.; Zhou, J. M. *Chinese Physics Letters*. "Growth of a -plane GaN films on r -plane sapphire substrates by metalorganic chemical vapour deposition", **21** (2004) 970-971.
135. Jasinski, J.; Liliental-Weber, Z.; Maruska, H.-P.; Chai, B. H.; Hill, D. W.; Chou, M. M. C.; Gallagher, J. J.; Brown, S. *Structural properties of free-standing 50 mm diameter GaN wafers with (10-10) orientation grown on LiAlO_2* ; Lawrence Berkeley National Laboratory: 2005.
136. Tham, D.; Nam, C. Y.; Fischer, J. E. *Advanced Functional Materials*. "Defects in GaN nanowires", **16** (2006) 1197-1202.
137. Stampfl, C.; Van de Walle, C. G. *Physical Review B*. "Energetics and electronic structure of stacking faults in AlN, GaN, and InN", **57** (1998) 15052-15055.
138. Yeh, C. Y.; Lu, Z. W.; Froyen, S.; Zunger, A. *Physical Review B*. "Zincblende-wurtzite polytypism in semiconductors", **46** (1992) 10086-10097.
139. Talin, A. A.; Wang, G. T.; Lai, E.; Anderson, R. J. *Applied Physics Letters*. "Correlation of growth temperature, photoluminescence, and resistivity in GaN nanowires", **92** (2008).
140. Wang, G. T.; Talin, A. A.; Werder, D. J.; Creighton, J. R.; Lai, E.; Anderson, R. J.; Arslan, I. *Nanotechnology*. "Highly aligned, template-free growth and characterization of vertical GaN nanowires on sapphire by metal-organic chemical vapour deposition", **17** (2006) 5773-5780.
141. Borgstrom, M. T.; Immink, G.; Ketelaars, B.; Algra, R.; Bakkers, E. P. A. M. *Nature Nanotechnology*. "Synergetic nanowire growth", **2** (2007) 541-544.
142. Suzuki, T.; Nishinaga, T. *Journal of Crystal Growth*. "First real time observation of reconstruction transition associated with Ga droplet formation and annihilation during molecular beam epitaxy of GaAs", **142** (1994) 49-60.
143. Tarsa, E. J.; Heying, B.; Wu, X. H.; Fini, P.; DenBaars, S. P.; Speck, J. S. *Journal of Applied Physics*. "Homoepitaxial growth of GaN under Ga-stable and N-stable conditions by plasma-assisted molecular beam epitaxy", **82** (1997) 5472-5479.

144. Vajpeyi, A. P.; Georgakilas, A.; Tsiakatouras, G.; Tsagaraki, K.; Androulidaki, M.; Chua, S. J.; Tripathy, S. *Physica E*. "Effect of substrate temperature on spontaneous GaN nanowire growth and optoelectronic properties", **41** (2009) 427-430.
145. Jagannathan, H.; Deal, M.; Nishi, Y.; Woodruff, J.; Chidsey, C.; McIntyre, P. C. *Journal of Applied Physics*. "Nature of germanium nanowire heteroepitaxy on silicon substrates", **100** (2006).
146. Tchernycheva, M.; Harmand, J. C.; Patriarche, G.; Travers, L.; Cirlin, G. E. *Nanotechnology*. "Temperature conditions for GaAs nanowire formation by Au-assisted molecular beam epitaxy", **17** (2006) 4025-4030.
147. Dubrovskii, V. G.; Sibirev, N. V.; Cirlin, G. E.; Harmand, J. C.; Ustinov, V. M. *Physical Review E*. "Theoretical analysis of the vapor-liquid-solid mechanism of nanowire growth during molecular beam epitaxy", **73** (2006).
148. Kashchiev, D. *Crystal Growth & Design*. "Dependence of the growth rate of nanowires on the nanowire diameter", **6** (2006) 1154-1156.
149. Dubrovskii, V. G.; Sibirev, N. V.; Cirlin, G. E.; Soshnikov, I. P.; Chen, W. H.; Larde, R.; Cadel, E.; Pareige, P.; Xu, T.; Grandidier, B.; Nys, J. P.; Stievenard, D.; Moewe, M.; Chuang, L. C.; Chang-Hasnain, C. *Physical Review B*. "Gibbs-Thomson and diffusion-induced contributions to the growth rate of Si, InP, and GaAs nanowires", **79** (2009).
150. Dubrovskii, V. G.; Sibirev, N. V.; Suris, R. A.; Cirlin, G. E.; Harmand, J. C.; Ustinov, V. M. *Surface Science*. "Diffusion-controlled growth of semiconductor nanowires: Vapor pressure versus high vacuum deposition", **601** (2007) 4395-4401.
151. Jensen, L. E.; Bjork, M. T.; Jeppesen, S.; Persson, A. I.; Ohlsson, B. J.; Samuelson, L. *Nano Letters*. "Role of surface diffusion in chemical beam epitaxy of InAs nanowires", **4** (2004) 1961-1964.
152. Kwon, J. Y.; Yoon, T. S.; Kim, K. B.; Min, S. H. *Journal of Applied Physics*. "Comparison of the agglomeration behavior of Au and Cu films sputter deposited on silicon dioxide", **93** (2003) 3270-3278.
153. Hofmann, S.; Sharma, R.; Wirth, C. T.; Cervantes-Sodi, F.; Ducati, C.; Kasama, T.; Dunin-Borkowski, R. E.; Drucker, J.; Bennett, P.; Robertson, J. *Nature Materials*. "Ledge-flow-controlled catalyst interface dynamics during Si nanowire growth", **7** (2008) 372-375.
154. Dubrovskii, V. G.; Sibirev, N. V. *Physical Review E*. "Growth rate of a crystal facet of arbitrary size and growth kinetics of vertical nanowires", **70** (2004).
155. Kawamura, F.; Imade, M.; Yoshimura, M.; Mori, Y.; Sasaki, T. *Japanese Journal of Applied Physics*. "Synthesis of GaN crystal using gallium hydride", **44** (2005) L1-L3.
156. Imade, M.; Yamada, N.; Kitano, Y.; Kawamura, F.; Yoshimura, M.; Kitaoka, Y.; Mori, Y.; Sasaki, T. *Physica Status Solidi C*. "Increase in the growth rate of GaN single crystals grown by gallium hydride vapor phase epitaxy method", **5** (2008) 1719-1722.
157. Kuo, D. H.; Yang, H. C.; Cheng, J. Y. *Journal of the Electrochemical Society*. "Catalytic effects on the growth of GaN nanowires by chemical vapor deposition with different Ga sources of GaCl₃ and Ga₂Cl₄", **158** (2011) K47-K51.
158. Weng, X. J.; Burke, R. A.; Redwing, J. M. *Nanotechnology*. "The nature of catalyst particles and growth mechanisms of GaN nanowires grown by Ni-assisted metal-organic chemical vapor deposition", **20** (2009).
159. Okamoto, H. *Journal of Phase Equilibria and Diffusion*. "Au-Ga (gold-gallium)", **34** (2013) 174-175.
160. Yuan, W. X.; Qiao, Z. Y.; Ipser, H.; Eriksson, G. *Journal of Phase Equilibria and Diffusion*. "Thermodynamic assessment of the Ni-Ga system", **25** (2004) 68-74.
161. Kodambaka, S.; Tersoff, J.; Reuter, M. C.; Ross, F. M. *Science*. "Germanium nanowire growth below the eutectic temperature", **316** (2007) 729-732.
162. Kamins, T. I.; Williams, R. S.; Basile, D. P.; Hesjedal, T.; Harris, J. S. *Journal of Applied Physics*. "Ti-catalyzed Si nanowires by chemical vapor deposition: Microscopy and growth mechanisms", **89** (2001) 1008-1016.
163. Wang, Y. W.; Schmidt, V.; Senz, S.; Gosele, U. *Nature Nanotechnology*. "Epitaxial growth of silicon nanowires using an aluminium catalyst", **1** (2006) 186-189.
164. Donaldson, A. T.; Rawlings, R. D. *Acta Metallurgica*. "Diffusion of nickel and gallium in intermetallic compound NiGa", **24** (1976) 285-291.
165. Dubrovskii, V. G.; Sibirev, N. V.; Harmand, J. C.; Glas, F. *Physical Review B*. "Growth kinetics and crystal structure of semiconductor nanowires", **78** (2008).
166. Gonzalez-Hernandez, R.; Lopez-Perez, W.; Rodriguez, J. A. *Applied Surface Science*. "Nickel adsorption and incorporation on a 2 x 2-T₄ GaN(0001) surface: A DFT study", **266** (2013) 205-208.
167. Moseley, M.; Lowder, J.; Billingsley, D.; Doolittle, W. A. *Applied Physics Letters*. "Control of surface adatom kinetics for the growth of high-indium content InGa_{1-x}N throughout the miscibility gap", **97** (2010).

168. Pantha, B. N.; Li, J.; Lin, J. Y.; Jiang, H. X. *Applied Physics Letters*. "Single phase $\text{In}_x\text{Ga}_{1-x}\text{N}$ ($0.25 \leq x \leq 0.63$) alloys synthesized by metal organic chemical vapor deposition", **93** (2008).
169. Qian, F.; Li, Y.; Gradecak, S.; Wang, D. L.; Barrelet, C. J.; Lieber, C. M. *Nano Letters*. "Gallium nitride-based nanowire radial heterostructures for nanophotonics", **4** (2004) 1975-1979.
170. Huang, Y.; Duan, X. F.; Cui, Y.; Lieber, C. M. *Nano Letters*. "Gallium nitride nanowire nanodevices", **2** (2002) 101-104.
171. Biju, K. P.; Subrahmanyam, A.; Jain, M. K. *Journal of Crystal Growth*. "Low-temperature growth of polycrystalline GaN films using modified activated reactive evaporation", **311** (2009) 2275-2280.
172. Knox-Davies, E. C.; Shannon, J. M.; Silva, S. R. P. *Journal of Applied Physics*. "The properties and deposition process of GaN films grown by reactive sputtering at low temperatures", **99** (2006).
173. Nagata, T.; Ahmet, P.; Sekiguchi, T.; Chikyow, T. *Journal of Crystal Growth*. "Low-temperature growth of GaN microcrystals from position-controlled Ga droplets arrayed by a low-energy focused ion beam system", **283** (2005) 328-331.
174. Xiao, R. F.; Liao, H. B.; Cue, N.; Sun, X. W.; Kwok, H. S. *Journal of Applied Physics*. "Growth of *c*-axis oriented gallium nitride thin films on an amorphous substrate by the liquid-target pulsed laser deposition technique", **80** (1996) 4226-4228.
175. Kruse, C.; Einfeldt, S.; Bottcher, T.; Hommel, D. *Applied Physics Letters*. "In as a surfactant for the growth of GaN (0001) by plasma-assisted molecular-beam epitaxy", **79** (2001) 3425-3427.
176. Khan, M. A.; Skogman, R. A.; Schulze, R. G.; Gershenson, M. *Applied Physics Letters*. "Electrical properties and ion implantation of epitaxial GaN, grown by low-pressure metalorganic chemical vapor deposition", **42** (1983) 430-432.
177. Wickenden, A. E.; Koleske, D. D.; Henry, R. L.; Gorman, R. J.; Twigg, M. E.; Fatemi, M.; Freitas, J. A.; Moore, W. J. *Journal of Electronic Materials*. "The influence of OMVPE growth pressure on the morphology, compensation, and doping of GaN and related alloys", **29** (2000) 21-26.
178. Wickenden, A. E.; Koleske, D. D.; Henry, R. L.; Twigg, M. E.; Fatemi, M. *Journal of Crystal Growth*. "Resistivity control in unintentionally doped GaN films grown by MOCVD", **260** (2004) 54-62.
179. Bi, Y.; Wang, X. L.; Wang, C. M.; Li, J. P.; Liu, H. X.; Chen, H.; Xiao, H. L.; Feng, C.; Jiang, L. J. *European Journal of Applied Physics*. "The influence of pressure on the growth of InAlN/AlN/GaN heterostructure", **57** (2012) 30103.
180. Mesrine, M.; Grandjean, N.; Massies, J. *Applied Physics Letters*. "Efficiency of NH_3 as nitrogen source for GaN molecular beam epitaxy", **72** (1998) 350-352.
181. Okamoto, H. *Journal of Phase Equilibria and Diffusion*. "Au-In (gold-indium)", **25** (2004) 197-198.
182. Mohan, P.; Motohisa, J.; Fukui, T. *Nanotechnology*. "Controlled growth of highly uniform, axial/radial direction-defined, individually addressable InP nanowire arrays", **16** (2005) 2903-2907.
183. Koukitu, A.; Taki, T.; Takahashi, N.; Seki, H. *Journal of Crystal Growth*. "Thermodynamic study on the role of hydrogen during the MOVPE growth of group III nitrides", **197** (1999) 99-105.
184. Bhuiyan, A. G.; Hashimoto, A.; Yamamoto, A. *Journal of Applied Physics*. "Indium nitride (InN): A review on growth, characterization, and properties", **94** (2003) 2779-2808.
185. Macchesney, J. B.; Bridenbaugh, P. M.; O'Connor, P. B. *Materials Research Bulletin*. "Thermal stability of indium nitride at elevated temperatures and nitrogen pressures", **5** (1970) 783-&.
186. Tambe, M. J.; Lim, S. K.; Smith, M. J.; Allard, L. F.; Gradecak, S. *Applied Physics Letters*. "Realization of defect-free epitaxial core-shell GaAs/AlGaAs nanowire heterostructures", **93** (2008).
187. Gao, Y.; Craven, M. D.; Speck, J. S.; DenBaars, S. P.; Hu, E. L. *Applied Physics Letters*. "Dislocation- and crystallographic-dependent photoelectrochemical wet etching of gallium nitride", **84** (2004) 3322-3324.
188. Jain, A.; Weng, X. J.; Raghavan, S.; VanMil, B. L.; Myers, T.; Redwing, J. M. *Journal of Applied Physics*. "Effect of polarity on the growth of InN films by metalorganic chemical vapor deposition", **104** (2008).
189. Northrup, J. E.; Neugebauer, J. *Physical Review B*. "Indium-induced changes in GaN(0001) surface morphology", **60** (1999) R8473-R8476.
190. Joyce, H. J.; Gao, Q.; Tan, H. H.; Jagadish, C.; Kim, Y.; Zou, J.; Smith, L. M.; Jackson, H. E.; Yarrison-Rice, J. M.; Parkinson, P.; Johnston, M. B. *Progress in Quantum Electronics*. "III-V semiconductor nanowires for optoelectronic device applications", **35** (2011) 23-75.
191. Hiramatsu, K.; Nishiyama, K.; Onishi, M.; Mizutani, H.; Narukawa, M.; Motogaito, A.; Miyake, H.; Iyechika, Y.; Maeda, T. *Journal of Crystal Growth*. "Fabrication and characterization of low defect density GaN using facet-controlled epitaxial lateral overgrowth (FACELO)", **221** (2000) 316-326.
192. Boukai, A. I.; Bunimovich, Y.; Tahir-Kheli, J.; Yu, J. K.; Goddard, W. A.; Heath, J. R. *Nature*. "Silicon nanowires as efficient thermoelectric materials", **451** (2008) 168-171.

193. Hillert, M.; Jonsson, S. *Metallurgical Transactions A*. "An assessment of the Al-Fe-N system", **23** (1992) 3141-3149.
194. Marezio, M. *Acta Crystallographica*. "Refinement of crystal structure of In_2O_3 at two Wavelengths", **20** (1966) 723-&.
195. *CRC Handbook of Chemistry and Physics*. 92nd ed. ed.; Taylor and Francis Group: Boca Raton, FL, 2011.
196. Lee, C. H.; Kim, D. R.; Zheng, X. L. *Proceedings of the National Academy of Sciences of the United States of America*. "Fabricating nanowire devices on diverse substrates by simple transfer-printing methods", **107** (2010) 9950-9955.
197. Spurgeon, J. M.; Plass, K. E.; Kayes, B. M.; Brunschwig, B. S.; Atwater, H. A.; Lewis, N. S. *Applied Physics Letters*. "Repeated epitaxial growth and transfer of arrays of patterned, vertically aligned, crystalline Si wires from a single Si(111) substrate", **93** (2008).
198. Li, Q. M.; Lin, Y.; Creighton, J. R.; Figiel, J. J.; Wang, G. T. *Advanced Materials*. "Nanowire-templated lateral epitaxial growth of low-dislocation density nonpolar *a*-plane GaN on *r*-plane sapphire", **21** (2009) 2416-+.
199. Cohen-Karni, T.; Timko, B. P.; Weiss, L. E.; Lieber, C. M. *Proceedings of the National Academy of Sciences of the United States of America*. "Flexible electrical recording from cells using nanowire transistor arrays", **106** (2009) 7309-7313.
200. Fan, Z. Y.; Razavi, H.; Do, J. W.; Moriwaki, A.; Ergen, O.; Chueh, Y. L.; Leu, P. W.; Ho, J. C.; Takahashi, T.; Reichertz, L. A.; Neale, S.; Yu, K.; Wu, M.; Ager, J. W.; Javey, A. *Nature Materials*. "Three-dimensional nanopillar-array photovoltaics on low-cost and flexible substrates", **8** (2009) 648-653.
201. Ju, S. Y.; Facchetti, A.; Xuan, Y.; Liu, J.; Ishikawa, F.; Ye, P. D.; Zhou, C. W.; Marks, T. J.; Janes, D. B. *Nature Nanotechnology*. "Fabrication of fully transparent nanowire transistors for transparent and flexible electronics", **2** (2007) 378-384.
202. Weisse, J. M.; Kim, D. R.; Lee, C. H.; Zheng, X. L. *Nano Letters*. "Vertical transfer of uniform silicon nanowire arrays via crack formation", **11** (2011) 1300-1305.
203. Asthana, A.; Momeni, K.; Prasad, A.; Yap, Y. K.; Yassar, R. S. *Nanotechnology*. "In situ observation of size-scale effects on the mechanical properties of ZnO nanowires", **22** (2011).
204. Yao, J.; Yan, H.; Lieber, C. M. *Nature Nanotechnology*. "A nanoscale combing technique for the large-scale assembly of highly aligned nanowires", **8** (2013) 329-335.
205. Ross, F. M.; Tersoff, J.; Reuter, M. C. *Physical Review Letters*. "Sawtooth faceting in silicon nanowires", **95** (2005).
206. Nebol'sin, V. A.; Dunaev, A. I.; Zavalishin, M. A. *Inorganic Materials*. "Effect of the line tension at the vapor-liquid-solid boundary on the growth of silicon nanocrystals", **44** (2008) 559-562.
207. Nebol'sin, V. A.; Shchetinin, A. A. *Inorganic Materials*. "Role of surface energy in the vapor-liquid-solid growth of silicon", **39** (2003) 899-903.
208. Filippetti, A.; Fiorentini, V.; Cappellini, G.; Bosin, A. *Physical Review B*. "Anomalous relaxations and chemical trends at III-V semiconductor nitride nonpolar surfaces", **59** (1999) 8026-8031.
209. Egry, I.; Brillo, J. *Journal of Chemical and Engineering Data*. "Surface tension and density of liquid metallic alloys measured by electromagnetic levitation", **54** (2009) 2347-2352.
210. Sutter, E.; Sutter, P. *Nano Letters*. "Phase diagram of nanoscale alloy particles used for vapor-liquid-solid growth of semiconductor nanowires", **8** (2008) 411-414.
211. Harmand, J. C.; Patriarche, G.; Pere-Laperne, N.; Merat-Combes, M. N.; Travers, L.; Glas, F. *Applied Physics Letters*. "Analysis of vapor-liquid-solid mechanism in Au-assisted GaAs nanowire growth", **87** (2005).
212. Spirkoska, D.; Morral, A. F. I.; Dufouleur, J.; Xie, Q. S.; Abstreiter, G. *Physica Status Solidi RRL*. "Free standing modulation doped core-shell GaAs/AlGaAs hetero-nanowires", **5** (2011) 353-355.
213. LaPierre, R. R. *Journal of Applied Physics*. "Numerical model of current-voltage characteristics and efficiency of GaAs nanowire solar cells", **109** (2011).
214. Hua, B.; Motohisa, J.; Kobayashi, Y.; Hara, S.; Fukui, T. *Nano Letters*. "Single GaAs/GaAsP coaxial core-shell nanowire lasers", **9** (2009) 112-116.
215. Krogstrup, P.; Yamasaki, J.; Sorensen, C. B.; Johnson, E.; Wagner, J. B.; Pennington, R.; Aagesen, M.; Tanaka, N.; Nygard, J. *Nano Letters*. "Junctions in axial III-V heterostructure nanowires obtained via an interchange of group III elements", **9** (2009) 3689-3693.
216. Paiman, S.; Gao, Q.; Joyce, H. J.; Kim, Y.; Tan, H. H.; Jagadish, C.; Zhang, X.; Guo, Y.; Zou, J. *Journal of Physics D*. "Growth temperature and V/III ratio effects on the morphology and crystal structure of InP nanowires", **43** (2010).

217. Heurlin, M.; Magnusson, M. H.; Lindgren, D.; Ek, M.; Wallenberg, L. R.; Deppert, K.; Samuelson, L. *Nature*. "Continuous gas-phase synthesis of nanowires with tunable properties", **492** (2012) 90-+.
218. Takebe, T.; Fujii, M.; Yamamoto, T.; Fujita, K.; Watanabe, T. *Journal of Applied Physics*. "Orientation-dependent Ga surface diffusion in molecular beam epitaxy of GaAs on GaAs patterned substrates", **81** (1997) 7273-7281.
219. Paladugu, M.; Zou, J.; Guo, Y. N.; Zhang, X.; Joyce, H. J.; Gao, Q.; Tan, H. H.; Jagadish, C.; Kim, Y. *Applied Physics Letters*. "Polarity driven formation of InAs/GaAs hierarchical nanowire heterostructures", **93** (2008).
220. Rudolph, D.; Funk, S.; Doblinger, M.; Morkotter, S.; Hertenberger, S.; Schweickert, L.; Becker, J.; Matich, S.; Bichler, M.; Spirkoska, D.; Zardo, I.; Finley, J. J.; Abstreiter, G.; Koblmüller, G. *Nano Letters*. "Spontaneous alloy composition ordering in GaAs-AlGaAs core-shell Nanowires", **13** (2013) 1522-1527.
221. Skold, N.; Wagner, J. B.; Karlsson, G.; Hernan, T.; Seifert, W.; Pistol, M. E.; Samuelson, L. *Nano Letters*. "Phase segregation in AlInP shells on GaAs nanowires", **6** (2006) 2743-2747.
222. Uccelli, E.; Arbiol, J.; Morante, J. R.; Morral, A. F. I. *ACS Nano*. "InAs quantum dot arrays decorating the facets of GaAs nanowires", **4** (2010) 5985-5993.
223. Wacaser, B. A.; Deppert, K.; Karlsson, L. S.; Samuelson, L.; Seifert, W. *Journal of Crystal Growth*. "Growth and characterization of defect free GaAs nanowires", **287** (2006) 504-508.
224. Zou, J.; Paladugu, M.; Wang, H.; Auchterlonie, G. J.; Guo, Y. N.; Kim, Y.; Gao, Q.; Joyce, H. J.; Tan, H. H.; Jagadish, C. *Small*. "Growth mechanism of truncated triangular III-V nanowires", **3** (2007) 389-393.
225. Tambe, M. J.; Allard, L. F.; Gradecak, S. *Journal of Physics: Conference Series*. "Characterization of core-shell GaAs/AlGaAs nanowire heterostructures using advanced electron microscopy", **209** (2010) 012033.
226. Fetzer, R. S., *Ternary Alloys*. VCH: 1995; Vol. 12.
227. Kolibal, M.; Kalousek, R.; Vystavel, T.; Novak, L.; Sikola, T. *Applied Physics Letters*. "Controlled faceting in <110> germanium nanowire growth by switching between vapor-liquid-solid and vapor-solid-solid growth", **100** (2012).
228. Cheze, C.; Geelhaar, L.; Trampert, A.; Brandt, O.; Riechert, H. *Nano Letters*. "Collector phase transitions during vapor-solid-solid nucleation of GaN nanowires", **10** (2010) 3426-3431.
229. Rupp, R.; Müller, G. *Journal of Crystal Growth*. "Experimental study of the surface tension of molten GaAs and its temperature dependence under controlled As-vapor pressure", **113** (1991) 131-139.
230. Thombare, S. V.; Marshall, A. F.; McIntyre, P. C. *Journal of Applied Physics*. "Size effects in vapor-solid-solid Ge nanowire growth with a Ni-based catalyst", **112** (2012).
231. Paiman, S.; Gao, Q.; Tan, H. H.; Jagadish, C.; Pemasiri, K.; Montazeri, M.; Jackson, H. E.; Smith, L. M.; Yarrison-Rice, J. M.; Zhang, X.; Zou, J. *Nanotechnology*. "The effect of V/III ratio and catalyst particle size on the crystal structure and optical properties of InP nanowires", **20** (2009).
232. Uccelli, E.; Arbiol, J.; Magen, C.; Krogstrup, P.; Russo-Averchi, E.; Heiss, M.; Mugny, G.; Morier-Genoud, F.; Nygard, J.; Morante, J. R.; Morral, A. F. I. *Nano Letters*. "Three-dimensional multiple-order twinning of self-catalyzed GaAs nanowires on Si substrates", **11** (2011) 3827-3832.
233. Matthai, C. C.; Moran, G. A. *Applied Surface Science*. "Adsorption and diffusion of Ga, In and As adatoms on (001) and (111) GaAs surfaces: A computer simulation study", **123** (1998) 653-657.
234. Foxon, C. T.; Joyce, B. A. *Surface Science*. "Interaction kinetics of As₄ and Ga on [100] GaAs surfaces using a modulated molecular-beam technique", **50** (1975) 434-450.
235. Kim, J. H.; Moon, S. R.; Yoon, H. S.; Jung, J. H.; Kim, Y.; Chen, Z. G.; Zou, J.; Choi, D. Y.; Joyce, H. J.; Gao, Q.; Tan, H. H.; Jagadish, C. *Crystal Growth & Design*. "Taper-free and vertically oriented Ge nanowires on Ge/Si Substrates grown by a two-temperature process", **12** (2012) 135-141.
236. Denbaars, S. P.; Maa, B. Y.; Dapkus, P. D.; Danner, A. D.; Lee, H. C. *Journal of Crystal Growth*. "Homogeneous and heterogeneous thermal-decomposition rates of trimethylgallium and arsine and their relevance to the growth of GaAs by MOCVD", **77** (1986) 188-193.